Electromagnetic Induction Imaging with Atomic Magnetometers

Cameron Deans

A dissertation submitted in partial fulfillment

of the requirements for the degree of

Doctor of Philosophy

of

University College London.

Department of Physics and Astronomy

University College London

December 3, 2018

I, Cameron Deans, confirm that the work presented in this thesis is my own. Where information has been derived from other sources, I confirm that this has been indicated in the work.

Signed ..... Date .....

Abstract

Electromagnetic induction imaging (EMI) is a technique for non-invasively mapping the passive electromagnetic properties of materials. It involves the active probing of samples with a radio-frequency magnetic field and recording the details of the magnetic field produced by the induced eddy current response. The performance of an EMI system is ultimately determined by the choice of magnetic field sensor used in the measurement. The sensor's sensitivity, range of operation frequency, and sensing volume are all crucial characteristics when considering the imaging platform's capabilities.

Atomic magnetometers (AMs) – based on the coherent precession of a polarised alkali atomic vapour – currently rate amongst the most sensitive devices for magnetic field measurements. Radio-frequency atomic magnetometers (RF-AMs) are ultra-sensitive detectors of oscillating magnetic fields across a broad range of frequencies. As such, they are ideally suited to EMI applications.

This work presents the development of EMI systems based on RF-AMs. The imaging performance and a wide range of applications are experimentally demonstrated.

The continuous development of a single-channel rubidium RF-AM is described. The final device operates in unshielded environments and near room temperature with a measured sensitivity of $55\,\mathrm{fT}/\sqrt{\mathrm{Hz}}$, a photon-shot noise limit of $10\,\mathrm{fT}/\sqrt{\mathrm{Hz}}$, and a linewidth of 36 Hz. Tunability of the device is proven by consistent, narrow-linewidth operation across the kHz – MHz band – operating in magnetic fields significantly greater than previous AM designs. The sensor was developed with a small effective sensor volume, which increases the spatial resolution of the imaging.

High-resolution EMI is performed across a broad range of materials. This spans the first EMI images with an RF-AM at $6 \times 10^7\,\mathrm{S\,m^{-1}}$ to low-conductivity, non-metallic samples at $500\,\mathrm{S\,m^{-1}}$. Typically, sample volumes are of a few cm^3 and with an imaging resolution around 1 mm. These numbers make EMI with AMs (EMI-AM) suitable for numerous

applications.

Techniques – including multi-frequency image analysis – are employed to discriminate sample properties. Further work developed novel image reconstruction approaches – based on machine learning – to maximise the amount of information that can be extracted from EMI images. Finally, the potential of biomedical imaging is discussed and its feasibility verified by simulating the application of EMI-AM to imaging the conductivity of the heart.

Impact Statement

The major impact of this thesis is the development of a new quantum-based imaging technology. Namely electromagnetic induction imaging (EMI) platforms based on radio-frequency atomic magnetometers (RF-AMs). I cover the development of such systems from the first measurements and images, to prototype systems of technology readiness levels (TRL) 4-6. Numerous applications are introduced, and proof-of-principle demonstrations performed. Benefits in a wide range of fields are discussed – from security screening, the oil and gas sector, to clinical use as a medical diagnostic tool. This has spawned a new research effort in AM based eddy current imaging. This is currently being pursued by several research groups worldwide.

Inside academia, the results of this research are reported in a number of journal publications [1, 2, 3, 4, 5, 6, 7, 8], and peer-reviewed conference proceedings [9, 10, 11, 12, 13]. This research has also fostered new collaborations with the National Physical Laboratory (NPL), the University of Siena (Italy), and the National Institute of Optics of the Italian National Research Council (INO-CNR) in Pisa (Italy). During the time frame of this work, new research directions have been uncovered and investigated. These include the first applications of machine learning to diffusive systems, maximising the amount of information that can be learnt from EMI images. This was the product of a new collaboration with the Department of Computer Science (UCL). Further research strands have been stimulated in EMI with cold and ultracold atomic sensors.

Outside of academia, this work has encouraged collaborations with both national and multi-national companies and agencies. These include Innovate UK, the UK Home Office, the UK Department for Transport, and the Defence Science and Technology Laboratory (DSTL). Companies include: Thales Research and Technology (TRT), Thales Maritime Systems, AtomSensors, and Witted. Many of these collaborations are aimed at the medium-term exploitation of this research in the security and screening sectors. AM based

EMI has the potential to provide a non-ionising screening system, which could replace or complement existing X-ray based technologies. Long-term exploitation paths in biomedical imaging have been explored in conversations with Prof. Pier Lambiase (UCL and Barts Heart Centre) and in collaboration with York Instruments. The progression of sample conductivities, demonstrated in this work, have brought the promise of high-resolution EMI of biological tissues significantly closer. Application areas are envisaged in the detection and diagnosis of cardiac arrhythmias. These conditions – and directly related health problems – currently cost the NHS in excess of £2.2bn per year (Office of Health Economics, 2009).

Finally, impact in education and knowledge transfer includes participation in UK National Quantum Technology Showcase events and the UCLQ Summer School. The latter involves lab sessions – based on AM research – aimed at encouraging undergraduate students to apply for a PhD.

Acknowledgements

Firstly, I would like to thank my supervisor Ferruccio Renzoni. His balance of insight and guidance with the freedom to explore one's own ideas has provided a stimulating environment in which to pursue my research. Thanks also to Luca Marmugi, whose input and encouragement has – in no uncertain terms – enhanced every aspect of my work.

Thank you to all the members of the group, both former and current, who have provided advice, assistance, and more importantly superb company, and friendship over these years. Alexandros, Krishna, Michela, Pik, Raffaele, Sarah, and Yuval, you have made it a pleasure to come to the lab each day, and to stay unnecessarily late each night.

Thank you to all the collaborators whose consultations and precious suggestions have greatly increased my understanding. In particular, to Valerio Biancalana and Yordanka Dancheva for kindly hosting me in Siena, and for going out of their way to ensure I felt welcome and enjoyed my time there.

Thank you to the staff and students of the CDT. To Dan and Andrew as the directors, and to the peerless Lopa for all the help, organisation, and gossip. To my fellow cohort of students, Andrew, Carlo, Claudia, Josh, Lorenzo, Johnnie, Sherif, Tim, and Tom, I have greatly enjoyed your company, our shared PhD experience, and all the associated memories.

Thank you to my family, who have always supported me and encouraged me to pursue my interests. They have always been willing to proofread my work, never claiming nor desiring to comprehend the contents. Finally, to my fiancée, Anjali, whose presence has been a source of constant laughter and great inspiration for many years.

To my grandparents.

Contents

List of Figures

List of Tables

Chapter 1

Introduction

1.1 Motivation

Imaging is widespread throughout everyday life, with numerous techniques and technologies extensively and routinely deployed. Uses range from recording quotidian occurrences to the probing of samples far beyond the optical limit. Nevertheless, certain regimes lie beyond the capabilities of current technologies – either as a result of current limitations or the lack of dedicated systems. One such example is the distribution of dielectric properties. An instrument for imaging these properties – of samples ranging from metals to low-conductivity materials and biological tissues – would find numerous applications. This thesis describes the development of such a device.

1.2 MIT and EMI

The first reports concerning magnetic induction tomography (MIT) date from around 1993 [14]. MIT is a technique for probing the electromagnetic properties of samples [15]. It can provide direct non-contact, non-invasive maps of all three passive electromagnetic properties, the conductivity σ, the relative permittivity ε_r, and the relative permeability μ_r.

In MIT an oscillating magnetic field – referred to as the primary field – is applied from an excitation coil to induce eddy currents in a sample. These eddy currents generate an additional magnetic field component (the secondary field). Details of the sample's electromagnetic properties are imprinted into the properties of this field. Therefore, its detection, via a magnetic field sensor, provides insight into them.

Electromagnetic induction imaging (EMI) of samples is performed by taking spatially resolved measurements of the secondary field. The tomographic nature comes from the fact that the depth of penetration of the primary field into the sample varies with frequency. As

such, one is – in principle – able to probe the dielectric properties in slices through the sample.

1.2.1 Applications of EMI

The detection and imaging of changes in the dielectric properties finds applications in a wide range of fields. EMI is an attractive method of medical imaging as it is non-invasive and no direct contact with the patient is required [16, 17]. Furthermore, the magnetic fields used are significantly smaller than those used in many currently available medical imaging technologies, and no ionising radiation is employed.

EMI could aid the diagnosis and treatment for a range of diseases and conditions where a change in conductivity plays – or is expected to play – an important role. Potential examples include the detection and diagnosis of cardiac arrhythmias [10, 18]. These are common conditions that are characterised by irregular beatings of the heart. The causes are related to the abnormal generation and conduction of the electrical pulses that control the heart's activity [19]. Atrial fibrillation (AF) is one of the most prevalent arrhythmias, affecting more than 10% of the population aged over 70. It manifests as a sustained turbulent heartbeat. Patients with AF are likely to suffer serious resultant health problems, including heart disease and strokes. It has been suggested that AF is a result of permanent local conductivity changes in the heart. These regions interrupt the flow of electrical pulses across the heart, resulting in deterministic sources of conductivity known as rotors. The first indirect indications of these local stable sources have recently been observed in patients with AF [20, 21, 22].

Currently deployed diagnostic tools (magnetocardiography (MCG) and electrocardiography (ECG)) do not provide any insight into the causes of AF or the structures producing it. Diagnosis with these tools is also only possible when a fibrillation crisis is ongoing. As a result, the current treatments of AF (surgical procedure or drug therapy [23]) have less-than-optimal success rates. In the case of surgical treatment, by radio-frequency catheter ablation (RFCA), the success rate is estimated to be $\approx$50% after 1 year, with multiple procedures often required [24]. In many cases patients with AF are treated symptomatically with the prescription of an anticoagulant to alleviate the risk of strokes.

EMI provides a framework for directly mapping the conductivity of the heart. As such, it can provide the missing insight into the fundamental causes of AF as well as aiding diagnosis and surgery guidance. A medical diagnostic tool – based on EMI-AM – is one of

the long-term applications of this research. Simulations investigating the potential of such a device are presented in Chapter 8.

Further examples of conditions that EMI could be applicable to include: skin healing after grafts or burns [18], the detection of cerebral haemorrhages and oedemas [25, 26, 27], and the detection of cancerous tissues [18]. In the case of tumour detection, experiments have shown significant differences is the dielectric properties of malignant tissue compared to that of the surrounding healthy tissue [28, 29].

Aside from medical imaging, EMI has a broad range of industrial applications. These include: the detection and location of foreign bodies [30, 31], the security scanning of cargo [3, 32, 33], batch quality control the detection of defects in components [34, 35], investigating the structural integrity and detection corrosion in pipelines [7], and tracking ferrite powders in transport and separation processes.

1.2.2 Alternatives to EMI

MIT is one of a family of techniques developed for the non-invasive, tomographic imaging of the passive electromagnetic properties of materials. Here, I briefly introduce alternative approaches.

1.2.2.1 Electrical impedence tomography

Electrical impedance tomography (EIT) is the oldest electromagnetic imaging technique [36, 37]. An array of electrodes are placed on the surface of the sample, defining the imaging region. The electrodes are used to inject currents whilst measuring the resulting potentials. Specific current patterns are required to identify each electrode. A systematic series of four-terminal measurements of transimpedance allows the calculation of cross sections of the dielectric properties. This is done by a reconstruction algorithm that uses the measured electrode voltages and exploits the known current patterns to solve the inverse problem.

EIT systems can be split into two types: applied potential tomography (APT) [38] and adaptive current tomography (ACT) [39]. In an APT system, currents are applied sequentially using pairs of adjacent electrodes, whilst the voltages between the other adjacent pairs are measured. In contrast, an ACT system applies currents simultaneously from all electrodes, whilst also measuring the voltages on each electrode. This approach has been shown to achieve better imaging contrasts [40]. Applications of EIT include the continuous monitoring of patients [41], for example, monitoring fluid accumulation in the lungs [42].

1.2.2.2 Electrical resistance tomography and electrical capacitance tomography

Electrical resistance tomography (ERT) and electrical capacitance tomography (ECT) are techniques that differ from EIT only in the way measurements are made. In ERT only the resistive component of the impedance is calculated. ERT is applicable mostly to underground and geological applications [43, 44]. Alternatively, in ECT the capacitance between pairs of electrodes is calculated. ECT is used when measuring low-conductivity and low-permittivity samples through insulating barriers. The most common application is in multi-phase fluid flow [45].

1.2.2.3 EMI with a resonant RLC system

An alternative approach to EMI based on a resonant RLC circuit, has recently been demonstrated [46, 47]. A single excitation coil – the inductor in a parallel RLC circuit – also acts as the sensor. The eddy current response from a conductive sample is coupled into the circuit changing the level of inductance. This is detected as changes in the circuit parameters (such as the resonant frequency and quality factor). The degree of change in these parameters is dependent on the properties of the sample. By changing the resistance and capacitance in the circuit, the resonant frequency can be tuned to control the degree of penetration through conductive barriers [48].

1.3 Atomic magnetometers

Magnetic field sensors have numerous applications. These range from the earliest uses of compasses for navigation, to long-range communications, and down to the study of fundamental physics.

Atomic magnetometers (AMs) – also known as optically pumped magnetometers (OPM) – offer a quantum approach to the ultra-sensitive detection of static and oscillating magnetic fields [49, 50]. AMs trace their roots to 1957, with the first experimental demonstrations by Bell and Bloom [51, 52]. In recent years, technological developments have seen them surpass super conducting quantum interference devices (SQUIDs) as the most sensitive magnetic field sensors available. AMs have experimentally demonstrated sensitivities below $1\,\mathrm{fT}/\sqrt{\mathrm{Hz}}$ [53, 54, 55]. The fundamental limit of current devices has been predicted to be $10\,\mathrm{aT}/\sqrt{\mathrm{Hz}}$ [56].

AMs exploit magneto-optical effects: light atom interactions in the presence of a magnetic field. Resonant (or near-resonant) light is used to control the magnetic momenta of an

alkali atomic vapour and measure the effect of magnetic fields.

Alkali atoms are used as they have a single valence electron. This electron – and the atom's nucleus – possess an intrinsic quantum mechanical property called spin. The coupling of the electron spin and the nuclear spin defines the total atomic magnetic momentum (atomic spin). AMs infer the properties of magnetic fields via their effect on atomic spins. The general principles that underpin most types of AMs are described by the following stages.

A vapour cell containing alkali atoms defines the sensor. With no external influence, the atomic magnetic momenta are randomly orientated. The first stage is to create a macroscopic ground state spin polarisation. This is done by optical pumping. It involves the exchange of angular momentum from circularly polarised light (pump laser beam) to the atoms.

The vapour is then left to evolve in any external magnetic field (that is to be measured). Additional fields exert a torque on the atoms, causing them to precess. This precession occurs at the Larmor frequency, $\omega_L = \gamma|\mathbf{B}|$ – where $|\mathbf{B}|$ is the magnitude of the magnetic field and γ is the gyromagnetic ratio. The measurement of the magnetic field is therefore reduced to the measurement of the frequency ω_L. Note that the gyromagnetic ratio is defined by only fundamental physical constants,

$$\gamma = \frac{e\, g_F}{2 m_e}\,, \tag{1.1}$$

where e the charge of an electron, g_F the Landé g-factor, and m_e the rest mass of an electron. Equation 1.1 implies a crucial advantage of AMs: they do not require calibration.

The optical detection of the Lamor precession is the final stage of operation. Interaction with a measurement beam involves the exchange of angular momentum between atoms and photons – a consequence of general conservation laws. Hence, by observing the changes in properties of light propagating through the atoms, the Larmor precession frequency can be extracted. From this, the properties of $\mathbf{B}$ can be inferred.

1.3.1 Types of AMs

A number of different AM designs have been demonstrated. These are briefly introduced here. Differing designs often operate in different measurement regimes. Each has intrinsic advantages and drawbacks. These have to be taken into account depending on the desired

application.

1.3.1.1 SERF magnetometer

Among the most sensitive approaches is the spin-exchange relaxation-free magnetometer (SERF), first demonstrated in 2002 [57]. A significant limitation in atomic magnetometry is the loss of coherence due to spin exchange collisions. SERF magnetometers eliminate this effect by operating in a high-density, low magnetic field regime. Under such conditions, the spin exchange rate is fast compared to the Lamor precession. As a result, the device measures the evolution of the average atomic spin and is immune to decoherence caused by spin exchange. SERF magnetometers have demonstrated sensitivities below $1\,\mathrm{fT}/\sqrt{\mathrm{Hz}}$ [58, 59]. They are only applicable to low-frequency measurements (due to their operation in near-zero magnetic fields), for example, zero-field nuclear magnetic resonance (NMR) [60].

1.3.1.2 Radio-frequency AM

Radio-frequency atomic magnetometers (RF-AMs) – the type used throughout this work – were first described in 2005 [61]. RF-AMs detect oscillating magnetic fields by bringing them into resonance with Zeeman transitions in the ground state. This is done by controlling the bias field. Inversely, a DC field can be measured by detecting the resonant frequency. Sensitivities below $1\,\mathrm{fT}/\sqrt{\mathrm{Hz}}$ have been demonstrated inside magnetic shielding [54, 62]. Importantly, RF-AMs can maintain high-sensitivities without such shielding [63, 64]. The operating frequency can be tuned over a wide range, from near DC to the MHz band [6]. Alternative schemes have demonstrated operation in the GHz band [65]. Their sensitivity and tunability mean RF-AMs can be applied to a range of applications, for example, nuclear quadrupole resonance (NQR) [54] and EMI – the topic of this work.

1.3.1.3 NMOR magnetometer

This approach is based on exploiting non-linear magneto-optical rotation (NMOR) effects [66]. Typically these devices employ a parallel pump and probe beam arrangement to determine the magnetic field along the propagation direction. One distinct advantage of this approach is that it is all-optical – there is no requirement of magnetic field excitation. NMOR based magnetometers have demonstrated sub-picotesla levels of sensitivity to both DC and oscillating magnetic fields [67, 68, 69].

1.3.1.4 CPT magnetometer

Magnetometers based on coherent population trapping (CPT) work by monitoring the the Zeeman splitting of CPT resonances due to magnetic fields. The resonances can be detected through CPT-related electromagnetic induced transparency. However, the sensitivity of CPT-based magnetometers is limited by frequency noise of the laser. This approach has demonstrated AC and DC sensitivities in the picotesla regime [70, 71].

1.3.1.5 Push-pull magnetometer

The push-pull magnetometer represents an alternative all optical approach. In this scheme, a single pump beam is used to measure the DC magnetic field perpendicular to it. The polarisation of the pump beam is switched between the two circular polarisations at the Larmor frequency. When initially pumping with σ^+ light, after half a period of the Larmor precession the sign of the polarisation will be reversed. Polarisation is thus increased by switching the pump beam to σ^- light. Continuous switching at the Larmor frequency yields precession of the spin polarisation with a constant amplitude. Push-pull atomic magnetometers have demonstrated sensitivities of $300\,\mathrm{fT}/\sqrt{\mathrm{Hz}}$ [72].

1.3.2 Applications of AMs

There are numerous applications for AMs. Proof-of-principle demonstrations have been performed in a wide range of fields. Medical applications include; magnetoencephalography (mapping brain activity by recording the magnetic fields produced by electrical activity) [73, 74, 75], magnetocardiography and foetal-magnetocardiography (measuring the magnetic fields produced by the heart's electrical pulses) [76, 77, 78], the detection the magnetic fields produced by nerve pulses [79], and magnetic resonance imaging (MRI) [80, 81]. AMs have further been used to demonstrate the detection of low-field NMR signals [82, 83, 84, 85], NQR signals [54], and magnetic nano-particles suspended in fluids [86]. Applications in underground evaluations include aiding archaeological excavations [87] and mapping of geophysical anomalies [88]. Finally, AMs are being used in tests of fundamental physics and exploring physics beyond the standard model [89, 90].

As AMs look to make the jump from lab-based trials to everyday applications, important progress has been made in portability and power consumption. Micro-fabricated vapour cells has driven the development of AMs towards chip-scale devices. Portable devices have been demonstrated and are now commercially available [91, 92, 93, 94].

1.3.3 Competitors of AMs

A number of technologies compete with AMs in the ultra-sensitive measurements of magnetic fields. This section introduces some of these approaches and briefly discusses some of their advantages and disadvantages.

1.3.3.1 SQUIDs

SQUIDs are the traditional competitors of AMs when considering ultimate sensitivities. A simple SQUID is a loop of superconducting material containing one or two Josephson junctions. The magnetic field is inferred from the voltage across the loop, which is dependent on the number of magnetic flux quanta threading the loop [95]. SQUIDs have demonstrated sensitivities below $1\,\mathrm{fT}/\sqrt{\mathrm{Hz}}$ for both DC and AC fields. Stringent cooling requirements are needed to reach the cryogenic temperatures necessary to transition to a superconducting state. Magnetic shielding is also required. This generally results in SQUID systems being inflexible and expensive to operate. Magnetoencephalography is the most common application of SQUIDs (with systems commercially available) [96].

1.3.3.2 Fluxgate magnetometers

Fluxgate magnetometers measure the induction of an AC current between two coils via a magnetically susceptible core [97]. Changes in the magnetic field modify the magnetic alignment of the core yielding a change in output current. The output is integrated to give a voltage proportional to the magnetic field. Fluxgates are robust, low power, affordable, and available as integrated circuit devices. As such, they lend themselves to field applications, for example, in maritime and space exploration [98]. Fluxgates are typically only sensitive down to the picotesla regime. Their sensitivity is fundamental limited to a predicted noise floor around $100\,\mathrm{fT}/\sqrt{\mathrm{Hz}}$ [99].

1.3.3.3 Inductive coils

Inductive pick-up coils are one of the oldest, and most widely used AC magnetic field sensors. Their operating principle is derived from Faraday's law of induction [100]. Pick-up coils are simple, robust, and cheap, finding numerous high-frequency applications, such as MRI. However, their sensitivity is significantly degraded at lower frequencies[1].

[1] At frequencies below 50 MHz, the fundamental sensitivity limit of an inductive pick-up coil is 10^7 times lower than an AM of the same volume [83].

1.3.3.4 Colour centres in diamond

Colour centre defects in diamond offer an alternative quantum approach to high-sensitivity magnetic field measurements. The most widely studied defect is the NV centre [101]. A negatively charged NV centre consists of a substitutional nitrogen atom and a corresponding vacancy at a nearest neighbour site in a diamond lattice. Combined with an extra electron (at the vacancy site) the system acts as artificial atom confined in the lattice. The NV centre ground state is a spin-triplet split in into a singlet ($m_s = 0$) and a doublet ($m_s = \pm 1$), that is degenerate at zero-field. The degeneracy of the doublet is lifted by magnetic fields. These changes can be detected by purely optical means. As such, an NV centre can be used as a highly-sensitive magnetic field sensor with an atom-sized sensing volume [102, 103]. Sensitivities in the nanotesla regime have been demonstrated for both DC and AC magnetic fields. An ensemble of NV centres confined to a small volume can be used to increase the stability and sensitivity (with sensitivities of $1\,\mathrm{pT}/\sqrt{\mathrm{Hz}}$ realised experimentally). NV centres can be operated in ambient conditions and are comparatively inexpensive when compared to SQUIDs and AMs. Positioning NV centres at the tip of an atomic force microscope (AFM) cantilever allows sensing and scanning extremely close to the surface of the sample – mapping the local magnetic field. This approach has found applications in the imaging of nanoscale ferromagnetic structures and the detection of few-spin systems [104, 105, 106, 107].

1.4 An EMI system based on AMs

The overall performance of an EMI system is ultimately determined by the choice of magnetic field sensor. The main considerations are the sensitivity (which limits the detection level), the sensing volume (which limits the spatial resolution), and the frequency tunability (which determines the range of samples and the penetration depth of images). Classical MIT systems rely on inductive coupling with pick-up coil, or set of coils, to detect the secondary fields. However, this choice places severe limitations on the overall performance – particularly regarding the sensitivity and the spatial resolution. For low-conductivity MIT measurements, coil-based systems typically have sensor coils around 50 mm in diameter. Eddy currents must be excited in volumes exceeding $1000\,\mathrm{cm}^3$ to generate a detectable signal [108].

The first MIT measurements with AMs date from 2013 [109, 110]. There are a number of advantages in using RF-AMs as the magnetic field sensor [1, 111]. Firstly, the sensitivity

of AMs across the frequency band relevant for EMI (spanning 100 Hz to several MHz). This overcomes the key limitation of classical systems – the low-frequency sensitivity of pick-up coils. The active sensing volume can be controlled by the size of the laser beams. Coupled with the potential for miniaturisation, the limits on the spatial resolution can be lowered significantly. This enables high-resolution EMI of small sample volumes. Tunability across the frequency band ensures the ability to adapt to a wide range of samples and provides control over the penetration depth.

In coil-based systems, an unwanted capacitive coupling exists between the excitation and detection coils. To ensure that only eddy current effects are recorded, this must be suppressed. Many methods have attempted to achieve this [112, 113, 108]. In contrast, no capacitive coupling is present in EMI-AM.

Finally, no physical connection is required between the sensor (the vapour cell), the control and read out electronics, or the sample. This is an important advantage in applications such as medical imaging, where infection control must be considered.

1.5 Structure of this thesis

In this thesis, the background, development, and performance of EMI systems based on RF-AMs is presented.

The theoretical background that underpins EMI and RF-AMs is introduced in Chapters 2 and 3, respectively. The experimental EMI-AM systems are described in Chapter 4. The results of the sensor performance are detailed in Chapter 5. The EMI-AM imaging performance is presented in Chapter 6. Chapter 7 covers novel image reconstruction and data extraction approaches developed in this work. Simulations exploring the use of EMI-AM as a medical diagnostic tool discussed in Chapter 8. Finally results from related projects, conducted during this work, are included in Chapter 9.

Chapter 2

Electromagnetic induction imaging

In this chapter the fundamental principles of EMI are introduced. Firstly, an overview of how sample properties are determined via EMI is provided. The theoretical response is then derived for a sample imaged in the configurations used in this work. This is used to briefly comment on the predicted MIT response for a range of different sample materials. Finally, image reconstruction in the context of EMI is discussed.

2.1 Principles of EMI

The general principle behind EMI is depicted in the Argand diagram of Figure 2.1. An AC magnetic field (referred to as the primary field, B_1) is applied to induce eddy currents in a sample. Eddy currents are closed loops of current flowing in a conductive sample generated by a changing magnetic field. This flow is a consequence of Faraday's law of induction. The density of these currents depends on the dielectric properties of the sample and its geometry. This flow of electrons in turn creates an additional oscillating magnetic field component (the secondary field, B_2), opposing the primary one (via Lenz's law). As the eddy current flow is determined by the electromagnetic properties of the sample, information regarding these properties is passed to B_2. The properties of B_2 can therefore be related to the electrical conductivity (σ), the relative permittivity (ε_r), and the relative permeability (μ_r) of the sample. The secondary field perturbs the primary field to give the combined effect of both – the total field (B_{tot}). A magnetic field sensor is used to detect B_{tot}. In this way, the details of B_2 can be inferred and the electromagnetic properties of the sample extracted.

The difficulty in EMI systems is detecting and correctly attributing the secondary field's contributions. In general, the magnitude of the secondary field is much smaller that that of the primary field. A highly-sensitive, stable magnetometer is therefore required.

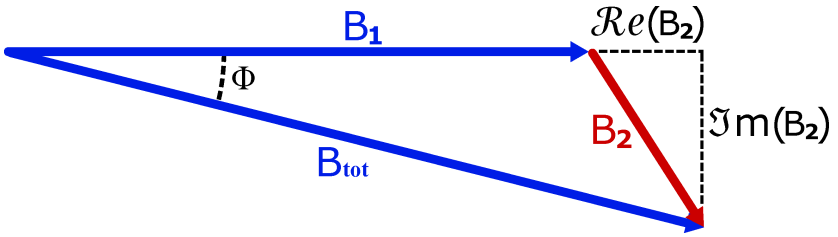

Figure 2.1: Electromagnetic induction imaging: Primary AC magnetic field (B_1) induces eddy currents in a sample. This generates a response magnetic field (B_2). The dielectric properties of the sample are imprinted in B_2. They can be inferred by measuring the total magnetic field B_{tot}. The total field lags behind the primary field by a phase Φ.

2.2 Skin effect

The skin effect is a phenomenon of eddy current flow that sees the current density concentrated near the surface. In addition, the current density decreases exponentially with depth. This effect can be described phenomenologically in two related ways. Firstly, the flow of eddy currents produces a secondary field response that opposes the primary field. At a given depth, this response will decrease the level of primary field propagating to subsequent depths – resulting in a decrease in the current density. Alternatively, one can consider the skin effect to be a consequence of the conversion of energy from the primary field into eddy current flow. As the field propagates into the sample its energy decreases leading to a reduction in the generation of eddy currents.

The skin effect can be simply described for the geometry of Figure 2.2(a). Let the primary field be infinite plane wave parallel to the surface of to an infinite half-space sample. The current density at a depth y (J_y) is governed by [114]

$$J_y = J_0 \, \mathrm{e}^{-y/\delta(\omega)} \, , \tag{2.1}$$

where J_0 is the current density at the surface. The distance (or depth below the surface) at which the current density has decreased to J_0/e is called the skin depth – $\delta(\omega)$. For the idealised case considered here, the relationship between the current density and depth is shown in Figure 2.2(b) – where the distance is scaled by $\delta(\omega)$ and the current density is scaled by J_0. In practical applications the current density also depends, in a non-trivial manner, on the shape and thickness of the sample. Nevertheless, Equation 2.1 provides a good approximation of the eddy current density decay.

In the idealised case, the phase-lag (Φ) between the primary field at the surface and the

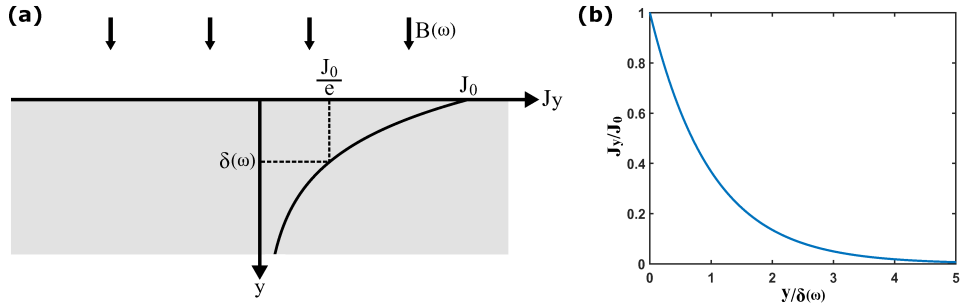

Figure 2.2: The skin effect: (a) Plane wave of angular frequency ω incident on a half-space sample. The current density, J_y, decays exponentially with depth. The skin depth, $\delta(\omega)$, is the $1/e$ decay length. **(b)** Relationship between the relative eddy current density and distance (scaled by $\delta(\omega)$).

eddy current density at a depth y is given – in radians – by [114]

$$\Phi = \frac{y}{\delta(\omega)} \,. \tag{2.2}$$

The skin depth parameter is given by [115]

$$\delta(\omega) = \frac{1}{\omega}\left[\frac{\mu\varepsilon}{2}\left(\sqrt{1+\left(\frac{\sigma}{\omega\varepsilon}\right)^2}-1\right)\right]^{-1/2}, \tag{2.3}$$

where $\mu = \mu_r\mu_0$, and $\varepsilon = \varepsilon_r\varepsilon_0$ (ε_0 and μ_0 are the permittivity and permeability of free space, respectively).

Note that Equation 2.3 is algebraically equivalent to [116]

$$\delta(\omega) = \sqrt{\frac{2}{\omega\mu\sigma}}\left[\sqrt{1+\left(\frac{\omega\varepsilon}{\sigma}\right)^2}+\frac{\omega\varepsilon}{\sigma}\right]^{1/2}, \tag{2.4}$$

with both formulae quoted interchangeably. A proof of this equivalence of is provided in Appendix A.

The skin depth is a critical parameter to consider in EMI systems. For each application and material the operation frequency must be chosen to appropriately set the penetration of the primary field.

2.2.1 High-conductivity samples

For conductive samples and low operation frequencies (such that, $\sigma \gg \omega\varepsilon$) the bracketed term of Equation 2.4 approaches unity. In this case, the skin depth equation reduces to

$$\delta(\omega) = \sqrt{\frac{2}{\omega\mu\sigma}}\,. \tag{2.5}$$

Unless stated otherwise, the simplified form of Equation 2.5 is used to calculate the skin depth values quoted throughout this work. It is applicable to the sample conductivities and frequencies explored in Chapter 6. For metallic samples the reduction holds for frequencies below 10×10^{18} Hz. For doped semiconductors the reduction is valid below 10×10^{12} Hz[1]. Despite this applicability, it is important to remember that this formula is not valid in all regimes, despite being widely quoted as the 'skin depth'.

2.2.2 Low-conductivity samples

For very low-conductivity samples and high operation frequencies (such that, $\omega\varepsilon \gg \sigma$) the behaviour is different. In this case, the skin depth equation approaches an asymptotic limit given by

$$\delta(\omega) = \frac{2}{\sigma}\sqrt{\frac{\varepsilon}{\mu}}\,. \tag{2.6}$$

A brief proof of this value is included in Appendix A.

In this regime the skin depth is likely to be significantly larger than the sample thickness. As a result, the skin effect no longer needs to be considered in practical applications, with the current density being considered uniform throughout the sample's cross-section.

2.3 Secondary field response: Small RF coil

Computing the secondary magnetic field response for a general system is complex. However, a qualitative understanding of the secondary field behaviour can be gained from solutions to simplified geometries. In this section the theoretical EMI response is derived for the imaging configuration used – for example – in Section 6.3. For the eddy current contribution the approach is adapted from Griffiths et al. (1999) [112]. For the permeability contribution a derivation is provided for the result first reported in Casañas et al. (2001) [117].

Consider a thin, uniform disk of radius R and thickness h positioned centrally between a small RF excitation coil and the AM (or any alternative sensor). Let the excitation angu-

[1] These values ensure $\delta(\omega)$ deviates by less that 1% from the exact calculation.

lar frequency be ω. The disk has a complex conductivity $\kappa = \sigma + i\omega\varepsilon_0\varepsilon_r$ and a relative permeability μ_r. Note the following further assumptions:

1. The thickness is small compared to the distances: $h \ll a, b$.

2. The RF coil is small compared to the distance a: $\rho \ll a$ where ρ is the radius of the RF coil.

3. The thickness is small compared to the skin depth: $\delta \gg h$.

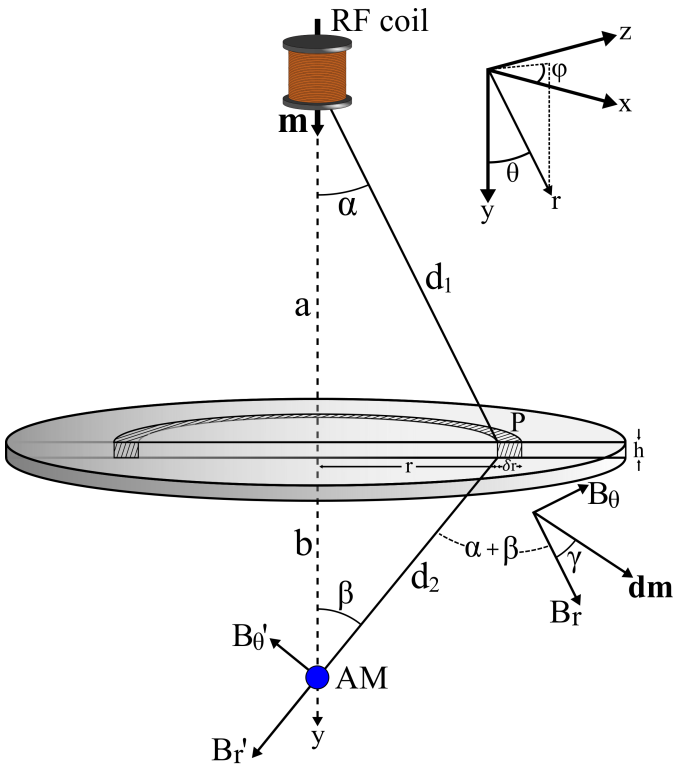

Figure 2.3: EMI configuration with a small RF coil: A thin, uniform disk is positioned between a small RF excitation coil and the AM. Note the choice of spherical polar coordinates.

2.3.1 Perturbation due to eddy currents

In this section, the secondary field contribution due to the induction of eddy currents in the disk is derived. The RF coil can be modelled as a magnetic dipole **m** in the y-direction. From this, the field at a point P on the disk is given by [118, 119]

$$\mathbf{B} = \frac{\mu_0 m}{4\pi d_1^3}\left(2\cos(\alpha)\,\hat{\mathbf{r}} + \sin(\alpha)\,\hat{\theta}\right) , \tag{2.7}$$

where I have used Assumption 2 and $m = \pi\rho^2 I$ is the magnetic dipole strength.

The field in the y-direction at the point P is therefore

$$B_y = B_r \cos(\alpha) - B_\theta \sin(\alpha) = \frac{\mu_0 m}{4\pi}\left(\frac{2a^2 - r^2}{(a^2+r^2)^{5/2}}\right) . \tag{2.8}$$

From this the flux in the loop with radius r is given by

$$\Phi = \iint_S B_y \, dS = 2\pi \int_0^r B_y(r')\, r' \, dr' = \frac{\mu_0 m}{2}\left(\frac{r^2}{(a^2+r^2)^{3/2}}\right) . \tag{2.9}$$

The induced electromotive force in the loop ($\mathscr{E}$) is given by Faraday's law of induction[2],

$$\mathscr{E} = -\frac{d\Phi}{dt} = -i\,\omega\,\Phi . \tag{2.10}$$

By definition $\mathscr{E}$ can also be written in terms of E_ϕ – the ϕ-component of the induced electric field

$$\mathscr{E} = \iint_S E_\phi \, dS = 2\pi \int_0^r E_\phi \, r' \, dr' = 2\pi r E_\phi . \tag{2.11}$$

Combining Equations 2.9, 2.10, 2.11 yields

$$E_\phi = \frac{-i\,\omega\,\mu_0 m}{4\pi} \frac{r}{(a^2+r^2)^{3/2}} . \tag{2.12}$$

The induced current density (including the eddy current density and the displacement current density) is given by Ohm's law as

$$\mathbf{J} = \kappa \mathbf{E} = (\sigma + i\,\omega\,\varepsilon_0\,\varepsilon_r)\,\mathbf{E} . \tag{2.13}$$

The current flowing in an annulus of the disk $[r, r+\delta r]$ (shaded region in Figure 2.3) is

$$dI = h\,\delta r\, J_\phi , \tag{2.14}$$

where I have taken the current to be uniform throughout the thickness of the disk – i.e. the disk causes minimal attenuation of the primary field (Assumption 3).

The secondary field contribution of the annulus at the AM's position can be calculated by the Biot-Savart law. Taking the annulus to be a single circular loop the field on the axis

[2]Note that – as a sinusoidal current is applied to the RF coil – $\Phi = \Phi_0 e^{i\omega t} \implies \frac{d\Phi}{dt} = i\omega\Phi$.

(y-direction) at a distance b is given by [119, 120]

$$dB_2^e = \frac{\mu_0\, dI\, r^2}{2(b^2+r^2)^{3/2}} \ . \tag{2.15}$$

By combining Equations 2.12 - 2.15 this contribution can be re-written as

$$dB_2^e = -i\,\omega\,\mu_0^2\,\kappa\, m\,\frac{h}{8\pi}\,\frac{r^3}{(a^2+r^2)^{3/2}(b^2+r^2)^{3/2}}\,dr \ . \tag{2.16}$$

The total secondary field contribution is given by integrating over the disk

$$B_2^e = -i\,\omega\,\mu_0^2\,\kappa\,\frac{h}{8\pi}\int_0^R \frac{r^3}{(a^2+r^2)^{3/2}(b^2+r^2)^{3/2}}\,dr \ . \tag{2.17}$$

The primary field at the AM (without the disk present) is

$$B_1 = \frac{\mu_0\, m}{2\pi\,(a+b)^3} \ , \tag{2.18}$$

using Equation 2.7.

Finally, one arrives at a relationship between the primary field and the eddy current contribution to the secondary field by combining Equation 2.17 and Equation 2.18;

$$\frac{B_2^e}{B_1} = -i\,\omega\,\mu_0\,\kappa\,\frac{h\,(a+b)^3}{4}\int_0^R \frac{r^3}{(a^2+r^2)^{3/2}(b^2+r^2)^{3/2}}\,dr \tag{2.19}$$

$$= A\,\mu_0\,\omega\,(\omega\,\varepsilon_0\,\varepsilon_r - i\,\sigma) \ . \tag{2.20}$$

The constant A depends only on the geometry of the system. In the symmetric case ($a = b$), the integral simplifies to give [112]

$$A = \frac{h\,a\,R^4}{2(a^2+R^2)^2} \ , \tag{2.21}$$

and for the asymmetric case

$$A = \frac{h\,(a+b)^3}{2}\left[\frac{a\,b\,\left(a\,b-(a^2+R^2)^{1/2}(b^2+R^2)^{1/2}\right)+R^2(a^2+b^2)}{(a^2-b^2)^2(a^2+R^2)^{1/2}(b^2+R^2)^{1/2}}\right] \ . \tag{2.22}$$

2.3.2 Perturbation due to permeability

In this section, the secondary field component due to the magnetisation of the disk is derived. The excitation coil is (again) treated as a magnetic dipole **m** to calculate the field at the point P (Equation 2.7). The magnitude of this field at P is

$$B_P = |\mathbf{B}| = \frac{\mu_0 m}{4\pi} \frac{(4a^2 + r^2)^{1/2}}{d_1^4} \ . \tag{2.23}$$

For a homogeneous medium, the magnetisation due to a field B_P is

$$M = \chi_m H = \frac{(\mu_r - 1)}{\mu_0 \mu_r} B_P \ , \tag{2.24}$$

where $\chi_m = (\mu_r - 1)$ is the magnetic susceptibility of the medium [118].

Consider the differential volume element at P; defined as $[r, r+\delta r] \times [\phi, \phi + \delta\phi] \times [0, h]$ – where I have used the assumption that the disk is thin (Assumption 1). The magnetic dipole induced in this element by B_P has magnitude

$$\begin{aligned} dm = M\,dV &= \frac{(\mu_r - 1)}{\mu_0 \mu_r} B_P\, h\, r\, dr\, d\phi \\ &= \frac{(\mu_r - 1)}{\mu_r} \frac{mh}{4\pi} \frac{r(4a^2 + r^2)^{1/2}}{d_1^4} \ , \end{aligned} \tag{2.25}$$

given by combining Equation 2.23 and Equation 2.24.

The direction of this dipole is displaced by an angle γ from B_r. The following relations can be constructed from the geometry of Figure 2.3 and are required later:

$$\begin{aligned} \cos(\alpha) = \frac{a}{d_1} \ , \quad \cos(\beta) = \frac{b}{d_2} \ , \quad \cos(\gamma) = \frac{B_r}{B_P} = \frac{2a}{(4a^2 + r^2)^{1/2}} \ , \\ \sin(\alpha) = \frac{r}{d_1} \ , \quad \sin(\beta) = \frac{r}{d_2} \ , \quad \sin(\gamma) = \frac{B_\theta}{B_P} = \frac{r}{(4a^2 + r^2)^{1/2}} \ . \end{aligned} \tag{2.26}$$

Each differential dipole element produces a different contribution to the secondary field at the position of the AM. Again considering the geometry of Figure 2.3, the contribution due to **dm** in the y-direction is given by

$$\begin{aligned} dB_2^m &= B'_r \cos(\beta) - B'_\theta \sin(\beta) \\ &= \frac{\mu_0\, dm}{4\pi d_2^3} \left[2\cos(\alpha + \beta + \gamma)\cos(\beta) - \sin(\alpha + \beta + \gamma)\sin(\beta) \right] \ . \end{aligned} \tag{2.27}$$

At this point it is only worth considering the symmetric case, $a = b$ (giving, $\alpha = \beta$, $d_1 = d_2$). The asymmetric case can be derived following the same steps to give a result that differs only in the form of the final constant.

Expanding the identities of Equation 2.27 to single-angle formulae and then substituting with the relations of Equation 2.26 yields

$$dB_2^m = \frac{\mu_0\, dm}{8\pi}\left[\frac{(2a^2-r^2)(a^2+r^2)+(6a^4-27a^2r^2+3r^4)}{(4a^2+r^2)^{1/2}(a^2+r^2)^3}\right] . \tag{2.28}$$

Substituting for the dipole strength dm (Equation 2.25) and simplifying gives

$$dB_2^m = \frac{\mu_0\, m\, h}{32\pi^2}\,\frac{(\mu_r-1)}{\mu_r}\,\frac{2r\left[4a^4-13a^2r^2+r^4\right]}{(a^2+r^2)^5}\,dr\,d\phi\ . \tag{2.29}$$

The secondary field due to the magnetisation of the disk is found by integration over the volume of the disk

$$\begin{aligned} B_2^m &= \frac{\mu_0\, m\, h}{32\pi^2}\,\frac{(\mu_r-1)}{\mu_r}\int_0^{2\pi}\int_0^{R}\frac{2r\left[4a^4-13a^2r^2+r^4\right]}{(a^2+r^2)^5}\,dr\,d\phi \\ &= \frac{\mu_0\, m\, h}{32\pi}\,\frac{(\mu_r-1)}{\mu_r}\,\frac{R^2(8a^2-R^2)}{(a^2+R^2)^4}\ . \end{aligned} \tag{2.30}$$

Recall that the primary field at the AM – without the disk present – is given (Equation 2.18) by

$$B_1 = \frac{\mu_0\, m}{16\pi a^3} \quad \text{for} \quad a = b\ . \tag{2.31}$$

Finally, by combining Equation 2.30 and Equation 2.31, one arrives at a relationship between the primary field and the permeability contribution to the secondary field

$$\frac{B_2^m}{B_1} = B\frac{(\mu_r-1)}{\mu_r}\ , \tag{2.32}$$

where the constant B depends only on the geometry of the system and is given by

$$B = \frac{a^3\, h R^2(8a^2+R^2)}{2(a^2+R^2)^4}\ . \tag{2.33}$$

In general, one is interested in paramagnetic or diamagnetic samples – for which $\mu_r \approx$

1. Applying this approximation gives the final form of the ratio[3] [117]

$$\frac{B_2^m}{B_1} = B(\mu_r - 1) \; . \tag{2.34}$$

2.4 Secondary field response: Helmholtz coil

The EMI response is now re-derived in the configuration used for the results in Section 7.2 [5]. The steps closely follow those of the previous section.

The RF excitation field is applied by a Helmholtz coil pair of radius R_c. The AM is positioned at the centre of these coils, where the field is uniform. Again consider a thin, uniform disk of radius R and thickness h positioned centrally, now a distance a above the AM. Let the excitation angular frequency be ω, the complex conductivity of the disk be $\kappa = \sigma + i\,\omega\,\varepsilon_0\,\varepsilon_r$, and relative permeability of the disk be μ_r. In addition one assumes:

1. The thickness is small compared to the distances: $h \ll a, R_c$.
2. The thickness is small compared to the skin depth: $\delta \gg h$.

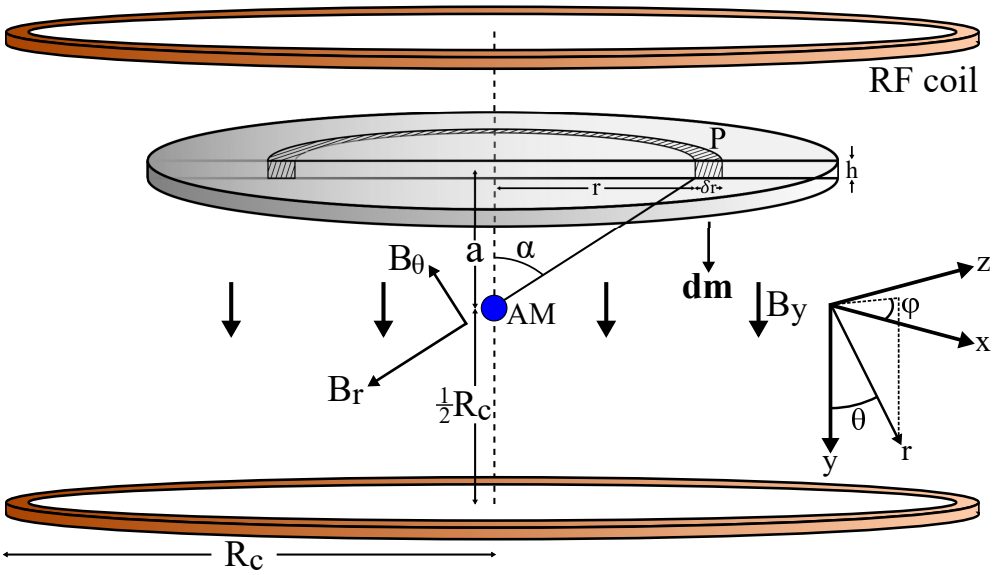

Figure 2.4: EMI configuration with a Helmholtz coil: The AM is positioned at the centre of the Helmholtz coils. A thin, uniform disk is positioned centrally a distance a above the AM. Note the choice of spherical polar coordinates.

2.4.1 Perturbation due to eddy currents

To calculate the perturbation due to the induction of eddy currents in the disk the field in the y-direction (at the point P) is required. This is given by the sum of the contributions from

[3] I.e. taking the first-order term in the Taylor series expansion of $f(x) = \frac{(x-1)}{x}$ at $x = 1$.

the two coils, each found by application of the Biot-Savart law [119, 120],

$$B_P^{\,y} = \frac{\mu_0 N I R_c^2}{2}\left[\frac{1}{\left(R_c^2+\left(a+\frac{R_c}{2}\right)^2\right)^{3/2}}+\frac{1}{\left(R_c^2+\left(a-\frac{R_c}{2}\right)^2\right)^{3/2}}\right], \tag{2.35}$$

where I the current and N is the number of turns in each coil. Note that this field is uniform across the disk, i.e. independent of r. Therefore, it can be treated as a constant throughout the following steps.

As before, the flux in the loop with radius r is calculated as

$$\Phi = B_P^{\,y}\iint_S dS = \pi r^2 B_P^{\,y}\,. \tag{2.36}$$

From Equations 2.10 - 2.13, one again arrives at a relationship between the induced eddy current density and the applied magnetic flux,

$$J_\phi = -\frac{i\omega\kappa}{2\pi r}\Phi\,. \tag{2.37}$$

It follows, from Equation 2.36, that

$$J_\phi = -\frac{i\omega\kappa r}{2}B_P^{\,y}\,. \tag{2.38}$$

The current flowing in an annulus of the disk $[r, r+\delta r]$ (shaded in Figure 2.4) is

$$dI = h\,\delta r J_\phi\,, \tag{2.39}$$

following Assumption 2.

The field contribution from the annulus at the AM can be calculated by the Biot-Savart law

$$dB_2^{\,e} = \frac{\mu_0\, dI\, r^2}{2(a^2+r^2)^{3/2}}\,. \tag{2.40}$$

By combining Equations 2.38, 2.39, and 2.40 this contribution can be re-written as

$$dB_2^{\,e} = -i\omega\mu_0\kappa\frac{h}{4}\frac{r^3}{(a^2+r^2)^{3/2}}B_P^{\,y}\,dr\,. \tag{2.41}$$

The total eddy current contribution to the secondary field is found by integrating over

the entire disk

$$B_2^e = -i\,\omega\,\mu_0\,\kappa B_P^y\,\frac{h}{4}\int_0^R \frac{r^3}{(a^2+r^2)^{3/2}}\,dr\ . \tag{2.42}$$

The primary field at the AM (without the disk) is the magnetic field at the centre point of the coils,

$$B_1 = \left(\frac{4}{5}\right)^{3/2}\frac{\mu_0 N I}{R_c}\ . \tag{2.43}$$

This can be seen by taking $a = 0$ in Equation 2.35.

Finally, the relationship between the primary field and the eddy current contribution to the secondary field is found by combining Equations 2.42 and 2.43

$$\frac{B_2^e}{B_1} = A\,\mu_0\,\omega\,(\omega\,\varepsilon_0\,\varepsilon_r - i\,\sigma)\ , \tag{2.44}$$

where

$$A = \frac{B_P^y}{B_1}\,\frac{h}{4}\left[\frac{2a^2+R^2}{(a^2+R^2)^{1/2}} - 2a\right]\ . \tag{2.45}$$

As with the previous configuration, the constant A depends only on the geometry of the system. In the case where a is small, one can take advantage of the uniformity of the Helmholtz current field – $B_P^y \approx B_1$ – to leave

$$A = \frac{h}{4}\left[\frac{2a^2+R^2}{(a^2+R^2)^{1/2}} - 2a\right]\ , \tag{2.46}$$

otherwise

$$A = \left(\frac{5}{4}\right)^{3/2}\frac{hR_c^3}{8}\left[\frac{2a^2+R^2}{(a^2+R^2)^{1/2}} - 2a\right]\left[\frac{1}{\left(R_c^2+\left(a+\frac{R_c}{2}\right)^2\right)^{3/2}} + \frac{1}{\left(R_c^2+\left(a-\frac{R_c}{2}\right)^2\right)^{3/2}}\right]\ . \tag{2.47}$$

2.4.2 Perturbation due to permeability

Finally, the permeability component of the secondary field is derived for the Helmholtz imaging configuration. Recall that the field at the point P in the y-direction is defined as B_P^y. Considering the differential volume element – $[r, r+\delta r]\times[\phi, \phi+\delta\phi]\times[0,h]$ – at P the

magnetic of the magnetic dipole induced in this element can be shown to be

$$dm = \frac{(\mu_r - 1)}{\mu_0 \mu_r} B_P^y h\, r\, dr\, d\phi \ , \tag{2.48}$$

by making use of Equation 2.24.

The secondary field contribution of this dipole (**dm**) at the AM in the y-direction is

$$dB_2^m = B_r' \cos(\alpha) - B_\theta' \sin(\alpha) = \frac{\mu_0\, dm}{4\pi} \left[\frac{2a^2 - r^2}{(a^2 + r^2)^{5/2}} \right] \ , \tag{2.49}$$

a result of Equation 2.7 and the geometry in Figure 2.4.

Substituting for dm, with Equation 2.48, yields

$$dB_2^m = \frac{h}{4\pi} \frac{(\mu_r - 1)}{\mu_0 \mu_r} B_P^y \left[\frac{r(2a^2 - r^2)}{(a^2 + r^2)^{5/2}} \right] dr\, d\phi \ . \tag{2.50}$$

The total permeability contribution to the secondary field is found by integrating over the volume of the disk

$$B_2^m = \frac{h}{4\pi} \frac{(\mu_r - 1)}{\mu_0 \mu_r} B_P^y \int_0^{2\pi} \int_0^R \left[\frac{r(2a^2 - r^2)}{(a^2 + r^2)^{5/2}} \right] dr\, d\phi \ . \tag{2.51}$$

Recalling the primary field B_1 in the absence of the disk (from Equation 2.43) the relationship between the primary field and the secondary field contribution is

$$\frac{B_2^m}{B_1} = B(\mu_r - 1) \ , \tag{2.52}$$

where I have used the assumption of a paramagnetic or diamagnetic material (see Section 2.3.2) and defined the constant B as

$$B = \frac{B_P^y}{B_1} \frac{h}{2} \left[\frac{R^2}{(a^2 + R^2)^{3/2}} \right] \ . \tag{2.53}$$

As in the previous section, when a is small one can take $B_P^y \approx B_1$ to leave

$$B = \frac{h}{2} \left[\frac{R^2}{(a^2 + R^2)^{3/2}} \right] \ , \tag{2.54}$$

otherwise

$$B = \left(\frac{5}{4}\right)^{3/2} \frac{hR_C^3}{4} \left[\frac{R^2}{(a^2+R^2)^{3/2}}\right] \left[\frac{1}{\left(R_c^2+\left(a+\frac{R_c}{2}\right)^2\right)^{3/2}} + \frac{1}{\left(R_c^2+\left(a-\frac{R_c}{2}\right)^2\right)^{3/2}}\right] . \tag{2.55}$$

2.5 Comments on the EMI response

The previous sections have provided a qualitative description of the sample response in EMI. For a sample of conductivity σ, relative permittivity ε_r, relative permeability μ_r, and an excitation field frequency ω the relationship between B_1 and B_2 was shown to be

$$\frac{B_2}{B_1} = A\omega\mu_0\left[\omega\varepsilon_0(\varepsilon_r-1) - i\sigma\right] + B(\mu_r - 1) , \tag{2.56}$$

where A and B are constants that depend on the geometry of the system. Following Griffiths et al. (2007) [108], the modification $\varepsilon_r \rightarrow (\varepsilon_r - 1)$ has been included.

Without this transformation, in the absence of a sample ($\sigma = 0, \varepsilon_r = 1, \mu_r = 1$) the secondary field includes a contribution from the displacement currents in the air. This is from the region where the sample would be present. The transformation removes this background contribution, effectively shifting it from B_2 to B_1. This ensures that the condition $\frac{B_2}{B_1} = 0$ holds with no sample present.

The first term on the RHS of Equation 2.56 is due to the induction of eddy currents in the sample (B_2^e). Whereas the second term arises from the magnetisation of the sample (B_2^m).

Using Equation 2.56, the following general observations about the response in EMI can be made:

1. Changes in the real part of the secondary field are related to changes in the relative permittivity (displacement current density) and relative permeability (magnetisation) of the sample.

2. Changes in the imaginary part of the secondary field are related to changes in the conductivity of the sample (eddy current density).

3. The presence of an imaginary component results in a phase-lag, Φ, of the total field with respect to the primary field. A phase sensitive detection scheme is therefore required to correctly characterise the response.

4. The contribution of B_2^e increases with increasing excitation frequency.

5. The contribution of B_2^m is not dependent on the excitation frequency. Therefore, it can often be isolated or removed.

It is important to note that Point 4 conflicts with Equation 2.5 (which states that the penetration distance decreases with ω). The choice of operation frequency therefore determines both the size of the EMI response and the depth at which the sample's properties are probed. This trade-off must be carefully examined in view of each desired application.

To comment further on the theoretical EMI response, consider the Argand diagrams in the following sections in which the predicted response of Equation 2.56 is explored for a number of measurement scenarios.

2.5.1 Conductive samples

For conductive samples – such as Cu and Al – the EMI response diagrams are depicted in Figure 2.5. The conductivity of the sample generates an imaginary contribution to the secondary field, leading to a phase-lag. The permittivity and permeability contributions can be neglected as $\{\varepsilon_r, \mu_r\} \approx 1$.

In practical applications, the operation frequency often dictates that the skin depth is comparable or smaller than the thickness of the object. Equation 2.56 is no longer valid in this case[4]. The sample partially attenuates the primary field – which manifests as a negative contribution to the real part of the secondary field in Figure 2.5(a). This effect increases the measured Φ and decreases B_{tot}.

At sufficiently low frequencies – where the primary field fully penetrates the sample – the ideal response of Figure 2.5(b) is recovered. Only the conductivity component contributes to the signal. This value could therefore be extracted by measuring Y (the change in the imaginary component of B_{tot}) or measuring $\Phi = \arctan(B_2/B_1)$.

The results presented in this thesis often lie between these two regimes. For Cu and Al samples the skin depth is often comparable to the sample thickness. The response in this regime is exploited in Section 6.5 to image concealed samples. In contrast, as the conductivity of the sample is lowered (for example in Section 6.4) one moves towards the regime of Figure 2.5(b).

[4] As Assumption 3 of Section 2.3 no longer holds.

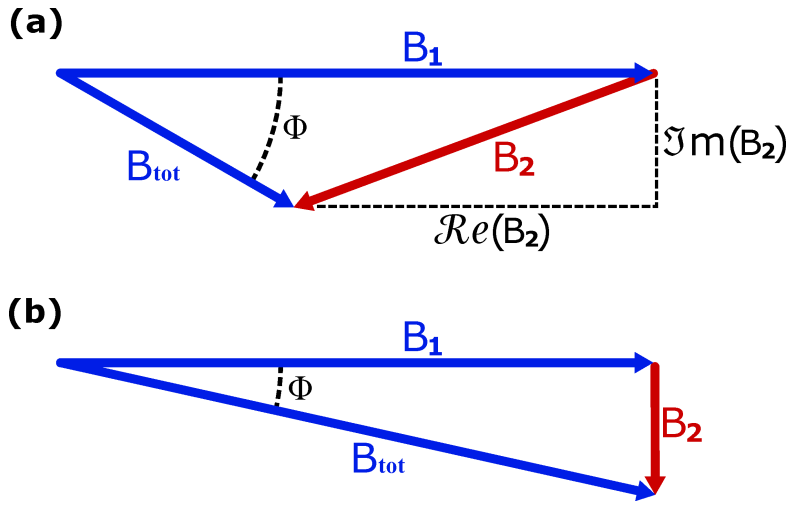

Figure 2.5: Argand diagram for a conductive sample: **(a)** Conductive sample where the skin depth is smaller or comparable to its thickness. **(b)** Conductive sample where the skin depth is much greater than its thickness.

2.5.2 Biomedical samples

The conductivities of biomedical tissues are many orders of magnitude below those of metallic samples[5]. The permeability contribution can again be removed – as $\mu_r = 1$. In the considered frequency band the skin depth is larger than the sample thickness – hence attenuation of the primary field due to eddy current generation can also be neglected.

Figure 2.6 depicts the predicted response for this scenario. A high operation frequency – typically several MHz – is required to excite a sufficient eddy current response. The secondary field includes a contribution to the real part (for displacement eddy currents) and the imaginary part (from conductive eddy currents). Therefore, measuring changes in the real and imaginary components (X and Y) of B_{tot} can allow imaging of ε_r and σ.

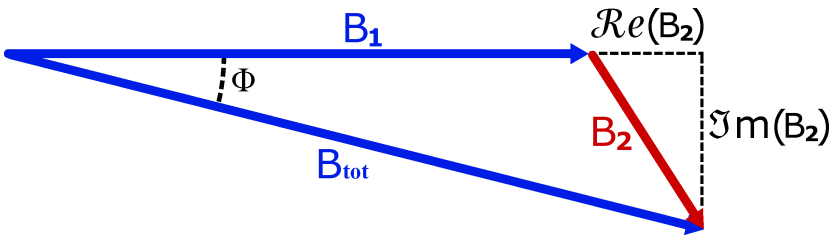

Figure 2.6: Argand diagram for a biomedical sample: Low-conductivity biomedical sample with a skin depth much greater than its thickness.

Conventional MIT systems (based on pick-up coils) have measured the response of large volume saline solutions – mimicking biological tissues [112, 113]. For low-

[5]Typically $< 10\,\text{S}\,\text{m}^{-1}$. For reference [121, 122].

conductivity solutions ($0.012\,\mathrm{S\,m^{-1}} \leq \sigma \leq 3.2\,\mathrm{S\,m^{-1}}$) the change in the imaginary component ($\mathrm{Im}(B_2/B_1)$) is $< 10\%$, whereas the change in the real component ($\mathrm{Re}(B_2/B_1)$) is $< 1.5\%$, for an operation frequency of 10 MHz and a large sample of thickness 120 mm and volume 2250 cm^3 [108].

Finally, the conductivity resolution of the images is considered. The secondary field response is weak ($|B_2| \ll |B_1|$) and dominated by its imaginary component. With reference to Figure 2.6, a Taylor expansion to first order in Φ gives

$$\Phi = \mathrm{Im}\,(B_2/B_1)\ . \tag{2.57}$$

Combining this with Equation 2.56 yields [15]

$$\Delta\Phi \propto \omega\,\Delta\sigma\ . \tag{2.58}$$

Hence, the detection of changes in conductivity is limited by the noise in the phase measurement. Increasing the stability of this measurement or increasing the operation frequency increases the resolution in conductivity.

2.5.3 Ferromagnetic samples

Finally, conductive ferromagnetic samples are considered (Figure 2.7). As for conductive samples, there is an imaginary component resulting from the conductivity contribution and the permittivity contribution can be neglected. In addition, there is a real and positive contribution arising from the permeability of the sample. This is due to an AC magnetisation generated in the region where the primary field penetrates the sample (see Section 2.3.2). Note that the approximation used for Equation 2.34 is not valid, as μ_r can vary significantly from 1.

For many practical applications, the skin depth will be comparable to the size of the sample. This results in a reduction in the real component due to attenuation of the primary field as a consequence of eddy current generation. The imaging of ferromagnetic samples is considered in Section 6.6.

2.6 Image reconstruction in MIT

For complex or cluttered images – or in 3D EMI – the solution to the inverse eddy current problem is required to reconstruct the sample properties [123]. This can be stated as finding

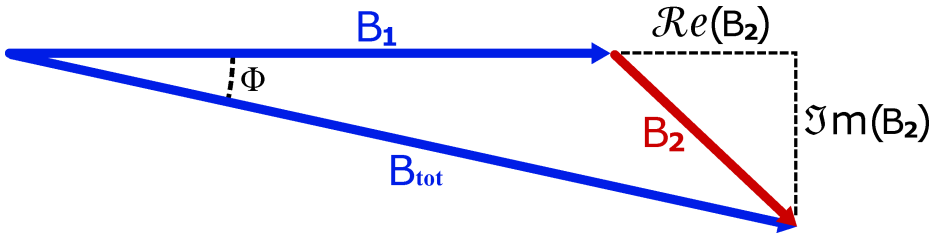

Figure 2.7: Argand diagram for a ferromagnetic sample: Conductive ferromagnetic sample with a skin depth much greater than its thickness.

the changes $\Delta\kappa$ of the complex conductivity distribution $\kappa = \sigma + i\omega\varepsilon$ that cause the changes ΔB in the detected magnetic field. Let the forward (eddy) current problem be

$$\mathbf{B} = \Psi(\kappa) \; . \tag{2.59}$$

This equation is the discretised, nonlinear forward mapping of κ to a vector of magnetic field measurements [124]. The corresponding inverse (eddy) current problem is

$$\kappa = \Psi^{-1}(\mathbf{B}) \; , \tag{2.60}$$

which is generally ill-posed and undetermined. The standard approach to this problem is an iterative algorithm on finite element mesh. Within each element of the mesh κ is assumed to be constant. The iterative nature of this approach renders it computationally complex. However, there are a number of methods for reducing the number of required computational steps [123, 125, 124].

Inverse problems are an extremely rich and active area of applied mathematics. It would not be prudent to comment in great detail on this topic. Borges et al. (1999) [126] provides an overview of image reconstruction algorithms in the context of EMI. Tarantola (2005) [127] summarises the general theory of inverse problems including the methods of solutions.

In Chapter 7, image reconstruction methods developed as part of this work are introduced and discussed. These take advantage of machine learning algorithms to circumvent the need of solving the inverse problem in the reconstruction of the complex conductivity distribution.

Chapter 3

Radio-frequency atomic magnetometers

In this chapter the physics underpinning the operation of RF-AMs is introduced. Firstly, the atomic structure and properties of Rb are reviewed for reference. The creation of macroscopic spin-polarisation via optical pumping and the detection of atomic precession by polarisation rotation are presented. The theoretical response of an RF-AM to oscillating magnetic fields is derived. Finally, the collisional and relaxational processes present in atomic vapour cells are reviewed and used to comment on both the practical and fundamental limits of sensitivity.

3.1 Rubidium: Atomic structure and density

There are two naturally occurring isotopes of Rb – ^{85}Rb and ^{87}Rb. They have respective relative abundances of 0.7217 and 0.2783 [128, 129]. Both isotopes are used as the core of the AM experiments described in this work. For each isotope, both the D_1 line $5^2S_{1/2} \rightarrow 5^2P_{1/2}$ and D_2 line $5^2S_{1/2} \rightarrow 5^2P_{3/2}$ transitions are used. The hyperfine energy level structures for these transitions are included on the following pages: Figure 3.1 for the ^{85}Rb D_1 and D_2 lines, Figure 3.2 for the ^{87}Rb D_1 and D_2 lines.

The operation of an RF-AM requires two types of transitions coupling different levels of the atomic structure. Optical transitions, between ground and excited hyperfine levels, are used for optical pumping and the detection of atomic precession. Usually electric dipole transitions are used. These have the properties $\Delta F = \pm 1, \Delta m_F = \{0, \pm 1\}$ (ΔF labels changes of the F quantum number and Δm_F of the magnetic quantum number, $m_F = [-F, -(F-1), \ldots, +(F-1), +F]$). Secondly, Zeeman transitions drive the atomic precession (see Section 3.2). These have the properties $\Delta F = 0, \Delta m_F = \pm 1$. Together, these transitions define the operation of an RF-AM.

Atomic vapour cells constitute the core element of an AM. In this work, the vapour

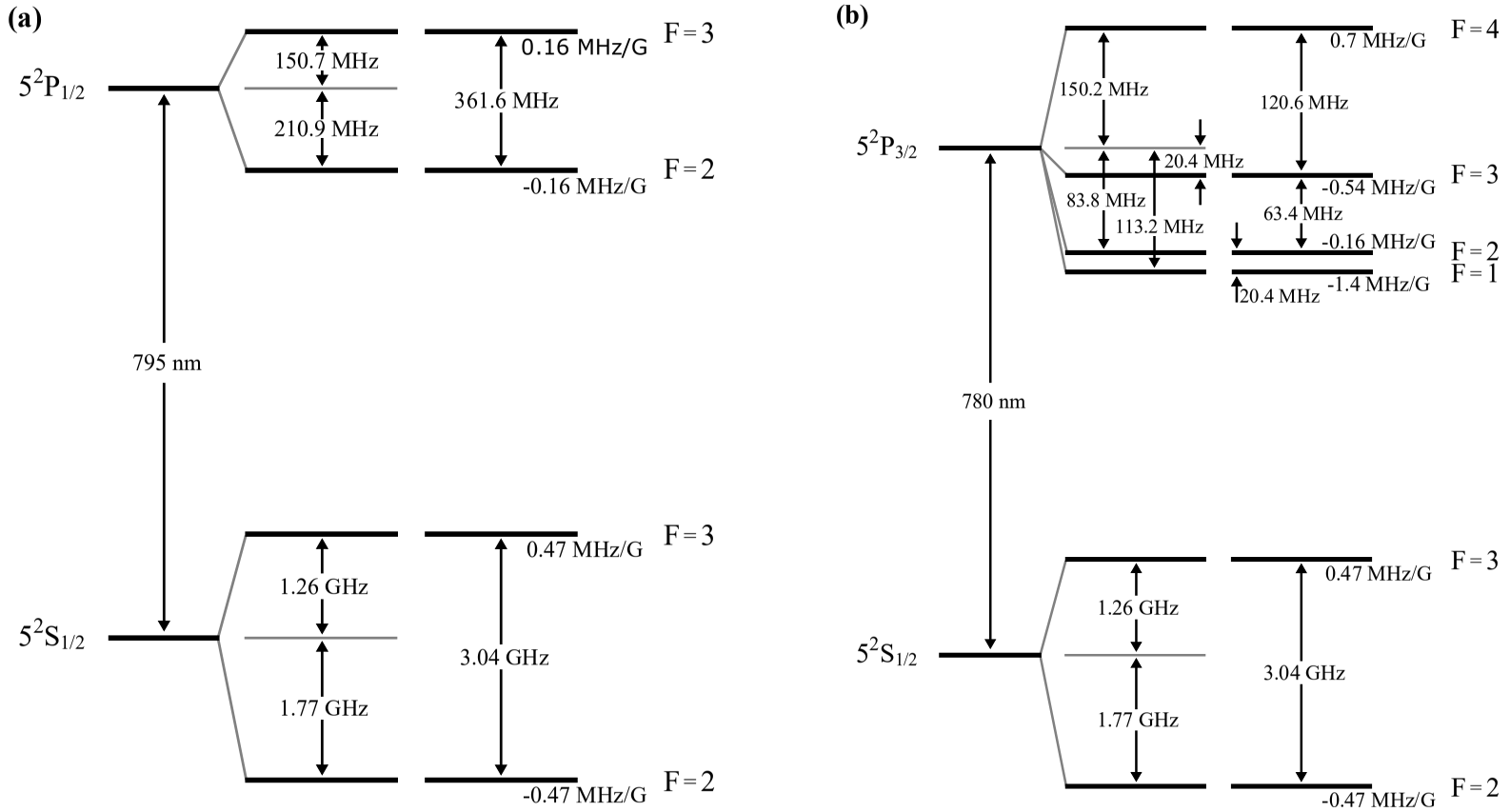

Figure 3.1: Rubidium 85 hyperfine energy level structure: **(a)** ^{85}Rb D_1 line, **(b)** ^{85}Rb D_2 line. The approximate Zeeman splittings for each level are included [128].

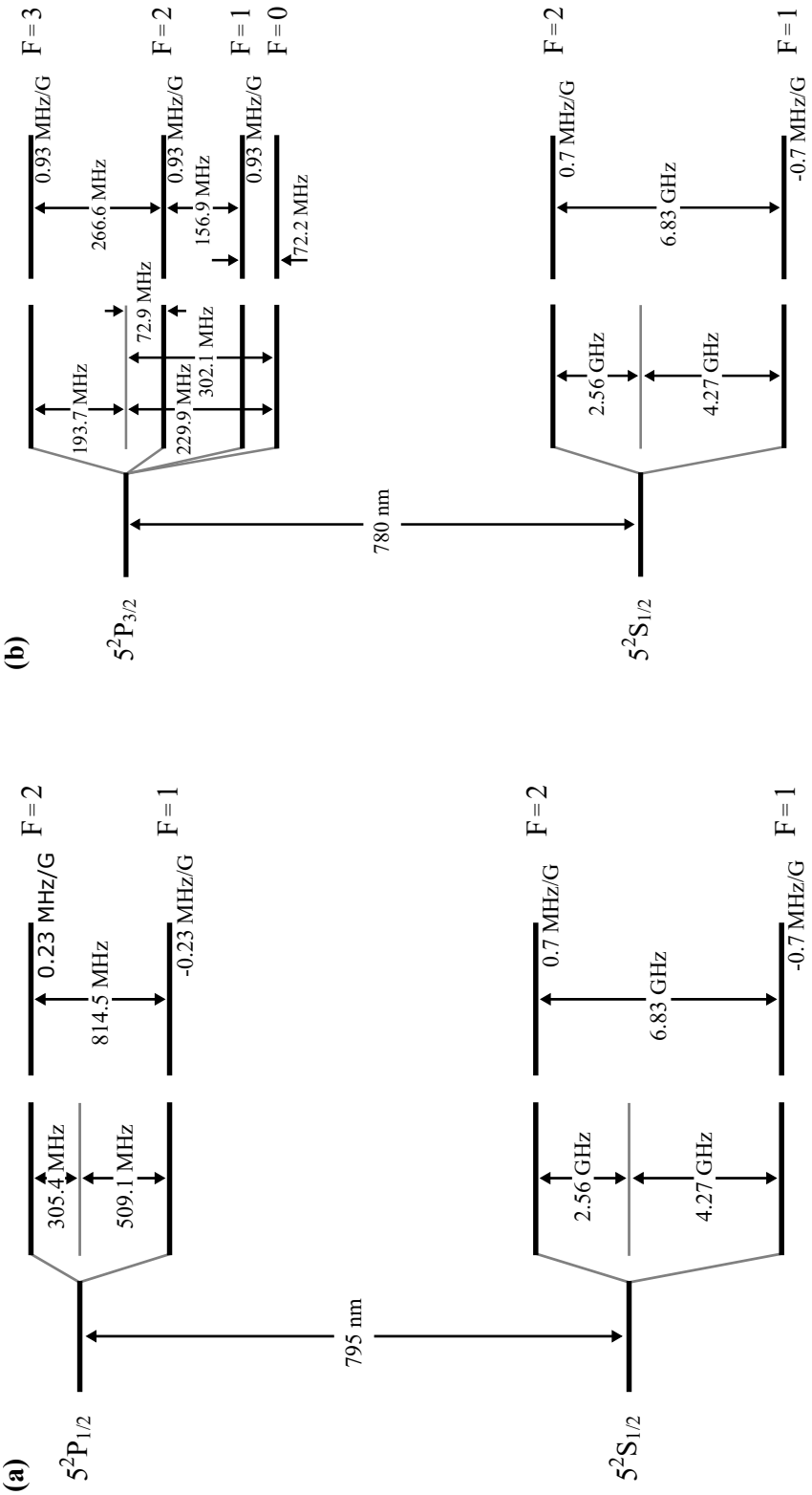

Figure 3.2: Rubidium 87 hyperfine energy level structure: (a) ^{87}Rb D_1 line, **(b)** ^{87}Rb D_2 line. The approximate Zeeman splittings for each level are included [129].

cells contain a small deposit of either naturally occurring isotopic Rb or isotopically-enriched ^{87}Rb. The abundance of Rb means the vapour pressure at a given temperature follows the vapour-pressure model given by [128]

$$\log_{10}\left(\frac{P_{85,87}}{\mu_{85,87}}\right) = 2.881 + 4.857 - \frac{4215}{T} \qquad \text{(solid phase, } <39.3\,^{\circ}\text{C)}\,, \tag{3.1}$$

$$\log_{10}\left(\frac{P_{85,87}}{\mu_{85,87}}\right) = 2.881 + 4.312 - \frac{4040}{T} \qquad \text{(liquid phase, } >39.3\,^{\circ}\text{C)}\,, \tag{3.2}$$

where $P_{85,87}$ is the pressure in Torr of the given Rb isotope, $\mu_{85,87}$ is the relative abundance of that isotope, and T is the temperature in Kelvin[1]. The two equations represent the phases either side of the melting point at 39.3 °C (at atmospheric pressure). From the pressure one can find the vapour density from the ideal gas law

$$n_{85,87} = \mu_{85,87}\,\frac{133.3\,P_{85,87}}{k_B\,T}\,, \tag{3.3}$$

where k_B is the Boltzman constant and the multiplication factor is for conversion to SI units. The vapour pressures and densities for the scenarios covered in this work are plotted in Figure 3.3. Both increase exponentially with increasing temperature. In general, the sensitivity of an AM increases with an increasing number of contributing atoms. Therefore, it is common to heat the vapour cell. In this work a temperature range of 20 °C – 60 °C was explored. This corresponds to a density range of $2.1\times10^{9}\,\text{cm}^{-3}$ – $3.8\times10^{11}\,\text{cm}^{-3}$, depending on the choice of isotope and cell.

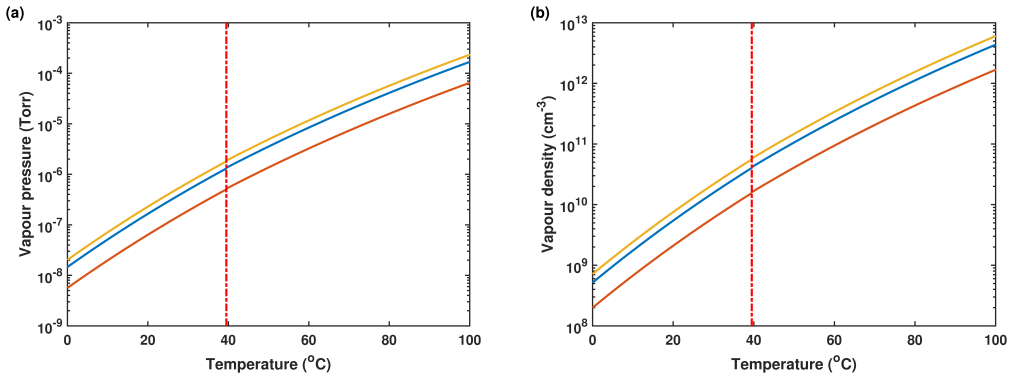

Figure 3.3: Vapour pressure and density of Rb: The dependence on temperature of the vapour pressure **(a)** and vapour density **(b)** of: ^{85}Rb in an isotopic mixture (blue line), ^{87}Rb in an isotopic mixture (red line), and isotopically-enriched ^{87}Rb (yellow line).

[1]For isotopically-enriched ^{87}Rb cells; $\mu_{87} = 1$ and $\mu_{85} = 0$.

3.2 The Zeeman effect

The Zeeman effect describes the perturbations of the hyperfine structure under the application of a static magnetic field. This effect defines the operation principle of all AMs. A magnetic field splits the magnetic sub-levels, which are degenerate at zero-field. Each magnetic sub-level represents a different projection of the atomic angular momentum onto the quantisation axis imposed by the magnetic field. This applies for any general magnetic field B. For the RF-AM a controlled DC field B_z is applied in the z direction. This field is referred to throughout as the bias field, $\mathbf{B}_{\text{bias}} = B_{\text{bias}}\,\mathbf{z}$.

For a weak magnetic field the energy levels are evenly displaced. For the state $|F, m_F\rangle$ the change in energy is given by

$$\Delta E_{|F,m_F\rangle} = g_F\,\mu_B\,m_F\,B\ , \tag{3.4}$$

where μ_B is the Bohr magneton and g_F is the hyperfine Landé g-factor, well approximated by

$$g_F \approx \frac{F(F+1)-I(I+1)+J(J+1)}{2F(F+1)}\,g_J\ , \tag{3.5}$$

with g_J the total angular momentum Landé g-factor.

The RF-AM experiments described in the latter chapters operate in fields below 5 G. In this regime the weak-field approximation of Equation 3.4 is valid.

The Zeeman effect defines the operating frequency of an RF-AM as

$$\nu_L = \frac{\Delta E_{|F,m_F+1\rangle} - \Delta E_{|F,m_F\rangle}}{h} = 2\pi\,\gamma B_{\text{bias}}\ , \tag{3.6}$$

where γ is the gyromagnetic ratio.

An RF field oscillating at ν_L coherently drives the Zeeman (or RF) transitions. These act within the same hyperfine level ($\Delta F = 0$) transferring atoms between different magnetic sub-levels. This generates the atomic precession.

3.2.1 The second-order Zeeman effect

The above approach assumes linearity in the response of each magnetic sub-level to a magnetic field. Although the first-order approximation is valid in the regimes considered in this work, it is not sufficient to completely describe the RF-AM response. For this, second-order effects must be considered.

The second-order Zeeman effect splits the RF resonances corresponding to specific transitions between neighbouring ground state magnetic sub-levels. This becomes more important at higher bias fields (i.e. higher operation frequencies).

To calculate the contribution of the second-order Zeeman effect I use the transition energies for each Zeeman state as a function of the applied magnetic field. These energies are described by the Breit-Rabi equation [130]

$$W(|F,m_{\mathrm{F}}\rangle) = -\frac{\Delta W}{2(2I+1)} + g_I\,\mu_B\,m_F\,B \pm \frac{\Delta W}{2}\sqrt{1+\frac{4\,m_F}{2I+1}x+x^2}\,, \tag{3.7}$$

where

$$x = \frac{(g_J - g_I)\mu_B}{\Delta W}\,B\,, \tag{3.8}$$

is the dimensionless field strength parameter. In addition: the choice of sign ($\pm$) is for $F_\pm = I \pm \frac{1}{2}$, $\Delta W/h$ is the $F_\pm$ hyperfine splitting (in Hz), and g_I is the nuclear g-factor.

Equation 3.7 can be used to compute the Breit-rabi diagrams shown in Figure 3.4. These show the shifts in each hyperfine ground state level due to magnetic fields from the weak-field (Zeeman) effect – highlighted in the insets – to the strong-field (Paschen-Back) regime.

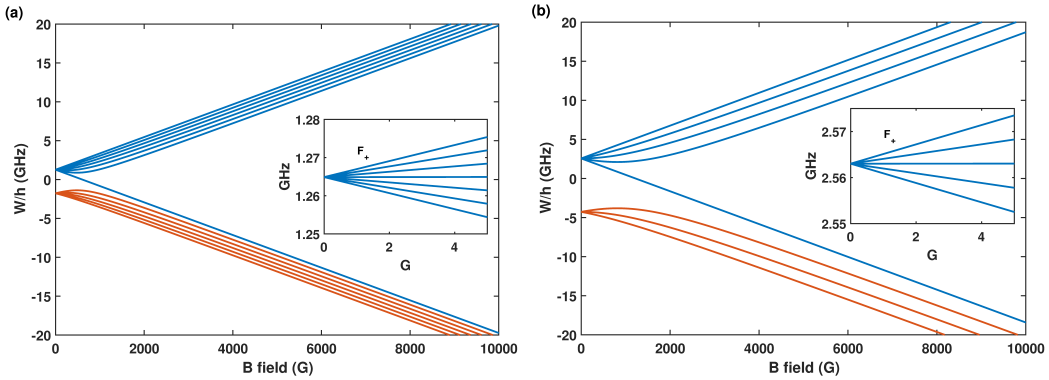

Figure 3.4: Breit-rabi diagrams for Rb: (a) ^{85}Rb. **(b)** ^{87}Rb. Insets: F_+ ground states in region of interest for RF-AM operation.

Equation 3.7 allows the calculation of the operation frequency of the RF-AM in a given magnetic field as

$$\nu_{(m_F \to m_{F-1})} = \frac{1}{h}\left[W(|F,m_F\rangle) - W(|F,m_{F-1}\rangle)\right]\,. \tag{3.9}$$

In our case the RF-AM operates on the F_+ ground state. Choosing the transition $m_F =$

$F \to m_{F-1} = F-1$, allows Equation 3.9 to be factorised. The operation frequency is thus described as

$$\nu_{RF} = \frac{g_I \mu_B B}{h} + \frac{\Delta W}{2h}\left[(1+x) - \sqrt{1+\left(2-\frac{2}{F}\right)x+x^2}\right] . \tag{3.10}$$

For the other transitions ($m_F \to m_{F-1}$), Equation 3.9 does not factorise. The exact operation frequencies for all the magnetic sub-level transitions are plotted in Figure 3.5. The transition frequencies are linear and in good agreement with the linear Zeeman effect (Inset: dot-dashed red line). Nevertheless, the exact transition frequency for each pair of nearest-neighbour Zeeman sub-levels is different due to second order effects (magnified in Inset for a bias field of around 2 G).

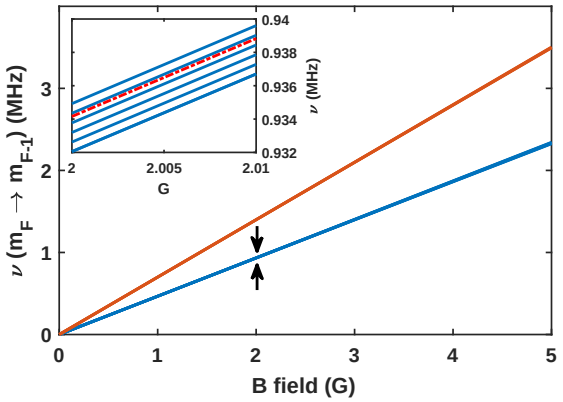

Figure 3.5: Resonant frequency against applied field: Calculated RF-AM operation frequency for ^{85}Rb (blue) and ^{87}Rb (red). Inset: Magnified transitions of ^{85}Rb split due to second-order effects (position of inset marked by arrows). Good agreement with linear approximation – Equation 3.4 (dot-dashed, red line). Adapted from Reference [6].

The second-order contribution can be calculated by subtracting neighbouring transition frequencies – of the form of Equation 3.9. By choosing the transitions that allow for the greatest simplification, the second-order contribution can be stated as

$$\begin{aligned}\Delta\nu_{RF} &= \nu_{(m_F=F-1\to m_{F-1}=F-2)} - \nu_{(m_F=F\to m_{F-1}=F-1)} \\ &= \frac{\Delta W}{2h}\left[2\sqrt{1+\left(2-\frac{2}{F}\right)x+x^2} - \sqrt{1+\left(2-\frac{4}{F}\right)x+x^2} - (1+x)\right] .\end{aligned} \tag{3.11}$$

Additionally, the x-axis can be converted from magnetic field to operation frequency. The resulting function is defined as $\Phi^{85,87}(\nu)$. This is simply $\Delta\nu_{RF}$ (from Equation 3.11) as a function of ν_{RF} (from Equation 3.10). $\Phi^{85,87}(\nu)$ is referred to as the second-order Zeeman

effect as a function of resonant frequency, for ^{85}Rb and ^{87}Rb respectively. These functions are plotted in Figure 3.6.

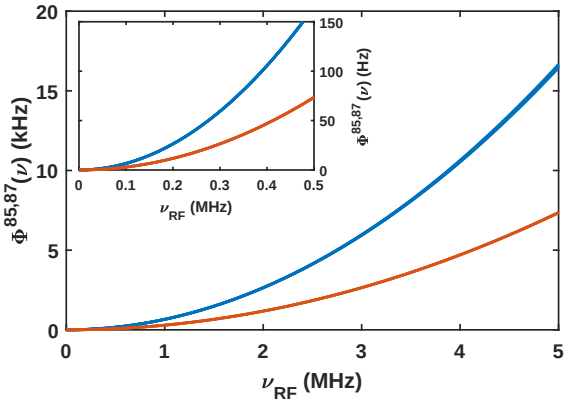

Figure 3.6: The second-order Zeeman effect: Second-order splitting of magnetic sub-levels as a function of operation frequency for ^{85}Rb (blue) and ^{87}Rb (red). Inset: Magnification of the region below 500 kHz. Adapted from Reference [6].

These calculations and the function $\Phi^{85,87}(\nu)$ are used in the results of Section 5.3.10. Table 3.1 lists the constants and values required for the calculations in this section.

	^{85}Rb	^{87}Rb
F_+	3	2
$\frac{\Delta W}{h}$	3.035 GHz [128]	6.835 GHz [129]
g_J	2.0023 [128]	2.0023 [129]
g_I	-2.936×10^{-4} [128]	-9.951×10^{-4} [129]
g_F	$\frac{1}{6} g_J$	$\frac{1}{4} g_J$
x	$9.233 \times 10^{-4}\,\mathrm{B(G)}$	$4.103 \times 10^{-4}\,\mathrm{B(G)}$

Table 3.1: Values required for calculations: The constants and values required for calculating the second-order Zeeman effect.

3.3 Optical pumping

The detected RF-AM signal is directly proportional to the degree of atomic polarisation (see Section 3.4). A high degree of polarisation is obtained via optical pumping. Optical pumping is a standard technique for manipulating atomic populations by the transfer of angular momentum from resonant laser light [131]. In this section I modify the approach of Seltzer (2008) [132] to describe process of optical pumping in the RF-AM implementations of this work.

Consider an atomic vapour irradiated with a beam of circularly polarised (σ^+) light. The direction of propagation of this beam is defined as the z-direction (parallel to the applied bias field). Firstly, the nuclear spin contribution is neglected and I describe the optical pumping of the electron spin.

The relative absorption rates and decay rates are calculated from the Clebsch-Gordan coefficients to give the branching ratios

$$\langle J, m_J, 1, \Delta m_J \,|\, J', m'_J \rangle^2 \ , \tag{3.12}$$

for the transition $|J, m_J\rangle \ \leftrightarrow \ |J, m'_J\rangle$.

σ^+ photons carry one unit of angular momentum, the total value of which must be conserved during light/atom interactions. Hence, upon absorption, the atoms transition to the corresponding excited state m'_J, with $\Delta m_J = +1$. The average rate at which an atom absorbs a photon from the pump beam is given by Γ_{op}, the optical pumping rate. The excited state lifetimes are very short ($\approx 26\,\text{ns}$ for the $5^2P_{1/2}$ and $5^2P_{3/2}$ states of Rb [133]). The atoms decay, with probabilities given by the branching ratios, to one of the permitted ground-state levels, emitting a correspondingly-polarised resonant photon in the process.

The experiments described in this work employ optical pumping on both the D_1 and D_2 lines. These cases are discussed separately.

3.3.1 D_2 line optical pumping

The process of D_2 line optical pumping is shown in Figure 3.7. An atom in either of the ground states can be excited by absorbing a photon. The decay channels are defined by the branching ratios and the parameter a. This parameter is defined as the probability of an atom undergoing collisional mixing. This is discussed further in Section 3.7. It involves collisions between the atoms in the excited state and buffer gas molecules. These act to redistribute atoms among the excited states. For complete mixing ($a = 1$) the result is an equal probability of decay to each ground state. For no mixing ($a = 0$) the branching ratios are recovered.

By defining the occupation probabilities of the ground state levels as $\mathbb{P}\left(m_J = -\frac{1}{2}\right) =$

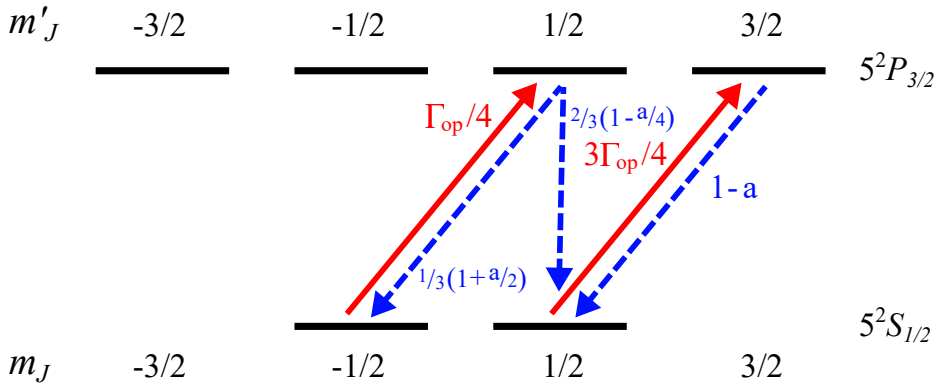

Figure 3.7: D_2 line optical pumping of the electron spin: Relative absorption and decay ratios for optical transitions – with a the degree of collisional mixing.

$\mathbb{P}(-)$ and $\mathbb{P}\left(m_J = +\frac{1}{2}\right) = \mathbb{P}(+)$, the evolution – under optical pumping – can be written as

$$\frac{d\mathbb{P}(-)}{dt} = -\frac{1}{4}\Gamma_{\text{op}}\,\mathbb{P}(-) + \frac{1}{3}\,(1+a/2)\,\frac{\Gamma\text{op}}{4}\,\mathbb{P}(-)\,, \tag{3.13}$$

$$\frac{d\mathbb{P}(+)}{dt} = -\frac{3\Gamma_{\text{op}}}{4}\,\mathbb{P}(+) + (1-a)\,\frac{3\Gamma_{\text{op}}}{4}\,\mathbb{P}(+) + \frac{2}{3}\,(1-a/4)\,\frac{\Gamma_{\text{op}}}{4}\,\mathbb{P}(-)\,. \tag{3.14}$$

The degree of spin-polarisation is

$$\langle S_z\rangle = \frac{1}{2}\,\left(\mathbb{P}(+) - \mathbb{P}(-)\right)\,. \tag{3.15}$$

This is in turn related to the atomic polarisation (P) by $P = 2\langle S_z\rangle$. One can write

$$\mathbb{P}(-) = \frac{1}{2}\,\left(1 - 2\,\langle S_z\rangle\right)\,, \tag{3.16}$$

by taking $\mathbb{P}(+)+\mathbb{P}(-) = 1$. This assumption is validated by the short excited state lifetimes.

By combining Equations 3.13 – 3.16, the evolution of the spin-polarisation is found to be

$$\frac{d\langle S_z\rangle}{dt} = \frac{(2-5a)}{24}\,\Gamma_{\text{op}} - \frac{(1+2a)}{6}\,\Gamma_{\text{op}}\,\langle S_z\rangle - \Gamma_{\text{loss}}\,\langle S_z\rangle\,, \tag{3.17}$$

where the inserted loss rate, Γ_{loss}, represents the combination of additional relaxation processes – discussed further in Section 3.7. The degree of atomic polarisation that can be attained is ultimately limited by these processes.

Solving Equation 3.17, subject to $\langle S_z\rangle(t=0) = 0$, yields

$$\langle S_z\rangle = \frac{(2-5a)\,\Gamma_{\text{op}}}{4(1+2a)\,\Gamma_{\text{op}} + 24\,\Gamma_{\text{loss}}}\left[1 - \mathrm{e}^{-\left(\frac{(1+2a)}{6}\,\Gamma_{\text{op}} + \Gamma_{\text{loss}}\right)t}\right]\,. \tag{3.18}$$

The maximum atomic polarisation is given by the asymptotic value (i.e after sufficient time has elapsed)

$$P = 2 \lim_{t\to\infty} \langle S_z \rangle = \frac{(2-5a)\,\Gamma_{\text{op}}}{2(1+2a)\,\Gamma_{\text{op}} + 12\,\Gamma_{\text{loss}}} \,. \tag{3.19}$$

The atomic polarisation as a function of a is plotted in Figure 3.8. Assuming $\Gamma_{\text{op}} \gg \Gamma_{\text{loss}}$, and in the absence of collisional mixing ($a = 0$), full polarisation is possible. This is a consequence of the closed cycling transition between the $m_J = +1/2$ and the $m'_J = +3/2$ levels. As the degree of mixing increases, this cycling transition is weakened – allowing atoms in the $m_J = +1/2$ level to transition to the $m_J = -1/2$ level. For complete mixing ($a = 1$), the atomic polarisation is limited to $P = -1/2$. Note that the atoms are polarised with negative angular momentum in this case. This is a consequence of how the rates of Figure 3.7 are modified for $a = 1$. On average each photon removes angular momentum from the atoms despite the σ^+ polarisation (see also Figure 3.11).

From Equation 3.19;

$$P = \frac{\Gamma_{\text{op}}}{\Gamma_{\text{op}} + 6\,\Gamma_{\text{loss}}} \quad \text{for} \quad a = 0 \,, \tag{3.20}$$

$$P = \frac{-3\,\Gamma_{\text{op}}}{6\,\Gamma_{\text{op}} + 12\,\Gamma_{\text{loss}}} \quad \text{for} \quad a = 1 \,. \tag{3.21}$$

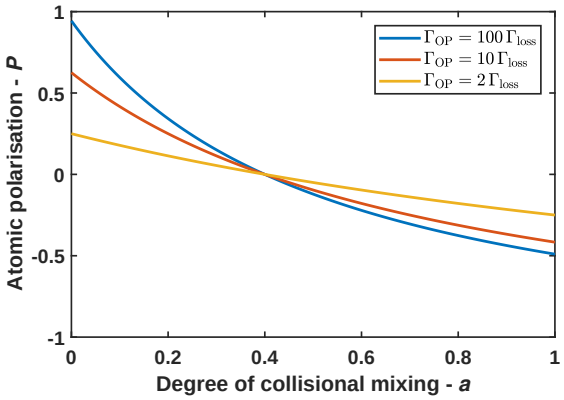

Figure 3.8: D_2 atomic polarisation: Atomic polarisation with D_2 line optical pumping as a function of a. Plotted for various optical pumping and loss rates.

3.3.2 D_1 line optical pumping

The scheme for D_1 line optical pumping is shown in Figure 3.9. An atom in the $m_J = -1/2$ level can absorb a photon and transition to the $m'_J = +1/2$ level, before decaying. Again, the decay channels are defined by the branching ratios and a. With $a = 1$ resulting in an

equal probability of decay to each ground state and $a = 0$ giving the branching ratios. An atom in the $m_J = +1/2$ level is unable to absorb a photon and will remain in that state.

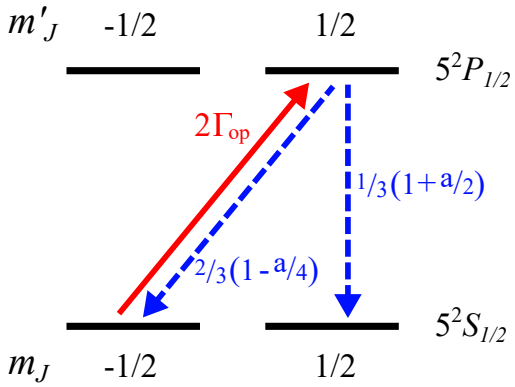

Figure 3.9: D_1 line optical pumping of the electron spin: Relative absorption and decay ratios for optical transitions – with a the degree of collisional mixing.

Note that $m_J = -1/2$ atoms absorb photons at a rate $2\Gamma_{\text{op}}$, as atoms in the $m_J = +1/2$ state are forbidden from absorption. In this case the dynamics of the ground state population probabilities are

$$\frac{d\mathbb{P}(-)}{dt} = -2\Gamma_{\text{op}}\,\mathbb{P}(-) + \frac{4}{3}\,(1-a/4)\,\Gamma_{\text{op}}\,\mathbb{P}(-)\,, \tag{3.22}$$

$$\frac{d\mathbb{P}(+)}{dt} = \frac{2}{3}\,(1+a/2)\,\Gamma_{\text{op}}\,\mathbb{P}(-)\,. \tag{3.23}$$

Following the approach of the previous section, by combining the rate equations with Equation 3.15 and Equation 3.16, the spin-polarisation evolution is shown to be

$$\frac{d\langle S_z\rangle}{dt} = \frac{(2+a)}{6}\Gamma_{\text{op}} - \frac{(2+a)}{3}\Gamma_{\text{op}}\langle S_z\rangle - \Gamma_{\text{loss}}\langle S_z\rangle\,, \tag{3.24}$$

where I have again inserted the additional loss rate, Γ_{loss}.

The solution of Equation 3.24 (subject to the same constraint – $\langle S_z\rangle(t=0) = 0$) is

$$\langle S_z\rangle = \frac{(2+a)\,\Gamma_{\text{op}}}{2\left((2+a)\,\Gamma_{\text{op}} + 3\Gamma_{\text{loss}}\right)}\left[1 - \mathrm{e}^{-\left(\frac{(2+a)}{3}\Gamma_{\text{op}} + \Gamma_{\text{loss}}\right)t}\right]\,. \tag{3.25}$$

The maximum atomic polarisation is now given by

$$P = 2\lim_{t\to\infty}\langle S_z\rangle = \frac{(2+a)\,\Gamma_{\text{op}}}{(2+a)\,\Gamma_{\text{op}} + 3\Gamma_{\text{loss}}}\,. \tag{3.26}$$

The atomic polarisation as a function of a, for the D_1 case, is plotted in Figure 3.10.

Assuming $\Gamma_{op} \gg \Gamma_{loss}$, full polarisation is possible regardless of the degree of collisional mixing. Repeated excitation depopulates the $m_J = -1/2$ level with all the atoms accumulating in the $m_J = +1/2$ level.

From Equation 3.26;

$$P = \frac{2\Gamma_{op}}{2\Gamma_{op} + 3\Gamma_{loss}} \qquad \text{for} \quad a = 0\,, \tag{3.27}$$

$$P = \frac{\Gamma_{op}}{\Gamma_{op} + \Gamma_{loss}} \qquad \text{for} \quad a = 1\,. \tag{3.28}$$

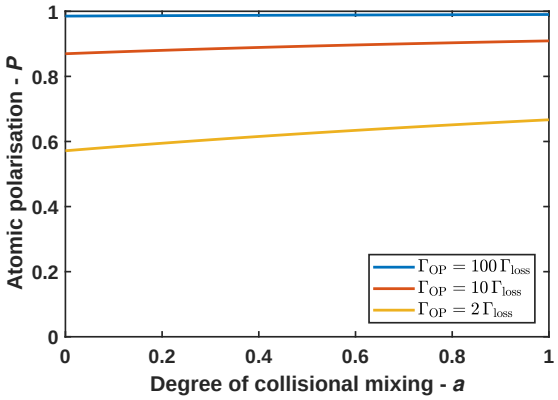

Figure 3.10: D_1 atomic polarisation: Atomic polarisation with D_1 line optical pumping as a function of a. Plotted for various optical pumping and loss rates.

The efficiency of the optical pumping schemes can additionally be described by the average degree of angular momentum added to the atoms by each absorbed photon. By considering Figure 3.7 and Figure 3.9 this value can be seen to be $\frac{1}{3}(1 + a/2)$ for the D_1 line case, and $\frac{1}{12}(2 - 5a)$ for the D_2 line case.

These values are plotted in Figure 3.11. The D_1 line scheme is always more efficient, with collisional mixing increasing the efficiency further. In contrast, mixing reduces the D_2 line efficiency and reverses the sign of the atomic polarisation – as previously noted.

3.3.3 Optical pumping of the total atomic spin

The total atomic spin includes the coupling between the electron spin and the nuclear spin. This splits the electron energy levels into the hyperfine structure. The application of the bias field (along z) defines the quantisation axis and lifts the degeneracy of the magnetic sub-levels. When considering the total spin, optical pumping transfers atoms between the hyperfine levels and within the magnetic sub-levels.

Transfer within the ground-state magnetic sub-levels is depicted in Figure 3.12. Fig-

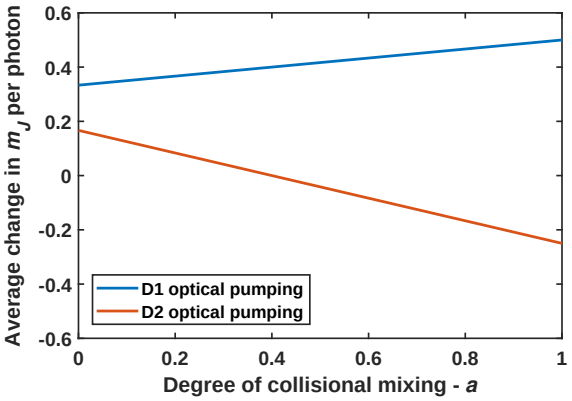

Figure 3.11: Angular momentum change per photon: Average change in atomic angular momentum per photon for both D_1 and D_2 line optical pumping.

ure 3.12(a) is the ^{87}Rb D_2 line and Figure 3.12(b) the ^{87}Rb D_1 line.

Generally, atoms in a ground state level, $|F = 2, m_F\rangle$, can absorb a σ^+ pump beam photon and transition to the corresponding excited state sub-level, with $\Delta m_F = +1$. The atom will then decay to one of the allowed ground-state levels. Repetition of this process sees the atoms step through the magnetic sub-levels to the state with the maximal projection of angular momentum along the quantisation axis.

In the case of Figure 3.12(a), the atoms accumulate in the $|F = 2, m_F = +2\rangle$ state. This is a consequence of the closed cycling transition $|F = 2, m_F = +2\rangle \leftrightarrow |F' = 3, m'_F = +3\rangle$.

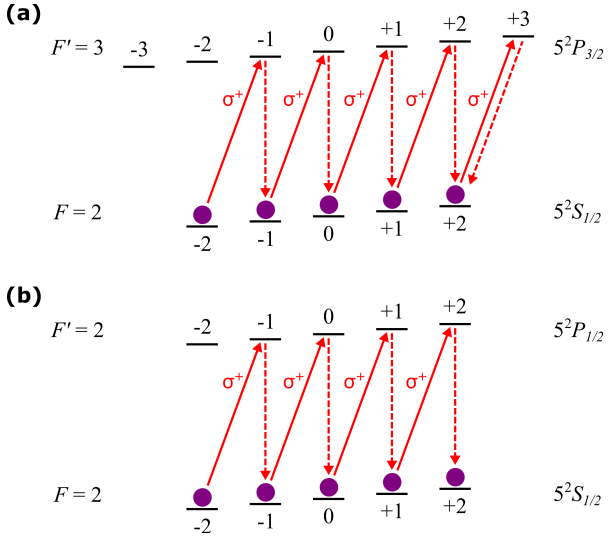

Figure 3.12: Optical pumping of the total atomic spin: **(a)** σ^+ light on the D_2 line of ^{87}Rb, $F = 2 \rightarrow F' = 3$ transition. **(b)** σ^+ light on the D_1 line of ^{87}Rb, $F = 2 \rightarrow F' = 2$ transition. In both cases, decay (dashed arrows) occurs to various allowed states with known probabilities. For clarity, only the relevant spontaneous emission transitions are shown.

For Figure 3.12(b), the atoms again accumulate in the $|F=2, m_F=+2\rangle$ state. In this case, atoms in this state are unable to absorb a σ^+ photon.

In the experiments using D_2 line optical pumping, the pump laser is tuned to the $F=2$ ($F=3$) to $F'=3$ ($F'=4$) hyperfine transition of ^{87}Rb (^{85}Rb), at 780 nm. This transition is chosen as the $F'=3$ ($F'=4$) state has the the greatest separation, in energy, from the other excited states. This minimises the probability of atoms being lost by decaying to the other ground hyperfine state.

For the experiments using D_1 line optical pumping, the pump laser is tuned to the $F=1$ ($F=2$) to $F'=2$ ($F'=3$) hyperfine transition of ^{87}Rb (^{85}Rb), at 795 nm. This approach efficiently depopulates the $F=1$ ($F=2$) ground state, creating strong atomic polarisation.

3.4 Magnetometer response

In this section the response of an RF-AM is discussed. The solution to the Liouville equation for the evolution of the density matrix is required to fully describe the atomic system. This is introduced in Section 3.4.5. However, the response can be well described by the phenomenological Bloch equations [134]. This is derived below.

3.4.1 Bloch equations description

In this section, I modify the approach of Abragam (1961) [135] to analyse the behaviour of an RF-AM.

Consider the total atomic spin vector, $\mathbf{F}=\{F_x, F_y, F_z\}$. $\mathbf{F}$ is simply the sum of all the individual atomic spins that contribute to the magnetometer signal. The evolution of $\mathbf{F}$ in an external magnetic field $\mathbf{B}$ is given by

$$\frac{d\mathbf{F}}{dt} = \gamma \mathbf{F} \wedge \mathbf{B} - \frac{F_x \hat{\mathbf{x}} + F_y \hat{\mathbf{y}}}{T_2} - \frac{F_z - F_0}{T_1} \hat{\mathbf{z}} \,, \tag{3.29}$$

where $\hat{\mathbf{x}}, \hat{\mathbf{y}}, \hat{\mathbf{z}}$ are the unit vectors in the laboratory frame and γ is the gyromagnetic ratio.

The terms on the right hand side of Equation 3.29 are, respectively, the equation of motion for free spins, the decay of any transverse spin components at a rate $1/T_2$ (T_2 is the transverse relaxation time), and the trend towards an equilibrium value ($F_z = F_0$) in the z-direction, at a rate $1/T_1$ (T_1 is the longitudinal relaxation time). In addition, Equation 3.29 requires the further assumption that any transverse perturbations to the field are small compared to the static field.

For the RF-AM systems discussed here, T_2 is the transverse spin relaxation time. This

is affected by a number of processes – such as alkali-alkali collisions – which are described in detail in Section 3.7. T_1 is effectively the optical pumping timescale. It is affected by the frequency, power, and polarisation of the pump beam.

The total field felt by the atoms is the sum of the static bias field and the RF field – $\mathbf{B} = \mathbf{B}_{\text{bias}} + \mathbf{B}_{\text{RF}}$. The bias field is applied along $\hat{\mathbf{z}}$. This imposes a resonant Zeeman transition frequency – which I define as ω_0 – via the Zeeman effect. This can be stated as

$$\mathbf{B}_{\text{bias}} = B_{\text{bias}}\,\hat{\mathbf{z}} = -\frac{\omega_0}{\gamma}\,\hat{\mathbf{z}}\,. \tag{3.30}$$

The RF field is applied along y-direction. Consider this field to be linearly polarised and oscillating at a frequency ω and with an amplitude $2B_1 = 2\frac{\omega_1}{\gamma}$ (i.e. $\mathbf{B}_{\text{RF}} = 2B_1 \cos\omega t$).

Moving to the rotating frame – about $\hat{\mathbf{z}}$ at frequency ω – the total effective field is

$$\mathbf{B}_{\mathbf{eff}} = \left(B_{\text{bias}} + \frac{\omega}{\gamma}\right)\hat{\tilde{\mathbf{z}}} + B_1\,\hat{\tilde{\mathbf{y}}} = \frac{\Delta\omega\,\hat{\tilde{\mathbf{z}}} + \omega_1\,\hat{\tilde{\mathbf{y}}}}{\gamma}\,, \tag{3.31}$$

where $\Delta\omega = (\omega - \omega_0)$ is the detuning of the RF field from the resonance and the unit vectors in the rotating frame are $\hat{\tilde{\mathbf{x}}}, \hat{\tilde{\mathbf{y}}}, \hat{\tilde{\mathbf{z}}} = \hat{\mathbf{z}}$. Note that the counter-rotating component of the RF field has been neglected – an implementation of the rotating wave approximation.

In the rotating frame the Bloch equations (Equation 3.29) becomes

$$\frac{d\widetilde{\mathbf{F}}}{dt} = \gamma\widetilde{\mathbf{F}} \wedge \mathbf{B}_{\mathbf{eff}} - \frac{\widetilde{F}_x\,\hat{\tilde{\mathbf{x}}} + \widetilde{F}_y\,\hat{\tilde{\mathbf{y}}}}{T_2} - \frac{\widetilde{F}_z - F_0}{T_1}\,\hat{\tilde{\mathbf{z}}}\,. \tag{3.32}$$

where the tilde terms ($\sim$) are the spin components in the rotating frame.

By combining Equation 3.31 and Equation 3.32 the equations of motion for the spin components in the rotating frame are shown to be

$$\begin{pmatrix} \frac{d\widetilde{F}_x}{dt} \\ \frac{d\widetilde{F}_y}{dt} \\ \frac{d\widetilde{F}_z}{dt} \end{pmatrix} = \begin{pmatrix} -\frac{1}{T_2} & \Delta\omega & -\omega_1 \\ -\Delta\omega & -\frac{1}{T_2} & 0 \\ \omega_1 & 0 & -\frac{1}{T_1} \end{pmatrix} \begin{pmatrix} \widetilde{F}_x \\ \widetilde{F}_y \\ \widetilde{F}_z \end{pmatrix} + \begin{pmatrix} 0 \\ 0 \\ \frac{F_0}{T_1} \end{pmatrix}\,. \tag{3.33}$$

One can see that the general solution is given by a series of exponential terms of the form $\widetilde{\mathbf{F}} = \mathbf{v}e^{\lambda t} + \mathbf{c}(t)$, where λ and $\mathbf{v}$ are the eigenvalues and eigenvectors of the matrix.

3.4.2 Steady-state solutions to the Bloch equations

The operation of an RF-AM is a continuous processes. Therefore, one can assume that sufficient time has elapsed to consider the steady-state solution of the Bloch equations. This is found by setting

$$\frac{d\widetilde{F}_x}{dt} = \frac{d\widetilde{F}_y}{dt} = \frac{d\widetilde{F}_z}{dt} = 0$$

in Equation 3.33.

The resulting system of linear equations yields

$$\widetilde{F}_x = \frac{\omega_1 T_2}{1+\omega_1^2 T_1 T_2 + \Delta\omega^2 T_2^2} F_0 \,, \tag{3.34}$$

$$\widetilde{F}_y = \frac{-\omega_1 \Delta\omega T_2^2}{1+\omega_1^2 T_1 T_2 + \Delta\omega^2 T_2^2} F_0 \,, \tag{3.35}$$

$$\widetilde{F}_z = \frac{1+\Delta\omega^2 T_2^2}{1+\omega_1^2 T_1 T_2 + \Delta\omega^2 T_2^2} F_0 \,. \tag{3.36}$$

Finally, substituting $\omega_1 = \gamma B_1$ (by definition) gives

$$\widetilde{F}_x = \frac{\gamma B_1 T_2}{1+\gamma^2 B_1^2 T_1 T_2 + \Delta\omega^2 T_2^2} F_0 \,, \tag{3.37}$$

$$\widetilde{F}_y = \frac{-\gamma\Delta\omega B_1 T_2^2}{1+\gamma^2 B_1^2 T_1 T_2 + \Delta\omega^2 T_2^2} F_0 \,, \tag{3.38}$$

$$\widetilde{F}_z = \frac{1+\Delta\omega^2 T_2^2}{1+\gamma^2 B_1^2 T_1 T_2 + \Delta\omega^2 T_2^2} F_0 \,. \tag{3.39}$$

3.4.3 Predicted resonance line shapes

Returning to the laboratory frame, $F_x = \widetilde{F}_x \cos(\omega t) + \widetilde{F}_y \sin(\omega t)$. Note that it is this spin component that is detected by the probe beam (see Section 3.5).

The RF-AM output thus comprises of components oscillating in phase and in quadrature with respect to the driving field. These correspond to absorptive $\left(\widetilde{F}_x\right)$ and dispersive $\left(\widetilde{F}_y\right)$ contributions. In practice, a dual-phase lock-in amplifier – referenced to the driving RF field at ω – is able to extract these two components from the probe beam.

The resonant line shapes refer to the shape of the components $\widetilde{F}_x$ and $\widetilde{F}_y$ as the driving RF field (ω) moves through the resonant frequency (ω_0). By defining

$$\Gamma = \frac{2}{T_2}\sqrt{1+\gamma^2 B_1^2 T_1 T_2} \tag{3.40}$$

as the full-width-half-maximum (FWHM), it follows immediately that the line shapes are given by Lorentzian distributions of the form

$$\widetilde{F}_x(\omega) = \frac{2A}{\pi}\left[\frac{\Gamma}{4(\omega-\omega_0)^2+\Gamma^2}\right], \tag{3.41}$$

and

$$\widetilde{F}_y(\omega) = \frac{2A}{\pi}\left[\frac{\Gamma(\omega_0-\omega)}{4(\omega-\omega_0)^2+\Gamma^2}\right], \tag{3.42}$$

which are centred at the resonant frequency – ω_0. The absorptive $\left(\widetilde{F}_x\right)$ component is a standard Lorentzian, whereas the dispersive $\left(\widetilde{F}_y\right)$ component is an anti-Lorentzian function. Example plots of $\widetilde{F}_x$ (blue) and $\widetilde{F}_y$ (red) are included in Figure 3.13.

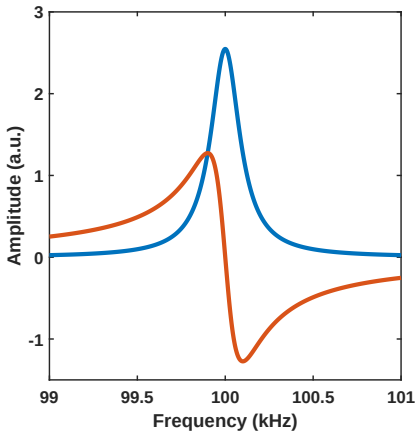

Figure 3.13: Example RF-AM resonance response: Theoretical plots of $\widetilde{F}_x$ (blue) and $\widetilde{F}_y$ (red). Centred at $\omega_0 = 100\,\text{kHz}$ with $\Gamma = 200\,\text{Hz}$.

3.4.4 Comments on the resonant line shapes

3.4.4.1 RF-AM sensitivity

In Section 3.6, the sensitivity of an RF-AM is shown to be inversely proportional to the gradient of the dispersive curve. It is clear that this gradient, and therefore the sensitivity, is maximised at resonance. The maximum value is given by

$$\left.\frac{d\widetilde{F}_y}{d\omega}\right|_{\omega=\omega_0} = \frac{-\gamma B_1 T_2^2 F_0}{(1+\gamma^2 B_1^2 T_1 T_2)}\,. \tag{3.43}$$

From this it is easy to show that the optimum RF field amplitude – that maximises the gradient – is $B_1 = B_{\text{ideal}}$, where

$$B_{\text{ideal}} = \frac{1}{\gamma\sqrt{T_1 T_2}}\,. \tag{3.44}$$

At this point the maximum dispersive gradient is

$$\left.\frac{d\widetilde{F}_y}{d\omega}\right|_{\omega=\omega_0,\ \max} = \frac{-F_0\,T_2^{3/2}}{2\sqrt{T_1}}\ . \tag{3.45}$$

3.4.4.2 RF-AM linewidth

The FWHM (Equation 3.40) increases with RF field amplitude. Note that, at B_{ideal}, the FWHM reduces to

$$\Gamma = \frac{2\sqrt{2}}{T_2}\ . \tag{3.46}$$

Therefore, the linewidth of the magnetometer response – at the position of peak sensitivity – is narrowed by increasing the lifetime of the transverse spin component.

3.4.4.3 Asymptotic limits of the lineshapes

The peak of the absorptive profile clearly occurs at resonance ($\Delta\omega = 0$), where the maximum is given by

$$\max\left(\widetilde{F}_x\right) = \frac{\gamma B_1\,T_2\,F_0}{1+\gamma^2 B_1^2\,T_1\,T_2}\ . \tag{3.47}$$

From this, it can be shown that B_{ideal} maximises the height of the peak – giving a maximum value

$$\max\left(\widetilde{F}_x\right) = \frac{F_0}{2}\sqrt{\frac{T_2}{T_1}}\ . \tag{3.48}$$

Below B_{ideal} the amplitude of the absorptive peak increases towards the maximum. Beyond it, the amplitude steadily decays towards zero (in the asymptotic limit)[2].

The peaks of the dispersive profile are found at the turning points of $\widetilde{F}_y(\omega)$. These are given by

$$\Delta\omega = \pm\frac{1}{T_2}\sqrt{1+\gamma^2 B_1^2\,T_1\,T_2} = \pm\frac{\Gamma}{2}\ . \tag{3.49}$$

The amplitudes at these points are found to be

$$\pm\frac{\gamma B_1\,F_0}{\Gamma}\ . \tag{3.50}$$

In contrast to the absorptive profile, the peaks of the dispersive profile continue increasing with RF amplitude to an asymptotic limit. This limit has the same value as Equation 3.48. It can be found by substituting for Γ in Equation 3.50, pulling out the square-root,

[2]This is easily seen by considering the behaviour of $\frac{x}{1+x^2}$ for $x > 0$.

and applying the power rule;

$$\lim_{B_1\to\infty}\left(\pm\sqrt{\frac{\gamma^2 B_1^2 T_2^2 F_0^2}{4(1+\gamma^2 B_1^2 T_1 T_2)}}\right)=\pm\frac{F_0}{2}\sqrt{\frac{T_2}{T_1}}\ . \tag{3.51}$$

3.4.5 Density matrix formalism

To fully characterise the atomic system, a density matrix approach is required. This is comprehensively described in Appelt et al. (1998) [136], where the evolution of the density matrix for the RF-AM system is given by

$$\frac{d\rho}{dt}=\frac{1}{i\hbar}[H,\rho]+\Gamma_{\rm op}[\phi(1+2\mathbf{s}\cdot\mathbf{S})-\rho]+\Gamma_{\rm se}[\phi(1+4\langle\mathbf{S}\rangle\cdot\mathbf{S})-\rho]+D\nabla^2\rho\ , \tag{3.52}$$

with only the terms that account for the significant processes in the system included.

The first term is the Liouville equation describing the free evolution under the Hamiltonian, H, defined as

$$H=H_{\rm g}+H_{\rm rf}\ . \tag{3.53}$$

H_g is the ground state Hamiltonian. It includes the hyperfine structure and the magnetic-dipole coupling between the bias field and both the electron and nuclear spins. $H_{\rm rf}$ is the Hamiltonian for the interaction between the electron spin and RF field,

$$H_{\rm rf}=2g_s\mu_B S_x B_1\cos(\omega t)\ , \tag{3.54}$$

where g_s is the electron g-factor.

Returning to Equation 3.52, the second term describes the effect of optical pumping at the rate $\Gamma_{\rm op}$. The third terms accounts for spin-exchange collisions between alkali atoms at the rate $\Gamma_{\rm se}$. The final term is the diffusion term. Note how these terms account for the same phenomena as the terms in the Bloch equations (Equation 3.29).

In the limit of large spin-polarisation (i.e. efficient optical pumping) and under the application of resonant RF field ($\mathbf{B_{rf}}=2B_1\cos\omega t$) the resulting transverse spin-polarisation component is the x-direction is[3]

$$P_x=\frac{1}{2}\gamma B_1 T_2\cos(\omega t)\ . \tag{3.55}$$

[3]This follows from Equation 169 of Reference [136].

This result can also be derived – up to the factor $1/2$ – from the Bloch equations description. In the limit of efficient optical pumping ($F_z \gg \{F_x, F_y\}$) and for a resonant RF field, the spin-polarisation component in the x-direction is

$$P_x = \lim_{\Delta\omega\to 0}\left(\frac{F_x}{F_z}\right) = \lim_{\Delta\omega\to 0}\left[\frac{\widetilde{F_x}\cos(\omega t)+\widetilde{F_y}\sin(\omega t)}{\widetilde{F_z}}\right] = \gamma B_1 T_2 \cos(\omega t)\ , \tag{3.56}$$

where I have made use of Equations 3.37 – 3.39.

3.5 Optical polarisation rotation

The previous section details how the presence of a resonant RF field results in the creation of a transverse spin-component (P_x). The detection of this atomic precession is achieved by an off-resonant, linearly polarised probe beam. Detuning is used to limit the perturbation of the atomic system during measurement.

The probe beam propagates through the cell in the x-direction. The linear polarisation can be decomposed into a combination of the two circular polarisations. For a circularly birefringent media the polarisation plane of the probe beam will be rotated by an angle ϕ when passing through it.

Using a semi-classical approach, the angle of rotation is derived in Erickson (2000) [137]. The resulting equation is

$$\phi = \frac{2\pi\nu l}{c}\left[n_+(\nu) - n_-(\nu)\right]\ , \tag{3.57}$$

where l is the distance travelled through the medium and $n_+(\nu)$ and $n_-(\nu)$ are the refractive indices of σ^+ and σ^- – respectively. For a circularly birefringent medium $n_+(\nu) \neq n_-(\nu)$ – this is also known as circular dichroism.

The circular dichroism of the atomic vapour is a consequence of the spin-polarisation created by optical pumping. The rotation angle is determined by calculation of $n_+(\nu)$ and $n_-(\nu)$. See, for example, References [138, 137, 132]. For an RF-AM the rotation angle is given by [61],

$$\phi = \frac{1}{2}\pi l r_e c f n P_x D(\nu)\ . \tag{3.58}$$

In this equation, l is the distance travelled by the probe beam through the sensing volume[4], $r_e = 2.82 \times 10^{-15}$ m is the classical electron radius, f is the absorption oscillator strength of the probe transition[5], n is the atomic vapour density, and $D(\nu)$ is the dispersive optical profile for the probe transition[6].

Equation 3.58 states that the rotation angle of the probe beam's plane of polarisation is proportional to P_x. Recall that P_x is the transverse spin-polarisation component generated by the RF field – given by Equation 3.55. Hence, during measurement, the probe beam is imprinted with the information P_x and, in turn, details of the oscillating magnetic field.

3.6 Magnetometer sensitivity

The sensitivity of a magnetometer is a fundamental parameter stating the smallest magnetic field the device is capable of detecting. For an RF-AM this can be expressed in two complementary ways, depending on the mode of operation. The DC field sensitivity is used when the magnetometer is used as a scalar DC magnetometer. The RF field sensitivity is used when the magnetometer is used as an AC magnetometer. This is the case for the EMI applications introduced in this work. Therefore, unless stated otherwise it is this value that is referred to as the 'sensitivity'.

3.6.1 DC sensitivity

The intrinsic DC sensitivity of an RF-AM is the smallest detectable shift in $\mathbf{B}_{\text{bias}}$. This is directly related to the gradient of the dispersive slope at the resonant frequency – the steeper the slope the larger the change in output for a given change in field.

The DC sensitivity, at a given operation frequency, is given by [68, 139]

$$\delta B_{\text{DC}} = \frac{\hbar}{g_F \mu_B} \frac{\Gamma}{\text{SNR}} , \tag{3.59}$$

where $\hbar$ is Planck's constant, μ_B is the Bohr magneton, g_F is the Landé g-factor ($g = \frac{1}{3}$ for ^{85}Rb, $g = \frac{1}{2}$ for ^{87}Rb [128, 129]), Γ is the FWHM resonance linewidth, and SNR is the signal-to-noise ratio.

Note that the slope of the dispersive response at the resonance frequency (see Section 3.4.4.1) is accurately described by the the response amplitude (i.e. the SNR) divided by

[4] For a coated vapour cell this is the length of the cell in the x-direction. For a perpendicular pump-probe arrangement in a buffer gas cell, this is approximately the beam-waist of the pump beam. See Section 3.7.4.

[5] For this work, $f = 0.696$ (the oscillator strength for the D_2 transition of ^{85}Rb and ^{87}Rb [128, 129]).

[6] $D(\nu) = \frac{(\nu - \nu_0)}{(\nu - \nu_0)^2 + \left(\frac{\Delta\nu}{2}\right)^2}$ – with ν_0 the probe transition frequency and $\Delta\nu$ the FWHM.

the response linewidth (Γ). Therefore, the ratio Γ/SNR (in Equation 3.59) implies that the sensitivity is inversely proportional to the gradient of the dispersive profile.

3.6.2 RF sensitivity

The RF field sensitivity is evaluated by determining the factors contributing to the noise in the spectrum of the magnetometer signal. A known calibration field (of magnitude B_{RF}) is applied and used to confirm the linearity and calibrate the spectrum response. In this work, this field is used to calculate the total noise floor – defined as the noise level when B_{RF} is turned off but with all other experimental parameters turned on. The total noise floor represents the minimum detection level of an RF field at the calibration frequency.

The RF sensitivity, at a given frequency, can therefore be written as [61, 69, 62]

$$\delta B_{\mathrm{RF}} = \frac{B_{\mathrm{RF}}}{\mathrm{SNR}} \,. \tag{3.60}$$

In both measurements of sensitivity the unit is $\mathrm{T}/\sqrt{\mathrm{Hz}}$. The square-root Hz comes from the fact that SNR is computed from the square-root of a power spectrum.

3.7 Collisional and relaxation processes

Fundamentally, the RF-AM operation is a measurement of changes in the precession generated by Zeeman transitions. A reduction in the linewidth of these transitions results in an increase in the sensitivity of the magnetometer. This is achieved by maximising the spin-polarisation lifetime: as the linewidth is governed by the relaxation processes. The spin-polarisation lifetime is described by the timescales introduction in Section 3.4. These are the longitudinal relaxation time (T_1) and the transverse spin-relaxation time (T_2).

The longitudinal relaxation time is limited by spin-destructive collisions in the vapour cell, the interaction with the probe beam, the rate of optical pumping, radiation trapping, and collisions with the cell walls. Spin-destructive collisions can be further split into alkali-alkali collisions and collisions with other species – such as buffer gas – contained in the cell.

The transverse spin-relaxation time is affected by spin-exchange collisions and magnetic field gradients, as these effects introduce dephasing in the atomic precession.

3.7.1 Spin-destructive collisions

Spin-destructive collisions are interactions for which the spin-polarisation of the atomic vapour is not conserved. They can occur between two alkali atoms (of the same or different

isotopes) and between alkali atoms and buffer gas molecules. For a colliding pair (A and B) this can be represented as

$$A(\Uparrow) + B(\Downarrow) \rightarrow A(\Downarrow) + B(\Downarrow) \, . \tag{3.61}$$

In general, the rate of these collisions is significantly smaller than that of spin-exchange collisions (discussed below). Therefore, it can often be neglected unless operating in a regime where spin-exchange is eliminated – e.g. SERF magnetometry.

3.7.2 Probe beam interaction

The measurement interaction between the atomic vapour and the probe beam results in depolarisation of the atomic spin. This relaxation rate is reduced by reducing the beam's intensity and detuning sufficiently far from resonance. However, this also results in a reduction in the detected optical polarisation rotation signal. This trade-off must be empirically evaluated to optimise the sensitivity of the magnetometer.

3.7.3 Radiation trapping

Optical pumping creates atomic alignment along the quantisation axis. Therefore, the optical pumping rate affects T_1. During optical pumping the excited atoms decay by emission of a resonant photon. At high atomic densities it becomes likely that this photon will excite a surrounding atom. As the direction and polarisation of the emitted photon are random, this can result in the depolarisation of the second atom. When the second atom decays the process can continue in a chain reaction, depolarising several atoms before a photon exits the cell. This process is called radiation trapping [140].

One can include a quenching gas in the vapour cell to overcome this effect. These gases – typically N_2 – possess a number of internal vibrational and rotational energy states that are near-resonant with the alkali optical transitions. Therefore, excited alkali atoms are able to decay non-radiatively when colliding with a N_2 molecule [141].

It is important to note that collisions between the alkali atoms and the buffer/quenching gases increase the degree of collisional mixing (a) – discussed in Section 3.3. This is because a quenching decay has an equal probability of returning the atom to either ground state – i.e. the decay is no longer governed by the branching ratios.

The cells used in this thesis contain 20 Torr of N_2. In the explored temperature range, approximately 80% of the excited state's decay channels are non-radiative quenching tran-

sitions. At the densities used (below $3.8 \times 10^{11}\,\mathrm{cm}^{-3}$) the degree of radiation trapping is negligible, the primary function of the N_2 is as a buffer gas – introduced below.

3.7.4 Wall collisions

A collision between a polarised alkali atom and a wall of the vapour cell is completely depolarising. During such a collision the atom is absorbed into the wall for a non-negligible period of time – before returning to the vapour. During this time, it experiences strong interactions from the atoms and molecules at the surface of the cell. These interactions act to randomise the orientation of the atomic spin.

There are two common approaches used to limit spin-relaxation due to wall collisions in atomic magnetometry. The first is the use of an organic surface coating, such as paraffin. Such coatings have low adsorption energies. This reduces the average time an atom spends at the surface, leading to virtually elastic collisions. This implies the internal degrees of freedom of the atoms are unchanged by such collisions, preventing depolarisation. Each atom can remain polarised through many thousands of wall collisions. The use of a coated cell generally implies an increased sensitivity as a greater number of atoms contribute to the signal. One can consider the magnetometer to be averaging the response over the entire cell volume.

Alternatively, one can insert an inert buffer gas into the cell. The buffer gas limits the speed at which the atoms diffuse to the cell walls. Consequently, the interaction time between the laser beams and the atoms is increased. The pressure of the gas must be chosen appropriately. With increasing pressure there is a balance between the decrease in wall collisions with an increase in pressure broadening.

Buffer gas cells are used for the experiments presented in this work. Using a buffer gas cell means the effective sensor volume is defined as the overlapping region of the pump and the probe beams. In the context of EMI, this provides an increase in the spatial resolution of the measurements/images (compared to averaging over the cell volume for coated cells).

3.7.5 Spin-exchange collisions

Spin-exchange collisions represent a major source of broadening. These result from alkali-alkali collisions and are, therefore, increasingly prevalent at increasing vapour densities.

Spin-exchange collisions see the total spin conserved whilst the electron spins of the

S	σ_{SE} (cm^2)	σ_{SD} (cm^2)
Rb	1.9×10^{-14} [142]	9.0×10^{-18} [57, 143]
N_2	–	1.0×10^{-22} [57, 144]

Table 3.2: Cross-sections for interactions with Rb: Collisional cross-sections for the spin-exchange and spin-destructive interactions – including Rb-Rb collisions and buffer gas collisions.

two colliding atoms are reversed. For two alkali atoms (A and B) this can be represented by

$$A(\Uparrow) + B(\Downarrow) \rightarrow A(\Downarrow) + B(\Uparrow) \ . \tag{3.62}$$

The origin of the spin-exchange interaction is the difference in energy between the singlet potential ($\Uparrow\Downarrow$) and the triplet potential ($\Uparrow\Uparrow$) for the system AB [131]. The consequence of these collisions is to limit the degree of atomic polarisation by redistributing the atomic populations between the m_F sub-levels – whilst the total atomic spin is preserved. Hence, they introduce dephasing (reducing T_2) without affecting T_1.

To discuss the dominant source of collisional noise in an AM I introduce the collision rate between Rb and a species S as

$$\Gamma_{\mathrm{Rb},S} = n_S \, \sigma_{\mathrm{Rb},S} \, \bar{v}_{\mathrm{Rb},S} \ , \tag{3.63}$$

where n_S is the density of the second species, $\bar{v}_{\mathrm{Rb},S}$ is the mean relative velocity, and $\sigma_{\mathrm{Rb},S}$ is the cross-section for the interaction.

These cross-sections can be used to judge the relative contributions of each type of collision to the relaxation of the polarisation. The cross-sections for the collisions discussed in this section are presented in Table 3.2. Spin-exchange is the dominant collisional process – orders of magnitude above the other collision rates.

3.7.6 Magnetic field gradients

Magnetic field gradients across the sensing volume broaden the RF-AM response. This is because atoms in different locations experience a different bias magnetic field. Hence, they have different resonant precession frequencies.

Suppressing the magnetic gradients decreases the linewidth – increasing the sensitivity. With a coated cell the motion of the atoms throughout the cell's volume acts to average the

gradients, reducing their effect.

In contrast, the use of buffer gas results in the slow diffusive motion of atoms. This means the atoms are more sensitive to magnetic field gradients. However, buffer gas cells allow the operation of multiple independent magnetometers in different regions of the same cell. This allows the local mapping of magnetic field gradients whilst suppressing of common noise (for example from distant sources or laser fluctuations). Magnetometers employing this approach generally achieve an order of magnitude reduction in the noise floor.

3.8 Practical limits of sensitivity

In practice, the high-sensitivity operation of an RF-AM requires control across the collision and relaxation processes and the accompanying experiment parameters.

The rate of spin-destructive collisions, spin-exchange collisions, wall collisions, and the effect of radiation trapping are fixed by the choice of the vapour cell and the operation temperature. The cell geometry (including the size, shape, and alkali source) and the inclusion of coatings, buffer and quenching gases all play an important role.

The optical pumping rate and the probe beam perturbation are dependent on the laser beams' frequencies and intensities. For buffer gas cells the beam waists also define the effective sensing volume. In addition, the vapour density (temperature) affects the degree of propagation of the beams through the cell. Furthermore, the impact of the strength of the applied RF field on the magnetometer's response and it's sensitivity has been discussed.

This experimental parameter space must be carefully explored to optimise the performance of the sensor.

For the RF-AMs developed in this work the magnetic field noise is by far the most important limiting effect. The dominant contribution to this noise is the power line noise – oscillating at 50 Hz. The majority of previous RF-AMs implementations feature multiple layers of mu-metal shielding enclosing the sensor. This protects the sensor against magnetic field noise and results in an increased sensitivity. However, the cost and footprint of the sensor are dramatically increased and such an approach is infeasible for many field applications (e.g. NQR detection of explosives, or EMI introduced here).

The limited practicality of shielded AMs motivates the development of unshielded AMs – used throughout this work. The approaches developed for actively stabilising the ambient magnetic field and reducing magnetic field gradients are introduced in the following chapter, and the results are (mainly) presented in Section 5.3.9 and Section 5.4.4.

3.9 Fundamental noise limits

Technological improvements have seen AMs overcome many experimental limitations to their sensitivity. As a result, devices have begun to approach the fundamental limits of sensitivity imposed by quantum mechanics. These are related to quantum fluctuations in the atomic vapour and probe beam. This section describes these limitations following the analysis of Savukov et al. (2005) [61] . The three quantum-limits are known as the spin-projection noise, the photon-shot noise, and the light-shift noise.

The total, fundamental quantum mechanical uncertainty in the measurement is given by the combination of the these limits

$$\delta B = \sqrt{\delta B_{\mathrm{spn}}^2 + \delta B_{\mathrm{psn}}^2 + \delta B_{\mathrm{lsn}}^2} \, . \tag{3.64}$$

3.9.1 Spin-projection noise

The spin-projection noise arises from the quantum mechanical uncertainty of projecting a spin-polarised atom during measurement. If the measurement basis is orthogonal to the direction of polarisation then the result of the measurement is random.

With complete spin-polarisation along z, the atomic ensemble can be described as an eigenstate of F_z. The traverse components (F_x and F_y) are governed by the commutation relation

$$[F_x, F_y] = i F_z \, , \tag{3.65}$$

and therefore they experience fluctuations arising from Heisenberg's uncertainty principle,

$$\sigma^2(F_x)\, \sigma^2(F_y) \geq \frac{|F_z|^2}{4} \, . \tag{3.66}$$

Assuming there is no spin squeezing ($\sigma(F_x) = \sigma(F_y)$), then the uncertainty in the measured parameter – F_x – is

$$\sigma(F_x) = \sqrt{\frac{F_z}{2}} \, . \tag{3.67}$$

Repeated uncorrelated measurements using an ensemble of N atoms improves this by $\sqrt{N}$.

The measurement of polarisation rotation in the RF-AM is a continuous process. As an atom's alignment is destroyed during interaction with a probe beam photon, all measurements cannot be considered to be uncorrelated. Subsequent measurements on the same individual atom will not provide additional sensitivity. Adapting the uncertainty in F_x for

continuous measurement gives [61]

$$\sigma(F_x) = \sqrt{\frac{2F_z T_2}{N}} \,. \tag{3.68}$$

The uncertainties in the measurement of F_x can be related to the uncertainty in the measurement of B_1 using Equation 3.55

$$\sigma(P_x) = \frac{\sigma(F_x)}{F_z} = \frac{\gamma T_2}{2}\,\delta B_{\text{spn}} \,. \tag{3.69}$$

The spin-projection contribution is the calculated by combining Equation 3.68 and Equation 3.69 [61]

$$\delta B_{\text{spn}} = \frac{1}{\gamma}\sqrt{\frac{8}{F_z n V T_2}} \,, \tag{3.70}$$

where V is the effective sensor volume and n is the atomic vapour density.

3.9.2 Photon-shot noise

Photon-shot noise is associated with the measurement of the angle of rotation (ϕ) of the probe beam with a finite number of photons. For a balanced polarimeter it arises from the uncertainty in the number of photons in each detection arm. This results in an uncertainity in the angle of rotation of [49]

$$\delta\phi = \sqrt{\frac{1}{2\Phi\eta}} \,, \tag{3.71}$$

where Φ is the photon flux of the probe beam and η is the quantum efficiency of the photodiode.

By recalling Equation 3.58, the uncertainty in P_x is related to the uncertainty in ϕ by

$$\sigma(P_x) = \frac{2}{\pi l r_e c f n D(\nu)}\,\delta\phi \,. \tag{3.72}$$

Finally, the photon-shot noise contribution is the calculated by combining Equation 3.69, Equation 3.71, and Equation 3.72,

$$\delta B_{\text{psn}} = \frac{2\sqrt{2}}{\pi l r_e c f n \gamma T_2 D(\nu)\sqrt{\Phi\eta}} \,. \tag{3.73}$$

3.9.3 Light-shift noise

The light-shift noise arises from polarisation fluctuations of the probe beam. Light shift, or the AC Stark effect, is the electric equivalent of the Zeeman effect. It sees the slight perturbation in atomic levels in the presence of resonant or near-resonant light.

The effect can be considered as a virtual magnetic field, B_{LS}. For a probe beam on the D_2 line, this field is given by [132]

$$B_{\mathrm{LS}} = \frac{\pi r_e c f \Phi D(\nu)}{2\gamma^e A} s_x \,, \tag{3.74}$$

where Φ is again the photon flux of the probe beam, γ^e is the gyromagnetic ratio for an isolated electron, A is the cross-sectional area of the probe beam, and s_x is the degree of circular polarisation of the beam.

For the linearly polarised probe $s_x \approx 0$. However, quantum fluctuations in the polarisation lead to an uncertainty in this parameter given by [61]

$$\delta s_x = \sqrt{\frac{2}{\Phi}} \,. \tag{3.75}$$

The light-shift noise contribution to the uncertainty in magnetic field measurements is therefore found by combining Equation 3.74 and Equation 3.75 [61, 132]

$$\delta B_{\mathrm{lsn}} = \frac{\pi r_e c f D(\nu) \sqrt{2\Phi}}{\gamma^e A} \,. \tag{3.76}$$

Chapter 4

Experimental apparatus

In this chapter the experimental setups of the EMI-AM instruments are described. Firstly, an overview of the components common to each implementation is provided. Each experimental development is then introduced chronologically – with the major advantages and advances of each stage described.

4.1 Overview of RF-AM implementation

A schematic sketch of the unshielded RF-AM setup is shown in Figure 4.1. The arrangement follows that first described in Savukov et al. (2005) [61]. An alkali vapour cell containing Rb is the core of the sensor. The atomic vapour is spin-polarised by optical pumping. This is done by the application of a circularly polarised pump beam and a parallel DC magnetic field (the bias field – $\mathbf{B}_{\mathrm{BIAS}}$). The direction of the pump beam is defined as the z direction. The σ^{+} polarisation of the pump beam is prepared immediately before the cell using a quarter-wave plate ($\lambda/4$).

The bias field is controlled by a series of Helmholtz coils. The magnitude of this field sets the operation frequency of the RF-AM – a consequence of the Zeeman effect. In this way, the operation frequency can be tuned in light of the desired application.

The magnetometer is calibrated with a known AC magnetic field ($\mathbf{B}_{\mathrm{RF}}$) in the y direction. This field excites spin coherences between nearest-neighbour ground state Zeeman sub-levels producing a transverse atomic polarisation rotation.

The atomic precession is read out by the rotation of the plane of polarisation of a linearly polarised probe beam. This crosses perpendicular to the pump beam at the centre of the cell. The overlapping region defines the sensing volume. The perpendicular arrangement allows fine control over the size of the sensing region. This allows a balance between the signal (larger with a larger sensing volume) and the spatial resolution of the measure-

ments (larger with a smaller sensor).

The probe beam is usually blue-detuned, from the reference transition, to minimise the disturbance of the atomic polarisation. The linear polarisation of the probe beam is set by a half-wave plate ($\lambda/2$) before the beam propagates through the cell in the x direction. The polarisation of the probe beam is chosen to balance the power on each arm of the polarimeter.

The polarimeter, consisting of a polarising beam splitter and a balanced photodiode (Thorlabs PDB210A), detects the probe beam's polarisation rotation. The output of the photodiode is interrogated by a lock-in amplifier (LIA, Ametek 7280 DSP) and a spectrum analyser (SA, Anritsu MS2718B). The LIA simultaneously extracts four streams of data: the in-phase (absorptive, X) and out-of-phase (dispersive, Y) components of the polarimeter single along with the radius $\left(R \equiv X^2 + Y^2\right)$ and phase $(\Phi \equiv \arctan(Y/X))$[1]. The desired outputs of the LIA (X, Y, R, and Φ) and the spectrum traces recorded by the SA are acquired on a laptop.

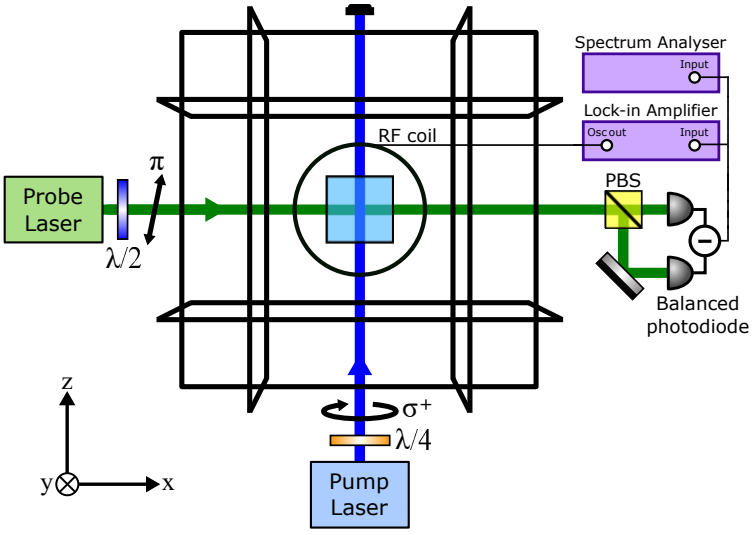

Figure 4.1: Overview of an RF-AM setup: Schematic of the general unshielded magnetometer setup (not to scale). A uniform bias magnetic field (along the pump beam) is provided by a Helmholtz coil system – described further in the text. Rb vapour is optically pumped with circularly polarised light. An RF coil provides a uniform calibration field. A linearly polarised probe beam crosses the pump beam perpendicularly and it's polarisation rotation is read out by a balanced photodiode. The photodiode output is interrogated by either a lock-in amplifier or a spectrum analyser. $\lambda/2$: half-waveplate, $\lambda/4$: quarter-waveplate, PBS: polarising beam-splitter. Adapted from Reference [6].

[1] Note that these equivalences are not equalities, with four separate measurements acquired.

4.1.1 Vapour cell

The vapour cells used are 25 mm×25 mm×25 mm cubic quartz cells supplied by Triad Technology (photographed in Figure 4.2). The cell has optical windows on four sides arranged in two orthogonal pairs – allowing access for both beams. Each cell contains either a naturally occurring vapour mixture of ^{85}Rb and ^{87}Rb, or isotopically enriched ^{87}Rb. The cells also contain 20 Torr of nitrogen as a buffer gas. No anti-relaxation wall coatings are used.

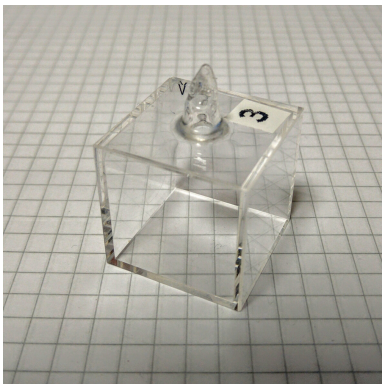

Figure 4.2: Photograph of a vapour cell: Cubic quartz cell side-length 25 mm of the type used throughout this thesis. Containing Rb vapour and N_2 as a buffer gas.

4.1.2 Lasers

The lasers are commercial distributed Bragg reflector lasers (Vescent Photonics D2-100-DBR). These emit on either the D_1 or D_2 lines for Rb at 795 nm and 780 nm, respectively. The lasers can be locked to the desired transitions by means of Doppler-free dichroic atomic vapour laser lock (DAVLL) or peak-locked via frequency modulated saturated absorption spectroscopy. This is controlled by a lock box (Vescent Photonics Lock-Box D2-125).

4.2 Overview of EMI with an RF-AM

A general schematic showing the principles of EMI with an RF-AM is provided in Figure 4.3.

An excitation coil provides the primary magnetic field ($\mathbf{B}_{\mathrm{RF}}$) – oscillating at ω_{RF} – in the y direction. The frequency is chosen on the basis of the desired skin depth.

When this field is incident on a sample it excites an eddy current (EC) response. The EC density decays exponentially along y (due to the skin effect). The ECs produce a secondary magnetic field B_{EC} opposing the primary one. In addition, the secondary field perturbation introduces a phase-lag (Φ) between the the total field B_{tot} and $\mathbf{B}_{\mathrm{RF}}$

Chapter 2 details how the characteristics of the sample are transferred onto the properties of B_{tot}. The field contains information on the sample's conductivity σ, relative permittivity ε_r, relative permeability μ_r, and its geometry.

The RF-AM is used to detect B_{tot}. In this way, the characteristics of the sample are imprinted into the precessing motion of the atomic spins. This is passed to the polarisation rotation properties of the probe beam before being extracted by the detection scheme.

By measuring B_{tot} at various positions non-invasive, contactless 2D maps of the sample's properties are constructed. These scans are performed by moving the sample relative to the excitation coil – exciting ECs in a different location for each measurement. An X,Y-stage (2×Thorlabs LTS150) provides the translational motion for the imaging. Computer control of the stage motion and measurement system allows the images to be constructed in real time by the laptop.

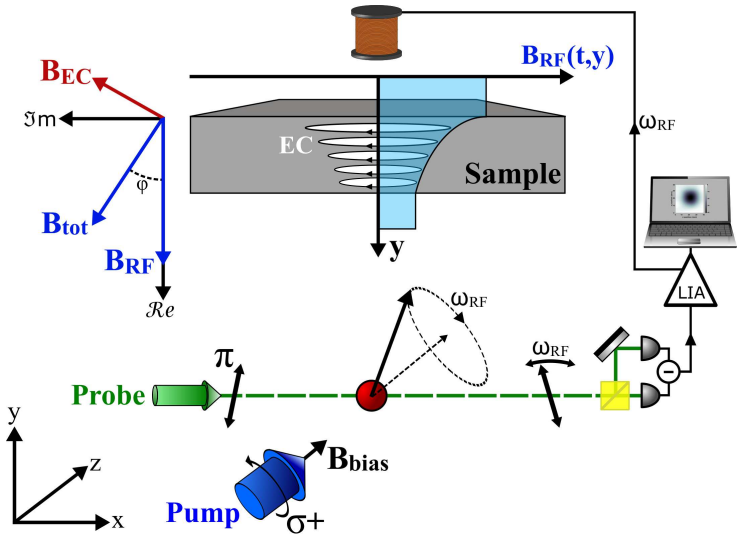

Figure 4.3: Overview of an AM-based EMI imaging system: An AC magnetic field $\mathbf{B}_{\text{RF}}(t,y)$ oscillating at ω_{RF} induces eddy currents (EC) in the sample. ECs produce a secondary field perturbation B_{EC} opposing $\mathbf{B}_{\text{RF}}$ and phase-lagged (by an angle Φ) with respect to it. B_{EC} contains information on the sample's conductivity σ, relative permittivity ε_r, relative permeability μ_r, and its geometry. The perturbation of the sample is detected by the RF-AM as changes in the precessing motion of the atomic spins. Position-resolved measurements allow 2D maps of the sample's characteristics to be constructed in real time. Adapted from Reference [8].

4.3 Overview of EMI-AM systems

The EMI-AM systems have been continuously developed and upgraded throughout this thesis. The experiments can be split into three major iterations of the design. For reference, these systems and their main features are summarised in Table 4.1. Each system is then

described in detail in the remainder of this chapter.

Experiment	Features and upgrades
EMI-AM I	Initial proof-of-principle
EMI-AM II	Transverse field compensation
	1-axis gradient compensation
	Active compensation system
	Active temperature stabilisation
	D1 line optical pumping
	Triggered data acquisition
EMI-AM III	Increased bias field homogeneity
	3-axes gradient compensation
	High-frequency operation
	Automated magnetic field optimisation

Table 4.1: Details of EMI-AM systems: Summary of the major features and upgrades for each of the EMI-AM experiments.

4.4 EMI-AM I

This section introduces the initial proof-of-principle system for EMI with an RF-AM. This setup was used for the results presented in Reference [1].

4.4.1 Optical setup

A sketch of the optical setup is shown in Figure 4.4. A single laser source is tuned to either the D_2 line $F = 2 \rightarrow F' = 3$ hyperfine transition of ^{87}Rb or to the D_2 line $F = 3 \rightarrow F' = 4$ hyperfine transition of ^{85}Rb. The beam is then split into two arms – the pump beam and the probe beam.

The pump beam is approximately 1 mW with a beam waist of around 4 mm. Assuming a uniform distribution, the intensity is therefore $7.9\,\mathrm{mW\,cm^{-2}}$. This is equivalent to $4.6\,I_s$, where I_s is the saturation intensity for the pumping transition [128, 129]. The probe beam is blue-detuned via a double pass acoustic optical modulator (AOM), with a total detuning of 400 MHz. The probe beam waist is 2.5 mm with a power of 25 µW – equivalent to an intensity of $0.52\,\mathrm{mW\,cm^{-2}}$.

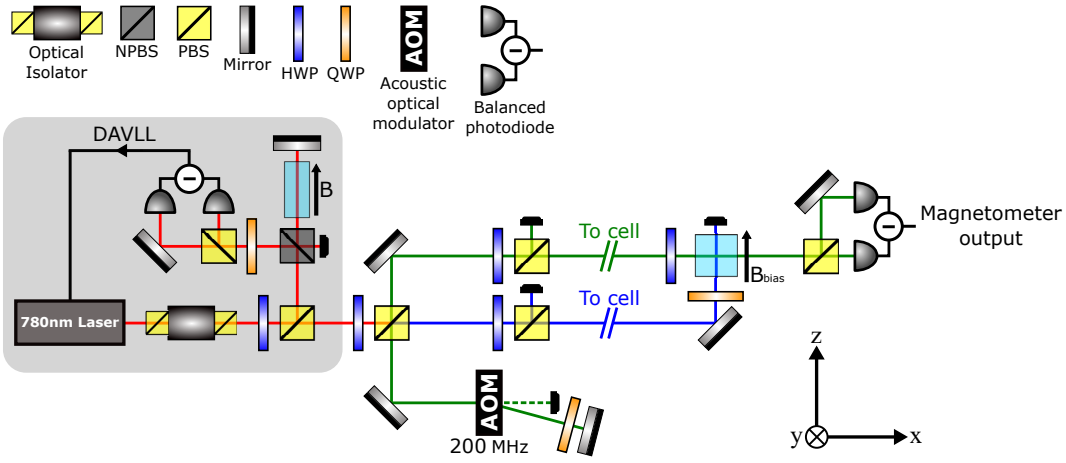

Figure 4.4: EMI-AM I optical setup: Pump beam (blue) and probe beam (green) cross orthogonally in the vapour cell. Beams provided by a single 780 nm laser. DAVLL: dichroic atomic vapour laser lock (grey region). HWP: half-wave plate ($\lambda/2$). QWP: quarter-wave plate ($\lambda/4$). NPBS: non-polarising beam-splitter. PBS: polarising beam-splitter.

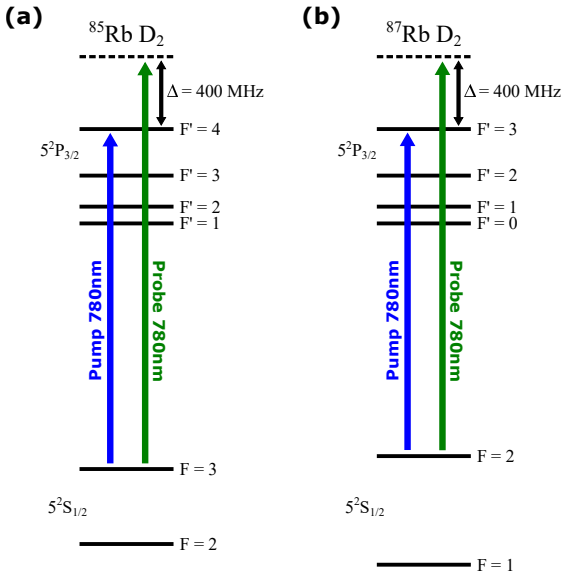

Figure 4.5: EMI-AM I level diagram: **(a)** ^{85}Rb. Pump tuned to the D_2 line $F = 3 \rightarrow F' = 4$ transition, probe blue-detuned by 400 MHz. **(b)** ^{87}Rb. Pump tuned to the D_2 line $F = 2 \rightarrow F' = 3$ transition, probe blue-detuned by 400 MHz.

4.4.2 Sensor design

A scale model of the sensor unit is shown in Figure 4.6. The bias magnetic field is provided by a pair of Helmholtz coils of diameter 80 mm.

The AC magnetic field is supplied by a single small ferrite-core coil (diameter = 7.8 mm, L = 680 µH at 1 kHz) centred on the cell, 63 mm above the beams. This field both drives atomic precession (when calibrating the sensor) and acts as the EMI primary field.

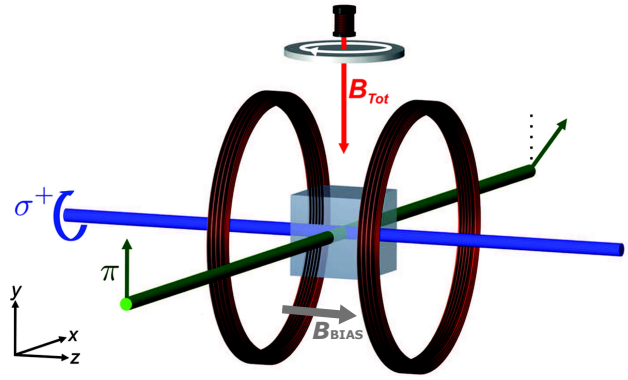

Figure 4.6: EMI-AM I sensor arrangement: Scale model of EMI-AM I sensor. Bias field provided by an 80 mm Helmholtz coil pair. RF coil induces eddy currents (white loop) in a sample. RF-AM detects B_{tot}, the combination of the primary field and the eddy currents' contribution. Adapted from Reference [1].

4.4.3 Array setup

The arrangement described thus far details a single sensor operation. The pump and probe beams were split further to create four such sensors. Figure 4.7 shows a schematic of the optical paths for the 2×2 sensor array. This array was used for the results presented in Reference [4].

Each of the four sensors are operated independently and simultaneously. They are positioned at the corners of a 105 mm$\times$105 mm square. Non-polarising beam splitters (NPBSs) evenly split the pump and probe beams to direct the same laser power to each cell. The polarisations of the eight beams are prepared independently, immediately before the cells.

4.5 EMI-AM II

To build on the results of the previous system, a number of limitations in the design are removed. Examples include the basic bias field control – limiting the sensitivity and tunability.

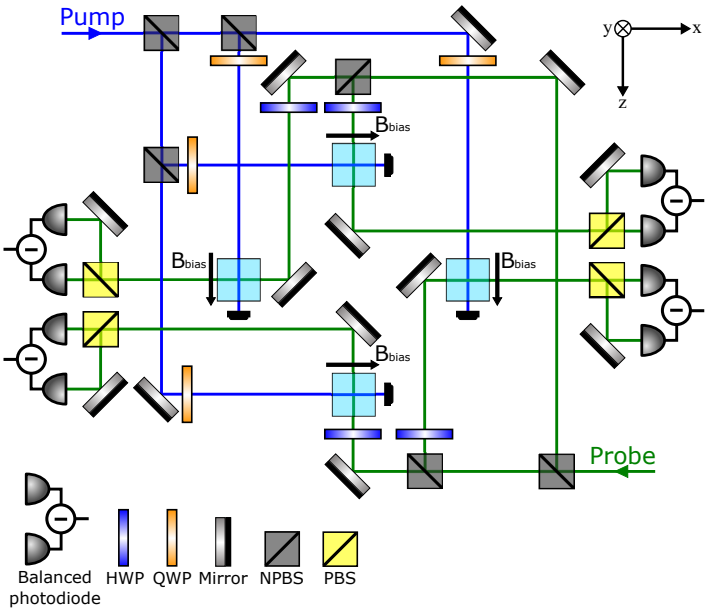

Figure 4.7: EMI-AM I array optical setup: Four sensors operated simultaneously. Cells positioned at the corners of a 105 mm×105 mm square. HWP: half-wave plate ($\lambda/2$). QWP: quarter-wave plate ($\lambda/4$). NPBS: non-polarising beam-splitter. PBS: polarising beam-splitter.

The EMI-AM II system represents the second iteration of the imaging platform. The modifications and upgrades, which improved the sensing and imaging performance, are described in this section. The EMI-AM II system was used for the results reported in References [3, 5, 6, 8].

4.5.1 Sensor design

The initial optical arrangement of the system was unchanged – although rearranged – from the previous design. The beam profiles were modified and additional control on the beam powers added. This is obtained by controlling the modulation depth of the AOM, thus changing the amount of light conveyed to the diffracted order in use. This achieved by exploiting the amplitude modulation of the AOM driver. This resulted in a pump beam with waist 5 mm and an intensity controlled up to a maximum of 21.4 mW cm^{-2}. The probe beam waist is 3 mm and its intensity can be controlled up to 18.6 mW cm^{-2}. Note that the saturation intensities for the pumping and probing transitions are 1.6 mW cm^{-2} and 2.5 mW cm^{-2}, respectively [128, 129, 145].

A scale model of the EMI-AM II design is presented in Figure 4.8. The design is dominated by the active magnetic field compensation system. The DC magnetic field at the position of the sensor is given by the Earth's magnetic field plus perturbations from other

sources. Therefore, it is unlikely that the bias field will be aligned parallel to the pump beam. This means that the field in each axis must be controlled to ensure that the quantisation axis is correctly aligned along the z-direction. The background magnetic field at vapour cell's position is $[-171\,\text{mG}, -323\,\text{mG}, 63\,\text{mG}]$ in the x, y, z basis. Recall that: the pump beam propagates along z, the probe beam along x, and the RF field is applied along y. For an operation frequency of 400 kHz this is equivalent to a misalignment of the quantisation axis by 25.4° (39.8°) from the desired direction for ^{87}Rb (^{85}Rb) – severely limiting the optical pumping efficiency.

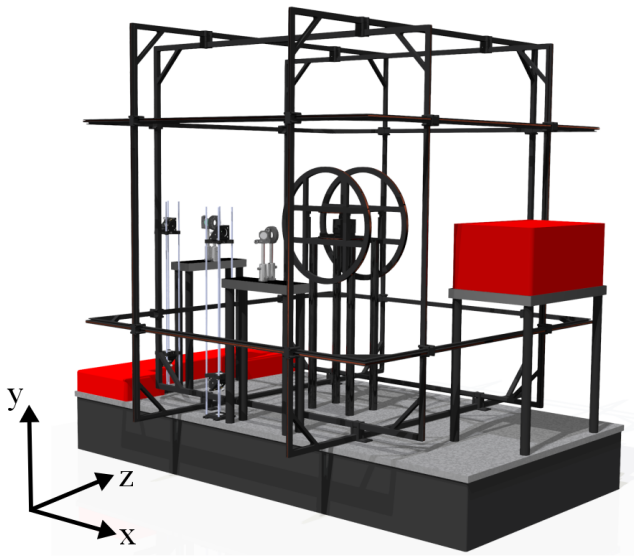

Figure 4.8: Scale model of the EMI-AM II system: Model of the experimental design. 3D printed sensor support and 3-axes coil system sits above the optical table. Red regions define the areas that contain the lasers and optical elements (left) and the measurement components (right). Further details included in the text.

To account for this, the sensor is surrounded by a 1.3 m 3-axes square Helmholtz coil system. This allows compensation of the Earth's magnetic field along all three axes. The 1.3 m side length maximises the region of magnetic homogeneity across the cell. Along z an additional 40 cm diameter circular Helmholtz coil (OP_z) provides the bias field for high-field operation. A 1.2 m square anti-Helmholtz coil along z further increases the bias field homogeneity by allowing gradient compensation.

The RF calibration field is generated by a further Helmholtz coil pair of diameter 18 cm (RF_y). This arrangement provides a uniform field across the cell. For imaging, the 7.8 mm ferrite core coil provides the primary field. Details of all the coils in the system are provided

in Table 4.2.

	Arrangement	Side-length/Diameter (cm)	No. turns	Wire diameter (mm)
x	Helmholtz	129.0	25	0.5
y	Helmholtz	124.7	25	0.5
z	Helmholtz	121.1	30	0.5
OP_z	Helmholtz	39.2	30	0.8
dz	anti-Helmholtz	120.4	25	0.5
RF_y	Helmholtz	18.0	2	0.5

Table 4.2: Details of magnetic field coils: Arrangement, size, number of turns, and wire diameter for each coil in the magnetic field system for the EMI-AM II experiment.

Eddy currents from conductive elements near the sensor introduce further noise. This effect is reduced by constructing the sensor support and Helmholtz coils from 3D printed PLA components. The coil cage alone comprises of 200 custom-made pieces. The vapour cell is lifted 650 mm above the top of the optical table to further reduce the proximity of metallic components.

4.5.2 Active compensation system

For many practical applications, operation in unshielded environments is required. In this case, magnetic field noise is the major limitation to the sensor's performance. The response of the atomic sample is susceptible to changes in the background magnetic field and to oscillating magnetic field noise. The dominant source of this noise is 50 Hz noise arising from mains power lines.

For EMI applications these need to be strongly suppressed. This is because a stable magnetometer response is required to reliably image samples. The active compensation scheme, shown schematically in Figure 4.9, achieves this by controlling the currents in the magnetic field coils around the sensor in response to changes in magnetic field.

The system is based on a 3-axes fluxgate magnetometer (Bartington MAG690-1000) positioned next to the cell, and PID controllers (Stanford Research Systems SIM960). The magnetic field for each axis is fed to the PID 'measure' input. In the z direction the desired magnetic field set-point (SP_z) is chosen to impose the desired operation frequency. The PID acts to minimise the error between the bias field (B_z, measured by the fluxgate) and SP_z. This works by regulating the current supplied to the z coil with a MOSFET whose gate voltage is driven by the PID output. In this way, ambient magnetic field variations and

oscillating magnetic noise are actively compensated. As a result, the bias field is locked at the desired set-point. Alternatively, for low-field operation ($\nu \lesssim 200\,\mathrm{kHz}$), the current in the bias field coils can be supplied and regulated directly by the PID output. The transverse ambient magnetic fields (along x and y) are zeroed and can be optionally maintained at that value with two further feedback loops. The compensation system performs well from DC up to the 3 dB bandwidth limit of the fluxgate at 1 kHz.

AMs operating in a gradiometric configuration offer an alternative approach to compensating magnetic field noise in unshielded environments [63, 64, 84, 146]. Such approaches can either subtract the signal from two (or more) separate magnetometers – cancelling the common noise, or take advantage of the AM's sensitivity to implement the feedback to the coil current. However, gradiometer arrangements are only suitable for measuring local, rapidly-decaying fields. Therefore, in the context of EMI, operation with a gradiometer configuration is complicated, and yet to be demonstrated. This is because any approach must be capable of decoupling (and suppressing) the magnetic field noise from the perturbations due to the sample that one aims to detect.

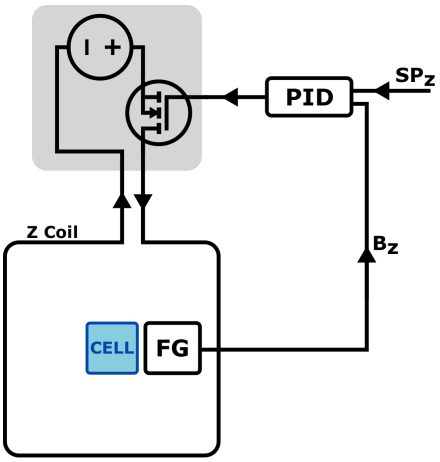

Figure 4.9: Active compensation system: Schematic diagram of the active compensation for a single axis. Three-axis fluxgate magnetometer (FG) measures the magnetic field at the cell's position. Fluxgate output (B_z) fed to a PID controller along with the desired field set-point (SP_z). The PID output drives the gate voltage of a MOFSET to control the current flowing in the z coil. Alternatively, the PID output can supply the coil current directly. The feedback loop minimises the difference between B_z and SP_z – actively stabilising the field. Active compensation is optionally extended to all three axes.

4.5.3 Active temperature stabilisation

The sensitivity of an AM scales with the atomic vapour density as $1/\sqrt{N}$. As a result, vapour cells are often heated. For EMI, long-term signal stability is required to accurately

determine features of the images. This places an additional constraint on the temperature stability. The active temperature stabilisation system described in this section achieves this. The design is shown in Figure 4.10.

The heating element consists of thin (0.22 mm diameter) copper wire wrapped in an anti-inductive arrangement around the cell. The current in the coil is modulated by an H-bridge (NJM2675), computer-controlled by a data acquisition (DAQ) device (National Instruments USB-6343). This provides up to 2.2 W of heating.

The H-bridge works in the following manner. A constant current source – typically around 600 mA – is applied to the input. The direction of current flow through the output (the heating coil) depends on the voltage state in the direction pins (DIR1 and DIR2). When DIR1 is high and DIR2 is low, the current flows one way through the coil. The current direction is reversed when DIR1 is low and DIR2 is high. Applying 50% duty cycle square waves that are completely out-of-phase to these pins results in an AC current of the same frequency being supplied to the coil. An AC current is desirable as it produces a smaller magnetic field perturbation (to the bias field) than a DC current. The perturbation is further reduced by the anti-induction winding. Furthermore, the heater frequency is set by the computer and is adjusted to a value far detuned from both the magnetometer resonance and the bandwidth of the active compensation system. A frequency of around 40 kHz was typically used in this work.

The enable pin provides additional control over the heating system. This pin acts as a simple digital switch, turning the current supply on or off. It is used in conjunction with a temperature sensor (described below) to create a relay controller. The cell temperature is stabilised by switching off the heater once the temperature reaches a controllable set-point. Additionally, the enable pin allows the heater to be momentarily paused whilst the atomic precession is probed. Completely removing the possibility of any stray magnetic fields affecting the measurements.

A temperature sensor (resistance temperature detector, Labfacility PT100RTD) provides the feedback for the temperature stabilisation. It consists of a thin platinum coil wound around an high-purity alumina (Al_2O_3) core – as such it has no magnetic components[2]. The sensor has a resistance/temperature relationship of $0.384\,\Omega/°C$ and a nominal resistance of $100\,\Omega$ at $0\,°C$. The sensor is also powered by the DAQ device, again allowing

[2]During optimisation of the setup, the magnetic contribution of a conventional sensor (Analog Devices AD590) noticeably degraded the RF-AM performance.

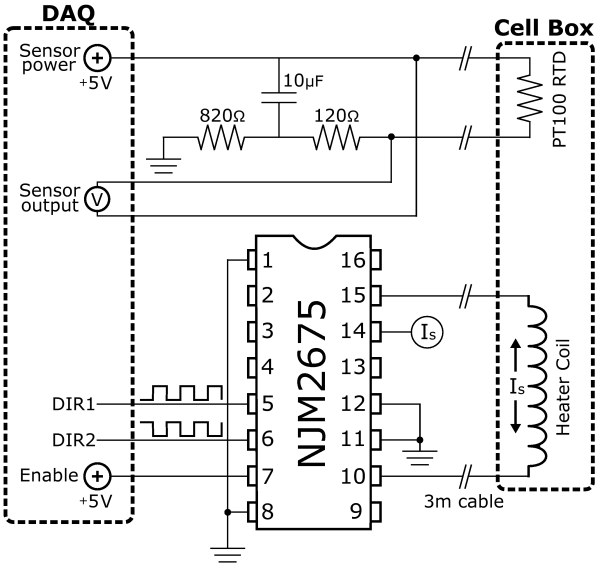

Figure 4.10: Active temperature stabilisation system: The heater is an anti-inductive wound coil supplied with an AC current from a computer-controlled H-bridge. Feedback provided by an resistance temperature detector (RTD). DAQ control allows the temperature to be stabilised and the currents momentarily paused during measurement windows. Further details in the text.

the sensor to be switched off during sensitive measurements. The 5 V supply is split across a voltage divider to supply an expected 5 mA to the sensor. The voltage across the resistor is measured by the DAQ. One expects to record a voltage change of around 2 mV/°C. After calibration the response was found to be 1.65 mV/°C. The system is able to maintain the vapour cell temperature to within 0.1 °C.

4.5.4 D_1 line optical pumping

An upgrade to the EMI-AM II system included the addition of a second laser emitting at 795 nm – resonant with the Rb D_1 line. This laser provided the pump beam in the updated optical setup (Figure 4.11). The potential benefits of optical pumping on the D_1 line in atomic magnetometry were discussed in Section 3.3.

This upgrade coincided with an additional double pass 350 MHz AOM being included in the probe beam path. This brings the total blue-detuning of the probe to 1.1 GHz from the D_2 line reference transition – see Figure 4.12.

4.5.5 Triggered data acquisition

I have discussed the effect of 50 Hz power line noise on unshielded AM operation (Section 3.8). The active field stabilisation system (described above) reduces the effect of this noise. Further improvements can be made by time-gating the data acquisition of the mea-

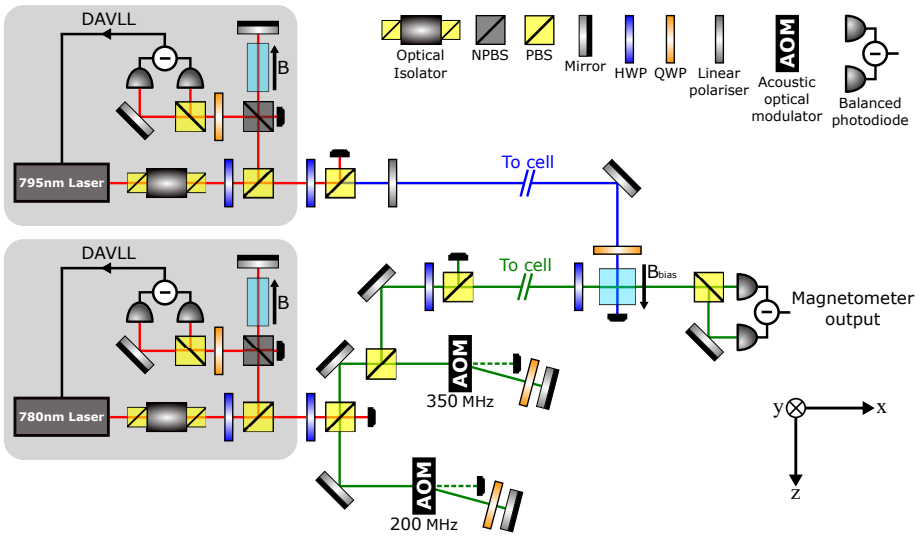

Figure 4.11: EMI-AM II D_1 line optical setup: Pump beam (blue) provided by a D_1 line laser at 795 nm. Probe beam (green) provided by a D_2 line laser at 780 nm. DAVLL: dichroic atomic vapour laser lock (grey region). HWP: half-wave plate ($\lambda/2$). QWP: quarter-wave plate ($\lambda/4$). NPBS: non-polarising beam-splitter. PBS: polarising beam-splitter.

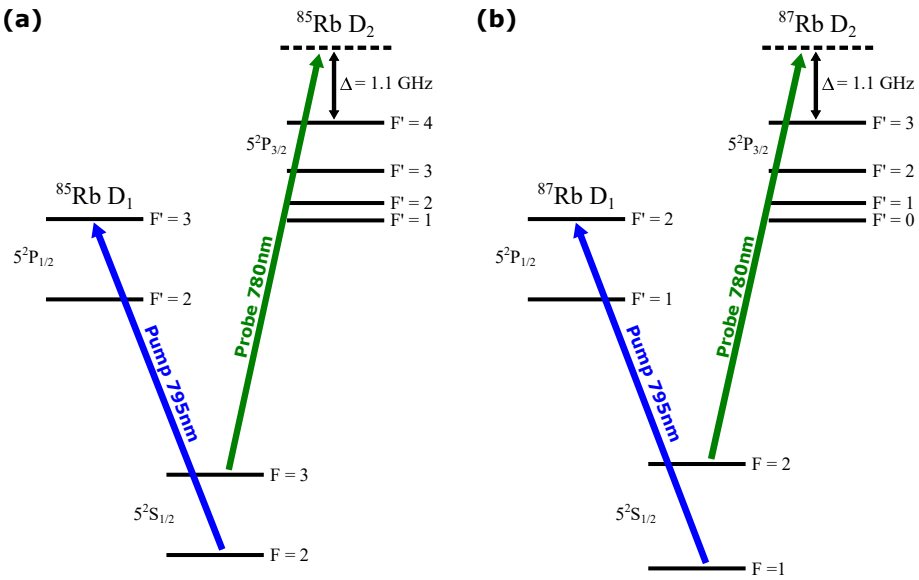

Figure 4.12: EMI-AM II D_1 line level diagram: **(a)** ^{85}Rb. Pump tuned to the D_1 line $F = 2 \rightarrow F' = 3$ transition. Probe blue-detuned by 1.1 GHz from the D_2 line $F = 3 \rightarrow F' = 4$. **(b)** ^{87}Rb. Pump tuned to the D_1 line $F = 1 \rightarrow F' = 2$ transition. Probe blue-detuned by 1.1 GHz from the D_2 line $F = 2 \rightarrow F' = 3$

surements at 50 Hz. The circuit diagram for the technique is depicted in Figure 4.13.

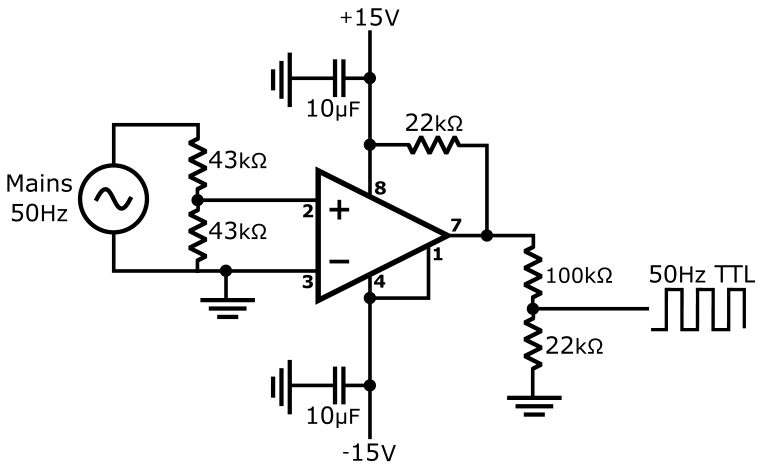

Figure 4.13: Triggered data acquisition: LM311N comparator configured as a zero-crossing detector converts the mains input to an in-phase 50 Hz square wave. This provides a TTL signal in-phase with the power line which triggers the measurement electronics.

The aim is to always acquire measurements at the same point of the 50 Hz oscillations. In this way, the standard deviation of measured values are minimised – suppressing the effect of the noise. Simply using a 50 Hz waveform is not sufficient. This is because the phase of the power line noise changes regularly as various equipment and devices are turned on and off. Instead, the data acquisition is triggered directly from the power line.

A 9 V AC power adapter (AD4120-09.0-09) is plugged into a spare mains socket. The output is split across a voltage divider to bring the supply into the input range of the comparator (LM311N). The comparator is configured as a zero-crossing detector. This converts the mains input to an in-phase 50 Hz square wave, the phase of which tracks the changes in the power line. A second voltage divider on the output coverts the TTL signal range to $0 \rightarrow 5$ V – suitable as a trigger signal for the measurement electronics. Passing this signal to the trigger input of the LIA ensures that the measurement are only taken on receipt of a trigger signal – i.e. always at the same point of the 50 Hz noise cycle. The effect of triggering the data acquisition is presented in Section 5.3.11.

4.6 EMI-AM III

The EMI-AM III system represents a further new experimental implementation for high-frequency EMI-AM. In Chapter 2 (see, in particular, Section 2.5.2), I discussed how higher primary field frequencies can give access to low-conductivity samples. The experiment described in this section is designed specifically with this is mind – with a view to performing

EMI-AM imaging of biological tissues.

4.6.1 Optical setup

The optical arrangement is a further evolution of the previous setups. In general, the setup is used with isotopically enriched ^{87}Rb vapour cells. This takes advantage of the higher operation frequency of ^{87}Rb for a given magnetic field (the frequency/field relationship of ^{87}Rb is 700 kHz/G, compared to 470 kHz/G for ^{85}Rb). Further advantages are found in the reduced effect of the second-order Zeeman splitting in ^{87}Rb – see Section 3.2.1 for details.

The pump beam path includes an 80 MHz AOM to allow the beam's power to be set by the software. This brings the pump beam slightly to the blue of the D_1 line $F = 1 \rightarrow F' = 2$ transition.

A 200 MHz AOM on the probe beam also provides control over the power. In this setup the probe is frequency-modulation locked to the ^{85}Rb D_2 line $F = 3 \rightarrow F' = 3/4$ crossover. This equates to a total probe detuning of 1.35 GHz to the blue side of the ^{87}Rb D_2 line $F = 2 \rightarrow F' = 3$ reference transition.

The light generation and preparation of the beams is performed on an optical table. The light is then transferred to a second 'sensor' table with a pair of polarisation maintaining fibre optic cables (Thorlabs P1-780PM-FC-5). This allows a further decoupling of the sensor from potential noise sources, such as the electronics and magnetic/metallic components.

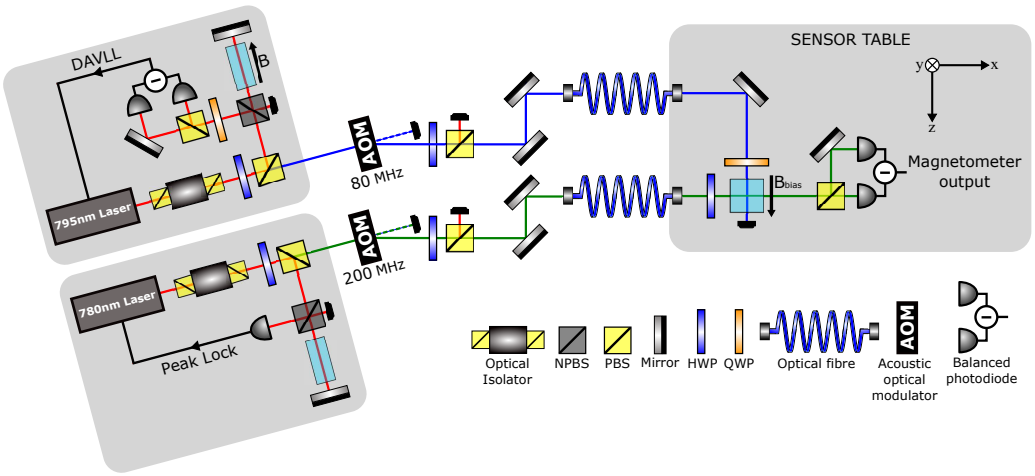

Figure 4.14: EMI-AM III optical setup: Pump beam (blue) on the D_1 line at 795 nm. Probe beam (green) on the D_2 line at 780 nm. AOMs on each beam allow computer control of the beams' intensities. Lasers and beam generation performed on an optical table. Light transferred via optical fibres to the sensor table (see text for details). HWP: half-wave plate ($\lambda/2$). QWP: quarter-wave plate ($\lambda/4$). NPBS: non-polarising beam-splitter. PBS: polarising beam-splitter.

4.6.2 Sensor design

Figure 4.15 is a scale model of the experimental design for the EMI-AM III system. The design features the separation of sensor from the electronics and light-generation. The vapour cell is positioned on a marble table supported by a wooden frame. Motional damping is provided by a set of passive Sorbothane vibrational isolators (Thorlabs AV6/M). The sensor is located at the centre of a 3-axes magnetic field and field-gradient system – made of perspex. This reduction in the quantity of metallic components in the vicinity of the sensor reduces the noise from eddy currents. The only metal comes from the required optical components. These are limited to: the two fibre output collimators, the two waveplates ($1 \times$ HWP, $1 \times$ QWP), two mirrors, and the balanced photodiode. The beam waists of both beams are increased to 8 mm.

The cell is secured in the centre of the table by a 3D printed PLA mount. This mount also secures the fluxgate (for active field stabilisation). An updated heating coil design increases the heating power to 4.6 W. The calibration field is generated by a 2 turn 200 mm Helmholtz coil in the y direction (RF_y).

4.6.3 Magnetic field and gradient suppression

An upgraded Helmholtz coil system is used to impose the desired bias field, cancel stray magnetic fields, and actively compensate for changes in these fields and oscillating magnetic field noise. In this design anti-Helmholtz coils are included on all axes to suppress magnetic field gradients.

Details of each coil in the experiment are given in Table 4.3. The dimensions of each coil range from 1.3 m to 1.41 m. The increased number of turns available in the z direction unlocks higher operation frequencies. Under application of the typical maximum currents (of Table 4.3) the operation frequency is predicted to be around 9.5 MHz. This is achieved despite the removal of the 40 cm diameter OP_z coil (from the previous arrangement). The magnetic field homogeneity across the cell is increased with all coils being greater than 1.3 m and the inclusion of gradient compensation along x and y.

During operation, a fixed DC current is applied to z_1 and/or z_2 to impose the majority of the bias field. The current in z_Δ is then regulated by the PID feedback to lock the field to the desired set-point. The fields from the traverse compensation coils (x and y) can also be locked to fix $B_x = B_y = 0$. When not locking these fields, the currents in these coils can be automatically calibrated and set by the control software which takes advantage of

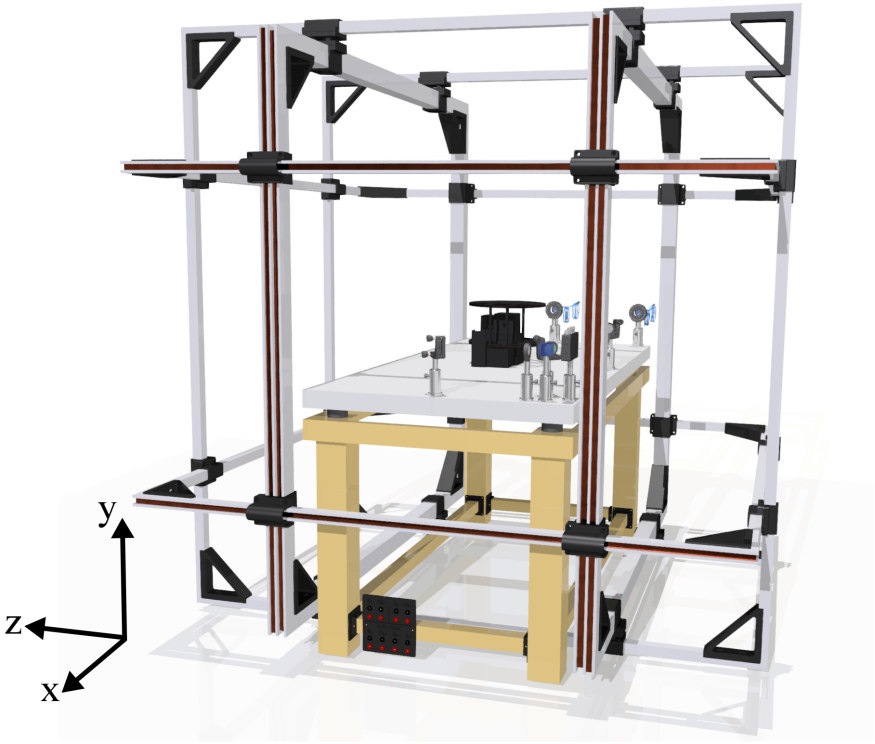

Figure 4.15: Scale model of the EMI-AM III system: Model of the sensor table arrangement. 3-axes coil system controls the magnetic field and gradients at the vapour cell position. Marble table top, wooden supports, 3D printed components, and acrylic coil formers reduce noise by removing a number of metallic components. Further details included in the text.

the magnetometer response. Further software enables the automatic optimisation of the anti-Helmholtz coils for gradient suppression.

4.6.4 High-frequency setup

Operation above 2 MHz requires an alternative approach to signal extraction from the RF-AM. This is provided by an RF gain and phase detector (Analog Devices AD8302). This chip provides the magnitude ratio and phase difference between two input signals from DC to 2.7 GHz. These are effectively equivalent to the R and Φ data streams extracted by the LIA.

The measurement setup is shown in Figure 4.16. Two phase-locked waveform generators (WGs, Agilent A33220A) provide the input signals for calibration and operation. One is supplied to an input of the AD8302 as a reference. A computer-controlled switch (Mini-Circuits ZYSWA-2-50DR) switches the other AD8302 input between the second WG (for calibration) and the magnetometer output (for operation). Both WGs output sine waves at the RF-AM resonant frequency, with one used to drive the RF coil. The corner frequency

	Arrangement	Side-length/ Diameter (cm)	No. turns	Wire (mm)	Length (m)	Current (A)	Field
z_Δ	Helmholtz	127.5	40	0.8	408	0.8	0.408 G
z_1	Helmholtz	124.0	100	1.5	992	5.0	6.56 G
z_2	Helmholtz	124.0	100	1.5	992	5.0	6.56 G
x	Helmholtz	137.5	40	0.8	440	1.0	0.474 G
y	Helmholtz	133.0	40	0.8	426	1.0	0.490 G
dx	anti-Helmholtz	137.5	40	0.8	440	1.0	4 mG/cm
dy	anti-Helmholtz	133.0	40	0.8	426	1.0	4 mG/cm
dz	anti-Helmholtz	127.5	40	0.8	408	1.0	4 mG/cm
RF_y	Helmholtz	20.0	2	0.5	2.51	0.26 mA	4.74 nT

Table 4.3: Details of magnetic field coils: Arrangement, size, number of turns, wire diameter, wire length, typical maximum current, and resultant magnetic field for each coil in the magnetic field system for the high-frequency EMI-AM III setup. z_1 and z_2 impose a static DC field in the z direction. z_Δ is supplied by the PID feedback system for active magnetic field stabilisation. x and y cancel the stray magnetic fields along their corresponding axes, and have the option of being actively maintained. dx, dy, and dz counteract stray magnetic field gradients. Current values and corresponding magnetic fields are the typical expected maximums for each coil. RF_y is the RF-AM calibration coil.

of the device is set to around 60 kHz by the 33 nF input capacitors[3]. This allows the chip to perform well across the desired frequency regime. The phase and gain outputs (P_{out} and R_{out}) are smoothed by 130 Hz low-pass filters before being acquired by a DAQ.

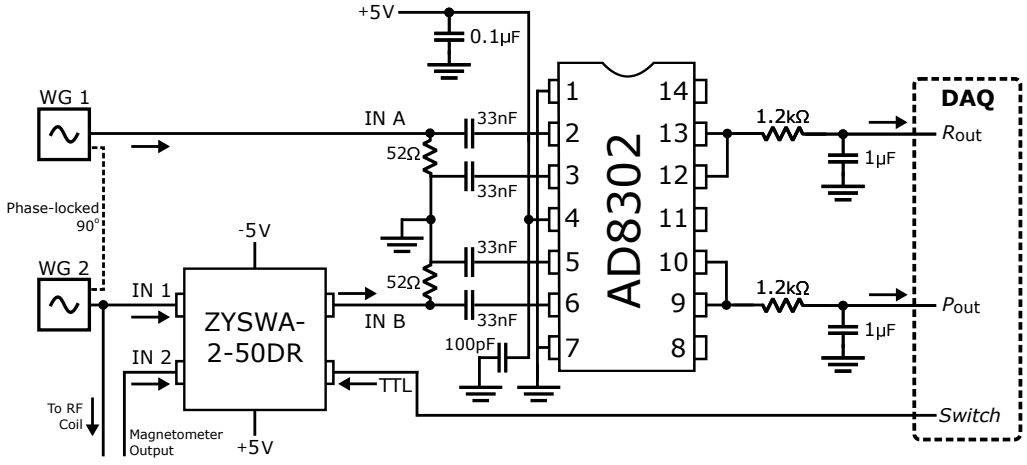

Figure 4.16: AD8302 measurement setup: WGs provide calibration signals and drive the RF-AM. Switch changes the AD8302 inputs between the calibration signal and the magnetometer output. Magnitude and phase outputs are recorded by a DAQ.

[3]This is the high-pass cut-off frequency of the input loop, defining the minimum operating frequency.

Typical calibration curves at 5 MHz are included in Figure 4.17. These are obtained by sweeping the phase (or amplitude) of one of the WGs and recording the response of the chip. The nominal response scales as 10 mV/deg for the phase detection and 30 mV/dB for the gain. From Figure 4.17(a), one sees that the phase response is most linear and the phase error minimum at a phase difference around $\pm 90^{\circ}$[4]. Therefore, this region defines the optimum operation point. The results of the calibration – detailed in Table 4.4 – are taken from this point. The amplitude error is small across the range of input ratios (Figure 4.17(b)). The calibration values are taken at a 0 dB input ratio. All calibration values are calculated from fits to the calibration curves at each frequency (e.g. dashed lines in Figure 4.17).

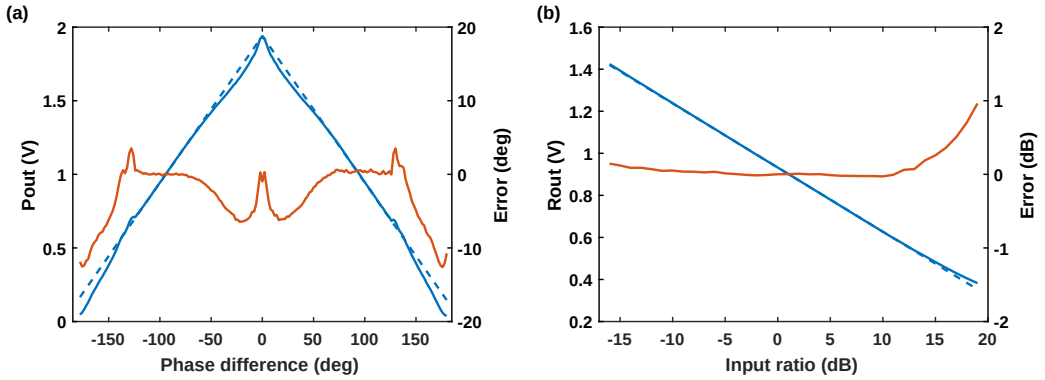

Figure 4.17: AD8302 calibration: Typical calibration curves of the **(a)** phase and **(b)** amplitude response at 5 MHz. Solid, blue lines are the outputs from the chip (P_{out} and R_{out}). Dashed, blue lines are fits to the outputs – used to calculate the values in Table 4.4. Red lines display the error, defined as the difference between the measured output and the corresponding fit.

To accurately investigate the magnetometer signal, a 90° phase difference between the magnetometer output and the reference input is therefore required. Prior to acquisition the chip is used to ensure such a phase difference exists between the WG providing the reference input and the WG driving the magnetometer (see Figure 4.16). The input is then switched to the polarimeter signal and the phase and amplitude responses recorded. The reference WG has an output amplitude of -24 dB to match the typical amplitude of the RF-AM signal. The results of the high-frequency operation are included in Section 5.4.5.

4.7 Experimental control software

In parallel to the incremental development of the experiment design, a software package has been developed and continuously updated to provide computer-control across all the

[4]This is in agreement with the AD8302 datasheet.

	100 kHz	1 MHz	2 MHz	3 MHz	4 MHz	5 MHz	6 MHz
P_{out} (mV)	1233	992	1329	1236	1108	1036	1012
P_{slope} (mV/deg)	10.9	10.9	7.9	7.1	8.8	10.0	10.2
R_{out} (mV)	918	904	959	958	963	909	909
R_{slope} (mV/dB)	-30.0	-30.7	-30.5	-30.5	-30.4	-30.5	-30.6

Table 4.4: Calibration values for the AD8302 chip: P_{out}, P_{slope}, R_{out}, and R_{slope} across a range of frequencies. Recorded for inputs of equal magnitude. Note that P_{out} and P_{slope} are independent of the input ratio.

experimental parameters. The suite consists of 58 LabVIEW .vis and SubVis. For reference, details of the software operation are provided in Appendix B.

Chapter 5

Sensor performance

This chapter reports on the performance of the sensors developed for EMI-AM, and on the improvements obtained as the experiments progressed. The characteristics of each system are then discussed. This includes the dependence on each experimental parameter and the capabilities of the various techniques aimed at suppressing magnetic field noise in unshielded environments.

5.1 Overview of sensor progression

For this overview, the performance is reduced to two simple characteristics. The sensitivity (i.e. the smallest detectable magnetic field) and the linewidth (the width of the magnetometer response). The sensitivity is found via the methods described in Section 3.6. For the linewidth, the half-width-half-maximum (HWHM, $\Gamma/2$) of the in-phase resonance profile is used.

Figure 5.1 charts the progression of the sensitivity. The sensitivity of the device has continually improved. The total improvement is more than four orders of magnitude – across the time frame of this thesis.

The first point (chronologically) is the EMI-AM I system sensitivity at $3.2\,\mathrm{nT}/\sqrt{\mathrm{Hz}}$. The red circles are measurements from the EMI-AM II system. The major changes providing the improvements over time are as follows. Firstly, the addition of the active compensation system for suppressing stray and oscillating magnetic field noise ($\delta B = 22\,\mathrm{pT}/\sqrt{\mathrm{Hz}}$). Secondly, the addition of the heating system to increase the vapour density and actively maintain it ($\delta B = 3.3\,\mathrm{pT}/\sqrt{\mathrm{Hz}}$). Finally, the addition of a second laser allowing optical pumping on the D_1 line ($\delta B = 130\,\mathrm{fT}/\sqrt{\mathrm{Hz}}$). The most recent data point comes from the EMI-AM III experiment characterisation. The reduced field inhomogeneity from larger bias field coils and all-axes gradient cancellation resulted in an improvement to $55\,\mathrm{fT}/\sqrt{\mathrm{Hz}}$. All

measurements were performed at an operation frequency of 100 kHz to ensure direct comparisons are possible.

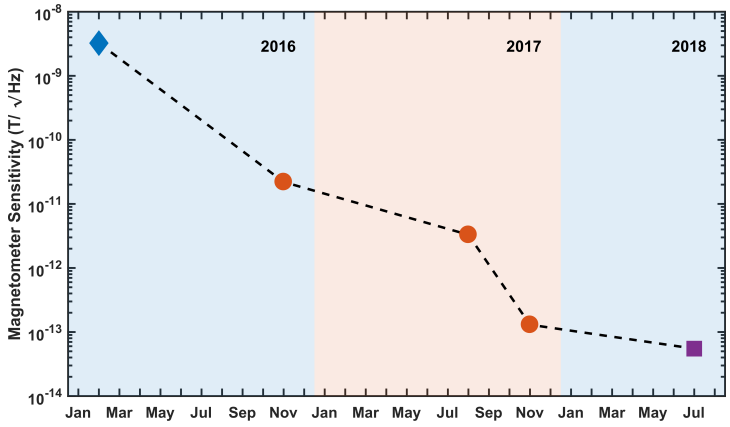

Figure 5.1: Overview of sensitivity progression: This figure charts the improvement in magnetometer sensitivity – from 3.2 nT/$\sqrt{\text{Hz}}$ to 55 fT/$\sqrt{\text{Hz}}$ – across the time frame of this thesis. Details of the major changes providing each improvement are in the text. EMI-AM I system – blue diamond, EMI-AM II system – red circles, and EMI-AM III system – purple square.

Figure 5.2 shows the progression of the in-phase (X) resonance response of each RF-AM implementation. These results are recorded by sweeping the frequency of the calibration field through the resonant frequency – imposed by the bias field. Each trace tracks the same changes over time as the sensitivity results (above).

Figure 5.2(a) displays the raw traces on a linear scale. This provides a direct comparison of the size of the signal response over time. The height of the peak is related to the magnetometer SNR. The linewidth and SNR are linked to the sensitivity by Equation 3.59. Therefore, effectively, the taller the peak the better the sensitivity. The progression of the peak height is emphasised in the inset which plots the peak height over time – an approximate 500 times increase.

Figure 5.2(b) plots the normalised traces of the same data. This charts the reduction of the magnetometer linewidth over time. The narrower the linewidth the better the sensitivity. The reduction in the HWHM over time is highlighted in the inset – from 3.3 kHz to 36 Hz.

5.2 EMI-AM I performance

Figure 5.3 shows a typical RF resonance profile for the EMI-AM I system. This experiment displayed a sensitivity of 3.2 nT/$\sqrt{\text{Hz}}$ and a HWHM of 3.3 kHz. The aim of the setup was to demonstrate EMI with an RF-AM for the first time. The results of the imaging are discussed in Section 6.3 and presented in Reference [1].

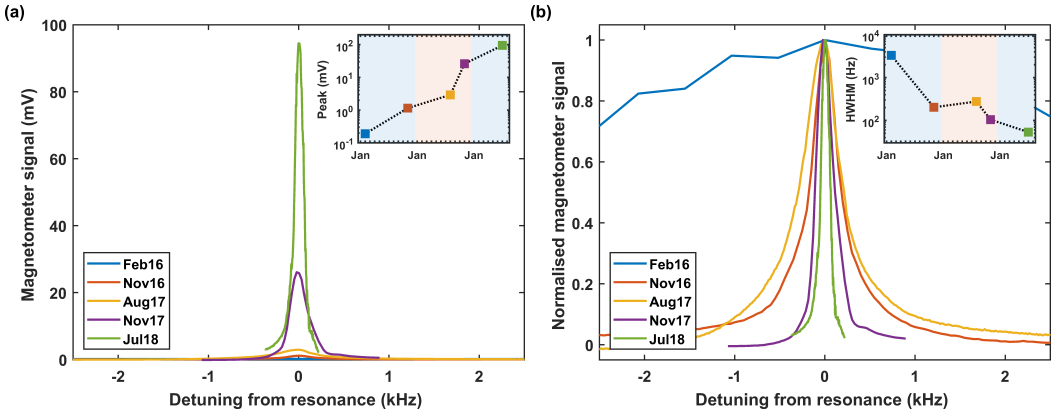

Figure 5.2: Overview of resonance progression: Improvements in the X resonance response. **(a)** Resonance response progression. Inset: Peak values over time. **(b)** Normalised traces show the reduction of the magnetometer linewidth. Inset: Magnetometer HWHM over time.

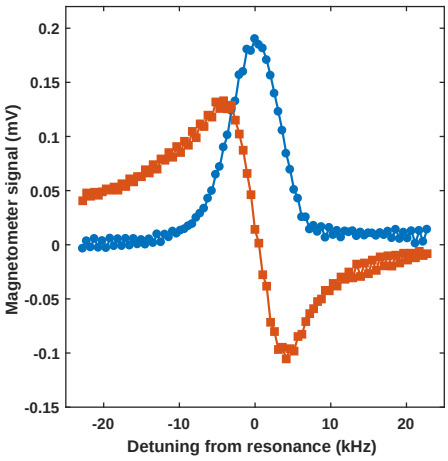

Figure 5.3: EMI-AM I resonance response: Typical in-phase (blue circles) and out-of-phase (red squares) response of the EMI-AM I system near 100 kHz ($B_z = 213$ mG for ^{85}Rb).

5.2.1 Performance limitations

The system's design suffered from a number of limitations. The dominant one being the lack of background field cancellation in the transverse directions, which severely reduces the optical pumping efficiency. Other factors (which are addressed below) include: the homogeneity of the bias field, the effect of AC magnetic noise, the ability to cycle through the experimental parameter space to optimise performance, the limited efficiency of optical pumping on the D_2 line, and control over the cell temperature.

5.3 EMI-AM II performance

The second-generation EMI-AM II system was designed and developed to remove these limitations. Details of the experiment are provided in Section 4.5. Many of the results also appear in Reference [6]. The system achieved a final measured sensitivity of $130\,\mathrm{fT}/\sqrt{\mathrm{Hz}}$ and a HWHM of 104 Hz. A typical profile of the RF-AM response at 100 kHz is shown in Figure 5.4. The inset shows the oscillations at the resonance frequency taken directly from the polarimeter output.

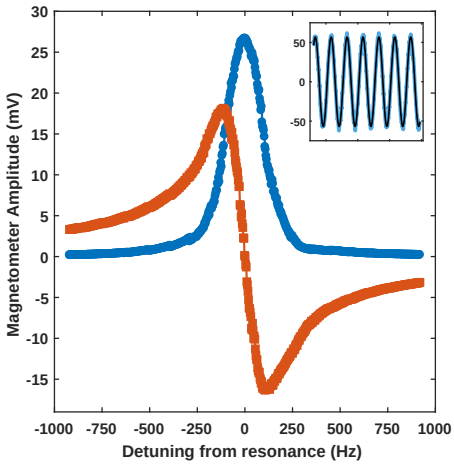

Figure 5.4: EMI-AM II resonance response: Typical in-phase (blue circles) and out-of-phase (red squares) response of the magnetometer near 100 kHz ($B_z = 213\,\mathrm{mG}$ for ^{85}Rb). Inset: polarimeter output at the resonant frequency fitted with sine wave of the same frequency. Adapted from Reference [6].

Optimising the magnetometer's performance requires one to find the optimum set of values from the experimental parameter space. This is done by recording the effect of each parameter on the magnetometer response. In particular, the in-phase (X) signal amplitude, linewidth ($\Gamma/2$), and the out-of-phase (Y) gradient are recorded from the LIA response. Further information is gained by examining the signal amplitude and SNR, along with the contributing factors limiting the noise from the SA.

The parameters of interest are the strength of the applied RF field, the pump and probe beam intensities, and the temperature. These are described in the sections below. Each of these parameters can broaden the atomic response. The aim is to find the point for each parameter that provides the largest response amplitude without broadening the linewidth. The operation frequency for optimisation was nominally chosen to be 100 kHz. The vapour cell used contained an isotopic mixture of ^{85}Rb and ^{87}Rb, along with 20 Torr of N_2 buffer

gas. Unless stated otherwise, the system was operating with the pump beam on the D_1 line of ^{85}Rb and a vapour cell temperature of 45 °C.

5.3.1 RF field response

The amplitude of the applied RF field is proportional the voltage applied to the calibration coil from the LIA oscillator output. The relationships between the RF-AM's amplitude and HWHM, and the RF voltage are shown in Figure 5.5. For completeness, note that each point in the figure is derived from a Lorentzian fit to the X response – of the form of the blue trace in Figure 5.4. For these measurements the pump and probe beam powers are set to comparatively small values to limit their effect – 300 µW and 25 µW, respectively.

From Figure 5.5, the optimum applied RF voltage was taken to be 130 mV. This value is just below the onset of RF power broadening [147]. It equates to an applied oscillating field of 6.03 nT. This value remains fixed throughout the following measurements.

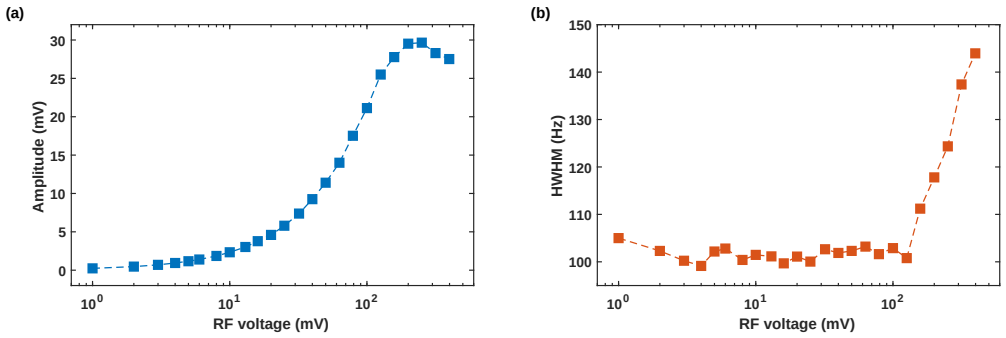

Figure 5.5: Magnetometer amplitude and HWHM as a function of applied RF voltage: 130 mV was chosen as the optimum value, just below the RF power broadening. This voltage was used throughout the remainder of the measurements. This represents an applied oscillating magnetic field of 6.03 nT at the operation frequency of 100 kHz. Fixed values: probe power 25 µW, pump power 300 µW.

5.3.2 Pump beam response

The pump beam intensity is the next parameter of interest. Changing the power of the beam is sufficient as the beam waist is fixed at 5 mm. The effect of pump power on the amplitude and HWHM of the magnetometer's response is shown in Figure 5.6. These measurements are performed with the optimum RF field (found above), whilst the probe remains fixed at 25 µW.

Again, the optimum value is chosen just below the regime of power broadening. At this point the power is 400 µW. This gives an average intensity of 2.0 mW cm^{-2}, equivalent to 1.2 I_s [145].

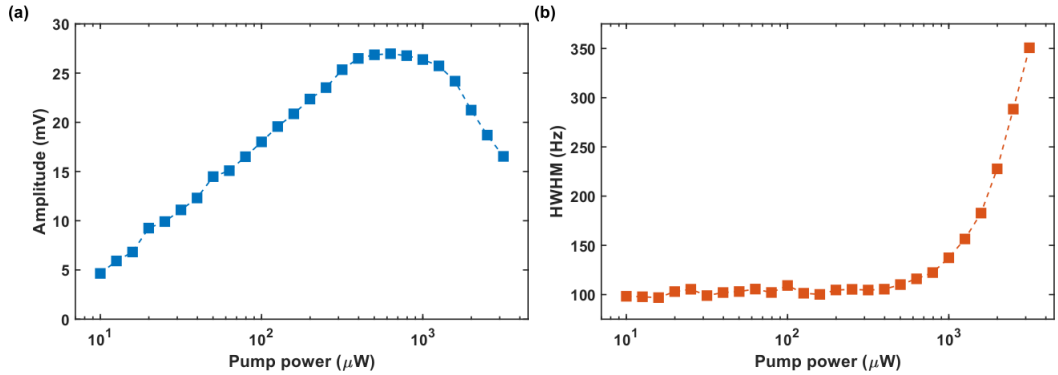

Figure 5.6: Magnetometer amplitude and HWHM as a function of pump beam power: 400 µW is the optimum value, below the pump power broadening. This value was used throughout the remaining of the measurements. Fixed values: probe power 25 µW, RF field amplitude 6.03 nT.

5.3.3 Probe beam response

Figure 5.7 presents the dependence of the amplitude and HWHM on the probe beam – controlled in the same manner as before. The magnetometer signal increases with the probe power before saturating at the point were the probe begins to broaden the atomic response.

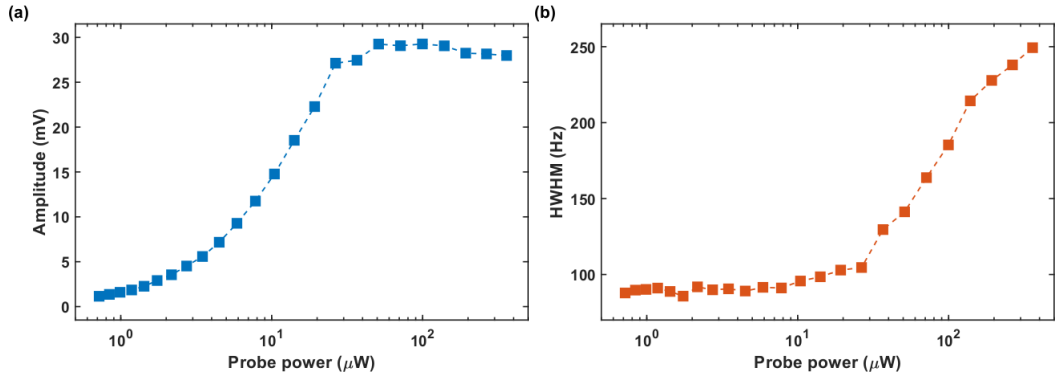

Figure 5.7: Magnetometer amplitude and HWHM as a function of probe beam power: Fixed values: pump power 400 µW, RF field amplitude 6.03 nT.

In parallel to the LIA results, the effect of the probe beam power on the magnetometer spectrum is examined by the SA. This is displayed in Figure 5.8. Here, each measurement point is the average of 15 traces of the polarimeter output spectrum.

The magnetometer amplitude from the SA (blue, filled circles) is analogous to Figure 5.7(a). The signal increases with probe beam power to at maximum around 300 µW – decreasing slightly beyond this. The saturation and decrease at higher powers is due to broadening, as the probe beam disrupts the population alignment created by the pump beam (pump beam power 400 µW). The red, filled squares mark the total noise level of the

RF-AM. This level – and other noise components – are discussed further in Section 5.3.6 (below). The SNR (black, open squares) is computed directly from the above measurements.

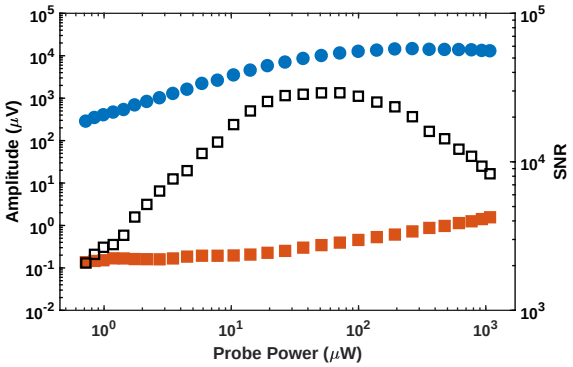

Figure 5.8: Magnetometer signal, noise, and SNR as a function of probe beam power: Signal (blue, filled circles), Noise - measured with the RF field off (red, filled squares), and corresponding SNR (black, open squares). Fixed values: pump power 400 µW, RF field amplitude 6.03 nT. Adapted from Reference [6].

5.3.4 Sensitivity: D_1 line optical pumping

From the above measurements the magnetic field sensitivity can now be computed and plotted against the probe beam power. The RF sensitivity is calculated following Equation 3.60. Similarly, the DC sensitivity is calculated following Equation 3.59. The results of both calculations are given by Figure 5.9.

The similarity between these two independent measures is expected, and confirms the validity of the measured results. The system achieves a maximum sensitivity with a probe beam power of around 70 µW, giving a total optical power of only 470 µW.

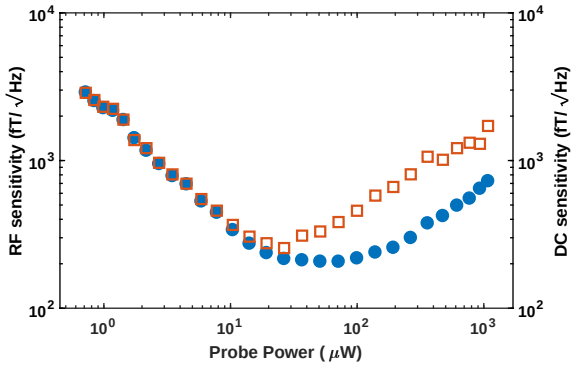

Figure 5.9: Magnetometer sensitivity as a function of probe beam power: RF sensitivity (blue, filled circles) and DC sensitivity (red, open squares) at 45 °C. Optimum parameters: Probe power 70 µW, pump power 400 µW, RF field amplitude 6.03 nT.

5.3.5 Y-channel gradient

The out-of-phase gradient has been introduced as an alternative figure-of-merit describing the sensitivity of an RF-AM. From Equation 3.59, one has that $\delta B_{\mathrm{DC}} \propto \Gamma/\mathrm{SNR}$. One can think of SNR/Γ as effectively equivalent to the out-of-phase gradient. Therefore, the out-of-phase gradient is inherently inversely related to the sensitivity.

This is confirmed in Figure 5.10, which plots the Y-channel gradient against the probe beam power. Each data point is calculated by a linear fit to the Y-channel response at resonance – e.g. fitting a straight line to the slope of the red curve in Figure 5.4 at zero detuning. For clarity, the computed gradients are inverted to give positive values. As expected, the gradient response mirrors that of the sensitivity – with the maximum gradient given by the same 70 µW probe beam power.

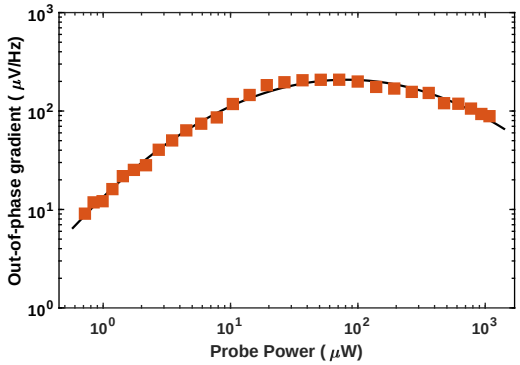

Figure 5.10: Magnetometer Y-channel gradient as a function of probe beam power: Fixed values: pump power 400 µW, RF field amplitude 6.03 nT. Line serves to guide the eye.

5.3.6 Noise analysis

Further analysis of the polarimeter signal with the SA can be used to determine the contributing factors to the noise that limit the sensitivity. Figure 5.11 characterises the noise components around 100 kHz with the magnetometer operating at 45 °C.

The technical noise (dashed, black line) arises from electrical noise in the measurement scheme. It is measured without the probe beam and is the dominant contribution at low probe beam powers.

The photon-shot noise is added to this to give the off-resonant noise (dot-dashed, red line). This is also referred to as the baseline noise. It is recorded with the bias field detuned from the RF resonance. The photon-shot noise becomes dominant with higher probe-beam power, scaling as the square root of the power (see also Figure 5.8).

The remaining noise terms arise from resonant noise sources. These include the spin-projection noise and the light-shift noise, along with environmental noise at the resonant frequency. I refer to this as the total noise (solid, blue line). It is recorded with the RF driving off and the bias field on. It is therefore the minimum detectable level of field at the resonant frequency in operating conditions – i.e. the sensitivity. The total noise floor is 165 fT/$\sqrt{\text{Hz}}$ at 45 °C. This level is marked by the arrows in Figure 5.11.

It is important to note that the total noise level – not the baseline noise – is used to calculate the SNR. This is in turn used to calibrate the SA scale and define the sensitivity. Some papers alternatively use the baseline noise as the measure for the sensitivity. In this case improved values are quoted – 147 fT/$\sqrt{\text{Hz}}$ for Figure 5.11. However, as this approach is somewhat less relevant to practical applications, the total noise is taken as the limiting factor for the RF-AM sensitivity throughout this work.

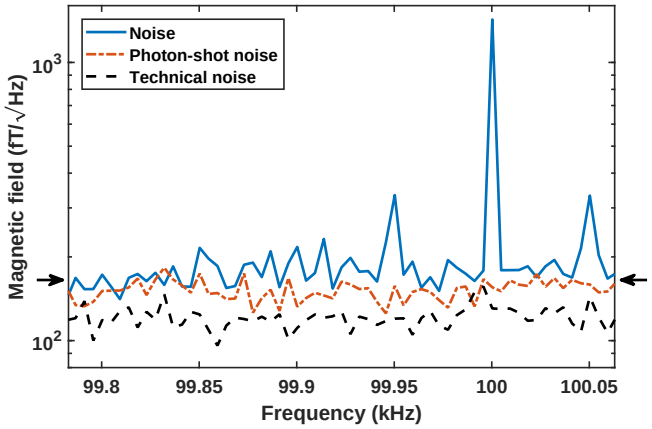

Figure 5.11: Magnetometer noise components: Magnetometer noise sources around 100 kHz recorded by the SA at 45 °C with other parameters optimised. Total noise (solid, blue line) measured with the RF field off and pump beam on. Total noise level of 165 fT/$\sqrt{\text{Hz}}$ marked by arrows. Dominated by the detection of a 100 kHz signal and corresponding 50 Hz side-bands. Photon-shot noise (dot-dashed, red line) measured with the bias field off. Technical noise floor (dashed, black line) measured without the probe beam. From Reference [6].

The total noise measurement (solid, blue line of Figure 5.11) reveals the detection of environmental interference at 100 kHz and of amplitude 1.4 pT. This signal, and the corresponding 300 fT 50 Hz side-bands, are assumed to originate from a neighbouring laboratory.

5.3.7 Temperature response

The atomic density is another significant experimental parameter to explore. Although the majority of AM experiments heat the vapour cell with the aim of increased sensitivity, the

goal of the heating system was originally long-term signal stability. In EMI this stability is required to allow accurate comparison between images taken at different times/on different days. A periodic change in the RF-AM signal was first noticed in the early analysis for the machine learning-aided image reconstruction results (see Section 7.2).

Figure 5.12 shows an example of the unwanted signal modulation. The change in the RF-AM signal – with a period of approximately 27 minutes – was traced to the AC unit in the room. The feedback for the AC unit creates slow oscillations in the room temperature, enough to severely disrupt the long-term magnetometer stability.

The temperature stabilisation system (Section 4.5.3) was designed to eliminate this effect. It provides continuous control over the cell temperature – to within 0.1 °C – over many days of operation.

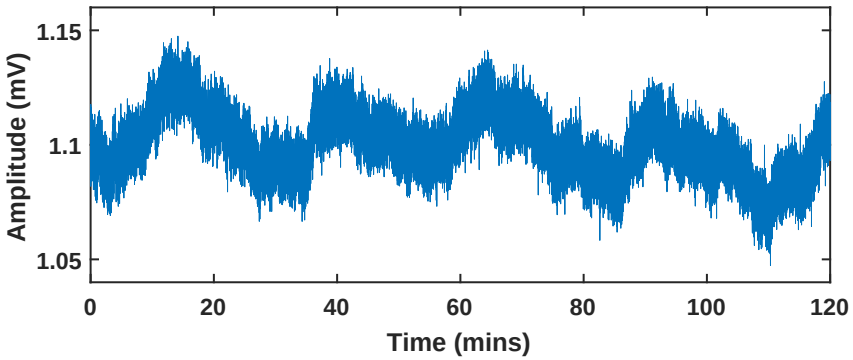

Figure 5.12: Effect of temperature oscillations: Oscillations with a period of 27 minutes in the RF-AM response. Due to the feedback for the AC creating slow oscillations in the room temperature.

The heating system allows control over the temperature from 21 °C to 60 °C. This corresponds to atomic densities in the range 6.1×10^9 cm^{-3} – 2.4×10^{11} cm^{-3} (when considering ^{85}Rb in an isotopically mixed cell). This range is significantly lower than that explored in many previous works [63, 64, 83]. However, the absence of an oven reduces the complexity of the sensor and increases the ease-of-operation and portability.

The results of changing vapour density are presented in Figure 5.13. This plots the magnetometer sensitivity and out-of-phase gradient against temperature. Increasing the vapour density increases the sensitivity but also increases the rate of spin-exchange collisions (broadening the linewidth), and increases radiation trapping of the probe beam (fixed at 70 µW across the measurements). Both of these effects can reduce the signal. Nevertheless, in the explored regime, increasing vapour density had a positive effect on the sensitiv-

ity. A maximum sensitivity of $130\,\mathrm{fT}/\sqrt{\mathrm{Hz}}$ was recorded at 60 °C. However, note that the rate of improvement slows above 42 °C. These observations are mirrored in out-of-phase gradient where the steepest response (and also the narrowest linwidth) are recorded around 45 °C. Sub-picotesla sensitivity was achieved with only modest heating to 29 °C.

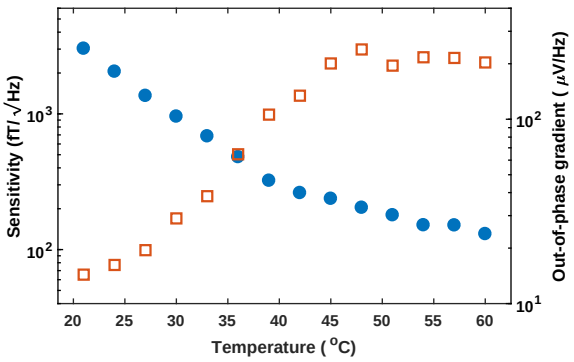

Figure 5.13: Magnetometer RF sensitivity and Y-channel gradient as a function of temperature: Magnetometer sensitivity (blue, filled circles) and out-of-phase gradient (red, open squares) as a function of vapour cell temperature. All results recorded at with pump beam power 400 µW and with probe beam power 70 µW. A peak sensitivity of $130\,\mathrm{fT}/\sqrt{\mathrm{Hz}}$ was recorded at 60 °C. From Reference [6].

5.3.8 Sensitivity: D_2 line optical pumping

The characterisation process detailed above involved the pump beam operating on the D_1 line. This section briefly presents the results when performing the same procedure with D_2 line optical pumping.

The optimisation – RF field amplitude, pump beam, and probe beam – was performed independently at 25 °C, 35 °C, and 45 °C. The resultant plots of RF and DC sensitivity are shown in Figure 5.14. With this pumping scheme the maximum recorded sensitivity was $3.3\,\mathrm{pT}/\sqrt{\mathrm{Hz}}$ at 45 °C. A figure of $22\,\mathrm{pT}/\sqrt{\mathrm{Hz}}$ was achieved at room temperature. For completeness, the results required to derive these values are included in Appendix C.

5.3.9 Active field stabilisation performance

This section evaluates the performance of the active compensation system. The technique is described in Section 4.5.2. This approach makes the consistent high-sensitivity operation of the magnetometer in unshielded environments possible. It also allows EMI images to be acquired without averaging – speeding up applications.

The design involves regulating the current in the magnetic field coils with a feedback loop. The current can either be controlled by a MOFSET-driven PID or supplied directly by

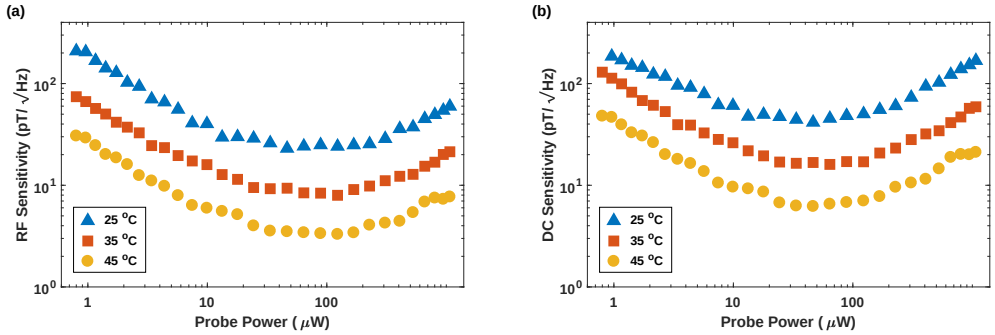

Figure 5.14: Magnetometer sensitivity as a function of probe beam power: **(a)** RF sensitivity and **(b)** DC sensitivity for the EMI-AM II system with D_2 line optical pumping.

the PID output. There is no difference in sensor performance between the two configurations. There is also the option to use a single-axis feedback system (in the z direction), or a three-axes system (which also maintains $B_x = B_y = 0$). The latter approach does not further improve the sensor's characteristics or sensitivity. However, it is inherently more suited to long-term data acquisition and field applications.

The Fourier transform of the PID output is presented in Figure 5.15. This indicates the frequencies that the system is working to compensate – up to the 3 dB bandwidth of the fluxgate at 1 kHz. The correction signal is dominated by a 50 Hz response to the power line noise and its higher order harmonics. This is as expected, with the 50 Hz noise component being the dominant source of noise for operation of AMs in unshielded environments.

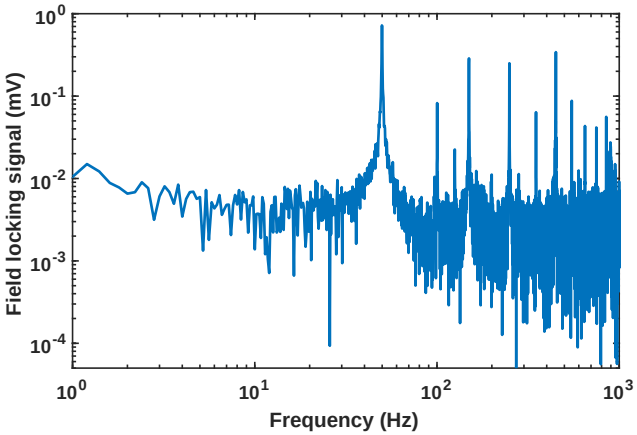

Figure 5.15: Magnetometer noise compensation frequencies: FFT of the PID output used to actively stabilise the bias field (B_z). The correction signal is dominated by 50 Hz noise and corresponding harmonics. From Reference [6].

The effect of magnetic field locking is highlighted in Figure 5.16. This graph displays consecutive traces of the resonance response without field stabilisation. The settings are

otherwise the same as in Figure 5.4. The severe distortion to the resonance lineshape and the non-repeatability of the response renders consistent operation of the sensor impossible.

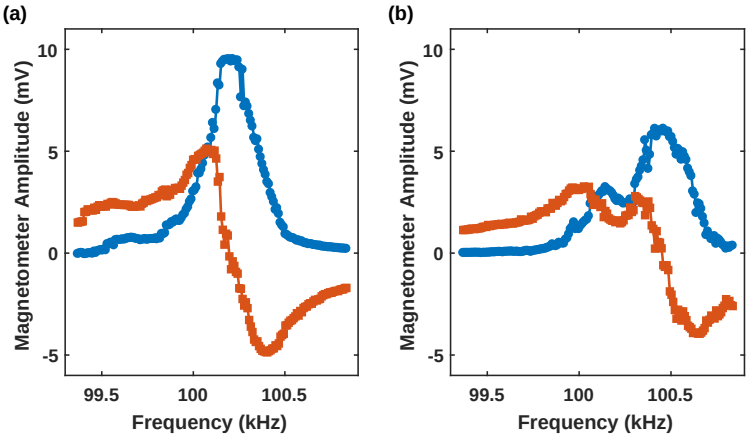

Figure 5.16: Effect of active compensation system on magnetometer resonance: Typical in-phase (blue circles) and out-of-phase (red squares) responses of the magnetometer without magnetic field compensation. **(a)** and **(b)** are consecutive traces, both recorded within a 30 s period. The response is non-repeatable and severely distorted in comparison to the field-stabilised case (Figure 5.4). From Reference [6].

Figure 5.17 plots the effect of the active field stabilisation on the magnetometer spectrum. In unshielded environments, the spectrum of an RF-AM exhibits a broad set of 50 Hz sidebands spread symmetrically about the resonant frequency. The magnetic field locking strongly suppresses these sidebands whilst increasing the magnetometer amplitude (Figure 5.17(a)). The degree of suppression is better seen in the insets. Here, the results are replotted against the same linear axis.

In addition to the loss of consistent operation, the sensitivity of the RF-AM is reduced by an approximate factor of 2 without the active stabilisation of the magnetic field. Both these effects are due to the modulation of B_z at 50 Hz.

I define the amplitude of this modulation as $B_z^{50\,\mathrm{Hz}}$. Without active compensation, this value was independently measured by two sensors. It was found to be 120 nT at the position of the vapour cell. For ^{85}Rb this generates an oscillation in the resonant frequency of 1.1 kHz. This value is similar to those reported for other unshielded atomic magnetometers [63].

When the compensation system is active, the residual oscillations in the bias field can be extracted directly from the LIA. This is shown in Figure 5.18. In these conditions the oscillations are 56 Hz. This is equivalent to $B_z^{50\,\mathrm{Hz}} = 11.9\,\mathrm{nT}$. The active compensation system reduces the dominant 50 Hz noise component by a factor of ten.

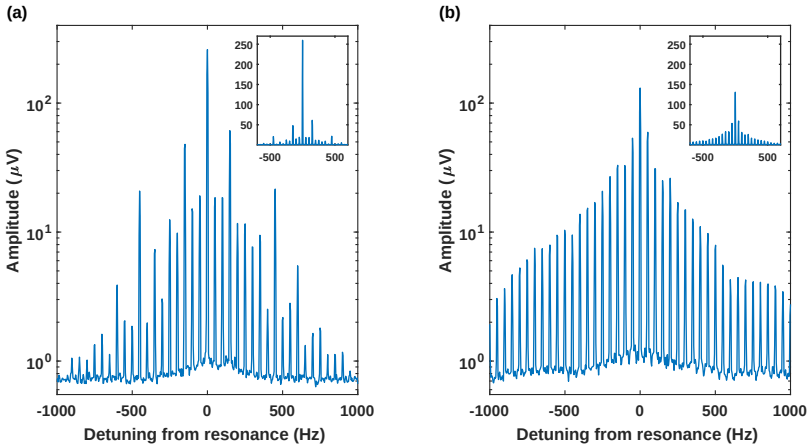

Figure 5.17: Effect of active compensation system on magnetometer sidebands: Polarimeter spectrum **(a)** with and **(b)** without active field stabilisation. Field locking increases the magnetometer signal and strongly suppresses the sidebands due to 50 Hz and higher-order harmonics. This is emphasised in the insets which compare the same data on a linear scale.

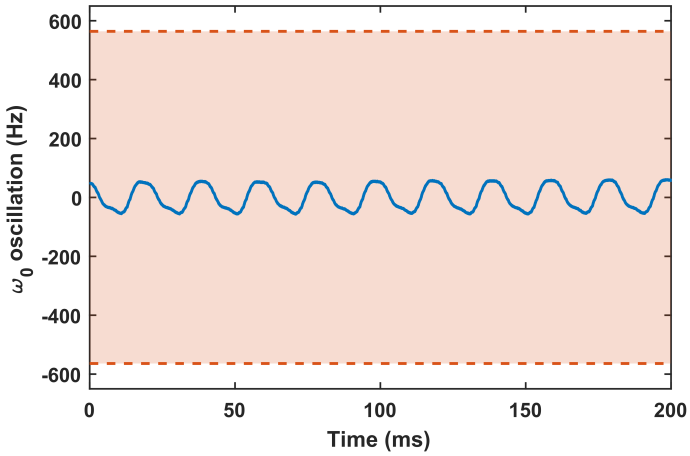

Figure 5.18: Noise reduction: 50 Hz oscillations in resonant frequency of the RF-AM. With field stabilisation, the modulation is ±56 Hz (blue line), this corresponds to $B_z^{50\,\mathrm{Hz}} = 11.9\,\mathrm{nT}$. Without stabilisation, $B_z^{50\,\mathrm{Hz}} = 120\,\mathrm{nT}$, giving a modulation of 1.1 kHz – level indicated by the shaded area. Active magnetic field locking reduces the 50 Hz noise by an order of magnitude. Adapted from Reference [6].

5.3.10 Range of operation frequency

In this section I explore the tunability of operation frequency of the magnetometer. A broad range is a crucial for many practical applications where a number of detection frequencies may be required. In particular, tuning the penetration depth or imaging samples of different conductivities in EMI.

To maintain relevance to practical applications, the experimental parameters are fixed at the optimum values found at 100 kHz (pump power 400 µW, probe power 70 µW, temperature 45 °C). It is important to note that the inductance of the calibration coil depends on the operation frequency. The value of B_{RF} at each frequency requires the coil to be calibrated across the range. This is performed *a priori*.

Recall that the device can easily be commuted between ^{85}Rb and ^{87}Rb. The latter demonstrates a larger tunability. This higher dynamic range is a consequence of a larger gyromagnetic factor ($\gamma_{87} \approx 1.49\,\gamma_{85}$).

The tunability of the operation frequency is shown in Figure 5.19. This highlights the large dynamic range of the system when operating as an ^{87}Rb RF-AM. The magnetometer resonance is plotted from 100 kHz to 2 MHz. This is equivalent to a spread in B_z from 0.14 G to 2.86 G. The RF-AM displays a relatively small degradation in performance – a factor of 8 in amplitude – across the range.

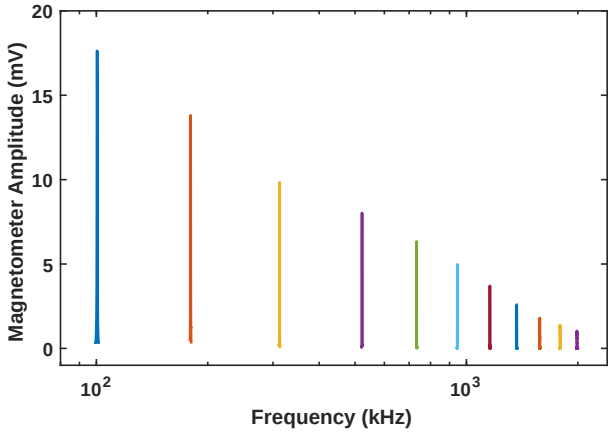

Figure 5.19: EMI-AM II range of operation frequency: RF resonance traces of the RF-AM demonstrating reliable operation between 100 kHz and 2 MHz – limited only by the detection electronics. Adapted from Reference [8].

Figure 5.20 presents the sensitivity and out-of-phase gradient when operating as an ^{85}Rb RF-AM. The range explored here is from 3.5 kHz – 1 MHz. This equates to a bias field regime of 7.47 mG – 2.13 G. The magnetometer operates with sub-picotesla sensitivity

from 30 kHz to 1.1 MHz at 45 °C. This increases to between 15 kHz and 1.4 MHz at 60 °C.

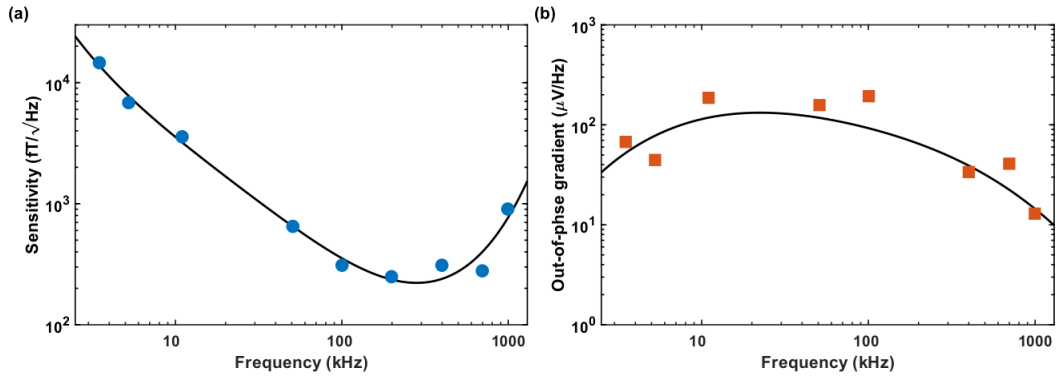

Figure 5.20: EMI-AM II range of operation frequency: (a) Magnetometer sensitivity as a function of operation frequency, demonstrating consistent operation across three orders of magnitude. From Reference [6]. **(b)** Gradient of the magnetometer Y-channel response across the same range. Lines serve to guide the eye.

Combined, the sensor demonstrates consistent operation without averaging across three orders of magnitude: from 3.5 kHz to 2 MHz. The upper end of this range is only limited by the maximum frequency of the LIA used. The range corresponds to a bias field values (B_z) between 7.47 mG and 2.85 G. This is significantly greater than those explored in other AM experiments.

The maximum sensitivity is found to be across the 100 kHz to 700 kHz regime. At lower frequencies an increase in the technical noise becomes the limiting factor. At higher frequencies the decrease in sensitivity is due to the broadening of the atomic response.

The source of this broadening is explored in Figure 5.21. This compares the high-frequency broadening for both an ^{85}Rb and ^{87}Rb RF-AM. The magnetometer HWHM for each isotope is fitted with a function

$$f(\nu) = \alpha_{85,87} + \beta_{85,87}\,\Phi^{85,87}(\nu)\,, \tag{5.1}$$

where $\Phi^{85,87}(\nu)$ is the second-order Zeeman effect as a function of operation frequency (ν). The function $\Phi^{85,87}(\nu)$ is derived in Section 3.2.1. The best fit parameters are $\alpha_{85} = 145\,\text{Hz}$, $\alpha_{87} = 160\,\text{Hz}$, $\beta_{85} = \beta_{87} = 1.6$. The strong agreement with experimental data confirms that the broadening results from second-order effects and not from the introduction of magnetic field gradients due to high-field operation.

The second-order broadening of the magnetometer resonance is further confirmed in Figure 5.22. This presents the X resonance response of the magnetometer operating on ^{87}Rb

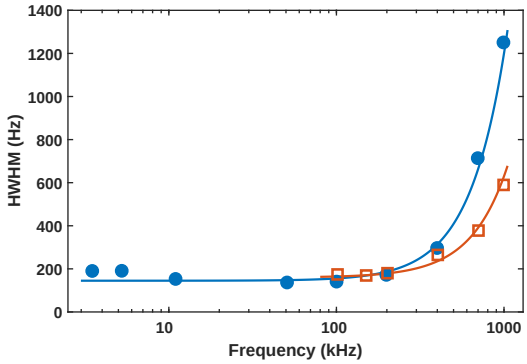

Figure 5.21: High-frequency broadening: Magnetometer HWHM as a function of frequency for both ^{85}Rb (blue, filled circles) and ^{87}Rb (red, open squares). Theoretical fits (solid lines) are calculated from the second-order Zeeman effect as a function of frequency $\left(\Phi^{85,87}(\nu)\right)$. From Reference [6].

near 2 MHz ($B_z = 2.85\,\mathrm{G}$). One can clearly discern the individual RF transitions between different pairs of nearest-neighbour magnetic sub-levels. Their separation exactly matches that predicted from the function of $\Phi^{87}(\nu)$ – 1.16 kHz. In these conditions the magnetometer exhibits a sensitivity of $4.3\,\mathrm{pT}/\sqrt{\mathrm{Hz}}$.

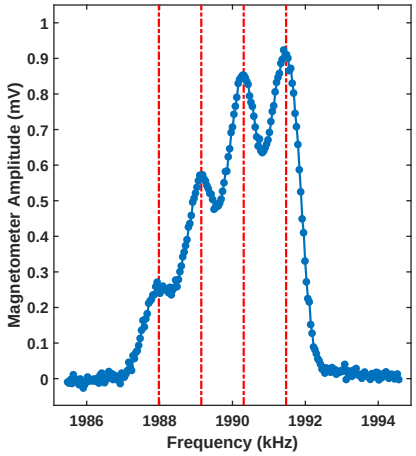

Figure 5.22: Second-order splitting: Second-order Zeeman splitting of magnetometer resonance – ^{87}Rb magnetometer operating at 2 MHz. Marked peaks and splittings (red lines) are calculated from $\Phi^{87}(\nu)$. From Reference [6].

5.3.11 Triggered data acquisition performance

During operation, the effect of the 50 Hz noise is further reduced by time-gated data acquisition triggered directly from the power line. This noise can be viewed as an amplitude modulation of the bias field. In turn, this modulates the resonant frequency of the RF-AM – by ±56 Hz with the active compensation system and 1.1 kHz without (Figure 5.18). Given

that the HWHM of the magnetometer resonance is around 140 Hz, such changes are enough push the magnetometer out of resonance.

The triggered data acquisition system – introduced in Section 4.5.5 – ensures that each measurement is taken at the same point of the 50 Hz oscillation. This point is when the oscillation crosses zero – i.e. when there is no modulation to the bias field. The effect is seen in Figure 5.23. This compares two traces of the RF-AM resonance. Without the triggered acquisition (Figure 5.23(b)) each measurement is near random due to modulation from the power line noise.

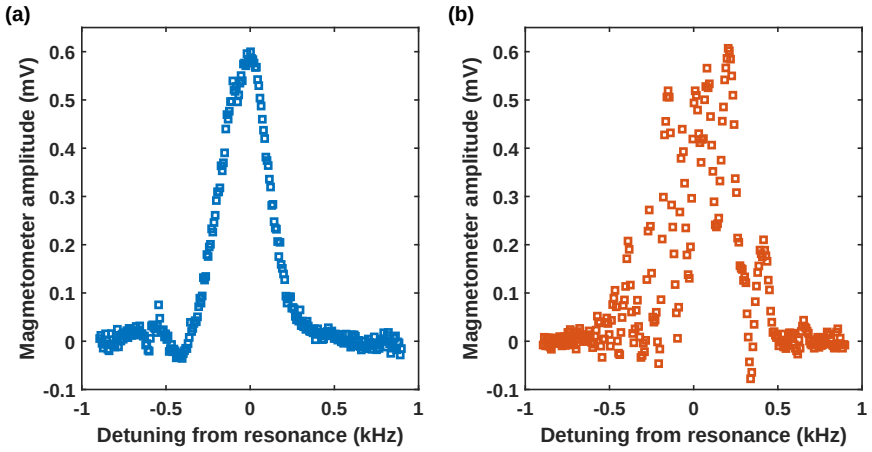

Figure 5.23: Effect of triggered data acquisition on resonance: Typical X traces of the magnetometer response **(a)** with and **(b)** without triggered data acquisition. Recorded at 100 kHz.

The effect can also be understood by imaging the magnetic field. Here, I only consider imaging the background field (no sample for EMI is present). The bias field is fixed and the frequency fixed to the corresponding resonance – i.e. the magnetometer operates at the top of the peak in, for example, Figure 5.23(a).

Without the triggered acquisition each consecutive pixel of the image is susceptible to noise. This leads to an image containing large variations in the signal level (Figure 5.24(a)). The noise can be removed by using a longer LIA time constant (T_c). The time constant can be seen as setting the cut-off frequency of a low-pass filter on the LIA output. The response is averaged for a given period of time, removing high-frequency noise. Figure 5.24(a) uses $T_c = 2\,\text{ms}$ (allowing 50 Hz to pass). In contrast, Figure 5.24(b) uses $T_c = 10\,\text{ms}$ – averaging out the 50 Hz noise. This results in a smooth image. However, the values recorded when averaging are root-mean-square averages (RMS). These are lower that the expected peak value, meaning a reduced sensitivity and a reduced contrast in the EMI images. Note

that, when sweeping the RF resonance with $T_c = 10\,\text{ms}$ the RMS average broadens the magnetometer linewidth by a factor $\sqrt{2}$. A smooth image is recorded for the $T_c = 2\,\text{ms}$ case using triggered data acquisition – Figure 5.24(c). The signal level is also greatly increased, due to the triggering point being set at the maximum value exactly on resonance.

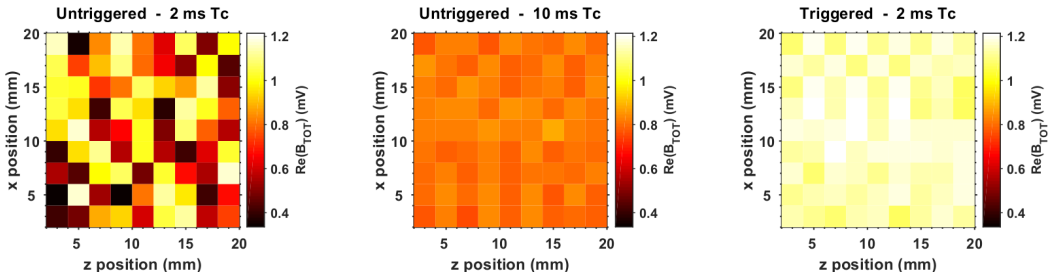

Figure 5.24: Effect of triggered data acquisition on imaging: Images of the background magnetic field. **(a)** and **(b)** without triggered acquisition. Noise in the $T_c = 2\,\text{ms}$ image is averaged out for $T_c = 10\,\text{ms}$. **(c)** with triggered acquisition and $T_c = 2\,\text{ms}$, 50 Hz noise is suppressed and sensitivity is higher. All images plotted against the same colour scale for comparison.

The variations within each background image and the increase of signal when using the triggered data acquisition is further highlighted in Figure 5.25. Here, the same data is displayed as a surface plot. From this it is clear to see that longer time constants average the effect of the noise. Whereas the triggered acquisition always records the peak value.

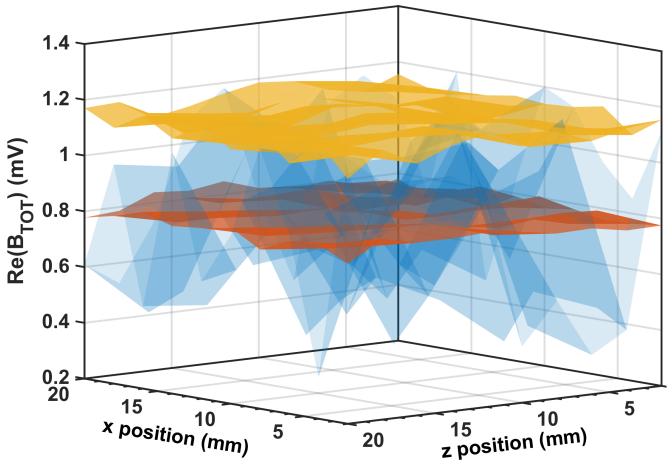

Figure 5.25: Effect of triggered data acquisition on imaging: Surface plot of the data from Figure 5.24. Untriggered acquisition with $T_c = 2\,\text{ms}$ (blue), untriggered acquisition with $T_c = 10\,\text{ms}$ (red), triggered acquisition with $T_c = 2\,\text{ms}$ (yellow).

Finally, the mean, standard deviation, and relative deviation for the three measurement schemes is compared. The details are found in Table 5.1.

	μ (mV)	σ (mV)	σ/μ
$T_c = 2$ ms, untriggered	0.816	0.263	0.322
$T_c = 10$ ms, untriggered	0.810	0.028	0.035
$T_c = 2$ ms, triggered	1.150	0.035	0.030

Table 5.1: Details of triggered data acquisition: Mean, standard deviation, and relative deviation for the three data acquisition measurement schemes.

5.4 EMI-AM III performance

The high-frequency EMI-AM III system represents the third-generation in the development of this new imaging platform. This system was designed to achieve this by building on the performance of the previous device and extending the range of operation frequency. This gives access to lower conductivity samples – as discussed in the previous chapters. With this in mind the system uses isotopically enriched ^{87}Rb vapour cells. This isotope provides a higher dynamic range and is less affected by the second-order Zeeman effect (see Figure 5.21). The experimental details are provided in Section 4.6.

Firstly, a typical response profile of the RF-AM at 100 kHz is presented in Figure 5.26. The inset shows the oscillations at the resonance frequency in the polarimeter output. Note that the response amplitude (HWHM) is significantly larger (narrower) than the response of the previous system (Figure 5.4).

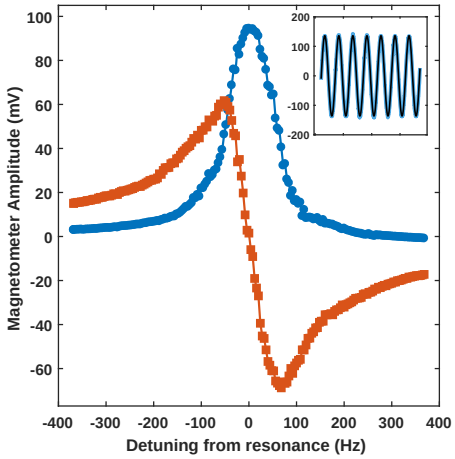

Figure 5.26: EMI-AM III resonance response: Typical in-phase (blue circles) and out-of-phase (red squares) response of the magnetometer near 100 kHz ($B_z = 142$ mG). Inset: polarimeter output at the resonant frequency fitted with sine wave of the same frequency. Near-optimised conditions: pump power 330 µW, probe power 60 µW, vapour cell temperature 45 °C.

Optimising the magnetometer's performance follows the same procedure as above. In particular, the effects of the applied RF field, the pump and probe beam intensities, and the temperature are explored. This was again done at 100 kHz to provide a direct comparison with the previous results. Only the main results of this process are included here. For reference, the results for each parameter are included in Appendix D.

All of the results in this section are obtained with the laser beams propagating to the sensor table in free-space. This followed the removal of the optical fibres (see Section 4.6.1) due to instabilities caused by a nearby AC unit.

5.4.1 Sensitivity

Figure 5.27 plots the RF and DC sensitivities at each explored temperature – 25 °C, 45 °C, and 65 °C. Again, the two independent measures of the sensitivity are closely matched. The system achieved a maximum measured sensitivity of 55 fT/$\sqrt{\text{Hz}}$ and a HWHM of 36 Hz. The new experiment also demonstrates clear sub-picotesla performance at room temperature.

This represents a clear improvement in the sensitivity. It is primarily the result of an increased magnetic field homogeneity, arising from all coils being greater than 1.3 m and the inclusion of automated gradient compensation.

These values are limited by the choice of the total noise for the SNR. The increased sensitivity and narrower bandwidth of the new system sees a significant contribution to the resonant noise. This is discussed further in Section 5.4.3.

Alternatively, one can use the photon-shot noise limit as the measure for the sensitivity. With this approach the values improve to: 29 fT/$\sqrt{\text{Hz}}$ at 45 °C and 10 fT/$\sqrt{\text{Hz}}$ at 65 °C. These numbers are similar for both the RF and DC sensitivity.

5.4.2 Y-channel gradient

Figure 5.28 plots the Y-channel gradient against the probe beam power. As before, the response confirms the inverse relationship between the gradient and the sensitivity. Note that the value of the gradients recorded in Figures 5.28(b)/(c) are an order of magnitude steeper than the values presented in Figure 5.10. This improvement reflects the degree of improvement seen in the sensitivity and the photon-shot noise level.

5.4.3 Noise components

Figure 5.29 plots the contributing factors to the noise around 100 kHz with the magnetometer operating at 45 °C. Recall that these components are: the technical noise in the

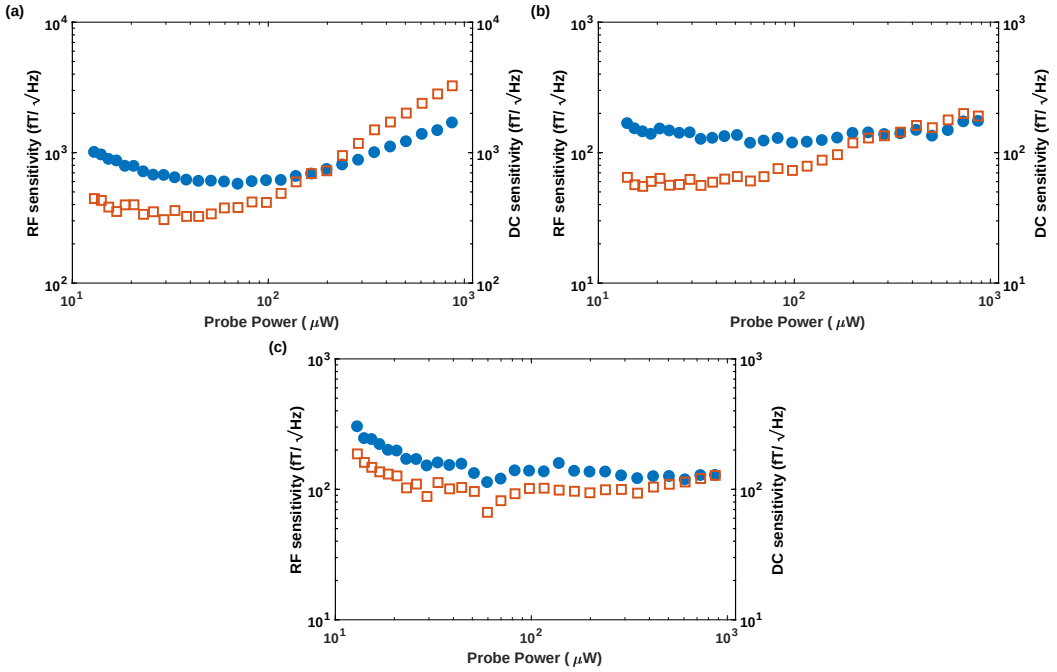

Figure 5.27: Magnetometer sensitivity as a function of probe beam power: **(a)** 25 °C, **(b)** 45 °C, and **(c)** 65 °C. RF sensitivity (blue, filled circles), DC sensitivity (red, open squares). Note the change in scale between **(a)** and **(b)**/**(c)**.

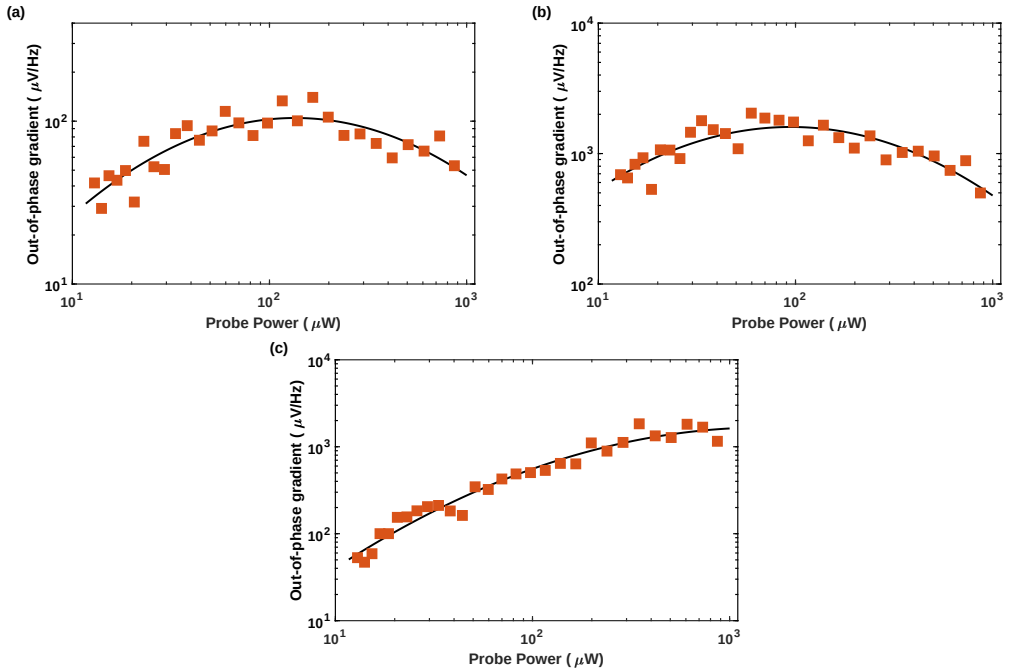

Figure 5.28: Magnetometer Y-channel gradient as a function of probe beam power: **(a)** 25 °C, **(b)** 45 °C, and **(c)** 65 °C. Lines serve to guide the eye. Note the change in scale between **(a)** and **(b)**/**(c)**. The values recorded at higher temperatures are an order of magnitude steeper than those of the previous system.

measurement electronics (black line) – measured with the probe beam blocked, the photon-shot, or baseline, noise (red line) – measured with the bias field detuned from the resonance, and the total noise (blue line) – measured with the RF driving off and the bias field on.

Resonant noise sources lift the level of the total noise above the photon-shot noise level. The signature of this noise is a Lorentzian profile with the same linewidth as the RF-AM resonance response (dashed, red line of Figure 5.29). This noise includes fundamental components – the spin-projection noise and the light-shift noise. In addition there is a significant contribution from environmental noise at the resonant frequency. However, the environmental contribution does not represent a fundamental limit to the sensitivity. This is because it can be (almost entirely) removed by shielding the sensor and would be different depending on the sensor location. For unshielded RF-AMs a gradiometric arrangement reduces the resonant noise close to the photon-shot noise level. This effect can be seen, for example, by comparing Figure 3(a) and 3(b) of Keder et al. (2014) [64].

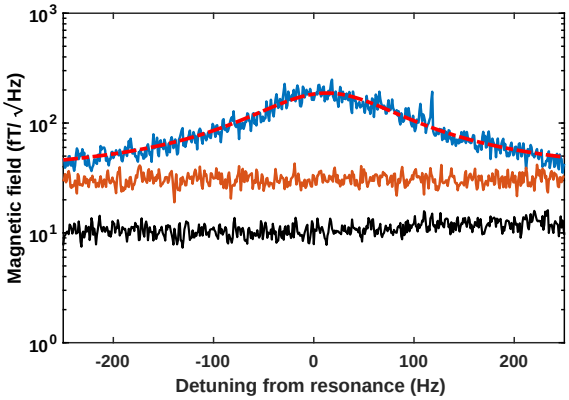

Figure 5.29: Magnetic field noise components: Noise sources around 100 kHz at 45 °C. Total noise – RF driving off (blue), photon-shot noise – bias field detuned from resonance (red), and technical noise – probe beam blocked (black). Resonant noise sources lift the total noise level above the photon-shot noise level. The fingerprint of these sources is given by the Lorentzian profile of the total noise with a comparable HWHM to the RF-AM response (dashed, red line).

For this reason the baseline noise if often quoted as the fundamental sensitivity limit of unshielded magnetometers. This level is given by 29 $\mathrm{fT}/\sqrt{\mathrm{Hz}}$ in this case of Figure 5.29. An improved level of 10 $\mathrm{fT}/\sqrt{\mathrm{Hz}}$ was recorded at 65 °C. However, the total noise level – with a maximum recorded value of 55 $\mathrm{fT}/\sqrt{\mathrm{Hz}}$ – defines the practical limit to the sensitivity for the EMI-AM applications developed in this work.

5.4.4 Automated magnetic field and gradient suppression

The major improvement – providing the gains in sensitivity – is the increase in magnetic field homogeneity. This is a result of larger bias field coils, gradient compensation across all axes, and the reduction in metallic components in the sensor's vicinity. The compensation coil system in this setup is controlled by two dedicated LabVIEW programs that optimise the magnetic fields based on the magnetometer response.

Firstly, consider the DC magnetic field in the transverse directions (x and y). The field in the z direction is fixed and regulated by the compensation system. The resonant frequency of the RF-AM has a quadratic dependence on the transverse coil currents. This follows from

$$\nu = \frac{\gamma\,|\mathbf{B}|}{2\pi} = \gamma\sqrt{B_x^2 + B_y^2 + B_z^2}\,, \tag{5.2}$$

where ν in the operation frequency and γ the gyromagnetic ratio. Therefore, when the transverse fields are fully suppressed ($B_x = B_y = 0$) the RF-AM resonance frequency is minimised.

The optimisation process performs a simple one dimensional hill climbing algorithm. The axes can be treated independently due to their orthogonality. Example results are presented in Figure 5.30. The program explores the quadratic dependence of the resonant frequency on the coil current. The currents are automatically set at the values that minimise the resonant frequency.

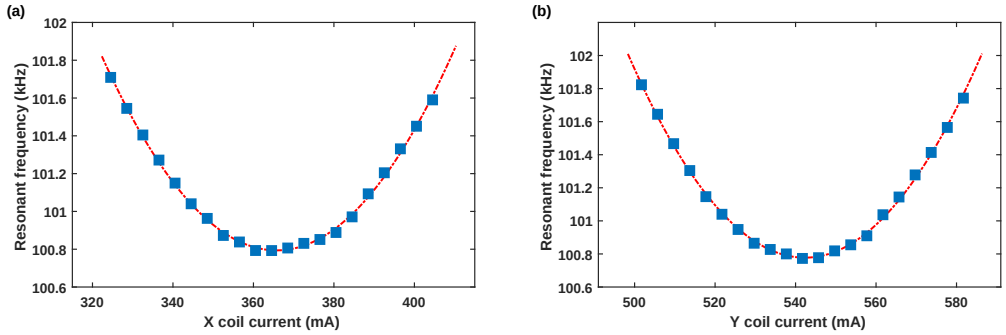

Figure 5.30: Automatic calibration of DC coils: Magnetometer resonant frequency as a function of **(a)** the X coil current and **(b)** the Y coil current. The program cycles through the currents, fits the response with the quadratic (shown), and automatically selects the optimum current value as the minimum of the fit.

A quantitative understanding of the effect of each coil can be gained from the quadratic coefficients of the fit. These describe the degree of change in resonant frequency to a change in current. The values are $5.45 \times 10^5\,\mathrm{Hz/A^2}$ for the x direction and $6.37 \times 10^5\,\mathrm{Hz/A^2}$ for

the y direction. The similarity of these values is expected from the symmetry of the system.

Secondly, consider the suppression of magnetic field gradients. Magnetic field gradients across the sensing volume broaden the atomic resonance as atoms at different locations precess at different frequencies (see Section 3.7.6).

Again one dimensional hill climbing algorithms are performed, taking advantage of the orthogonality of the coils. The effect of each gradient coil on the RF-AM linewidth is plotted in Figure 5.31. Each response is fitted with a quadratic relationship. The currents are automatically set at the values that minimise Γ – increasing the sensitivity.

The RF-AM is inherently more sensitive to gradients along the quantisation axis, as expected. This is borne out in the quadratic coefficient of each fit. For dx and dy the values are 1.26×10^3 Hz/A^2 and 4.33×10^3 Hz/A^2, respectively. In contrast, the value for dz is an order of magnitude larger – at 1.75×10^4 Hz/A^2.

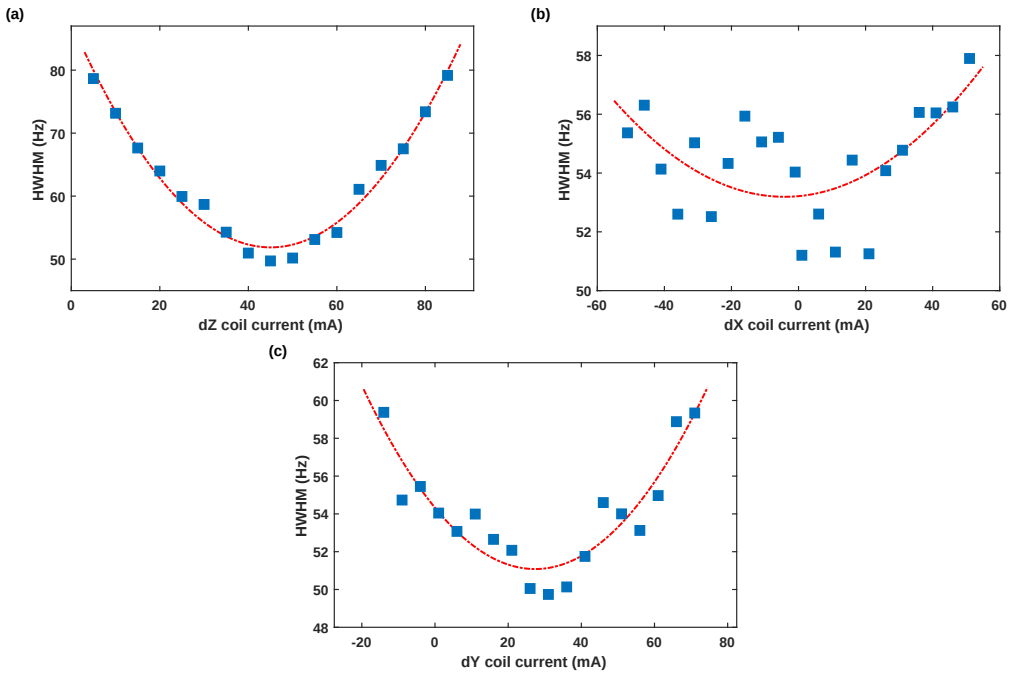

Figure 5.31: Automatic calibration of gradient coils: Magnetometer HWHM as a function of **(a)** the dZ coil current, **(b)** the dX coil current, and **(c)** the dY coil current. The system cycles through the currents, fits the response with the quadratic (shown), and automatically selects the optimum current value as the minimum of the fit. Note that the response is significantly more sensitive to gradients in the z direction.

5.4.5 High-frequency operation

The high-frequency setup (Section 4.6.4) is designed to operate at frequencies that exceed the 2 MHz limit of the LIA. Figure 5.32 presents a comparison of the magnetometer outputs

at this limit. Figures 5.32(a) and 5.32(b) are the amplitude and phase responses recorded by the LIA. Note that the splitting due to the second-order Zeeman effect is more clearly defined in comparison to the previous response of the EMI-AM II system (Figure 5.22). This is a consequence of the narrower linewidth of the EMI-AM III experiment. Figures 5.32(c) and 5.32(d) are recorded by the AD8302 chip in the same conditions. The responses have been converted according the the calibration values in Table 4.4. The R responses are near indistinguishable. The Φ responses record the same features, however the values do not match. This is due to the initial phase difference between the RF-AM output and the reference signal (reference phase). For the LIA this is set to 0°. However, the AD8302 requires a 90° phase difference for optimum performance. In addition, the LIA phase response ranges from $-180°$ to 180°. In contrast, the AD8302 phase response is periodic over 0° to 180° (see Figure 4.17(a)). Nevertheless, the combined amplitude and phase response validates

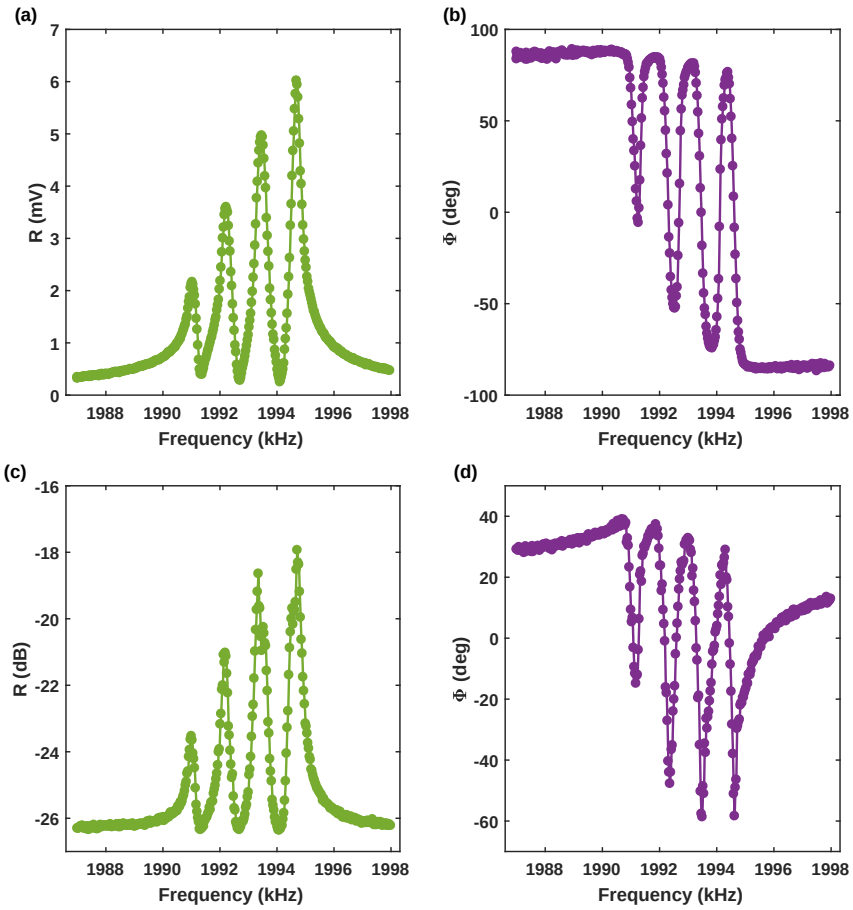

Figure 5.32: Comparison of LIA and AD8302: The magnetometer R response **(a)** and phase response **(b)** recorded by the LIA. These compare well with the R response **(c)** and phase response **(d)** recorded by the AD8302. Recorded around 2 MHz, equivalent to $B_z = 2.85\,\mathrm{G}$ for ^{87}Rb.

this alternative approach of the extracting the magnetometer signal at higher frequencies and in larger magnetic fields.

Operation at higher frequencies is proven by Figure 5.33. This displays the magnetometer phase response at around 5 MHz, recorded in a bias field of 7.13 G. This is the largest magnetic field that an AM has operated in. It is close to the 8.2 G (5.75 MHz) limit imposed by the currently installed power supplies. Note that, the peaks in the corresponding amplitude response are only just visible above the noise level, and the separation between the peaks exactly matches the calculations from the second-order Zeeman effect.

This result further significantly extends the operation range of RF-AMs beyond both the EMI-AM II system and all previous AM experiments. Increasing the operating band increases the scope of applications to those requiring detection at high frequencies – including the EMI-AM imaging of very low-conductivity samples.

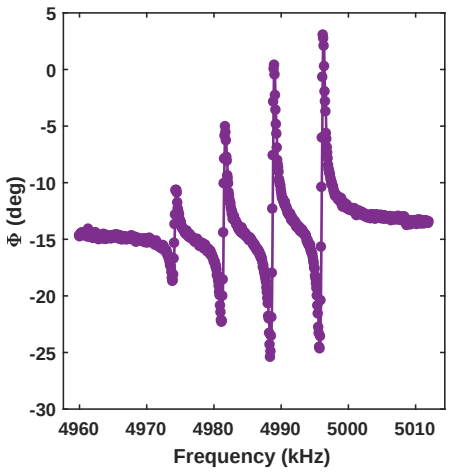

Figure 5.33: EMI-AM III system high-frequency response: Typical phase response of the magnetometer near 5 MHz. Recorded in a bias field $B_z = 7.13\,\mathrm{G}$ with an ^{87}Rb RF-AM. The separation of 7.34 kHz between peaks exactly matches the calculation from $\Phi^{87}(\nu)$.

5.5 Discussion

This chapter has detailed the development of a single-channel RF-AM operating in unshielded environments. The device has been continuously improved to a demonstrated sensitivity of $55\,\mathrm{fT}/\sqrt{\mathrm{Hz}}$ and a photon-shot noise limit of $10\,\mathrm{fT}/\sqrt{\mathrm{Hz}}$. To date, the low-temperature single-channel unshielded RF-AM is the most sensitive of its kind reported in literature. The sensor has a narrow linewidth response tunable across several orders of magnitude in operation frequency. This range, equivalent to a bias field of up to 7.13 G,

is an order of magnitude larger than previous AMs have achieved. The consistent response without averaging or magnetic shielding is based on the active locking of the magnetic field. This increases the stability of the signal and results in a factor 10 reduction of the power line noise. Finally, by retaining a single-channel configuration, the device is suitable to the detection of both local and remote magnetic field sources. Together, the demonstrated flexibility of the magnetometer greatly increases its applicability in comparison to other RF-AM implementations.

Chapter 6

Imaging performance

This chapter details the imaging performance in EMI-AM systems. Firstly, an overview detailing the range of samples imaged in this work is presented. This provides context for the work and for the technique of EMI-AM in general. A number of example images are included to demonstrate the range and performance of the EMI-AM systems. Imaging low-conductivity materials and imaging through conductive barriers are then described in more detail. Finally, the use of EMI-AM for non-destructive evaluation (NDE) applications and imaging ferromagnetic materials is introduced.

The results presented in this chapter are reported in References [1, 3, 7, 8].

6.1 Overview of imaging performance

In EMI/MIT, for many materials the dominant component of the secondary field arises from the conductivity (σ) – and that this component scales with the operation frequency (ω) as $\sigma\,\omega$. For an EMI system to be applicable to imaging a wide range of materials it must have: (i) a broad tunability in its operation frequency, and (ii) a high-sensitivity across this range. The RF-AM sensors realised in this thesis have been designed and developed to have these characteristics. This has allowed a range of materials to be explored by EMI-AM.

The landscape of EMI-AM is presented in Figure 6.1. It charts the range of imaged materials and their conductivities. Each material is listed in accordance with its first reported occurrence. Closed symbols are used for materials first imaged as part of this work. The shaded region is used to define work done with shielded AMs.

The range of conductivity spans more than five orders of magnitude – from Cu at $5.98 \times 10^7\,\mathrm{S\,m^{-1}}$ to an n-doped Si sample at $500\,\mathrm{S\,m^{-1}}$. The operation frequencies required cover the range from around 1 kHz to 2 MHz.

The geometry of the samples is a crucial parameter that requires discussion. The sizes

of all the samples in this thesis are detailed in their respective sections. In summary, all samples are 50 mm × 50 mm or less (in the imaging plane) and have a thickness of 10 mm or below. For reference, the largest sample volume is 12.5 cm^3, for the lowest conductivity samples (n-doped Si) the volume is 6.25 cm^3. Furthermore, eddy currents are only locally excited within these samples. This allows detailed high-resolution EMI of the sample's features to be performed.

This is in stark contrast to early work with coil-based MIT systems. These systems demonstrated the ability to detect conductivities at (or below) the 1 $S\,m^{-1}$ level. However, the test samples used were significantly larger (for example 2262 cm^3 in Griffiths et al. (2007) [108]). The volume in which eddy currents are excited renders high-resolution EMI imaging impossible.

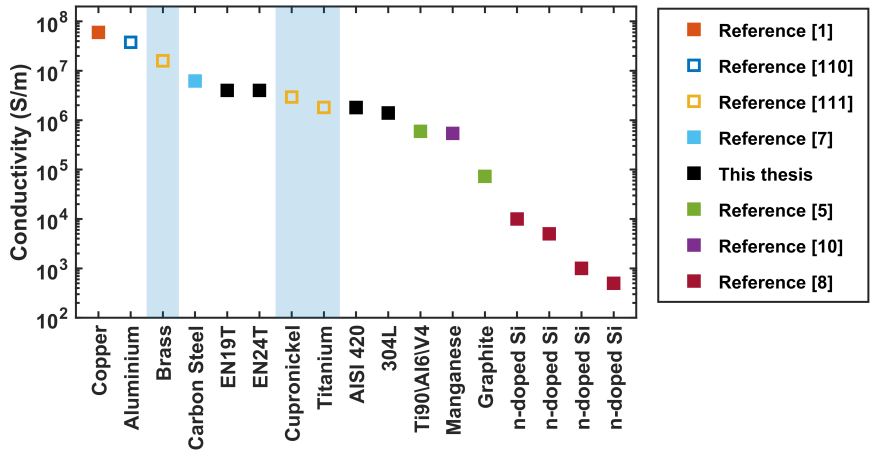

Figure 6.1: The progression of sample conductivities imaged by EMI with AMs: Materials reference to their first appearance. The shaded area indicates magnetometers operating in shielded environments. Closed symbols are for materials first imaged as part of this thesis.

6.2 EMI data acquisition and display

EMI images are constructed by moving the samples via the computer-controlled two-axis stage. The stage rasters the sample across the field of view in the x,z-plane. At each position the EMI-AM systems automatically record the response of the RF-AM. As shown, the secondary magnetic field contribution perturbs the atomic motion of the atoms. This is in turn imprinted in the rotation of the probe beam's plane of polarisation. The probe beam signal is selectively amplified by the LIA. The LIA extracts four streams of data: the amplitude (R), phase (Φ), and the real (X) and imaginary (Y) components. The results at each point

are added to a corresponding matrix, building up an image of each parameter in real time.

The datasets are smoothed to ease the recognition of the image features. The first stage is the convolution of the dataset with a nearest-neighbour Gaussian filter – typically of radius 1 or 2 pixels. This accounts for any fluctuations in the measured values. A piecewise cubic interpolation then applied.

The high-contrast colour scale is chosen to ease the identification of the sample's shape and highlight further features. For the majority of images, the colour map is scaled between the maximum/minimum of the secondary field response within the image and the equilibrium value. This is defined as the average value from a region where the sample is not present. This conveys the idea of a variation in the imaging parameter (due to the secondary field) from the equilibrium value (due to the primary field only). In addition, this allows an easier direct comparison of the secondary field contributions from different samples in different conditions. No background image subtraction is required – or applied – in any of these results. This is a paramount in view of translating the technology to practical applications

6.3 Electromagnetic induction images

In this section a number of EMI-AM images are presented. These are shown in Figure 6.2 and Figure 6.3. They are chosen to demonstrate the power of EMI with an RF-AM operating in unshielded environments.

The samples consist of a range of shapes and materials. The conductivity ranges from $5.98 \times 10^7\,\mathrm{S\,m^{-1}}$ for Cu to $500\,\mathrm{S\,m^{-1}}$ for n-doped Si. The operation frequency correspondingly varies between 1 kHz and 2 MHz. The results emphasise the need to adapt the frequency based on the sample material and thickness. By appropriately adjusting the excitation frequency similar levels of signal change are recorded, despite the large differences in conductivity.

Images are shown for a number of the parameter streams extracted by the LIA. Each of these represents a different property of the secondary field and can be associated to different electromagnetic properties of the sample (see Chapter 2). The full details of the scans displayed in Figure 6.2 and Figure 6.3 are reported in Table 6.1.

In all cases the images accurately reproduce the size and shape of the sample. The "rounding-off" of corners is attributed to the limited flow of eddy currents in those regions. As eddy current flows are circular their density is reduced in areas containing sharp angles.

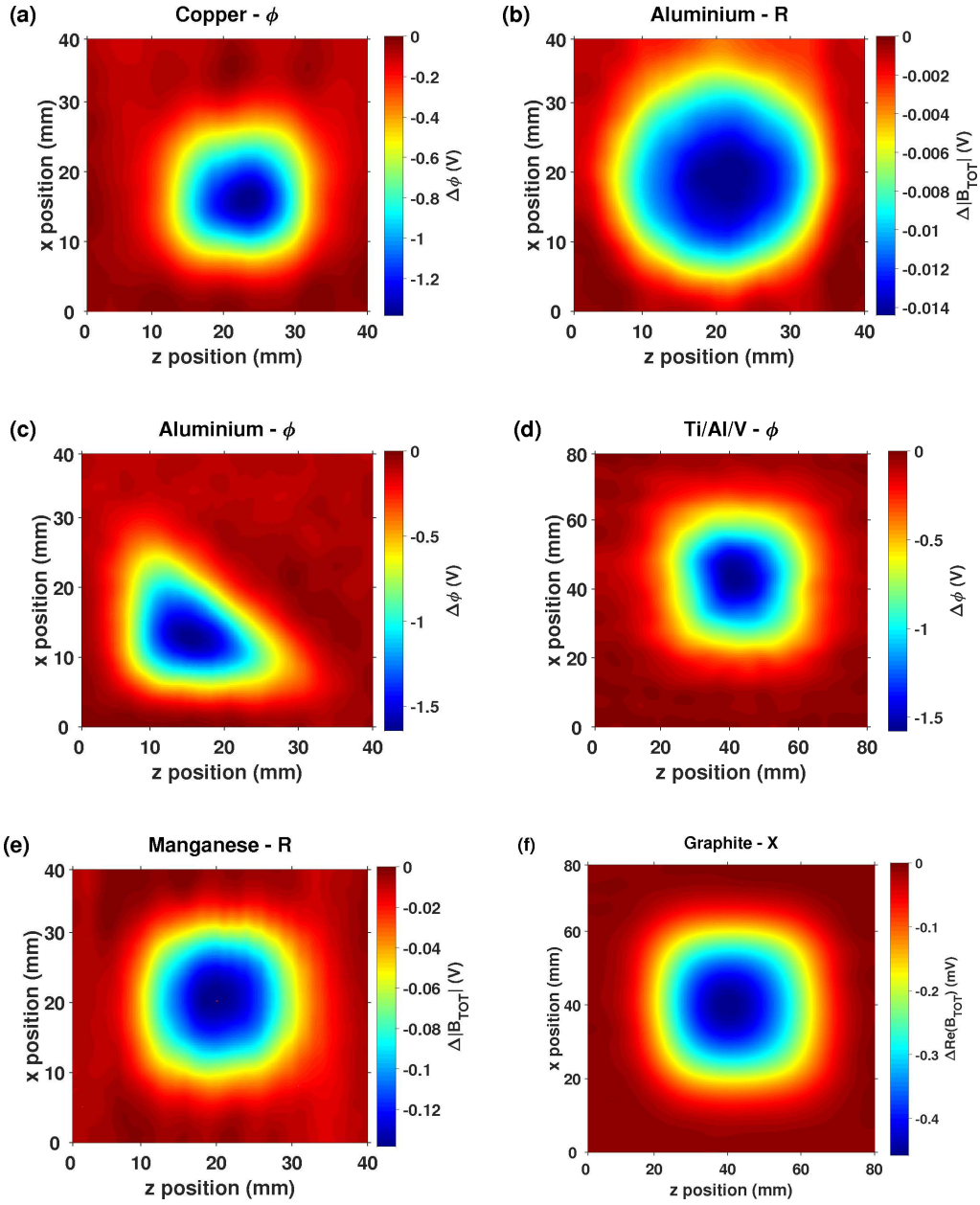

Figure 6.2: Electromagnetic induction imaging with with an atomic magnetometer (i): Example electromagnetic induction images of various materials and parameters using an RF-AM. Images accurately reproduce the size and shape of sample objects. See Table 6.1 for details of the scan parameters.

In addition, the application of nearest-neighbour filtering naturally contributes to this effect.

These images are a collection from across the time frame of this work. Chapter 5 charts the increase in sensor performance of the EMI-AM systems as they have been developed. The results of Figure 6.2 and Figure 6.3 include examples from the initial EMI-AM I experiment and throughout the development of the EMI-AM II system. As such, the results include RF-AMs operating with different isotopes of Rb, and results using both D_1 and D_2

line optical pumping. These details can be found in Table 6.1.

On the surface the imaging performance may not appear to have changed greatly as the systems have been developed. However, it is important to note that the latest imaging of low-conductivity samples is only possible due to the improvements in sensitivity, stability, and range of tunability of the sensor.

This is best seen by comparing the background (dark-red regions) of Figure 6.2(f) (taken with the EMI-AM II system) to the background in Figures 6.2(a) – (e) (taken with the EMI-AM I system). The increased signal stability of the EMI-AM results in a reduction in the background noise. As a consequence, the image outline is more clearly defined.

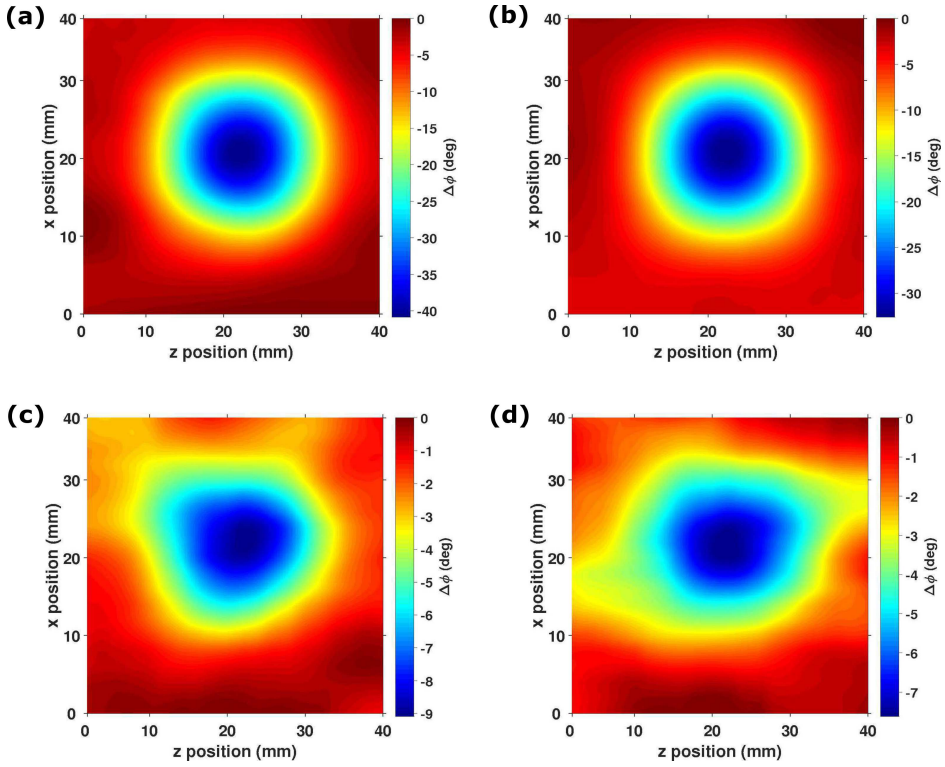

Figure 6.3: Electromagnetic induction imaging with with an atomic magnetometer (ii): Example electromagnetic induction images of low-conductivity materials using an RF-AM. Successful imaging down to 500 S m^{-1}. See Table 6.1 for details of the scan parameters. Adapted from Reference [8].

The experimental control software has been developed and improved in parallel to the system development. For the EMI-AM I system the LIA data streams were recorded with a DAQ (NI USB-6009) from the LIA's analogue output channels. The outputs are given in volts. In particular, the Φ parameter is converted as 1 V/20°. For the EMI-AM II system onwards, the data is read directly from the device. The $X, Y,$ and R channels are the signal in mV and Φ in degrees.

Details of Figure 6.2 and Figure 6.3									
	Material	Dimensions	σ (S m^{-1})	ν (kHz)	δ (mm)	Parameter	Setup	Isotope	Pumping
6.2(a)	Copper	25 mm×25 mm, 1 mm thick	5.98×10^7 [148]	1.89	1.50	Φ	EMI-AM I	^{87}Rb	D_2
6.2(b)	Aluminium	⌀ 37 mm, 2 mm thick	3.77×10^7 [148]	1.00	2.59	R	EMI-AM I	^{87}Rb	D_2
6.2(c)	Aluminium	31 mm×38 mm, 3 mm thick	3.77×10^7 [148]	1.00	2.59	Φ	EMI-AM I	^{87}Rb	D_2
6.2(d)	Ti/Al/V	50 mm×50 mm, 1 mm thick	5.95×10^5 [149]	250	1.30	Φ	EMI-AM I	^{85}Rb	D_2
6.2(e)	Manganese	25 mm×25 mm, 1 mm thick	5.40×10^5 [148]	208	1.50	R	EMI-AM I	^{87}Rb	D_2
6.2(f)	Graphite	50 mm×50 mm, 5 mm thick	7.30×10^4 [150]	150	4.81	X	EMI-AM II	^{85}Rb	D_2
6.3(a)	n-doped Si	25 mm×25 mm, 10 mm thick	1×10^4	1370	4.30	Φ	EMI-AM II	^{87}Rb	D_1
6.3(b)	n-doped Si	25 mm×25 mm, 10 mm thick	5000	1580	5.66	Φ	EMI-AM II	^{87}Rb	D_1
6.3(c)	n-doped Si	25 mm×25 mm, 10 mm thick	1000	1790	11.9	Φ	EMI-AM II	^{87}Rb	D_1
6.3(d)	n-doped Si	25 mm×25 mm, 10 mm thick	500	2000	15.9	Φ	EMI-AM II	^{87}Rb	D_1

Table 6.1: Details of electromagnetic induction images: The material, sample dimensions, conductivity (ω), operation frequency (ν), skin depth (δ), imaging parameter, experimental setup, Rb isotope, and optical pumping configuration for the EMI-AM images shown in Figure 6.2 and Figure 6.3.

6.4 Semiconductor imaging

I have discussed the lack of instrumentation for imaging the bulk electromagnetic properties of low-conductivity materials and biological tissues. In this section, imaging the doping concentration of low-conductivity semiconductors – down to $500\,\mathrm{S\,m^{-1}}$ – via EMI-AM is demonstrated. The results are reported in Reference [8].

Current semiconductor imaging technologies suffer from a number of limitations. For example, scanning electron microscopy requires dedicated preparation of the samples and is usually destructive in nature [151]. Raman microscopy offers an alternative approach but is only sensitive to relatively high-dopant concentrations $\left(>10^{18}\,\mathrm{cm^{-3}}\right)$ [152]. However, these methods are confined to surfaces and interfaces. In addition, they are limited to small areas $\left(\text{around } 10^{4}\,\mu\mathrm{m}^{2}\right)$ and do not map the electrical conductivity and the related distribution of dopants.

In contrast EMI-AM provides direct non-destructive access to dopant concentrations, without any former preparation of the sample. The imaging, characterisation, and identification of low-conductivity semiconductors is relevant to applications in semiconductor devices [153], solar cells [154], as well as other fields including recycling – by identifying and isolating valuable and potentially pollutant semiconductor waste [155, 156].

6.4.1 Details of Si samples

The semiconductors are float-zone Si samples supplied by PI-KEM Ltd. The dimensions are $25\,\mathrm{mm} \times 25\,\mathrm{mm}$, with a thickness of 10 mm (controlled to within $\pm 50\,\mu\mathrm{m}$). The electrical conductivities are tailored by adjusting the abundance of n-donors (phosphorus). Each phosphorus atom contributes five valance electrons. Four are required for bonding to the surrounding Si lattice, the fifth acts as a charge carrier – increasing the conductivity. The details of each sample are summarised in Table 6.2.

Material	ρ ($\Omega\,\mathrm{cm}$)	σ $\left(\mathrm{S\,m^{-1}}\right)$	Donor concentration $\left(\mathrm{cm^{-3}}\right)$
n-doped Si	1×10^{-2}	1×10^{4}	5×10^{18}
n-doped Si	2×10^{-2}	5000	2×10^{18}
n-doped Si	1×10^{-1}	1000	8×10^{16}
n-doped Si	2×10^{-1}	500	3×10^{16}

Table 6.2: Details of semiconductor samples: The material, resistivity (ρ), conductivity (σ), and donor concentration of each semiconductor sample.

6.4.2 Low-conductivity EMI-AM imaging

Chapter 2 describes how the operation frequency and the sample conductivity effect both the skin depth (via Equation 2.4) and the EMI response (via Equation 2.56). In summary, as

As discussed in Chapter 2, the operation frequency increases the penetration of the primary field is progressively confined to the surface (via Equation 2.4). The secondary field response is proportional to $\omega\sigma$ (Equation 2.56). Therefore, the EMI imaging of low-conductivity samples requires an increase in ω and a highly-sensitive detector. The operation range and sensitivity of the EMI-AM II system provides these characteristics. For these results, the primary field is provided by a small ferrite-core coil to locally excite eddy currents in the samples.

Figure 6.3 presents phase maps of the semiconductor samples. Φ is used as it can be directly related to σ – and hence the donor concentration. Furthermore, changes in Φ can only be caused by the contribution of eddy currents – not mere shielding of the RF-AM.

The most doped sample $\left(1\times10^{4}\,\mathrm{S\,m^{-1}}\right.$, Figure 6.3(a)$\left.\right)$ produces the largest phase variation, $\Delta\Phi=-40°$. The $5000\,\mathrm{S\,m^{-1}}$ sample (Figure 6.3(b)) exhibits a maximum variation of $\Delta\Phi=-32°$. In both cases, the large response creates a well defined boundary corresponding to the size and position of the sample. This definition is partially degraded for the lowest conductivity samples – $2000\,\mathrm{S\,m^{-1}}$ (Figure 6.3(c)) and $500\,\mathrm{S\,m^{-1}}$ sample (Figure 6.3(d)). The maximum variations are $\Delta\Phi=-9°$ and $\Delta\Phi=-7.5°$, respectively. For each sample the operation frequency is adjusted to optimise the contrast in $\Delta\Phi$. For decreasing sample conductivity, the respective frequencies are: 1.37 MHz, 1.58 MHz, 1.79 MHz, and 2 MHz. The expected EMI response (given by Equation 2.56) is confirmed by the linear relationship between $\Delta\Phi$ and $\omega\sigma$ $\left(R^{2}=0.96\right)$.

Figure 6.4 displays EMI images comparing different dopant concentrations. The scans simultaneously acquire the details of two of the semiconductor samples. This demonstrates the direct, non-destructive imaging of the distribution of bulk doping in Si.

As expected, samples of different dopant concentrations produce different responses. Figure 6.4(a) compares the two highest conductivity samples. The recorded responses $\Delta\Phi$ (taken from the centre of each sample) are consistent with the differing values of σ. The same behaviour is observed in the comparative responses of the two least doped samples – see Figure 6.4(b). The similar ratio between the responses of the two samples in

(1.17 in Figure 6.4(a) and 1.23 in Figure 6.4(b)) is a consequence of the identical ratio between the conductivities.

Figure 6.4(c) presents a single EMI scan comparing the most and least doped Si samples. The difference in conductivity (a factor 20) represents the largest difference imaged in a single scan with an AM. The $1 \times 10^4\,\mathrm{S\,m^{-1}}$ sample (left hand side) is well defined and produces a comparable response to that of the other configurations. The lowest conductivity sample ($500\,\mathrm{S\,m^{-1}}$, right hand side) has a lower contrast in the colour scale used. However, it's clearly discernible and produces a signal level consistent with the previous cases. In summary, the EMI-AM technique demonstrates a large dynamic range in its ability to detect large differences in conductivity – in the same image at a single frequency.

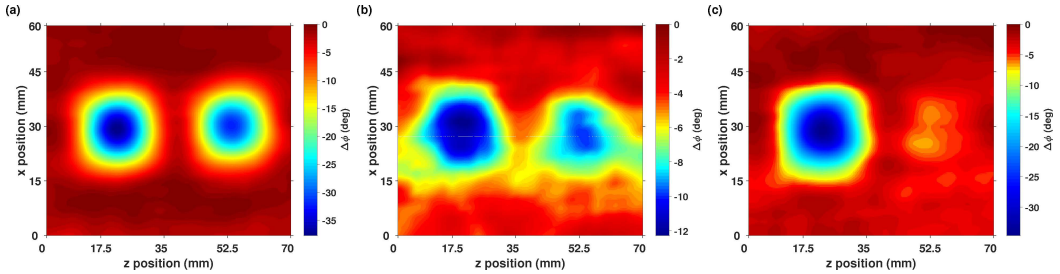

Figure 6.4: Simultaneous EMI imaging and comparison of n-doped semiconductors: (a) Φ images at 1.58 MHz of the $1 \times 10^4\,\mathrm{S\,m^{-1}}$ (left) and $5000\,\mathrm{S\,m^{-1}}$ (right) samples. Corresponding dopant concentrations $5 \times 10^{18}\,\mathrm{cm^{-3}}$ and $2 \times 10^{18}\,\mathrm{cm^{-3}}$. **(b)** Φ images at 2 MHz of the $1000\,\mathrm{S\,m^{-1}}$ (left) and $500\,\mathrm{S\,m^{-1}}$ (right) samples. Corresponding dopant concentrations $8 \times 10^{16}\,\mathrm{cm^{-3}}$ and $3 \times 10^{16}\,\mathrm{cm^{-3}}$. **(c)** Φ images at 2 MHz of the $1 \times 10^4\,\mathrm{S\,m^{-1}}$ (left) and $500\,\mathrm{S\,m^{-1}}$ (right) samples. Corresponds to a factor 167 difference in donor concentration. Adapted from Reference [8].

6.4.3 Discrimination of n-dopant concentration

Finally, this section explores the capability of EMI-AM in the characterisation of materials. For this I follow a procedure derived from eddy current impedance spectroscopy [157, 158]. The approach is adapted to the images produced by the EMI-AM systems.

Recalling Equation 2.56, the secondary field response has both real and imaginary components. The real part perturbs the atomic precession in-phase with the primary field. The imaginary part's perturbation is in-quadrature with respect to the primary field. Both of these components vary with ω – the primary field frequency. In addition, the penetration of the primary field into the sample changes from complete to zero as ω increases. These effects are combined to write the EMI response as

$$S(\omega) = X(\omega) + iY(\omega)\,. \tag{6.1}$$

The variations of X and Y as a function of ω can be attributed to different characteristics of the sample.

X initially increases with ω. At sufficiently high frequencies, where the skin depth is negligible compared to the sample thickness, eddy currents are confined to the surface. At this point X becomes a function of the surface geometry, saturating at this value.

In contrast, the Y response peaks at a given frequency (depending on the sample) before decaying. The Y response is sensitive to the bulk conductivity of the sample. At low frequencies ($\omega \to 0$) the primary field passed through the sample with virtually no attenuation. At high frequencies ($\omega \to \infty$) the field does not sufficiently penetrate the bulk. In both these cases the generation of eddy currents is limited and the Y response is near zero. At intermediate frequencies the skin depth is a significant proportion of the sample's thickness. Efficient generation of eddy currents in the bulk results in a peak Y response in this region. By acquiring X and Y images of each sample at different frequencies, it is possible to discriminate between materials. This approach is applied to discriminate the n-dopant level in semiconductors. It is equally applicable to p-doping along with other materials and geometries.

Multi-frequency EMI analysis of each sample is used to test the discrimination of the donor concentrations. Eleven images are acquired of each sample in the same conditions. The frequencies used were $\nu = \{100, 180, 311, 522, 733, 944, 1116, 1370, 1580, 1790, 2000\}$ kHz. The responses (ΔX and ΔY) are taken as the value change within the respective parameter image. These values are then normalised with $|S|$ – the total signal. For reference, example multi-frequency imaging results are included in Appendix E.

The normalised values are plotted against frequency. This is shown in Figure 6.5. The data points corresponding to each sample are fitted with a quadratic polynomial of the form $f(\nu, \{\Delta X, \Delta Y\}) = \alpha\,\nu^2 + \beta\,\nu + \gamma$. No potentially anomalous points are excluded from the fit. For all fits the point $(\nu = 0, \{\Delta X, \Delta Y\} = 0)$ is added. This reproduces the zero level observed at $\nu = 0$, where no eddy currents are generated and the RF-AM cannot operate.

For ΔX (Figure 6.5(a)), the analysis clearly distinguishes the $1 \times 10^4\,\mathrm{S\,m^{-1}}$ sample and the $5000\,\mathrm{S\,m^{-1}}$ sample from the data corresponding to the two lowest-conductivity samples. For ΔY (Figure 6.5(b)), four clearly defined curves allow the unambiguous identification of the conductivity of each sample – i.e. the level of n-doping in semiconductors. The peaks of the curves are displaced (in frequency) due to the relative differences in conductivity

and the associated penetration into the bulk. Although the frequency spectrum is limited to 2 MHz (by the LIA), the fits exhibit trends similar to the predictions above. This is also in agreement with observations obtained via eddy current impedance spectroscopy with metallic samples [157].

In summary the EMI-AM technique is shown to provide unambiguous discrimination of different n-dopant concentrations in semiconductors spanning two orders of magnitude – 10^{16} cm^{-3} to 10^{18} cm^{-3}. Changes is dopant levels as small as a factor 2.5 are distinguished.

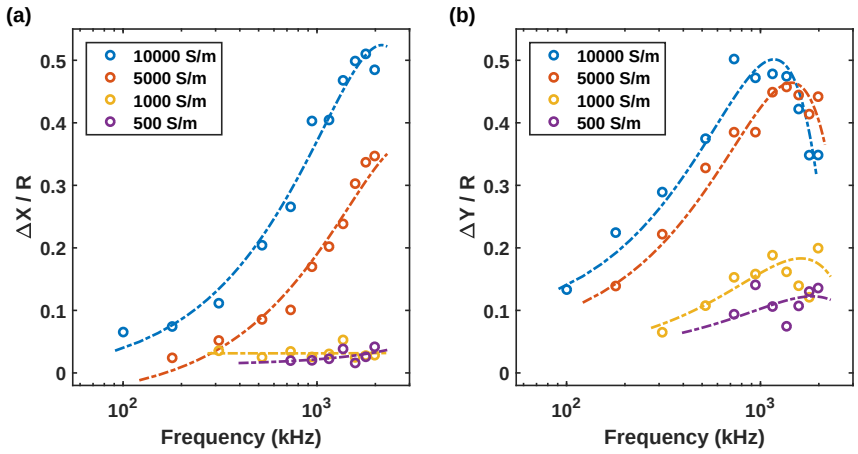

Figure 6.5: Characterisation of n-doped semiconductors via multi-frequency analysis: (a) Normalised in-phase response $(\Delta X/|S|)$ and **(b)** normalised quadrature response $(\Delta Y/|S|)$ for each sample as a function of frequency. Fits (dot-dashed lines) are quadratic polynomials. From Reference [8].

6.5 Through-barrier imaging

The detection and identification of hidden illicit or dangerous items in cargo and vehicles is paramount for the security industry. In this context, the ability to image through ferromagnetic and metallic shields is a crucial feature in security screening applications.

Currently deployed technologies are based on x-ray or gamma-ray radiography [159, 160, 161]. Other techniques include neutron-based systems, such as pulsed fast neutron analysis [162, 163]. However, these approaches have the inherent risk of delivering doses of radiation to both operators and potential stowaways.

EMI represents an alternative, non-radiating, active approach to imaging through metallic enclosures. Tomographic measurements can be constructed by varying the frequency of the applied field, thus varying the penetration depth into the sample. In this way an EMI device can be tuned to penetrate shields and detect objects concealed beneath them.

In this section the potential for EMI-AM based security screening is demonstrated. This is done by imaging samples concealed beneath shields of differing electromagnetic properties – including both ferromagnetic and non-magnetic materials. The results are reported in Reference [3].

The EMI-AM II imaging system was used for these experiments. The primary field is provided by a small ferrite-core coil centered 30 mm above the sensor. Low frequency operation is the key to increasing the penetration of AC magnetic fields through barriers. The choice of operation frequency is therefore based on the required penetration range. At 500 Hz, the skin depth (δ) enables penetration of thick conductive barriers. A bias magnetic field of around 1 mG is required to impose an RF-AM operation frequency around this value.

The shields and samples are positioned between the inductor and the vapour cell. Figure 6.6 displays the arrangements used. Initially, a sample concealed between two shields is considered (Figure 6.6(a)). In practice, the attenuation of the primary field due to the top shield can be compensated for by increasing the amplitude of the field. Instead, the detection of samples is limited by the shielding of the weaker secondary field from the RF-AM by the bottom shield. The arrangement in Figure 6.6(b) is therefore used to evaluate the performance of the system. Both shields affect the secondary field only and, therefore, the EMI performance. This configuration is tested with both a single shield and a combination of two shields. The shield materials are ferromagnetic steel and Al. The dimensions of the shields are such that they extend over the entire field of view – therefore any eddy current edge effects can be neglected. The choice of sample size and material is arbitrary. 2D images are constructed by sweeping the samples across the field of view using the x, y-stages – whereas the shields remain stationary.

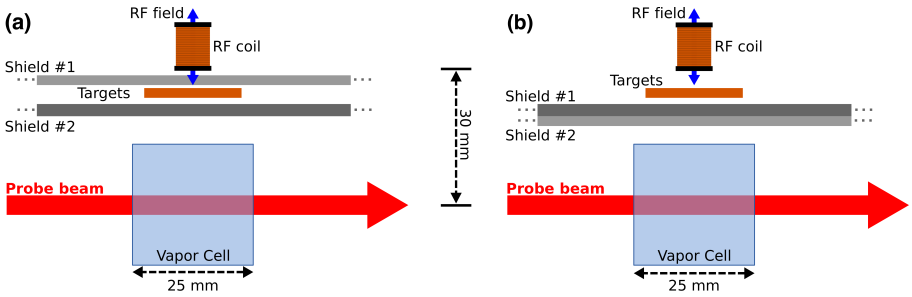

Figure 6.6: Through-barrier imaging measurement setup: Drawn to scale. **(a)** sample concealed between shields. **(b)** sample, and the weak secondary field contribution, shielded from sensor. From Reference [3].

Example EMI images of concealed samples are presented in Figures 6.7(a) – 6.7(c).

In this section, only images of the phase parameter of the oscillating field are used. As discussed previously, this is because a detected change in Φ can only be caused by eddy current generation in the sample behind the shield. The magnitude of the changes in Φ depend on the conductivity, geometry, and thickness of the concealed sample. In all images an increase in the phase lag is observed in the region of the sample. This is consistent with an increased imaginary component of the secondary magnetic field due to the excitation of eddy currents.

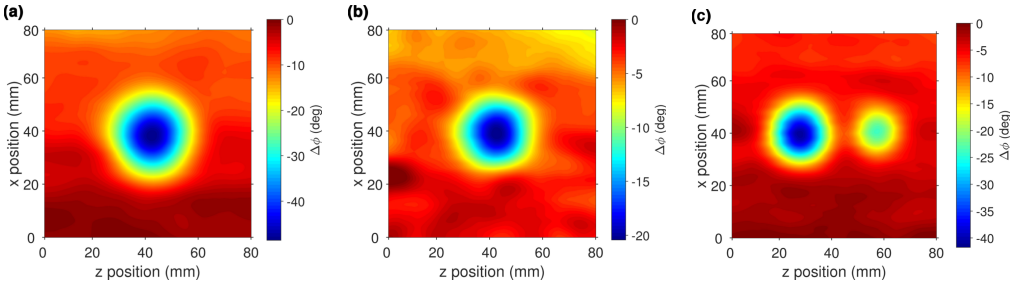

Figure 6.7: EMI phase images of concealed samples: **(a)** Cu disk (diameter 40 mm, thickness 2 mm) concealed between Al shields, thickness 1 mm and 2 mm ($\nu = 630$ Hz, $\delta_{\mathrm{Cu}} = 2.6$ mm, $\delta_{\mathrm{Al}} = 3.3$ mm). This corresponds to the arrangement of Figure 6.6(a). **(b)** Cu disk (diameter 30 mm, thickness 2 mm) concealed behind a 2.5 mm thick magnetic steel shield ($\nu = 470$ Hz, $\delta_{\mathrm{Cu}} = 3$ mm). This corresponds to the arrangement of Figure 6.6(b), with a single shield. **(c)** Cu disk (diameter 30 mm, thickness 2 mm) and Cu square (side-length 20 mm, thickness 2 mm) concealed behind a 2 mm thick Al shield ($\nu = 580$ Hz, $\delta_{\mathrm{Cu}} = 2.7$ mm, $\delta_{\mathrm{Al}} = 3.4$ mm). From Reference [3].

The ferromagnetic steel shield is 142 mm × 142 mm and 2.5 mm thick. The exact magnetic and dielectric properties of the steel are unknown. This mimics practical scenarios, where the magnetic history of shields/containers would not be known[1]. The DC magnetic field from the steel shield has a 38 mG component along the bias field and a total magnitude of over 102 mG. This would result in a change in the resonant frequency of over 47 kHz without the active control of the magnetic field vector (see Section 4.5.2). This would push the RF-AM far out of resonance, rendering detection and imaging impossible. The Al shield is 150 mm × 210 mm and 2 mm thick.

An applied AC primary field of just 1.0 μT is sufficient to drive the magnetometer through all the shields – in both configurations of Figure 6.6. The driving amplitude is further reduced to 0.2 μT when using the Al shield only. The primary field attenuation due to the steel shield is approximately 15 times greater than that of the Al shield. The decrease in skin depth is attributed to the non-unity magnetic permeability of the steel.

[1] Cutting, heating, and exposure to magnetic fields are among the effects that alter the magnetic properties of steels.

All the images in this section – and throughout this thesis – are single scans. This is in contrast to previous EMI/MIT works where the presence of a concealed sample was only revealed after background image subtraction. This can be done by simply subtracting a background ('empty box') image of the shield/enclosure [33]. However, this is infeasible for practical screening applications. An alternative approach is multi-frequency image subtraction [32]. This takes advantage of the skin effect. A low-frequency image penetrates the enclosure and acquires information about any objects within. A high-frequency image then records information only from the surface of the enclosure. Subtracting the two removes the enclosure's contribution, revealing the contents.

A single-acquisition approach is desirable in practical applications where prior knowledge of the shield/enclosure (or stable conditions for dual-frequency imaging) may not be available. Furthermore, it is particularly advantageous for time sensitive applications – when a high throughput is required.

6.5.1 Imaging through ferromagnetic and metallic shields

In this section a series of systematic measurements of different shields and concealed samples are presented. The results are shown in Figure 6.8. In all cases the concealed sample is clearly detected and resolved by the system. A maximum phase change of 19.3° is recorded in the most challenging measurement scenario – for the smallest sample (Cu disk, diameter 30 mm, thickness 2 mm) concealed behind the thick combination of shields. This compares to typical maximum phase fluctuations of 3.7° when no sample is present. The shape and size of each sample is also faithfully reproduced. This is explored in more detail in Section 6.7.3.

For each sample – i.e. a row of Figure 6.8 – the images are plotted against the same colour scale for comparison. This highlights the relative attenuation of the secondary MIT field by each shield material. On average, the maximum detected phase lag is 2.1 times smaller for the steel shield compared to the Al shield. In addition, the combination of shields sees a further 5% reduction above that of the steel alone.

6.5.2 Imaging through metallic enclosures

Finally, the detection of an object contained within a metallic enclosure is explored. The sample is imaged directly in a single acquisition. Example results are displayed in Figure 6.9.

The metallic enclosure is an Al box with all sides, top, and bottom of thickness 2 mm.

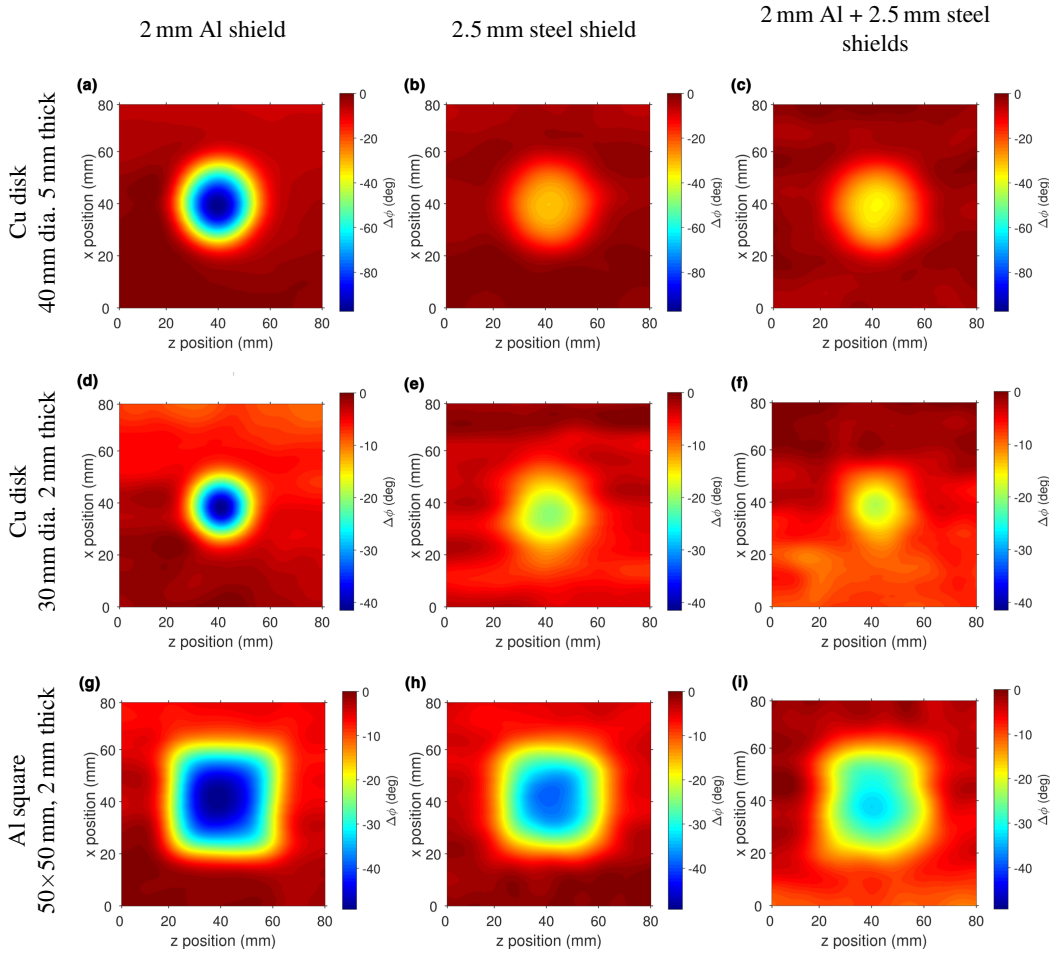

Figure 6.8: EMI phase imaging through various shields: First column, 2 mm Al shield. $\nu = 560\,\text{Hz}, \delta_{\text{Cu}} = 2.8\,\text{mm}, \delta_{\text{Al}} = 3.5\,\text{mm}$. Second column, 2.5 mm magnetic steel shield. $\nu = 470\,\text{Hz}, \delta_{\text{Cu}} = 3.0\,\text{mm}, \delta_{\text{Al}} = 3.8\,\text{mm}$. Third column, combination of the 2.5 mm steel shield and 2 mm Al shield. $\nu = 330\,\text{Hz}, \delta_{\text{Cu}} = 3.6\,\text{mm}, \delta_{\text{Al}} = 4.5\,\text{mm}$. Each row is plotted against the same colour scale to highlight the relative effect of each shield. From Reference [3].

The outer dimensions of the box are 105 mm × 105 mm × 29 mm. A 40 mm diameter and 5 mm thick Cu disk is concealed within.

The EMI-AM approach is able to reveal the sample without the need of any background image subtraction. The presence, location, and approximate size of the sample can be seen directly in the image in both examples – Figures 6.9(a) and 6.9(b). A typical background scan of the empty enclosure is included in Figure 6.9(c). The same colour scale is used for all three images to allow a direct comparison.

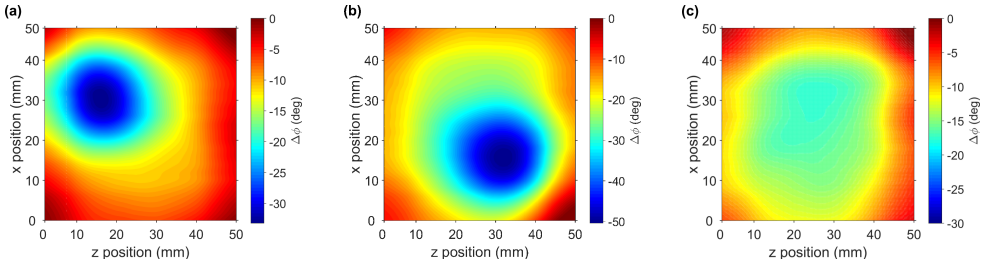

Figure 6.9: EMI phase images through a metallic enclosure: Al box enclosed on all sides with a wall thickness of 2 mm. $\nu = 430\,\text{Hz}, \delta_{\text{Cu}} = 3.15\,\text{mm}, \delta_{\text{Al}} = 3.95\,\text{mm}$ for all scans. **(a)** and **(b)** Cu disk (diameter 40 mm, thickness 5 mm) centered at (18,32) and (32,18), respectively. **(f)** EMI of an empty enclosure. All images on the same colour scale for comparison.

6.6 Non-destructive evaluation and ferromagnetic materials

Non-destructive evaluation (NDE) is a traditional application area for eddy current methods [114]. As such, these applications should lend themselves to EMI-AM. They include the detection of anomalies, material fatigue, and inspection of welding – critical throughout manufacturing and construction.

6.6.1 Material fatigue

The first demonstration of EMI-AM applied to NDE involved the detection of defects/fatigue in components. This is simulated by a sub-mm crack in a 2 mm thick Al ring – see Figure 6.10(a). The crack disrupts the flow of eddy currents in the local region. This results in a reduction in the secondary field and is detected as a local decrease in the signal.

The EMI-AM I system was used to investigate the EMI response of this sample. The results are presented in Figure 6.10(b) [1]. This displays an R map of a $20\,\text{mm} \times 20\,\text{mm}$ region centred on the crack. The primary field excitation frequency is 10 kHz. The presence of the defect is clearly revealed as a decrease in the R response. The image accurately reproduces the features of the sample.

The secondary field response does not drop to zero at the position of the crack. This is because the primary field coil (ferrite core, 7.8 mm diameter) is larger than the dimensions of the defect. The dipolar spread of the primary field has a FWHM of approximately 6 mm at the samples' position. The EMI response therefore probes a region significantly larger than the crack itself – lifting the response above zero. This effect is further increased as a consequence of the nearest-neighbour filtering.

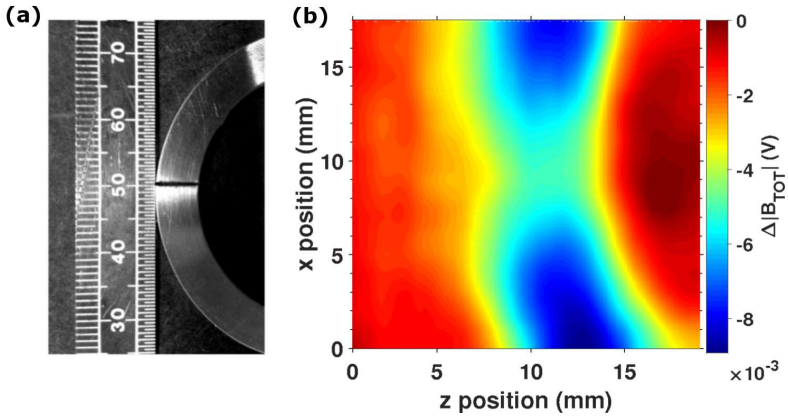

Figure 6.10: Non-destructive evaluation: (a) Photograph of the sample: 6 mm aluminium ring, 2 mm thick, the width of the crack is <1 mm. Adapted from Reference [1] **(b)** High-resolution EMI *R* image at 10 kHz.

6.6.2 Steel discrimination

The majority of NDE applications involve the investigation of steel structures. This section reports on work done with the EMI-AM I system into EMI of steels. The details of each sample are given in Table 6.3.

Material	Dimensions	σ (S m^{-1})
Stainless steel 304L	⌀38 mm, 6 mm thick	1.4×10^6 S m^{-1}
Alloy steel EN19T (AISI 4140)	25 mm × 25 mm, 1 mm thick	4.0×10^6 S m^{-1}
Alloy steel EN24T (AISI 4340)	25 mm × 25 mm, 1 mm thick	4.0×10^6 S m^{-1}
Stainless steel AISI 420	25 mm × 25 mm, 1 mm thick	1.8×10^6 S m^{-1}

Table 6.3: Details of steel samples: The material, dimensions, and conductivity (σ) of the steel samples investigated in this section.

The first sample is 304L. This is the most widely used grade of stainless steel. It is austenitic – rendering it effectively non-magnetic. As a consequence, the EMI-AM response is similar to other non-magnetic metallic materials (such as the Cu and Al samples of Figure 6.2). The secondary field response is dominated by conductive eddy currents, which oppose the primary field. An example Φ image of the sample is presented in Figure 6.11. The excitation frequency of 5 kHz is chosen such that the skin depth/thickness ration is approximately 1 ($\delta_{304L} = 5.6$ mm). As seen throughout this chapter, the EMI-AM technique reproduces the position, shape, and size of the object with high-fidelity.

The remaining samples are ferromagnetic. EN19T and EN24T are high-carbon steel

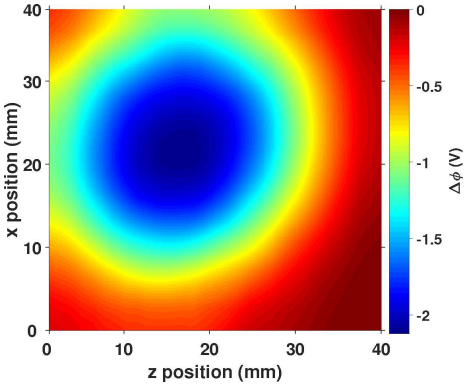

Figure 6.11: EMI-AM of non-magnetic steel: EMI Φ map of a 38 mm diameter, 6 mm steel disk at 5 kHz ($\delta_{304\mathrm{L}} = 5.6\,\mathrm{mm}$). Disk centred at $(18, 22)$.

alloys (equivalent codes are AISI 4140 and 4340, respectively). The 'T' indicates that they have been heat treated. Both steels have similar properties and are near-interchangeable in their uses. The final sample is AISI 420, another commonly used stainless steel.

All these samples have a relatively high permeability. This affects the measured signal in two ways. Firstly, the dominant contribution to the secondary field results from oscillating local magnetisation in the sample – not from the generation of eddy currents (for details, see Section 2.3.2). This magnetisation is aligned with the primary field, increasing its effect. This is depicted in Figure 2.7. Secondly, ferromagnetic samples have a macroscopic non-zero magnetic moment. This changes throughout the history of the sample. For example, during cutting and heat treatment. The result is unknown variations in of the magnetic moment across the material surface. This perturbs the DC magnetic field that imposes the magnetometer operating frequency – modifying the response of the sensor. Recall that these measurements are performed with the EMI-AM I system without any active magnetic field stabilisation to counteract these effects. However, due to the broad linewidth of the EMI-AM I system (around 3 kHz HWHM), the response generally remained within the resonance profile.

The EMI-AM images of these samples include a combination of these effects. As a result, the sample geometry and features are not recognisable in the recorded images. However, it is assumed that the charateristics of the sample are in some way imprinted into the measured response.

The EMI-AM response can be examined to distinguish between each sample. This is done via a similar multi-frequency approach that was later applied to low-conductivity semiconductors (in Section 6.4.3). An image of each sample was acquired in the same con-

ditions at six different frequencies – $\nu = \{100\,\text{Hz}, 500\,\text{Hz}, 1\,\text{kHz}, 2\,\text{kHz}, 3\,\text{kHz}, 4.5\,\text{kHz}\}$. All samples are of the same dimensions (squares of side 25 mm and 1 mm thick). This rules out any geometric effects.

The results are presented in Figure 6.12. Again, the normalised in-phase response ($\Delta X/R$, Figure 6.12(a)) and normalised quadrature response ($\Delta Y/R$, Figure 6.12(b)) are plotted against frequency. The EMI-AM response very clearly distinguishes the EN19T sample from the two other materials (EN24T and AISI 420). This is a surprising result as the properties of EN19T and EN24T are similar, with both materials having a conductivity of $4 \times 10^6\,\text{S}\,\text{m}^{-1}$. These results demonstrate the potential for EMI-AM in steel detection, identification, and in recycling.

In contrast, the system is unable to clearly discriminate between the EN24T and the AISI 420 stainless steel sample. The properties of these samples differ greatly, such that they can easily be distinguished by eye. This apparently odd behaviour could be explained by the unknown permittivities and permeabilities of the tested samples, and their specific history.

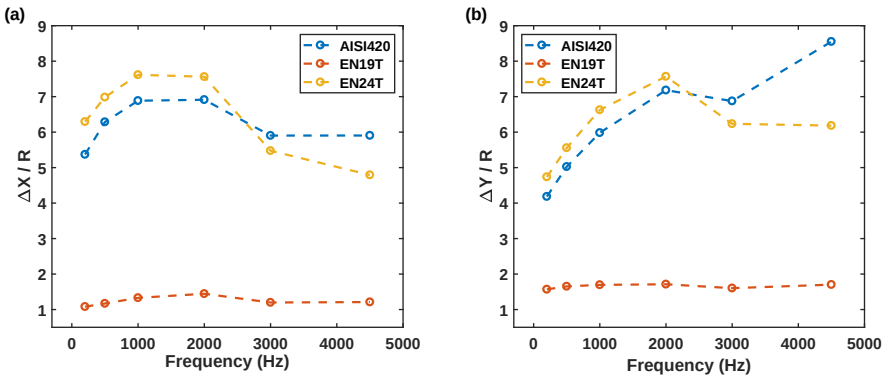

Figure 6.12: Steel discrimination via multi-frequency EMI-AM: (a) Normalised in-phase response ($\Delta X/R$) and **(b)** normalised quadrature response ($\Delta Y/R$) for each sample as a function of frequency.

6.6.3 Non-destructive inspection of steelwork

Work in EMI-AM based NDE was expanded on in collaboration with the the National Physical Laboratory (NPL)[2]. This work focuses on the particular application of corrosion under insulation (CUI). The results are briefly discussed in this section, further details can be found in Reference [7].

CUI is responsible for 60% of leaks in pipework, resulting in significant environmen-

[2]With Patrick Bevington, Dr Rafal Gartman, and Dr Witold Chalupczak.

tal and economic impacts. The presence of insulation both conceals corrosion and limits the applicability of testing methods, which often require direct access to the material surface. In contrast, EMI-AM allows non-invasive and non-contact investigations of material structures.

This was demonstrated by measuring changes in the thickness of industry-grade carbon steel via EMI with a caesium RF-AM [7, 62]. The magnetic contribution of the sample on the bias field was nullified in three ways. Firstly, by the active compensation of the magnetic field – using the approach detailed in Section 4.5.2 and Section 5.3.9. Additionally, the sample was positioned 30 cm from the vapour cell. Together, these reduced the samples' perturbation of the resonant frequency to below 850 Hz. Finally, each pixel of the images was acquired by sweeping the RF field to find position of the resonance – rather than operating at a single frequency. This removes the DC field effect of the sample completely.

The results demonstrated the detection of 24.5 mm diameter recesses in the centre of 150 mm $\times$ 150 mm and 6 mm thick samples. The EMI-AM technique was shown to resolve 0.1 mm changes in the recess depth. And to image the recess when concealed beneath a 0.5 mm thick Al sheet – mimicking conductive insulation. A Φ map of this case, recorded at 12.6 kHz, is included in Figure 6.13.

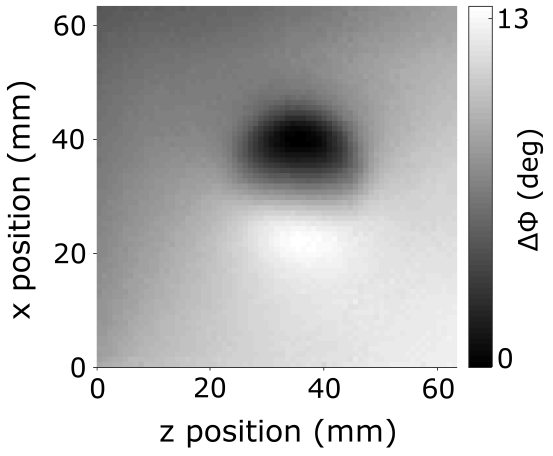

Figure 6.13: Corrosion under insulation: EMI Φ map of a 24.5 mm diameter, 3.6 mm deep recess in a 6 mm thick carbon steel plate at 12.6 kHz. The recess is concealed behind a 0.5 mm thick aluminium sheet mimicking a layer of conductive insulation. Adapted from Reference [7].

6.7 EMI-AM imaging performance

In this chapter, EMI with atomic magnetometers has been demonstrated across a wide range of sample conductivities with a number of applications explored. In all cases, the technique has been shown to faithfully reproduce the characteristics of the samples used with a spatial resolution around 1 mm. This section aims to quantify the imaging performance by examining the accuracy of the EMI-AM response via edge detection.

6.7.1 Edge detection

Edge detection encompasses a number of algorithms which are widely employed in image processing [164]. The aim is to detect sharp changes in brightness – i.e. discontinuities in the image. This breaks up images into segments allowing the detection and extraction of features. These techniques are used throughout computer and machine vision.

Edge detection techniques have previously been applied in the context of EMI. In particular, *Canny* edge detection in a coil-based planar array [32, 165]. This method – and other commonly used approaches – did not perform satisfactorily when applied to the EMI-AM images produced in this work. Instead, a bespoke edge detection algorithm was developed.

6.7.2 Edge detection algorithm

The aim of the algorithm is to extract the position (localisation) and estimate the size of samples from EMI-AM Φ maps. These can then be compared to the known values.

The first step is to sort the interpolated raw data into two distinct sets. These are referred to as the background set and the sample set. Recall that the phase lag increases in the presence of a sample. The background set is therefore constructed from the points with smallest detected phase lag ($\Delta\Phi$). This set grows until the standard deviation of the set, σ_{BG}, exceeds 2.9°. The standard deviation – rather than the measured phase change, $\Delta\Phi$ – is used as the threshold parameter as $\Delta\Phi$ varies greatly with changing sample material, size, and application. The threshold value, $\sigma_{\mathrm{BG}} = 2.9$, is fixed after repeated tests on the basis of the overall system performance. This value is approximately 4 times the standard deviation observed for a background image with no sample. The sample set consists of all the points that are not in the background.

The edge set is defined as the points in the image that form the boundaries between the two sets. The edge set is then sorted into distinct edge components. This is required for the automatic detection of multiple samples (Figure 6.14(c), for example) or the separation of the sample from any other regions where the threshold is exceeded.

Formally, for the edge set $E = \{e_i\}$ and edge components E_i

$$1) \quad E = \bigcup_i E_i \quad : \quad \forall E_i, E_j \subset E, \quad E_i \cap E_j = \emptyset \,, \tag{6.2}$$

$$2) \quad \forall e_i \in E_i, \quad \exists e_j \in E_i \quad : \quad ||e_i - e_j|| < \rho \,, \tag{6.3}$$

where ρ is a constant that depends on the scan size. Equation 6.2 simply states that the edge set is composed of any number of distinct components. Equation 6.3 states that each edge component consists of edge points that have a nearest-neighbour within the set less than a distance ρ apart.

Each edge component is then programmatically fitted with a circle or a square fit, with the parameters of the best performing fit recorded. This gives a position and estimated size for each detected component.

Figure 6.14 displays examples of EMI-AM phase maps overlaid with the edges detected by the algorithm. For these images, with a scan size of 80 mm, $\rho = 1.7$ mm.

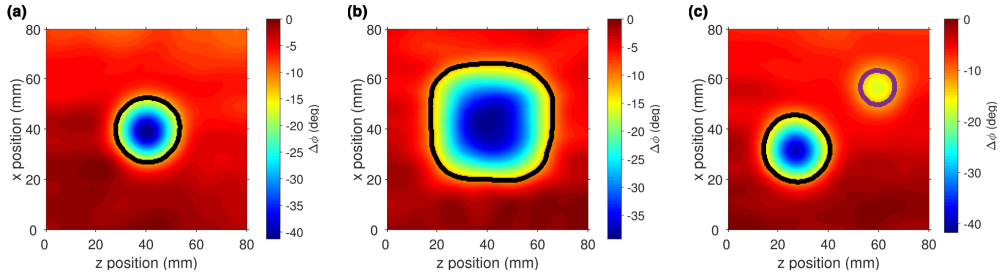

Figure 6.14: Edge detection examples: Shape, size, and position reconstruction via edge detection and EMI-AM. **(a)** and **(b)**, edge-detection algorithm applied to Figures 6.8(c) and 6.8(h), respectively. **(c)** Multiple sample detection. Cu disk (left, diameter 30 mm, thickness 2 mm) and Al square (right, side-length 20 mm, thickness 2 mm), concealed by 2 mm Al shield ($\nu = 580$ Hz, $\delta_{\mathrm{Cu}} = 2.7$ mm, $\delta_{\mathrm{Al}} = 3.4$ mm). From Reference [3].

6.7.3 Edge detection in through-barrier imaging

Here, the edge detection algorithm is used to evaluate the performance of EMI-AM for the detection of concealed samples. The algorithm is applied to each image displayed in Figure 6.8.

Figure 6.15(a) shows the extracted center positions. For each image the algorithm correctly identifies the position of the sample to be in the vicinity of the actual position (40,40). The average distance between the estimated position and actual position is 2.4 mm with the greatest deviation being 5.1 mm.

Figure 6.15(b) shows the estimated sample sizes. This is a diameter or a side-length,

depending on whether the best fitting shape was a circle or a square. The algorithm correctly identifies the size order of the samples for each shield. The estimated sample sizes are in good agreement with the actual sizes. The average deviation between the estimated and actual sizes is 3.3 mm with a largest difference of 6.0 mm. The results of Chapter 7 surpass this level of performance using machine learning techniques [5].

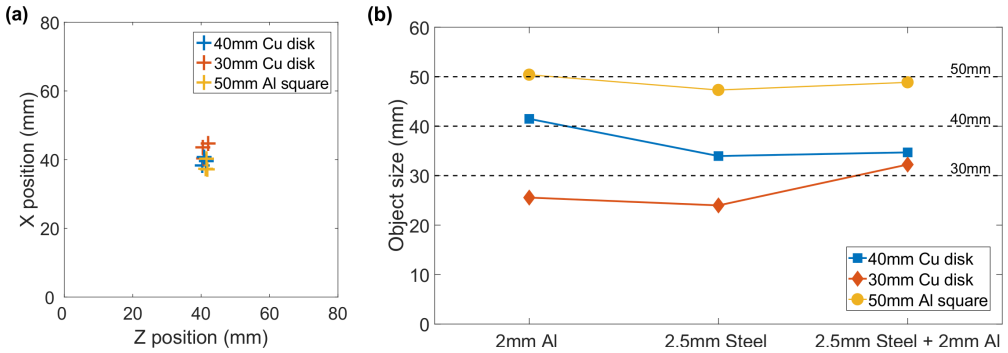

Figure 6.15: Sample properties via edge detection: Sample size and localisation via edge detection. Positions and sizes are accurately reproduced in all cases. **(a)** Extracted centre point of concealed samples imaged in Figure 6.8. $\sigma_z = 0.61\,\text{mm}$, $\sigma_x = 2.58\,\text{mm}$. **(b)** Estimated size (diameter/side-length) for the same images. Actual sizes included to guide the eye (dotted lines). From Reference [3].

6.8 Discussion

This chapter has demonstrated the technique of EMI-AM. The performance of the RF-AM sensor (Chapter 5) is exploited to perform high-resolution EMI of a wide range of samples and to explore a number of potential applications.

Sample conductivities span $500\,\text{S}\,\text{m}^{-1}$ to $1\times10^{7}\,\text{S}\,\text{m}^{-1}$, with operation frequencies across the Hz to MHz band. In the low-conductivity regime the measured sample volumes are orders of magnitude lower than coil-based MIT results. All images are acquired in a non-destructive, non-contact manner with no sample preparation, image processing, or background subtraction required. In all cases the images accurately reproduce the characteristics of the samples, with detection of sub-mm features validated.

Applications include the discrimination of materials via multi-frequency imaging. Non-ionising penetration of ferromagnetic and metallic barriers is also performed. This has obvious advantages in the security screening of cargo and vehicles. Finally, the imaging of ferromagnetic materials is successfully explored in the context of NDE of corrosion in structural steelwork and pipelines.

Chapter 7

Image reconstruction

In this chapter the first viable alternative to the solving the inverse problem is introduced and evaluated. This aims to maximise the amount of information that can be extracted from EMI images. The results were obtained in collaboration with Dr Lewis Griffin and Dr Matthew Caldwell of the Department of Computer Science, UCL (CS).

7.1 Overview of machine learning aided EMI

The benefits and applications of imaging the electromagnetic properties of materials have been discussed throughout this work. The preceding chapters have introduced and demonstrated the potential of EMI-AM for this problem. However, for more complex distributions of dielectric properties image reconstruction algorithms are required to infer the structures from the measurements.

The electromagnetic inverse problem is the conventional approach to image reconstruction in EMI/MIT. This is discussed in Section 2.6. The problem is ill-posed and computationally complex to solve numerically. The approach described here employs machine learning algorithms (ML) to circumvent the need of solving the inverse problem. Algorithms are trained using a set of images acquired by EMI-AM. The performance of these algorithms is then tested against a blind dataset for a number of different scenarios. This approach shifts the computational burden to the acquisition of training data and the optimisation of the algorithm's parameters. However, once performed, the evaluation of additional images can be performed (effectively) in real time.

For this work, the measurement approaches were planned in collaboration with CS. An iterative approach informed the choices of test scenarios and the quantity/structure of the training data (within the experimental limitations). The datasets where acquired with the EMI-AM systems and corresponding dedicated software. In total around 68,000 images

were taken. 31,584 image files are used for the results in this chapter. The ML algorithms were implemented and tested by CS using a combination of Wolfram Mathematica and Python 3.6.

ML techniques require a large number of training images. The time-limiting factor in the imaging process is the step size of the translational stage. The majority of images in Chapter 6 use a step size of 2 mm to accurately reproduce the EMI features of the scene. These images typically take around 15 minutes to acquire. For the ML datasets the imaging resolution was significantly decreased to reduce the acquisition time by an approximate factor 10. Examples of the resulting raw data are shown in Figure 7.1. The top images are R-maps and the bottom the corresponding Φ-maps of a $50\,\text{mm} \times 25\,\text{mm} \times 3\,\text{mm}$ Al rectangle. The centre-point of the rectangle is marked by a dot and the orientation of the longest side by a dotted line. The decrease in resolution results in a severe degradation in the image quality. The recognition of the sample's position, material, size, and orientation are no longer possible by eye. However, I show that the ML approach is able to maximise the information extracted from the images by performing all these tasks with a low error rate.

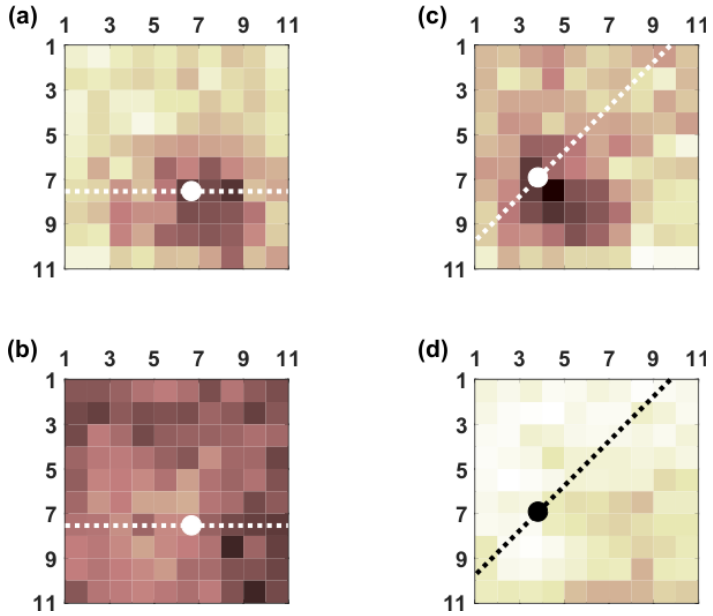

Figure 7.1: Example images from ML dataset: Low-resolution R (top row) and Φ (bottom row) EMI images of a $50\,\text{mm} \times 25\,\text{mm} \times 3\,\text{mm}$ Al rectangle. Dots mark the centre-point of the sample, dotted lines mark the orientation of the longest side.

The trade-off between number of training images, image resolution, and data acquisition time was explored in the early stages of the collaboration with CS. The data was

acquired using the EMI-AM II system. Long-term image acquisition ran continuously over several days. This took advantage of the signal stability provided by the active compensation system. RF-AM resonance traces from across the acquisition runs (Figure 7.2) demonstrate this robustness. The consistency of the operation was further increased by operating the RF-AM above its optimum sensitivity.

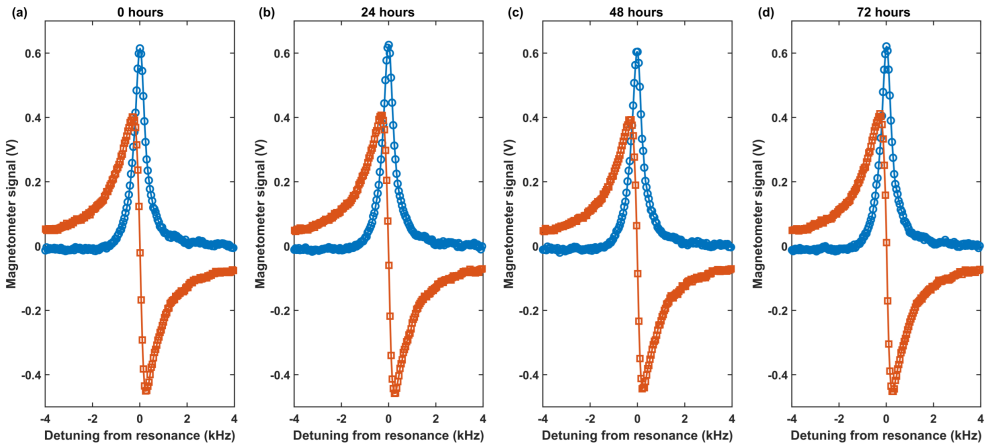

Figure 7.2: Long-term stability of the system: RF-AM resonance traces across several days of data acquisition. Adapted from Reference [5].

7.2 Images of single samples

This section considers a single sample positioned randomly within each image. The algorithms aim to infer the position (localisation) of the sample along with additional properties such as material, shape, and orientation. The results of this section are also reported in Reference [5].

7.2.1 Structure of the data

Each scan is of an 80 mm × 80 mm scene in the $\{x, z\}$-plane, producing images in four features $\{X, Y, R, \Phi\}$. The centre-position of the sample is varied randomly within a $[0, 30] \times [0.30]$ mm^2 region in the centre of the scene. The step resolution is typically 8 mm – resulting in each image being an 11×11 matrix. In some cases a higher 4 mm resolution is used, giving 22×22 matrices. The primary field was applied across the entire field of view using the 180 mm diameter calibration coils. This results in eddy current excitation across the entire sample, further reducing the resolution of local features. A fixed operation frequency of 200 kHz was used throughout.

The problems (tasks) for each image are divided into two classes: localisation – es-

timating the centre-position $\{x, z\}$ of the sample, and classification – identification of the sample's material, shape, or orientation.

Each image can be described as a 121-element vector $\mathbf{m}$ of measured values. Each image also has a underlying ground-truth. This is described by a vector $\mathbf{t}$ which details the true centre-position and classification. Typically, 1020 images were taken for each of the 12 classifications (4 materials, 4 shapes, 4 orientations). 160 blind images were also acquired for each task in a different measurement run. The ground-truths for the blind data were randomised and unknown during the ML analysis. All data used for these results is available online – see Reference [166].

7.2.2 Machine learning models

A general algorithm, $\mathbf{f}$, generates a prediction $\mathbf{p}$ for the ground-truth vector

$$\mathbf{p} = \mathbf{f}(\mathbf{m}) \ . \tag{7.1}$$

In this sense it is analogous to the inverse problem, returning an estimate of the distribution of complex conductivity from the measured values. The performance of a number of different algorithms is discussed in the following.

For each task, the algorithms are tested and tuned by cross-validation. This involves randomly splitting the training data into training and testing subsets. The algorithm's parameters are tuned by optimising over the random splits. This approach reduces the influence of any potential erroneous data in the training set.

The optimised algorithms are then applied to the blind datasets. Again, the tests are repeated on random splits of the blind data to compute standard deviations as a measure of consistency.

For the localisation tasks the positions of the sample are effectively continuous across the region. Position estimation is formulated as a linear regression model of the form

$$\mathbf{p} = \mathbf{W}\mathbf{m} \ , \tag{7.2}$$

where $\mathbf{W}$ is a weights matrix. $\mathbf{W}$ is determined from training data by minimising the difference between the predicted positions and the ground-truth positions. Preliminary results showed linear regression to be the best performing approach for localisation. This is attributed to the underpinning linear nature of the problem. It is important to note that the

algorithms were not restricted to choosing positions within the $[0,30] \times [0.30]$ mm^2 region.

Classification tasks require a model that chooses between discrete classes. Standard approaches – such as k-nearest neighbours (kNN), logistic regression (LR), support vector machines (SVM), and random forests (RF) – where tested. All these algorithms attempt to find boundaries within the sets of images that separate the different classifications. Details of these techniques can be found in Reference [167], among others.

7.2.3 Evaluation

A measurement detailing the performance of each model is required. Such evaluations are used during the tuning phase to optimise the model parameters. They are also used to compare the performance of different algorithms and different datasets. Finally, they are used to validate the approach when testing against blind data.

The models are evaluated against the baseline and ceiling levels. The baseline level is the level achieved when always performing the best random guess. The ceiling level is the best that can be achieved given the limitations of the data (data variability).

The localisation tasks are evaluated using the root-mean-squared-error (RMSE) – the expectation value of the squared difference between the predictions and the ground-truths. This difference is represented by the distance

$$d_i = \sqrt{(x_{p,i} - x_{t,i})^2 + (z_{p,i} - z_{t,i})^2} \,, \tag{7.3}$$

where the subscripts p and t represent the predicted and ground-truth positions, respectively.

The RMSE then becomes

$$\text{RMSE} = \sum_i^N \frac{d_i}{\sqrt{N}} \,. \tag{7.4}$$

For the localisation tasks, the baseline level is 12.4 mm. The ceiling performance is half of the step size that defines the spatial resolution – 4 mm in most cases.

For classification tasks the success rate, S, is used to evaluate the performance of the algorithms. It is defined as

$$S = \sum_i^N \frac{s_i}{N} \,, \qquad \text{where} \qquad s_i = \begin{cases} 1 & \text{for} \quad p_i = t_i \,, \\ 0 & \text{for} \quad p_i \neq t_i \,. \end{cases} \tag{7.5}$$

The analogous error rate, ε, is also used. It is expressed as a percentage by

$$\varepsilon = 100\,(1 - S)\ . \tag{7.6}$$

The baseline performance for classification tasks is an error rate of 75%. The ceiling performance is 0%.

7.2.4 Feature set and algorithm selection

The optimum feature set is the best performing combination of parameters from $\{X, Y, R, \Phi\}$. This set was identified by evaluating the performance of different combinations on the training data. Figure 7.3 shows the results of localisation and classification for the materials dataset using different combinations of features. The materials dataset is discussed in more detail below.

The results for the localisation task are presented in Figure 7.3(a). For all combinations the algorithms performed significantly better than the baseline level. In many cases the ceiling performance was also exceeded. The R and X parameters perform best for the localisation tasks. Results cannot be improved by adding further features. This performance is explained by the origins of this pair of features. Changes in R and X are dominated (or exclusively) due to perturbations in the real part of the primary field. This is in turn dominated by the attenuation of the primary field due to the skin effect – shielding the sensor from the primary field. Changes in R and X are therefore largest at the sample's location, hence their performance in localisation tasks.

Changes in Y and Φ arise from eddy current generation in the sample. The size of these changes are related to the conductivity of the material and the volume of eddy current excitation. As the primary field extends over the entire scene, this volume is proportional to the surface area and the skin depth. The Y and Φ parameters are therefore naturally more suited to the classification tasks rather than localisation. This is borne out in Figure 7.3(b). Here, combining one parameter from $\{X, R\}$ with one from $\{Y, \Phi\}$ yields a significant improvement. One parameter from each of these pairs is required for optimum performance. The feature set $\{R, \Phi\}$ was therefore chosen. Note that the addition of a third/fourth parameter does not give any further improvement, whilst increasing the amount of data and processing required.

The best performing ML algorithms for each task are found by comparing their perfor-

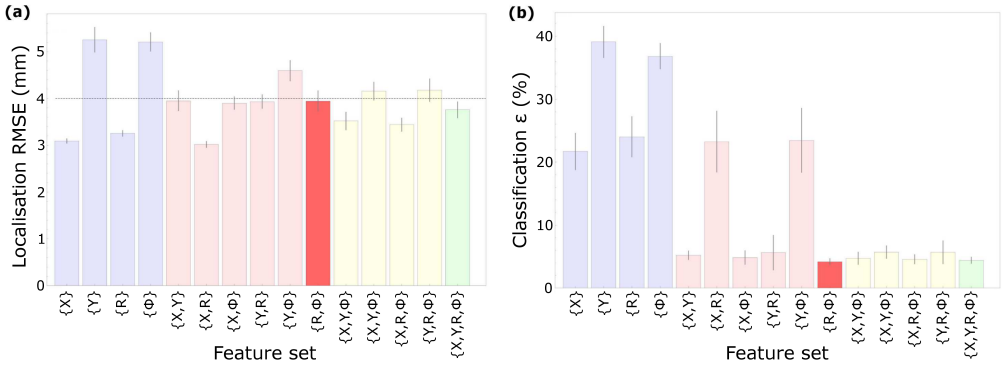

Figure 7.3: ML feature set selection: Different combinations of features from the materials dataset and their performance in **(a)** localisation and **(b)** classification. For localisation the random choice level is 12.4 mm and the ceiling performance (half the spatial resolution of the images) is 4 mm. For classification the random choice level is 75%, and the ceiling performance is 0%. Adapted from Reference [5].

mance for the same training set. Linear regression was clearly the best performing approach to the localisation task. This is attributed to the underpinning linearity of the problem. For the classification task the best performance was given by SVM with a radial basis function (RBF) kernel. The RBF kernel allows non-linear boundaries to separate each class. This is done by expressing the boundaries as a weighted sum of Gaussian functions centred on each data point [168].

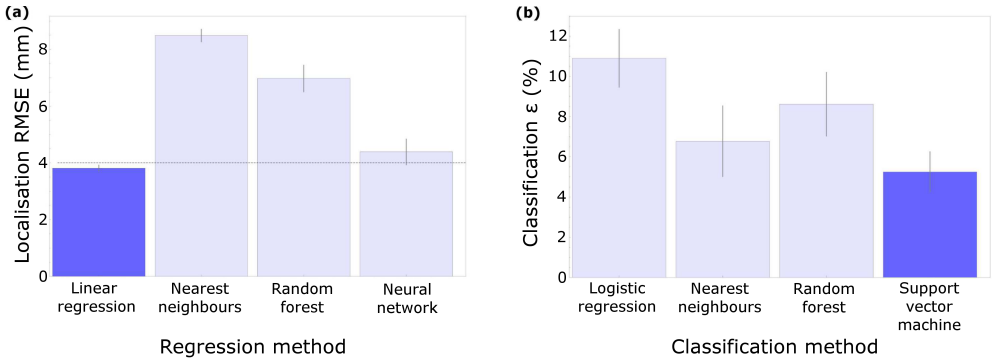

Figure 7.4: ML algorithm selection: Comparison of algorithm performance for **(a)** localisation and **(b)** classification with the materials dataset. Linear regression was chosen for the localisation tasks and SVM-RBF for the classification tasks. Adapted from Reference [5].

7.2.5 Material classification and localisation

The materials dataset comprised of four 50 mm × 50 mm squares of different materials. Details of each sample are given in Table 7.1.

The material classification error as a function of the training set size (N) is presented

Material	$\sigma\ (\mathrm{S\,m^{-1}})$	$\delta(200\,\mathrm{kHz})$ (mm)	Thickness: $\delta(200\,\mathrm{kHz})$
Al	3.77×10^7	0.183	11.0
Cu	5.98×10^7	0.146	13.7
Ti/Al/V	5.95×10^5	1.63	0.6
Graphite	7.3×10^4	3.61	1.4

Table 7.1: Details of materials: Conductivity (σ), skin depth at 200 kHz, and thickness to skin depth ratio for each sample in the materials dataset.

in Figure 7.5[1]. The material classification performs excellently across all values of N. With an error rate of 12% for just 8 images, decreasing monotonically to 2% for the full training dataset.

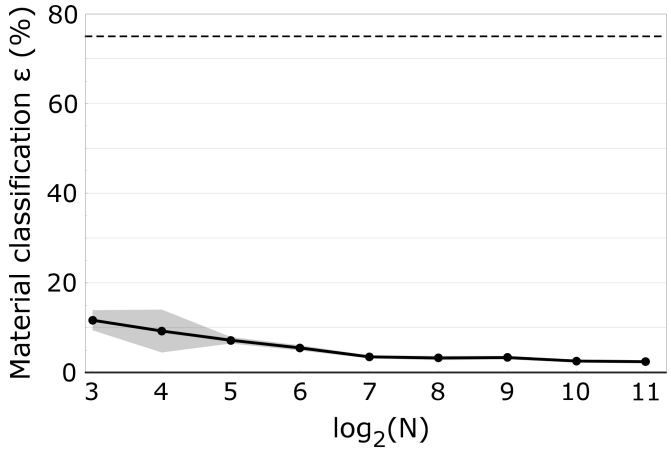

Figure 7.5: Classification error for the material dataset: Dashed line marks the baseline performance. Error rate significantly outperforms chance for all values of N. Adapted from Reference [5].

The performance of ML-aided EMI for material identification is not surprising as the secondary field response contains all the information regarding the sample's properties (via Equation 2.56). The difference in the responses is highlighted in the R-Φ scatter plot of Figure 7.6. Each data point represents the mean R and Φ value for a given scan, colour coded by material. The points for each material are clearly grouped into defined regions. The algorithm is therefore able to separate each material class – even with relatively few training images.

Successful material classification is further confirmed by the confusion matrix (Ta-

[1]For all graphs of this type the shaded region marks the 95% confidence intervals.

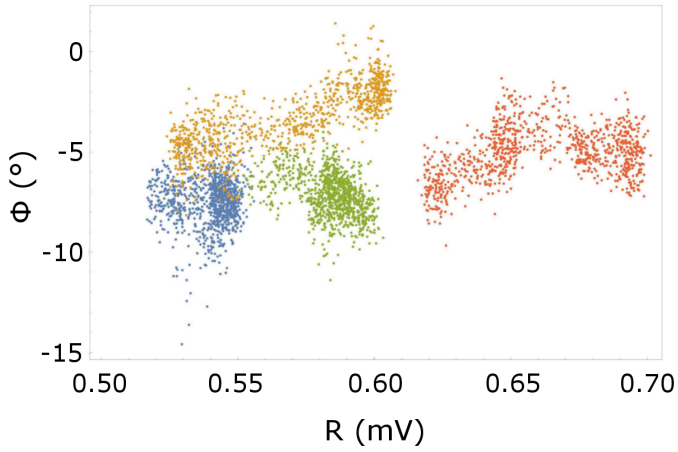

Figure 7.6: Scatter plot of the material dataset: Mean values of R and Φ for each scan. Colour coded by material: Al (blue), Cu (orange), Ti/Al/V (red), and Graphite (green). Adapted from Reference [5].

ble 7.2). A confusion matrix gives a simple visualisation of an algorithm's performance, allowing one to spot whether the algorithm is regularly confusing two classes. Correct classifications are found on the diagonals. The off-diagonals are the levels of confusion between each pair of classes. This is simply the error rate when distinguishing between the pair. Classification is correct in >94% of cases. The highest level of confusion – of around 5% – occurs symmetrically between Al and Cu. These materials have the most similar properties and, therefore, similar responses. This is further emphasised by the closer overlapping of the blue (Al) and orange (Cu) regions in Figure 7.6.

	Al	Cu	Ti/Al/V	Graphite
Al	95.0%	4.9%	0.0%	0.1%
Cu	4.8%	94.5%	0.0%	0.7%
Ti/Al/V	0.0%	0.0%	99.9%	0.1%
Graphite	1.9%	1.2%	0.0%	96.9%

Table 7.2: Confusion matrix for material classification: Rows are the ML predictions, columns are the ground-truths – i.e. diagonals are correct classifications ($> 94\%$), with off-diagonals incorrect classifications ($< 5\%$).

The corresponding results for the localisation task are shown in Figure 7.7. The algorithm performs better than the baseline level for all values of N. As the training set increases the RMSE decreases, crossing below the ceiling performance beyond $N = 64$. The ML algorithms are able to locate the position of the sample well beyond the 8 mm step size of

the images. The RMSE error reaches a final value of 3.1 mm with a confidence interval of [3.0 mm, 3.2 mm]. This error level is 2.6 times smaller than the physical spatial resolution of the system (imposed by the step size).

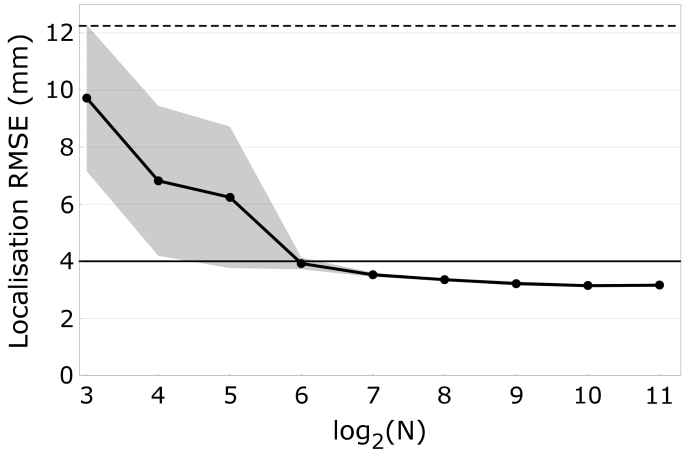

Figure 7.7: Localisation error for the material dataset: Dashed line marks the baseline performance, solid line marks the ceiling performance. Localisation RMSE outperforms chance for all values of N. The minimum achieved error is 2.6 times better than the spatial resolution of the system. Adapted from Reference [5].

7.2.6 Shape classification and localisation

For the shape classification the samples used were of the same material (Al) and thickness (3 mm). The shapes were: a 50 mm square, a 50 mm diameter disk, a 50 mm $\times$ 25 mm rectangle, and a isosceles triangle – base 50 mm, height 50 mm.

The results of the shape classification are shown in Figure 7.8. Again, the classification already outperforms chance with $N = 8$. The error rate decreases with increasing training data to just 3% with a confidence interval [2%. 4%]. When tested against the blind data, the error was 22%, with the confidence interval [9%, 35%]. The larger variations within the blind data are attributed to the small sample size. However, these values remain significantly below the baseline. This proves that ML-aided EMI is robust against fluctuations in the input data. This represents a significant advantage over the inverse problem, where this is not the case.

Again, a confusion matrix for the shape classification highlights the performance (Table 7.3). There were virtually no incorrect classifications for the square and the disk ($< 0.5\%$). In contrast, there is around 6.5% symmetrical confusion between the rectangle and the triangle. This is due to the equal volumes of eddy current excitation in these two cases – both have surface areas of 1250 mm^2.

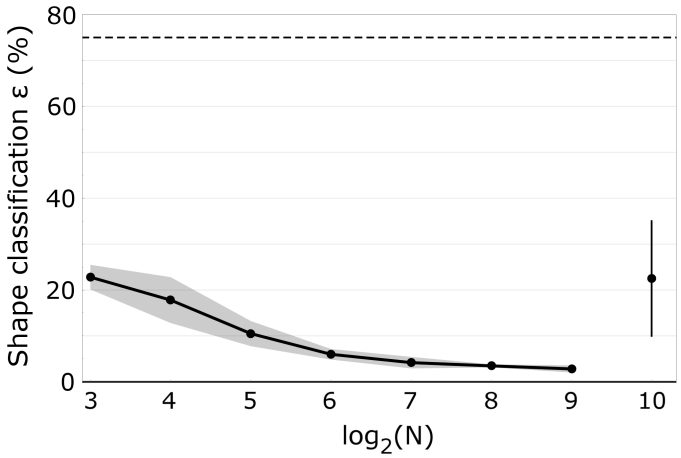

Figure 7.8: Classification error for the shape dataset: Dashed line marks the baseline performance. Error rate significantly outperforms chance for all values of N. Cross-validated algorithm applied to the blind data (isolated symbol) also significantly outperforms chance. Adapted from Reference [5].

	Square	Disk	Rectangle	Triangle
Square	99.5%	0.5%	0.0%	0.0%
Disk	0.2%	99.8%	0.0%	0.0%
Rectangle	0.0%	0.2%	93.6%	6.2%
Triangle	0.0%	0.0%	6.7%	93.3%

Table 7.3: Confusion matrix for shape classification: Rows are the ML predictions, columns are the ground-truths – i.e. diagonals are correct classifications ($> 93\%$), with off-diagonals incorrect classifications ($< 7\%$).

The localisation RMSE error for the shape dataset is presented in Figure 7.9. The results are consistent with the material dataset. The error is below the baseline for all values of N. For higher values the localisation error is below the spatial resolution set by the step size – 4.8 mm with a confidence interval [4.6 mm, 5.2 mm]. This is also the case for the blind data (4.5 mm, [3.6 mm, 5.4 mm]).

7.2.7 Orientation classification and localisation

The final classification task is orientation. This is inherently more challenging as the same sample is present in every image. Two Al rectangles, $50\,\text{mm} \times 25\,\text{mm} \times 3\,\text{mm}$ (sample A) and $40\,\text{mm} \times 20\,\text{mm} \times 3\,\text{mm}$ (sample B) were tested. In addition to the randomised central position, the samples are aligned with their longest edge along one of four orientations. These are $\{0°, 45°, 90°, 135°\}$ with respect to the z direction – the quantisation axis imposed

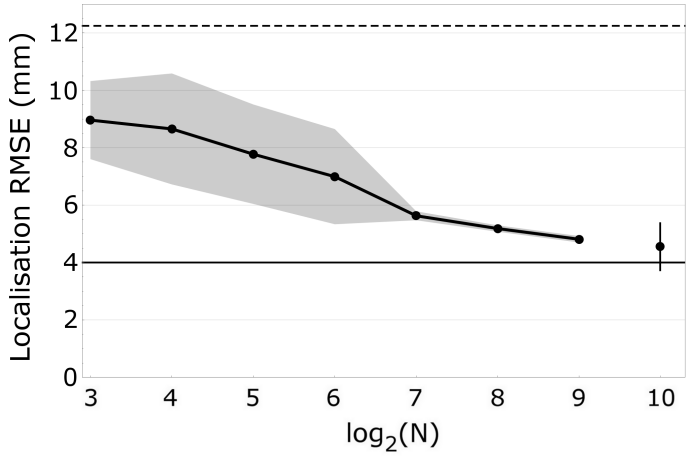

Figure 7.9: Localisation error for the shape dataset: Dashed line marks the baseline performance, solid line marks the ceiling performance. Localisation RMSE outperforms chance for all values of N, approaching the ceiling performance for larger training sets. Blind data (isolated symbol) has a localisation RMSE below the resolution of the system. Adapted from Reference [5].

by the bias magnetic field. Step sizes of 8 mm where used for both samples, with additional dataset of step size 4 mm tested for sample B.

The orientation classification error for each of these cases is plotted in Figure 7.10; sample A – green squares, sample B (4 mm resolution) – orange circles, sample B (8 mm resolution) – blue triangles. Again, the algorithm performs better than the baseline level in all cases. A monotonic reduction in the error rate is observed with increasing N.

Sample A reaches a minimum error rate of just 4% for the full $N = 512$ training sample. For sample B a weaker performance is recorded. This is due to the smaller size of the sample (surface area 1.56 times smaller) reducing the volume of eddy current generation, and therefore the EMI response. The results are still significantly below the random chance level, 35% for the 8 mm step size. Increasing the resolution increases the performance to around 25%.

The performance of the blind test data followed the same pattern. For sample A the blind classification error was 20% with a confidence interval [8%, 32%]. The larger variation in the blind data is again attributed to the small number of blind images.

These results can be compared to the level achievable by a human observer by considering Figure 7.1. These plots display example raw imaging data from the orientation dataset for the best performing sample A.

The localisation results for the orientation dataset are plotted in Figure 7.11. The recorded RMSE error levels are consistent with the previous cases – below the baseline

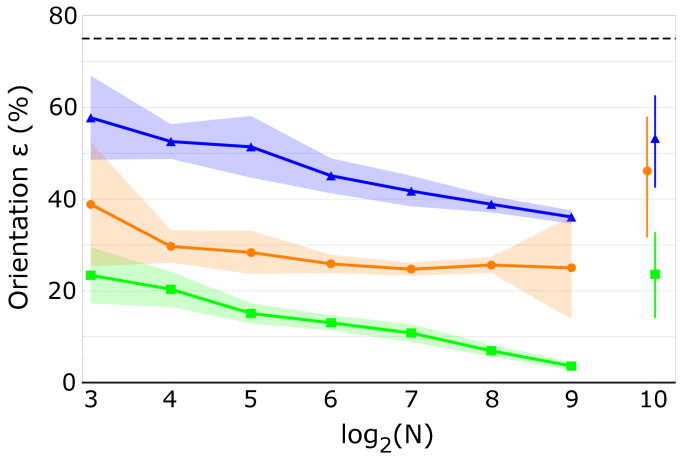

Figure 7.10: Classification error for the orientation dataset: Dashed line marks the baseline performance. Sample A (8 mm resolution) – green squares, sample B (4 mm resolution) – orange circles, sample B (8 mm resolution) – blue triangles. Error rate significantly outperforms chance for all values of N. Cross-validated algorithm applied to the blind data (isolated symbols) also significantly outperforms chance. Adapted from Reference [5].

for all values of N and below the physical spatial resolution at higher values. The same performance is recorded for the three blind data sets. The localisation results are unchanged even for the cases where the classification is challenged – sample B, 8 mm steps (blue triangles).

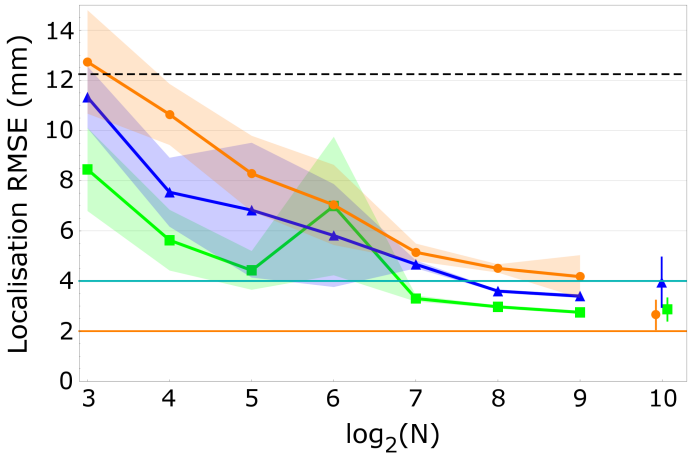

Figure 7.11: Localisation error for the orientation dataset: Dashed line marks the baseline performance, solid, cyan line marks the ceiling performance an 8 mm step size, solid, orange line marks the ceiling performance a 4 mm step size. Localisation RMSE outperforms chance for all values of N, approaching the ceiling performance for larger training sets. Blind data (isolated symbols) have localisation RMSEs below the resolution of the system. Adapted from Reference [5].

7.3 Images of multiple samples

The natural extension of the single sample work is to explore more complex and cluttered scenes. For this, a single sample class (small Al squares) is used with the number and position of the squares varied. Following the approach above, inverse models aim to reconstruct how many samples were present and their locations. Forward models are also investigated. These aim to predict the EMI-AM image for a given arrangement.

All the graphs in this section are adapted from those produced by Dr Matthew Caldwell (CS).

7.3.1 Structure of the data

Each sample is a 14.5 mm × 14.5 mm Al square of thickness 3 mm. Up to 25 such samples are distributed randomly across a 5×5 imaging grid (scene). The total scene area is 80 mm × 80 mm. 101 scans were acquired, broken down into the following measurements: 6 empty scenes (i.e. the background), 25 basis images (with a single sample at one grid position), 1 full scene (with all 25 samples), and 3 scenes each for between 2 and 24 randomly positioned samples (total 69). As before, each scan produces four simultaneously acquired parameter images (X, Y, R, Φ).

The effect of the primary field size is also explored by taking two sets of this data – one with a 7.8 mm excitation coil (small coil) and the other with a 50 mm excitation coil (medium coil)[2]. This will allow the exploration of the degree of potential interactions between samples in the scene. Such interactions could include the (additional) generation of eddy currents in a sample in response to the secondary field of another sample.

A translational stage step size of 10 mm was used. The images are therefore recorded as 8×8 matrices. Each image is again represented as a 64-element vector, $\mathbf{m}$, of measured values. Each scene is set of discrete statistics describing the presence or absence of a sample at a given grid position. These can therefore be represented by a vector $\mathbf{s} \in \{0,1\}^{5\times5}$.

Following the results of the previous section, the analysis focusses on the R and Φ data. The mean values of these parameters for each image are plotted as a function of object count in Figures 7.12(a) (R channel) and 7.12(b) (Φ channel). The small coil results (red) and medium coil results (blue) are plotted separately. For the small coil the R data displays a strong relationship with the object count. In contrast, the medium coil R data has a less clear response. There is no clear distribution of the Φ data across the images. This suggests

[2]Investigations with the large Helmholtz RF coils (180 mm) were not successful.

these changes are either the result of random fluctuations or the information is captured by a more complex relationship that requires a larger number of training images evaluate. For this reason the Φ data is excluded from the following discussions. Note that the previous similarity in the responses of the pairs $\{X, R\}$ and $\{Y, \Phi\}$ remains present throughout this dataset.

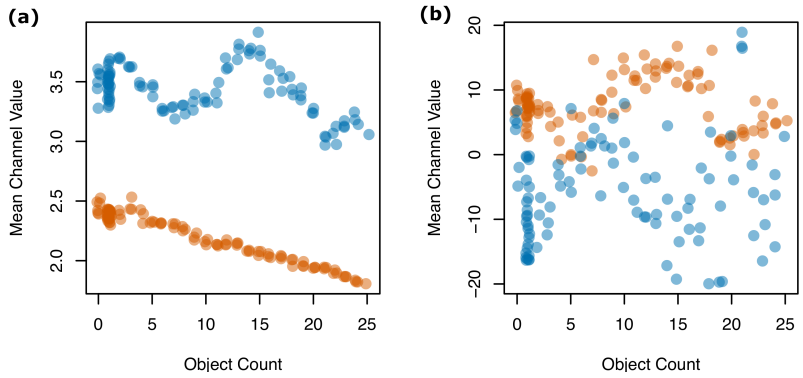

Figure 7.12: Relationship between imaging parameters and object count: **(a)** Mean per-image R data as a function of the number of samples for the small coil (red) and medium coil (blue). **(b)** Mean per-image Φ data as a function of the number of samples for the small coil (red) and medium coil (blue).

7.3.2 Forward Models

A forward model attempts to simulate the EMI-AM process. A model that accurately captures the EMI-AM process would allow additional synthetic (computer-generated) EMI images to be produced. This would be highly beneficial in view of the large experimental cost of obtaining real data. Synthetic data could be used to supplement the training data and increase the performance inverse models for scene reconstruction.

A general forward model $\mathbf{f}$ maps a given scene $\mathbf{s}$ to a prediction $\hat{\mathbf{m}}$ (of the real measurement $\mathbf{m}$)

$$\hat{\mathbf{m}} = \mathbf{f}(\mathbf{s}) \, . \tag{7.7}$$

Two ML forward models are tested – random forest and ridge regression. Terms are also included to allow the models to explore interactions between samples in each scene. Three types of interactions are considered:

- Full – pairwise interactions between every sample present in the scene,
- Local – pairwise interactions included between nearest-neighbour samples in each of the four cardinal directions,

- None – no interactions.

Symmetry is also explored in the modelling. Exploiting symmetries and rotations is a common technique in optical (or ray-like) image processing. As equivalent images are recorded under symmetry transformations, they can be used to significantly expand the size of the training dataset without additional costs. However, it is unclear that such equivalency will be present in the more complex diffusive regime of EMI. For the square EMI-AM images generated here the D_4 dihedral symmetry group is applied to test this. This group consists of the 4 rotational and the 4 reflectional symmetries of a square. Being able to exploit this would be advantageous as it would expand the training data by a factor 8. Note that, in general no relationship is imposed between the measured images and the scenes. When D_4 augmentation is applied one must impose that the centre of the images is aligned with the centre of the scene.

The model parameters are trained on repeated random splits of the data into training (75%) and testing (25%) subsets. The performance of each model is evaluated by computing the difference between the predicted and real images across the test dataset. For each prediction this is defined as the Euclidean distance (or L^2-norm) between the vectors $\hat{\mathbf{m}}$ and $\mathbf{m}$

$$||\hat{\mathbf{m}} - \mathbf{m}||_2 = \left(\sum_i (\hat{m}_i - m_i)^2 \right)^{1/2} \tag{7.8}$$

Forward model performance is compared against the L^2 error of a baseline ('null') model. This model ignores the scene entirely and always predicts the per-pixel mean image – averaged across all the measurements.

The comparative performance of a number of forward models is displayed in Figure 7.13. These results are for the R dataset with the small excitation coil. This is the only configuration for which the models reliably outperformed the baseline. All combinations of different degrees of interaction and with and without D_4 augmentation were tested. In general, the models performed better without symmetry (although the performance with symmetry was still better than the baseline and was beneficial for smaller training samples). Random forest records marginally better results than ridge regression. The interaction parameters do not improve performance, increasing the error for ridge regression with full interaction. This is perhaps not surprising as the small excitation coil only generates eddy currents in local regions – not across the entire scene.

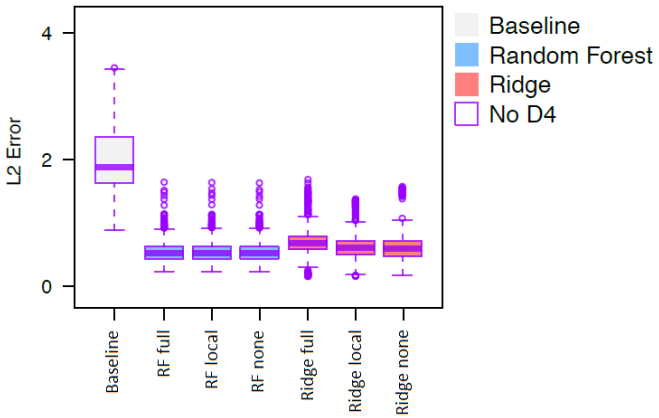

Figure 7.13: Comparison of forward models: R channel data with the small coil compared to the baseline. For each model the distribution of L^2 errors for 30 repetitions of the training/testing split is presented.

An example of the forward model prediction in comparison to the real measured data is presented in Figure 7.14. Figure 7.14(a) is the distribution of sample objects across the scene. Figure 7.14(c) is the forward model generated prediction of the EMI image. This compares well with Figure 7.14(b) – the EMI-AM recorded R image of the scene.

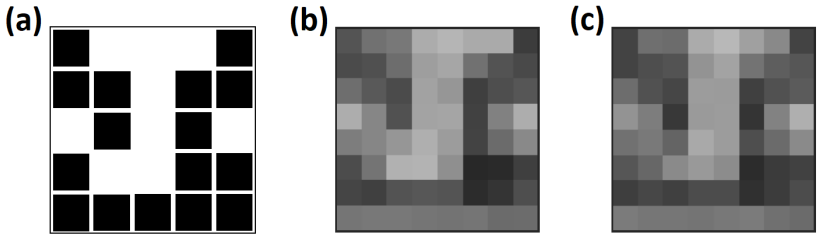

Figure 7.14: Example forward model image generation: **(a)** Scene arrangement. **(b)** Real measured EMI-AM R image of the scene. **(c)** Predicted EMI image via ML forward model.

7.3.3 Inverse Models

An inverse model attempts to recover the scene from a given EMI-AM image. A general inverse model $\mathbf{f}$ generates a prediction $\hat{\mathbf{s}}$ of the true scene $\mathbf{s}$ from the measured data $\mathbf{m}$

$$\hat{\mathbf{s}} = \mathbf{f}(\mathbf{m}) \, . \tag{7.9}$$

A simplified approach to the inverse modelling is to estimate the number of samples in the scene, disregarding their arrangement. Ridge regression was the best performing model in this case. The actual sample counts against the predicted counts are plotted in Figure 7.15. The results (solid lines) are strongly aligned with the ideal values (dashed line of $y = x$).

Together with the similarity in the errors (Training RMS = 1.58, Testing RMS = 1.55), these highlight the suitability of the model to this task. The same approach does perform satisfactorily on the medium coil dataset – with training RMS = 4.15 and testing RMS = 4.90.

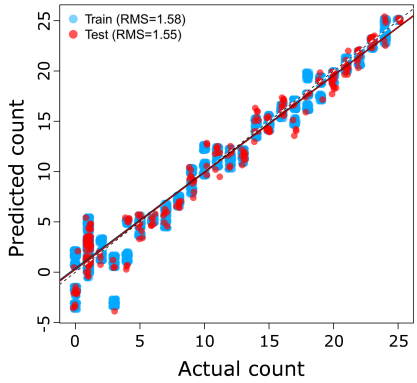

Figure 7.15: Inverse model of sample count: Predicted sample count against actual count for each image in the small coil *R* dataset. Blue line is the fit for the training data, red line the fit for the test data (they are essentially indistinguishable). These compare well with the ideal result – dashed line $y = x$.

The full scene reconstruction is a classifier problem with 25 binary outputs. These predict whether a sample was (1) or was not (0) present at each position in the scene. In practice, the inverse models instead return a probability score for each position. A simple probability threshold of 0.5 is then used to generate the binary values[3].

A range of classification models were tested along with the full possible combinations of feature sets. As expected from the preceding results, the *R* channel alone was the best performing feature. This contrasts with the classifier models of the previous section (see Section 7.2.4), where the addition of complimentary features is required for optimum classification. Among the ML algorithms, random forest had the best performance. The inverse model results for this best-performing configuration (random forest on *R* data) are presented in Figure 7.16.

The size of the training set is an important parameter to consider. This is due to the high experimental cost of acquiring extra data. Firstly, this is done by varying the fraction of data available for training between 0.1 and 0.9. A consistent improvement is recorded for both coil sizes until the training fraction reaches about 0.6. Beyond this there is limited advantage in using additional measurements. Note that the confidence intervals tend to grow for larger

[3]This threshold can be adjusted for real world applications where there is a trade-off in cost between false positives and false negatives.

training set sizes. This is simply a natural consequence of the greater statistical variability in the small number of left-over test images. It does not imply that the performance is worse for larger training sets.

Secondly, D_4 augmentation is included for Figure 7.16. Recall that this approach expands the available training data by a factor of 8. It gives a notable improvement in performance across the range – although it becomes less advantageous at higher training set sizes. Inclusion of D_4 transformations gives a significantly smaller improvement than would be gained by using eight times more real training data. This is not surprising as more information is gained from a new real measurement than from a simple translation of an existing image.

The overall performance is evaluated with the per-location error rate (Figure 7.16(a)) and the per-scene error rate (Figure 7.16(b)). For the small coil, with sufficient training data, the model correctly identifies the presence of individual sample positions with success rates exceeding 98%. This leads to successful full scene reconstruction – correctly identify the number and position of every sample – in around 70% of cases. For the medium coil, the per-location success rate only reaches 75%. As a result the model is not successful in reconstructing the full scene – the error rate is above 90% in all cases.

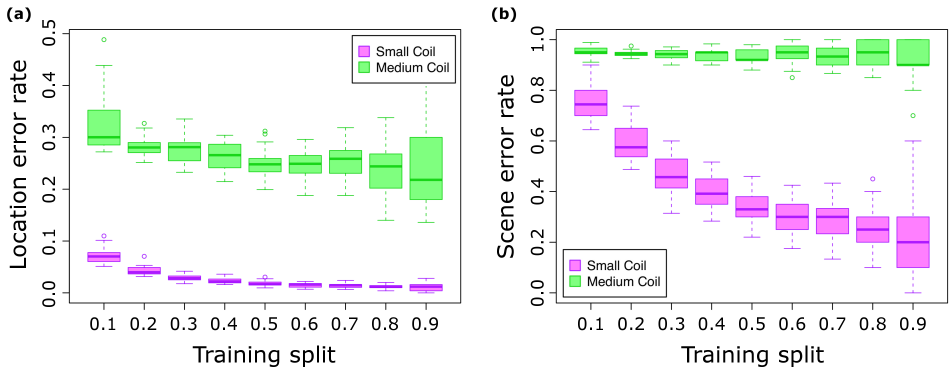

Figure 7.16: Inverse model of multiple samples: **(a)** per-location and **(b)** per-scene error rates for the best performing inverse model (random forest with D_4 augmentation on the R dataset). For the small coil scene reconstruction is successful in around 70% of cases. Reconstruction is not successful with the medium coil.

7.3.4 Forward-inverse models

Throughout this chapter the availability of training data has been limited by the cost (i.e. time) required to acquire large numbers of EMI-AM images. However, this only applies to input data for inverse modelling. The inputs for the forward model are simply the binary scene vectors **s**. There are 33.5 million possible scenes, with only 101 explored experi-

mentally. Additional scenes can be generated synthetically and, coupled with a sufficiently accurate forward model, be used to generate additional EMI training images to increase the inverse model performance. This is the idea of the forward-inverse model. Only the small coil R data is tested. This is because the forward model for the medium coil and other features was not able to accurately simulate the EMI-AM process, and would therefore provide no benefit.

The key result is the comparison in performance between the forward-inverse model and the inverse model using only real raw data. This is presented in Figure 7.17. The inverse model alone is in magenta and the forward-inverse model in green.

The inverse model for both cases is random forest with D_4 augmentation, as before. The random forest forward model is trained on the real raw data. This model is then to generate 2000 additional EMI images. In this case, D_4 symmetry was only beneficial for smaller training sets ($< 20\%$). To optimise performance, D_4 augmentation was applied below this threshold but not above it. The threshold is marked by the dashed lines in Figure 7.17.

The results show that the forward-inverse model outperforms the raw-trained model in all cases. The per-location success rate now exceeds 99%. This translates into successful full scene reconstruction in 90% of cases.

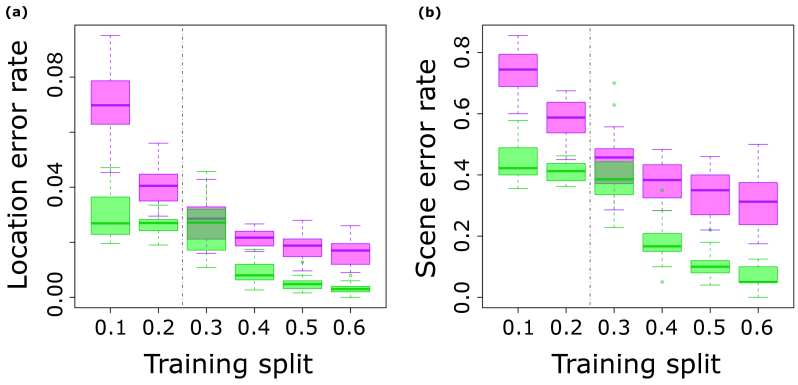

Figure 7.17: Forward-inverse model of multiple samples: Comparison of the synthetically trained forward-inverse model (green) and the raw data trained inverse model (magenta). The addition of synthetic forward-trained data improves the full scene reconstruction success to 90%.

7.4 Discussion

This chapter has demonstrated that ML algorithms can be used to maximise the amount of information extracted from EMI-AM images. This proves the applicability of ML techniques to complex, diffusive physical systems. This first investigation highlights the poten-

tial advantages that ML could achieve in research of other diffusive regimes.

For images restricted to a single sample, this approach is able to extract the position, material, shape, and orientation from low-resolution images. Localisation up to 2.6 times better than the physical spatial resolution and sample classification successes above 95% were recorded. ML aided EMI-AM therefore represents the first viable alternative to solving the inverse problem.

The technique was then extended to more complex scenes with multiple samples present. For the *R* dataset, ML models were shown to accurately simulate the EMI-AM response (forward model) and reconstruct the original scene from a measured image (inverse model). The most important result – when considering future applications – is the improvement when using synthetic forward model generated data. Creating large training datasets from a forward model trained on limited experimental data is a significant benefit (due to the high experimental cost of acquiring images). This forward-inverse approach warrants further investigation.

Chapter 8

EMI-AM for biomedical imaging

In this chapter one potential biomedical application is explored – the *in vivo* mapping of anomalous conductivity in the heart. This arises from the need of a dedicated diagnostic tool for atrial fibrillation (AF) – introduced in Section 1.2.1 [18]. Permanent changes in the heart's conductivity are speculated as a possible cause of AF. Such an area is referred to as an *arrhythmogenic locus*. Finite element method simulations (performed with *COMSOL multiphysics*) are used to assess the feasibility of applying a future medical imaging system – based on EMI-AM – to detecting these regions. The results detailed in this chapter are presented in Reference [10].

8.1 Simulations: EMI of anomalous conductivity in the heart

A schematic of the model built in the simulation package is shown in Figure 8.1. A primary field excitation coil is positioned above a virtual phantom consisting of the different tissue layers that surround the heart. The thicknesses of each layer was set in line with average values and the electromagnetic properties of each layer were calculated following the methods described in the literature [18, 122, 169]. The parameters for the various simulations are detailed in Table 8.1. An additional anomalous region at the surface of the heart is inserted. This region's conductivity is varied independently and represents a potential *arrhythmogenic locus*.

For each simulation the voltage and frequency applied to the RF coil is fixed. The simulation then records the resultant magnetic field by numerically solving the forward eddy current problem across the finite element mesh. The reported values of the magnetic field are taken from a plane 6 mm above the surface of the skin. This position represents a viable location of an RF-AM vapour cell performing EMI-AM.

The EMI response of biological samples was discussed in Section 2.5.2. We have

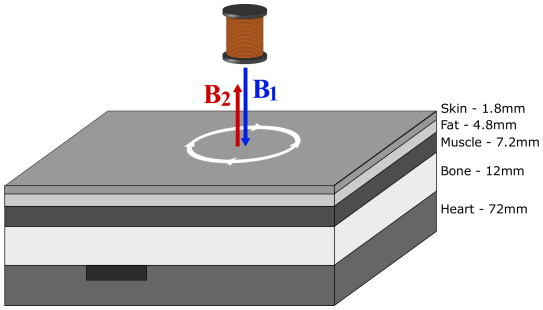

Figure 8.1: Model used in finite element simulations: Model of the heart and its surrounding tissues (not to scale). Electromagnetic properties and thicknesses are set to their expected values. A conductivity anomaly mimicking the source of cardiac fibrillation (*arrhythmogenic locus*) is positioned at the surface of the heart (in black). Adapted from Reference [10].

		1 MHz		10 MHz		50 MHz		100 MHz	
Tissue	Thickness (mm)	σ ($\mathrm{S\,m^{-1}}$)	ε_r	σ ($\mathrm{S\,m^{-1}}$)	ε_r	σ ($\mathrm{S\,m^{-1}}$)	ε_r	σ ($\mathrm{S\,m^{-1}}$)	ε_r
Skin	1.80	0.304	991	4.53	362	9.30	107	11.3	72.9
Fat	4.80	0.026	50.8	0.031	29.6	0.038	14.5	0.040	12.7
Muscle	7.20	0.585	1640	0.705	146	0.763	71.3	0.791	62.9
Bone	12.0	0.024	145	0.043	36.8	0.057	17.7	0.064	15.3
Heart	72.0	0.571	400	0.875	59.7	1.14	24.0	1.28	18.5

Table 8.1: Details of tissue properties: The thickness of each layer of tissue, along with their calculated conductivities and relative permittivities at each operating frequency. The relative permeability (μ_r) of each tissue is 1.

seen that the secondary field response is dominated by the imaginary contribution and that this component is dependent on both the conductivity and the excitation frequency (scaling as $\omega\sigma$). For low conductivity samples, one expects to find that increasing the operation frequency increases both the secondary field response and the response to changes in conductivity.

The simulated change in magnetic field as a function of both the operation frequency and the conductivity of the heart layer is plotted in Figure 8.2. At each frequency, the conductivity of the heart layer is systematically modified, with the resulting magnetic field change at the sensing level computed. The same scale is used to allow direct comparison of the magnetic field response across the explored frequencies. The secondary field response is

shown to increase with frequency across the range 1 MHz – 100 MHz. Within this, the magnetic field change increases with an increase in conductivity and decreases with a decrease in conductivity. This behaviour is consistent with Equation 2.56. A decrease in response at high frequencies (due to the skin effect) is not recorded as the skin depth is large in the biomedical regime.

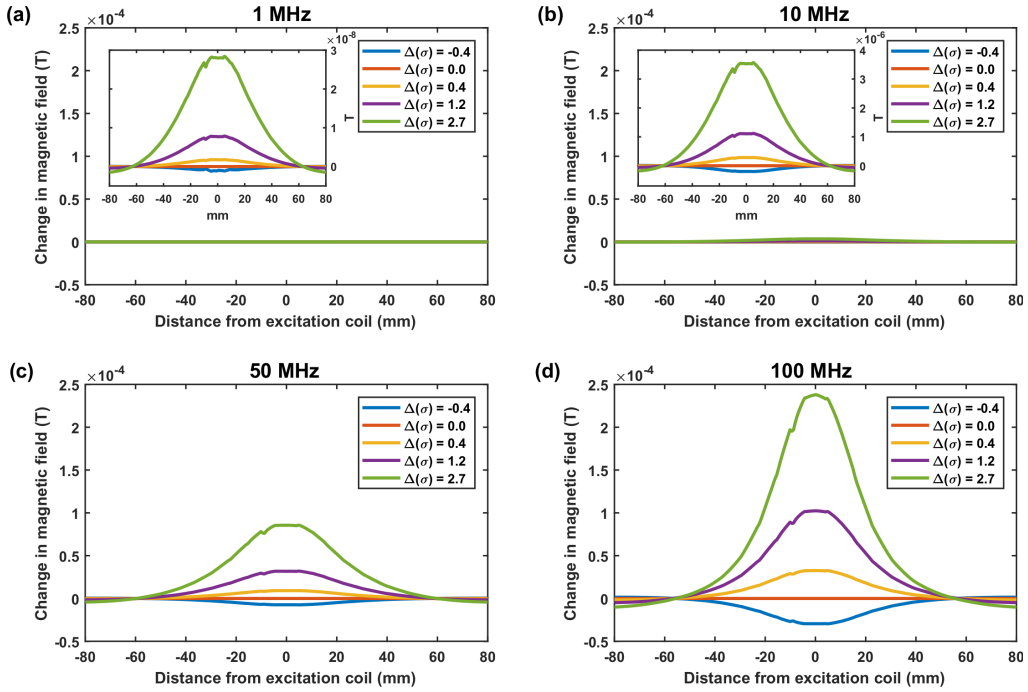

Figure 8.2: Response to changing conductivity in the heart: Primary field excitation frequency; **(a)** = 1 MHz, **(b)** = 10 MHz, **(c)** = 50 MHz, **(d)** = 100 MHz. At each frequency the conductivity of the heart layer is changed by a value $\Delta(\sigma)$ from the expected value (see Table 8.1), with all other properties held constant. Main plots show the resulting change in the magnetic field against the same scale. For clarity, the insets display an expanded view of the field change. Adapted from Reference [10].

The potential detection of conductivity anomalies is simulated by independently varying the conductivity of a small region on the heart's surface. This region is of size 10 mm × 10 mm × 5 mm and is centred at (10 mm, 10 mm) with respect to the excitation coil. In view of the previous results, the operation frequency was fixed at 100 MHz.

In Figure 8.3(a), the magnetic field change is computed along a line above the anomaly and 6 mm above the surface of the skin. The conductivity is varied in multiples of $\sigma_0 = 0.875\,\mathrm{S\,m^{-1}}$ (the conductivity of the surrounding heart tissue at 100 MHz). A peak in the response is recorded above the anomaly in the regime $\sigma \geq 10\sigma_0$. The size of the response is again proportional to the change in conductivity.

Figure 8.3(b) displays the magnetic field change across the sensing plane for $\sigma = 20\sigma_0$.

The increased response above the anomalous region has a peak value of 22 nT at position (17, 19), with respect the the excitation coil. This feature is the result of the increased local contribution of eddy currents resulting from the increased conductivity. A general feature – a symmetric ring around the coil – is also observed. This feature is attributed to the flow of eddy currents from the anomalous region around the excitation coil due to the shape of the magnetic field. The decrease in the centre of the ring is the result of the conservation of the total magnetic flux. It is common to all the simulations.

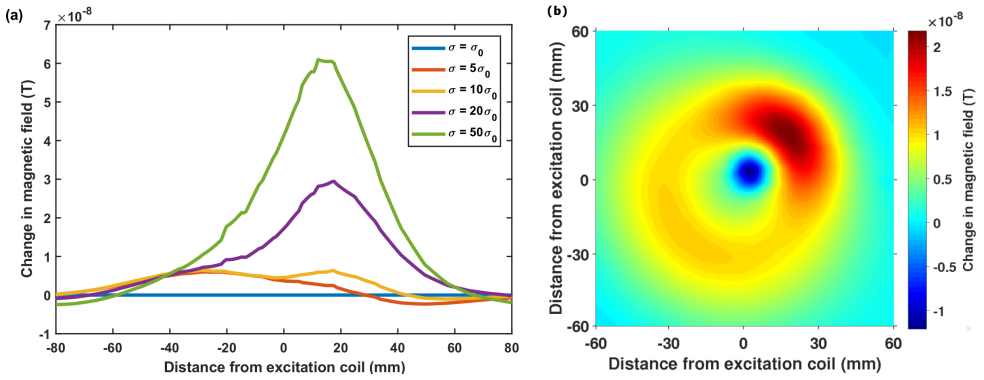

Figure 8.3: Response to anomalous conductivity in the heart: Magnetic field change 6 mm above the skin. 10 mm×10 mm×5 mm conductivity anomaly centred at (10 mm, 10 mm), primary field excitation 100 MHz. **(a)** Magnetic field change as the conductivity of the anomaly is varied ($\sigma_0 = 0.875\,\mathrm{S\,m^{-1}}$). **(b)** 2D image of the field change above the surface for an anomaly conductivity of $\sigma = 20\sigma_0$. Adapted from Reference [10].

8.2 Discussion

The simulations reported here detail the feasibility of *in vivo* detection and imaging of conductivity changes in biological samples with EMI-AM. Combined with the results of the previous chapters (the tunability and sensitivity of the RF-AM – Chapter 5, and the range of low-conductivity samples imaged – Chapter 6), they represent a significant step towards the realisation of a novel imaging and diagnostic tool. As a result of the progress made in this thesis, the first proof-of-principle demonstrations of biomedical imaging with EMI-AM systems now appears achievable in the short-term.

Chapter 9

Further projects

As a result of the work performed for this thesis, the scope of potential applications and techniques with AMs has increased. In this chapter the results of other projects, related to the EMI-AM framework, are briefly discussed. The results from this chapter are reported in Reference [2] and Reference [4].

9.1 Active underwater detection with an AM array

Existing underwater detection techniques are often ineffective [170], acoustic methods – for example – are increasingly ineffectual at shallow depths [171]. In this section, I present the detection of underwater objects using an 2×2 array of RF-AMs. The active detection, localisation, and real-time tracking of conductive, non-metallic samples is demonstrated. Only an overview of the results is provided here, further details and results can be found in Reference [4].

The optical setup is detailed in Figure 4.7, with the measurement setup shown in Figure 9.1. Four RF-AM sensors are arranged at the corners of a square with side length 105 mm. The sensors are simultaneously driven by a single square RF coil (side 230 mm, 15 turns) positioned 45 mm above the sensing plane. Each sensor operates simultaneously, with a sensitivity of $3\,\mathrm{nT}/\sqrt{\mathrm{Hz}}$. The presence of the sample is detected as perturbations to the primary magnetic field as a result of eddy current induction. This technique is intrinsically active. The response from conductive samples is unavoidable, rendering conventional countermeasures – such as demagnetisation – ineffective. The secondary field perturbations are imprinted onto the atomic precession and read out as changes in the amplitude ($\Delta|B_{\mathrm{tot}}| = R_{\mathrm{sample}} - R_{\mathrm{background}}$) of each sensor in the array. The array outputs are recorded and analysed in real-time via LabVIEW. The software includes detection thresholds for each position in the grid – this demonstrates the live detection and localisation of samples

(see Video 1 [172]). Finally, note that in the measurement setup – Figure 9.1(b) – the entire system is positioned on one side of the sample. This is important in many practical applications, where access to both sides may be precluded.

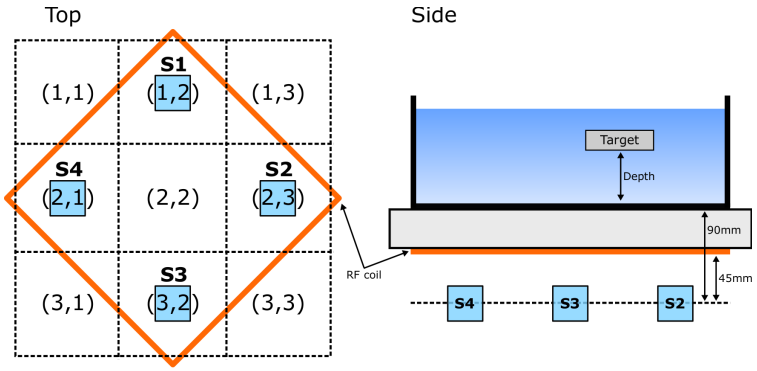

Figure 9.1: Setup for active underwater detection: **(a)** The sensing and coordinate grid using for localisation. Each square of the grid is 77.5 mm × 77.5 mm. All the sensors are operated simultaneously with a single large RF coil. **(b)** Measurement setup for the active detection of underwater samples. Adapted from Reference [4].

Figure 9.2 displays the $\Delta|B_{\text{tot}}|$ response of each sensor for five of the grid positions. At the four vertices of the grid none of the sensors recorded a noticeable change ($\Delta|B_{\text{tot}}| \approx 0$). This is because those positions lie mostly outside of the excitation field and, as such, no eddy current response is generated. These positions are excluded from the results. In Figure 9.2, the sample was a 105 mm × 110 mm × 10 mm Al plate positioned 90 mm above the sensing plane. An increase in $\Delta|B_{\text{tot}}|$ is recorded when the sample is in the proximity of a given sensor. In addition, a decrease is detected for all the sensors when the sample is positioned near the centre of the grid. Together the responses allow the unambiguous detection and localisation across five grid positions.

This is further emphasised by Figure 9.3. Here, the response of the array is plotted for each of the five grid positions. The software computes and displays these values in real-time. Automatic alarm triggering alerts the user to the presence and position of a sample – Video 1 [172]. The differing responses of each sensor is due to their independent optimisation.

The array recorded a 100% correct automatic detection and localisation rate for the Al plate. For a smaller Al sample (44 mm × 50 mm × 13 mm) an approximate ×5 decrease in the response was recorded. This is a result of the 5.25 times ratio between the surface areas of the two samples and the 20 kHz operating frequency[1]. For this sample the correct

[1]The skin depth at these operating conditions is $\delta_{\text{Al}} = 0.58$ mm – significantly smaller than the thickness

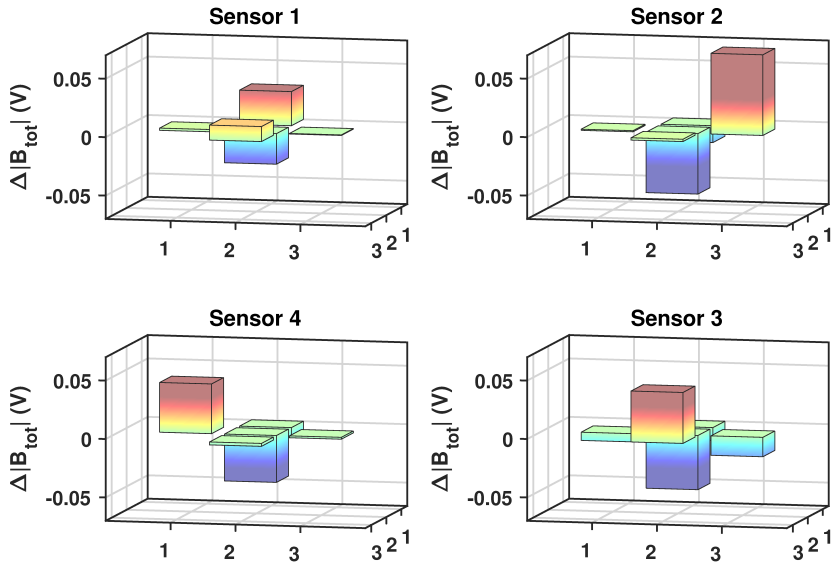

Figure 9.2: Response of each sensor to different sample positions: $\Delta|B_{\text{tot}}|$ recorded by each sensor due to an Al plate (105 mm × 110 mm × 10 mm) moved across the coordinate grid, 90 mm above the sensing plane. The four vertices of the grid are excluded. $\Delta|B_{\text{tot}}|$ is simultaneously, independently recorded by each sensor at each position. Differing levels of response are due to the independent optimisation of each sensor. Operation frequency 20 kHz. Adapted from Reference [4].

automatic detection and localisation rate was 95.2% (across 21 repetitions).

For underwater detection a saline solution test bed was used to reproduce the average electrical characteristics of sea water. An NaCl solution with a salinity of 22.1 matches the electromagnetic properties of salt water[2]. At 20 kHz the skin depth in sea water is approximately 1.9 m. Potential penetration of several km can theoretically be achieved at lower frequencies. Automatic detection and localisation was performed for a number of samples, at various depths. For the large Al plate the overall success rate was 91% across 22 test measurements.

The success rate is strongly dependent on the distance from the sensing plane. The range of underwater detection for a thin Al plate (105 mm × 73 mm × 3 mm) positioned above S2 is shown in Figure 9.4. The overall success rate is 91%. However, this is split between 95% at depths shallower than 50 mm to 70% at 65 mm. This decrease in performance is due to a reduction in the measured response as the depth increases. Although salt water attenuates both the primary and secondary fields, such decays are not significant across the distances evaluated here. Instead, the major limitation is the geometry and the spread of

of the samples. The surface area is therefore the relevant parameter in comparing the size of the eddy current response.

[2] $\sigma = 3.3\,\text{S m}^{-1}, \varepsilon_r = 80, \mu_r = 1$ [173, 174].

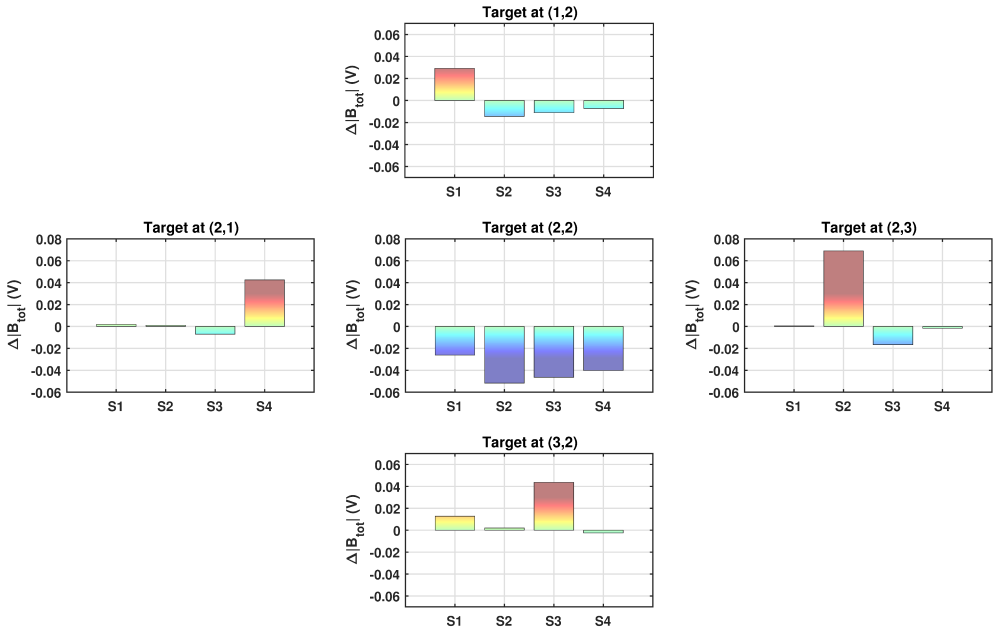

Figure 9.3: Localisation with an AM array: Simultaneous response of the sensing array to the position of an Al plate (105 mm × 110 mm × 10 mm) 90 mm above the sensing plane. The sensors' response unambiguously reveals the location of the sample at 5 positions across the grid. The four vertices of the grid are excluded. Operation frequency 20 kHz. Adapted from Reference [4].

the primary field, produced by the comparatively large RF coil. An optimised primary field excitation scheme is be required to improve the detection range.

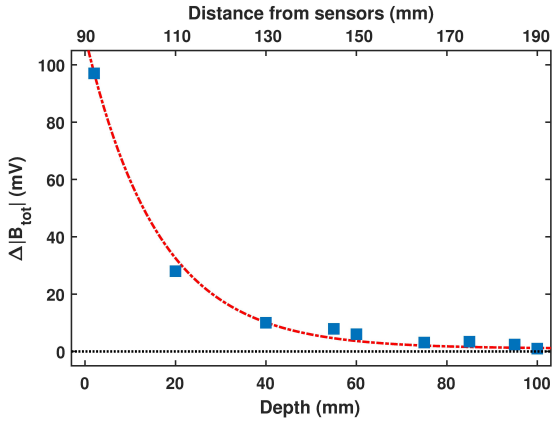

Figure 9.4: Active underwater detection: $\Delta|B_{\text{tot}}|$ response of S2 as a function of the underwater depth of a thin Al plate (105 mm × 73 mm × 3 mm) at position $(2,3)$. Error bars are contained within the points. Dashed level marks the detection limit (at $\Delta|B_{\text{tot}}| = 0$), this corresponds to 100 mm underwater – 190 mm from the sensing plane. Adapted from Reference [4].

Finally, the automatic detection software was used to further demonstrate:

1. the detection and localisation of multiple samples,

2. the suppression of background structures,

3. the live tracking of moving samples,

examples of these can be seen in Video 1 [172].

9.2 Remote detection of rotating machinery with AMs

In this section, I discuss the remote detection of AC magnetic signatures from rotating machinery. Potential applications span the detection of illicit activities to the continuous monitoring of machinery. Only an overview is provided here, further details and results can be found in Reference [2].

A table-top RF-AM contained within a $40\,\text{cm} \times 60\,\text{cm}$ footprint is used. The optical setup is the same as Figure 4.4. The magnetometer spectrum is recorded by the SA. For an unshielded RF-AM, driven by a calibration field (B_{RF}), the power spectrum is dominated by a single peak at ω_{RF} and a symmetric set of 50 Hz (and higher order) sidebands.

Rotating motors produce an AC magnetic field (B_{AC}) – oscillating at ω_{AC}, say. This field perturbs the precession of the atoms due to coupling with the RF driving field. In the time domain, the B_{RF} is modulated by B_{AC}. In the frequency domain, B_{AC} produces sidebands in the power spectrum at $\omega_{\text{RF}} \pm m\omega_{\text{AC}}$, $m \in \mathbb{N}$. Effectively, ω_{RF} acts as a carrier for the information stored in the sidebands. One can therefore choose ω_{RF} to avoid environmental noise sources and increase the detection sensitivity. This is important for the detection of low-frequency oscillating signatures ($B_{\text{AC}} < 50\,\text{Hz}$), where conventional magnetometers are limited by poor sensitivity and $1/f$ noise.

In Figure 9.5, an example of the technique is shown. Figure 9.5(a) demonstrates the detection of a 24 V DC fan (Sunon, KDE2412PMB1-6AB) positioned 1 m away from the sensor. When the fan is on an additional set of sidebands at $\omega_{\text{AC}} = \pm(167 \pm 1)\text{Hz}$ is detected. These peaks detail the magnetic signature of the motor, appearing at three times the rotation frequency ($56 \pm 1\text{Hz}$).

Figure 9.5(b) additionally demonstrates the detection of an AC motor – from a 120 V pillar drill (Dumore, 37-021). Detection is revealed as an increase in the sidebands at 100 Hz and the corresponding $m = 2$, $m = 3$ harmonics. The sideband frequencies are independent of the rotational speed of the drill. They can be related to the structure and operation of the motor. In principle, the information stored in the sidebands could be used to monitor the performance of the machinery [2, 175].

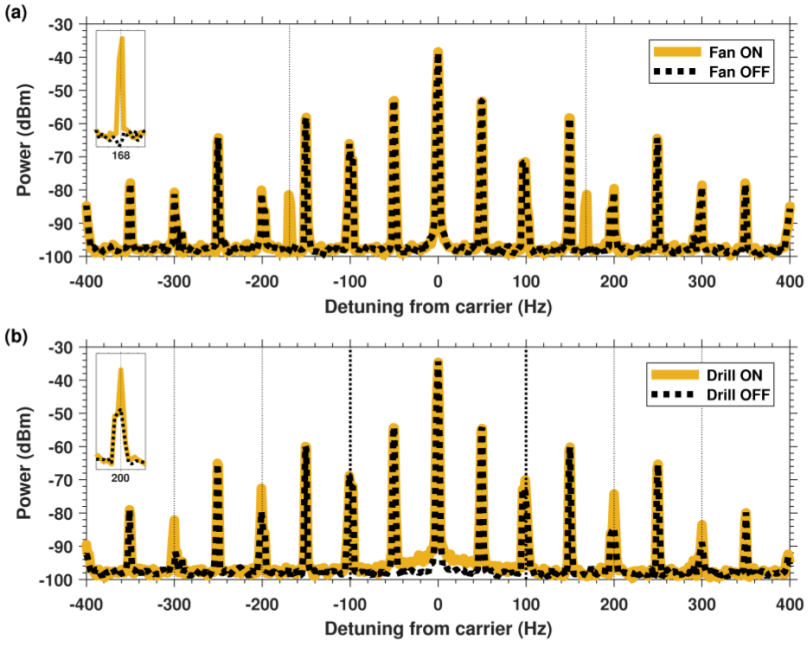

Figure 9.5: Sideband detection of rotating motors: Power spectrum sideband detection of DC and AC motors – from Reference [2]. **(a)** Magnetic signature of DC fan appears at $\pm(167 \pm 1)$Hz, marked by vertical lines. **(b)** Magnetic signature of AC drill recorded as increases in sidebands at 100 Hz and higher order harmonics, marked by vertical lines. Insets show expanded views of the detection regions. All traces are averaged 20 times. Adapted from Reference [2].

9.3 Portable EMI-AM system

This section reports on the development of a portable RF-AM unit for EMI applications. A scale model of the device is included in Figure 9.6.

The design borrows elements from across the EMI-AM systems designed in this work. The active stabilisation of the bias magnetic field is performed by a 14 cm 3-axes Helmholtz coil cube (as in Section 4.5.2). The feedback is provided by a miniaturised 3-axes fluxgate (Bartington MAG612U). The vapour cell is gently heated and temperature stabilised using the same H-bridge controlled feedback circuit as discussed in Section 4.5.3. The optical arrangement is the same crossed pump-probe configuration pumping on the D_1 line of ^{87}Rb. The polarisation rotation signal is selectively amplified by a LIA (Ametek 7230 DSP). Light propagates to the sensor through two optical fibres. Two fibre output collimators and waveplates prepare the beams prior to entering the cell.

The unit is entirely constructed from acrylic and 3D printed plastics (PLA/ABS). The only metallic components are the required optical elements. This is to reduce the contribution from spurious eddy currents. Overall, the system measures 153 mm $\times$ 180 mm $\times$

154 mm and weighs 1.49 kg. In addition to the two fibres, the only connections are: the fluxgate cable, the polarimeter output (SMA), and a 25-pin D-sub connector. The latter provides the RF field (B_{RF}), the currents for magnetic field control (B_x, B_y, B_z), the heating current, the temperature sensor read out, and a ± 15 V supply for the polarimeter.

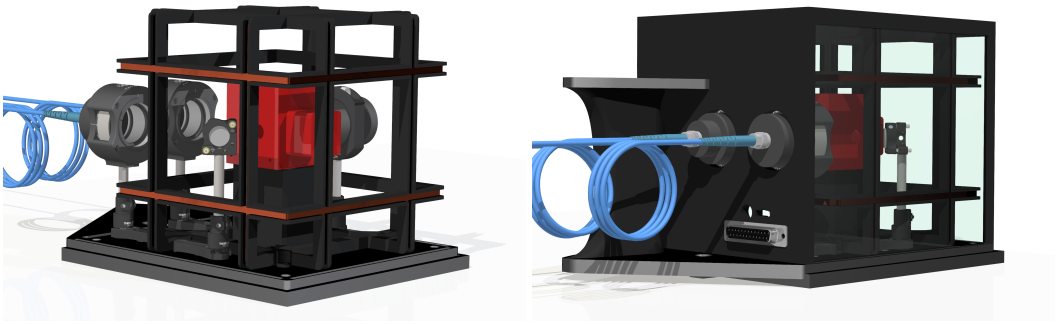

Figure 9.6: Portable EMI-AM system: Scale model of the design. Overall dimensions 153 mm × 180 mm × 154 mm, weight 1.49 kg.

An initial profile of the resonance response is presented in Figure 9.7. This is for a bias field of 123 mG – the corresponding operation frequency is 86 kHz. This response is recorded at room temperature without the optimisation of the experimental parameters.

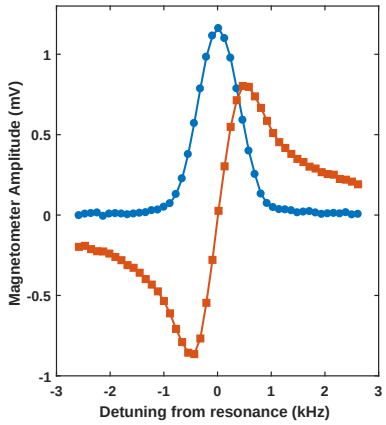

Figure 9.7: Portable EMI-AM system response: Initial in-phase (blue circles) and out-of-phase (red squares) response of the magnetometer near 86 kHz ($B_z = 123$ mG for ^{87}Rb).

The initial linewidth (HWHM) of the magnetometer was 404 Hz. This corresponds to an initial sensitivity of around 30 pT/$\sqrt{\mathrm{Hz}}$ (at room temperature). Based on the data from the previous setups, one can anticipate that this level would be improved by an order of magnitude at higher atomic densities.

The comparatively broad response is mostly attributed to the lack of parameter opti-

misation. However, the smaller dimensions of the magnetic field system place fundamental limitations on the homogeneity of the bias field.

Chapter 10

Conclusions and outlook

This thesis has described the development of a novel imaging technology coupling electromagnetic induction imaging (EMI) with radio-frequency atomic magnetometers (RF-AMs).

This has included the development of a single-channel Rb RF-AM operating in unshielded environments. The device has a demonstrated sensitivity of $55\,\mathrm{fT}/\sqrt{\mathrm{Hz}}$, a photon-shot limit of $10\,\mathrm{fT}/\sqrt{\mathrm{Hz}}$, and a linewidth of 36 Hz. The single-channel configuration is applicable to the detection of both local and remote magnetic fields. This contrasts with gradiometric unshielded RF-AMs which can only be used to detect local, rapidly decaying sources. A large dynamic range sees the detection frequency tuned across several orders of magnitude – from the Hz to MHz bands. This corresponds to magnetic fields between 1.1 mG and 7.13 G, a much greater range than explored in other AM devices. A magnetic field compensation system is designed to achieve a consistent sensor response without magnetic shielding (or averaging). The system is shown to lock the magnetic field, increasing the stability of the signal and reducing noise sources by an order of magnitude. Together, the characteristics of the magnetometer greatly increase its applicability to practical applications.

The performance of the RF-AM has been exploited to demonstrate the power EMI. High-resolution EMI is performed across a broad range of materials. Sample conductivities span $1 \times 10^7\,\mathrm{S\,m^{-1}}$ down to low-conductivity, non-metallic samples at $500\,\mathrm{S\,m^{-1}}$. The sensitivity of the magnetometer enables the probing of small sample volumes. This leads to a typical image resolution of around 1 mm, and is used to demonstrate the detection of sub-mm features. In the low-conductivity regime, sample volumes are orders of magnitude below those explored in previous, coil-based experiments. The imaging approach is non-contact and non-destructive, with no prior sample preparation. All images are acquired in a

single measurement scan – no background subtraction is required.

A number of proof-of-principle EMI applications were demonstrated. These included the detection and discrimination of the dopant level in Si, non-ionising penetration of metallic and ferromagnetic barriers, and non-destructive evaluation (NDE) in the context of material fatigue and corrosion under insulation. In all cases the images accurately reproduced the characteristics of the samples.

Novel image reconstruction approaches – based on machine learning (ML) – were developed and employed to maximise the amount of information extracted from EMI images. The technique was able to extract the position, material, shape, and orientation from low-resolution images. Position detection 2.6 times better than the physical spatial resolution was recorded. Classification algorithms consistently achieved success rates above 95%. ML-aided EMI represents the first viable alternative to solving the electromagnetic inverse problem. With the further benefit of being robust against small input variations. In addition, this proved the applicability of ML techniques to diffusive physical systems, highlighting the potential advantages that could be achieved in other regimes.

By extending the technique to complex cluttered scenes, ML models were shown to accurately simulate EMI (forward modelling) and reconstruct scenes from measured images (inverse modelling). Synthetically generated images were shown to improve the successful full scene reconstruction rate to 90%. This represents a significant advantage in practical applications due to the high experimental cost of acquiring data.

The long-term outlook for this work is a medical imaging and diagnostic tool based on EMI-AM. The reported imaging of low-conductivity samples suggests the first demonstration of EMI-AM in the biomedical regime is now achievable in the short-term. This requires the continued development of the sensor, further increasing the operation frequency to provide access to lower conductivities. Supporting these devices with the developed ML techniques will allow the rapid processing of imaging data for diagnosis – even when unclear to a human observer. The benefits of ML-aided diagnosis have already been demonstrated for other medical imaging technologies [176]. This thesis therefore represents a relevant step towards a new generation quantum-based, diagnostic tools for imaging of the dielectric properties of biological tissues.

Appendix A

Details of proofs for Section 2.2

A.1 Equivalence of skin depth formulae

Equivalence of Equation 2.3 and Equation 2.4.

$$
\begin{aligned}
\delta(\omega) &= \frac{1}{\omega}\left[\frac{\mu\varepsilon}{2}\left(\sqrt{1+\left(\frac{\sigma}{\omega\varepsilon}\right)^2}-1\right)\right]^{-1/2} \qquad \text{(Equation 2.3)} \\
&= \frac{1}{\omega}\left(\frac{2}{\mu\varepsilon}\right)^{1/2}\frac{1}{\left(\sqrt{1+\left(\frac{\sigma}{\omega\varepsilon}\right)^2}-1\right)^{1/2}}\frac{\left(\sqrt{1+\left(\frac{\sigma}{\omega\varepsilon}\right)^2}+1\right)^{1/2}}{\left(\sqrt{1+\left(\frac{\sigma}{\omega\varepsilon}\right)^2}+1\right)^{1/2}} \\
&= \left(\frac{2}{\mu\varepsilon}\right)^{1/2}\frac{\varepsilon}{\sigma}\left(\sqrt{1+\left(\frac{\sigma}{\omega\varepsilon}\right)^2}+1\right)^{1/2} \\
&= \left(\frac{2\varepsilon}{\mu\sigma^2}\right)^{1/2}\left(\frac{\sigma}{\omega\varepsilon}\right)^{1/2}\left(\sqrt{\left(\frac{\omega\varepsilon}{\sigma}\right)^2+1}+\frac{\omega\varepsilon}{\sigma}\right)^{1/2} \\
&= \sqrt{\frac{2}{\omega\mu\sigma}}\left(\sqrt{1+\left(\frac{\omega\varepsilon}{\sigma}\right)^2}+\frac{\omega\varepsilon}{\sigma}\right)^{1/2} \qquad \text{(Equation 2.4)}
\end{aligned}
$$

A.2 Asymptotic limit of the skin depth

Proof of the asymptotic limit of the skin depth in the high-frequency, low-conductivity regime – Equation 2.6. Equation 2.4 can be written as

$$
\delta(\omega) = \frac{1}{\sigma}\sqrt{\frac{2\varepsilon}{\mu}}\left[\frac{\sqrt{1+x^2}}{x}+1\right]^{1/2} \quad \text{where} \quad x=\frac{\omega\varepsilon}{\sigma}\,. \tag{A.1}
$$

For the case of a low-conductivity sample and high-frequency operation ($\omega \gg \sigma/\varepsilon$, i.e. $x \gg 1$), the asymptotic limit of $\delta(\omega)$ follows directly from Equation A.1 via the power

rule

$$\begin{aligned}\lim_{x\to\infty}\delta(\omega) &= \frac{1}{\sigma}\sqrt{\frac{2\varepsilon}{\mu}}\left[\sqrt{\lim_{x\to\infty}\left(\frac{1+x^2}{x^2}\right)}+1\right]^{1/2} \\ &= \frac{2}{\sigma}\sqrt{\frac{\varepsilon}{\mu}}\,. \end{aligned} \tag{A.2}$$

Appendix B

Details of the experimental control software

This appendix briefly describes the operation of the programs that make up the experimental control package.

B.1 The .vi tree

Figure B.1 is a .vi tree detailing the software hierarchy. The package consists of the top-level program – MAIN.vi, 20 sub-programs, 11 SubVis, 2 global parameter variables, 14 global settings variables, 9 LabVIEW type definition controls, and one initialisation file.

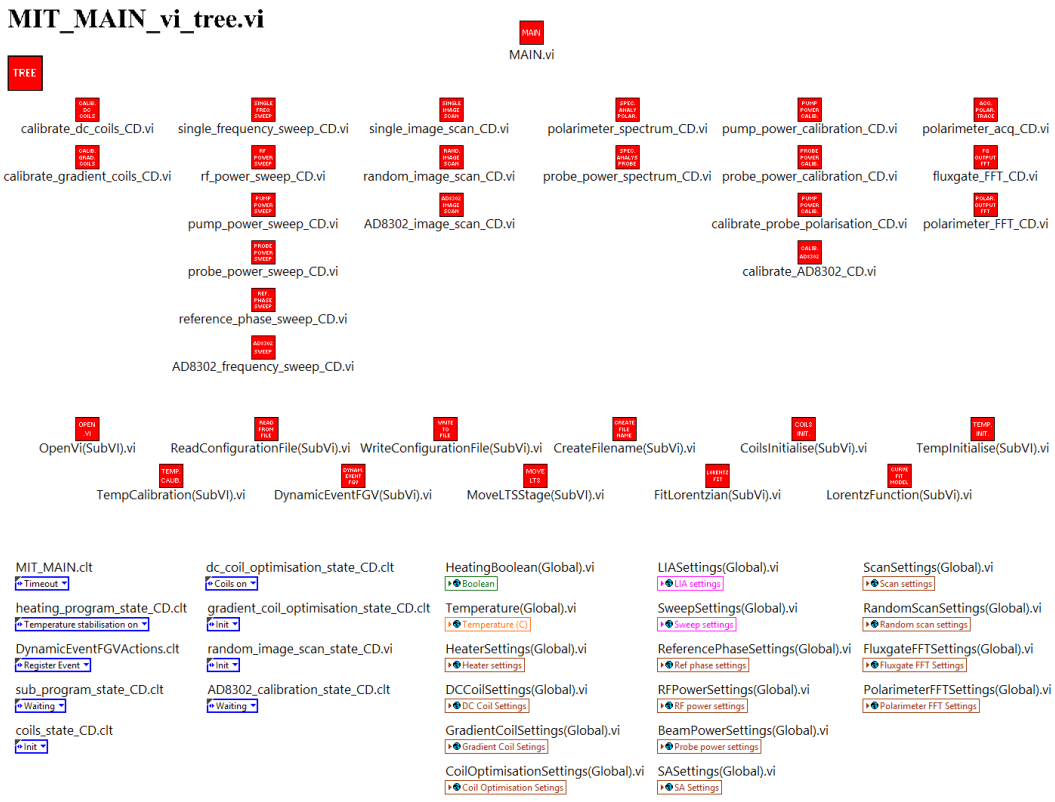

Figure B.1: Experimental control software: .vi tree showing the program hierarchy of the software package.

B.2 Main program

MAIN.vi: This main program provides links to all sub-programs and experimental settings. When run, the program reads the saved initialisation file and generates a list of global settings variables. When a sub-program is opened the required settings are loaded from the global variables. Any variables that are changed by sub-programs are automatically saved into the global variables when closed. Finally, when MAIN.vi is closed the initialisation file is overwritten with the new values. In this way, all settings are transferred and updated across the software package without any user input required.

MAIN.vi also controls the heating and temperature stabilisation of the vapour cell. The program is able to pause the heating during the measurement windows of sub-programs. This top-level program also controls the currents in the compensation coil system.

B.3 Sub-programs

B.3.1 Magnetic field calibration programs

calibrate_dc_coil_CD.vi: This sub-program runs an optimisation procedure for the currents in the transverse compensation coils (x and y). This takes advantage of the orthogonality of the coils to run a simple hill climbing optimisation in each direction.

The resonant frequency of an RF-AM has quadratic dependence on the transverse magnetic field (hence, on the current also). The program loads the previous optimum current in each direction and records the magnetometer frequency for a set of currents spread symmetrically about this value. A quadratic fit of resonant frequency against coil current is performed. The new current value is automatically set to the value that minimises the resonant frequency.

calibrate_gradient_coil_CD.vi: This sub-program runs an optimisation procedure for the gradient coil currents (dx, dy, and dz). Again by taking advantage of orthogonality to run hill climbing algorithms in each direction.

In this case the linewidth of the RF-AM response has a quadratic dependence on the gradient fields/currents. For each direction the program records and plots the linewidth against the coil current. The currents are again spread symmetrically about the previously found optimum. The new value is taken as one that minimised the current/linewidth relationship.

B.3.2 RF frequency sweep programs

single_frequency_sweep_CD.vi: This sub-program records the basic response of the RF-AM. It performs a user-defined sweep of the RF frequency recording the X, Y, R, and Φ response.

rf_power_sweep_CD.vi: This sub-program records the RF frequency sweep response whist systematically sweeping the calibration field amplitude.

pump_power_sweep_CD.vi: This sub-program records the RF frequency sweep response whist systematically sweeping the pump beam power. The amplitude modulation voltages supplied to the AOM driver and the corresponding pump beam powers are read from the pump_power_calibration file.

probe_power_sweep_CD.vi: This sub-program records the RF frequency sweep response whist systematically sweeping the probe beam power. The amplitude modulation voltages supplied to the AOM driver and the corresponding probe beam powers are read from the probe_power_calibration file.

reference_phase_sweep_CD.vi: This sub-program records the RF frequency sweep response whist systematically changing the LIA reference phase.

AD8302_frequency_sweep_CD.vi: This sub-program records the RF frequency sweep response acquiring R and Φ data from the AD8302 chip – rather than the LIA. At each frequency the waveform generators (WGs) are calibrated to provide a 90° phase difference between them. The input to the AD8302 is then programmatically switched to the magnetometer output and the response recorded.

B.3.3 Imaging programs

single_image_scan_CD.vi: This sub-program takes a single EMI image of a sample. The scan area and resolution are defined by the user. Images of the X, Y, R, and Φ parameters are recorded in real time.

random_image_scale_CD.vi: This sub-program runs a defined number of consecutive images. The centre of each scan is randomly positioned within a user-defined area. This program is used for the results of Chapter 6.

AD8302_image_scan_CD.vi: This sub-program runs the same single EMI image scan but with the data acquired by the AD8302 chip.

B.3.4 Spectrum analyser programs

polarimeter_spectrum_CD.vi: This sub-program records the spectrum of the RF-AM polarimeter output, averaging a given number of times. It is used to evaluate the SNR and the noise components of the magnetometer.

probe_power_spectrum_CD.vi: This sub-program records and averages the spectrum of the polarimeter output whist systematically sweeping the probe beam power.

B.3.5 Calibration programs

pump_power_calibration_CD.vi: This sub-program allows the user to calibrate the pump beam power. The amplitude modulation voltages supplied to the AOM driver are swept through defined values, with the user prompted to input the pump power at each point. The results are saved in the pump_power_calibration file.

probe_power_calibration_CD.vi: This sub-program allows the user to calibrate the probe beam power. The amplitude modulation voltages supplied to the AOM driver are swept through defined values, with the user prompted to input the probe power at each point. The results are saved in the probe_power_calibration file.

calibrate_probe_polarisation_CD.vi: This sub-program is used to check/calibrate the polarisation of the probe beam (i.e. equilibrate the power sent to each arm of the balanced photodiode).

calibrate_AD8302_CD.vi: This sub-program is used to calibrate the AD8302 chip. Both the phase and amplitude responses are calibrated at a user-defined frequency. One WG has a set output. The other is swept (in phase or amplitude across a programmable range) and the response of the chip recorded.

B.3.6 Other programs

polarimeter_acq_CD.vi: This sub-program records a trace directly from the output of the polarimeter.

fluxgate_FFT_CD.vi: This sub-program takes the fast Fourier transform of each axis of the fluxgate. It is used to measure the level of magnetic field noise at the position of the sensor independently from the magnetometer operation.

polarimeter_FFT_CD.vi: This sub-program takes the fast Fourier transform of the polarimeter output.

B.4 SubVis

OpenVi(SubVi).vi: This SubVi is used to run the desired sub-program whilst leaving the main .vi running in the background. This allows the main program to continue to control the heater and coil settings whilst other programs perform their functions.

ReadConfigurationFile(SubVi).vi: This SubVi is called when the main program opens. It reads the stored initialisation file (MIT_experiment_settings.ini) and populates the settings global variables with the stored values.

WriteConfigurationFile(SubVi).vi: This SubVi is called when the main program closes. It writes the file MIT_experiment_settings.ini with the current values.

CreateFilename(SubVi).vi: This SubVi is used to generate a default filename for any data saved by the program.

CoilsInitialise.vi: This SubVi runs each time the magnetic field system is initialised. It defines the currents are the corresponding channels for each of the system's power supplies.

TempInitialise.vi: This SubVi runs each time the heating system is initialised. It defines the temperature sensor power, temperature measurement and the channels for controlling the H-bridge pins DIR1, DIR2, and enable.

TempCalibration(SubVi).vi: This SubVi converts the voltage measured across the temperature sensor into °C. The calibration constant is approximately $1.65\,\mathrm{mV}/^{\circ}\mathrm{C}$.

DynamicEventFGV(SubVi).vi: This SubVi handles dynamic functional global variables (FGVs) between sub-programs and the main program. Such events are used to 'fire' events from sub-programs that are then 'registered' by the main program. In this package FGVs are used to disable, close, and enable visa resources being used by the main program when these resources are required by a sub-program. Such events are automatically handled when the sub-program opens and closes.

MoveLTSStage(SubVi).vi: This SubVi is called by the imaging sub-programs. It handles the positioning of the translational stages.

FitLorentz(SubVi).vi: This SubVi fits a standard Lorentzian function to data and outputs the fit parameters.

LorentzFunction(SubVi).vi: This SubVi defines the Lorentzian function used by FitLorentz(SubVi).vi.

B.5 Global variables

Heating(Global).vi: The heating global variable is an boolean control that is read by the main program and controls when the heating system is active. Sub-programs are able to modify this control in order to turn the heater on/off either side of data acquisition.

Temperature(Global).vi: The temperature global variable records the temperature set-point making it accessible across all the programs. In this way, each sub-program is able to wait until the cell temperature reaches the desired value before running each measurement. This prevents the loss of temperature across long-term measurement runs.

Settings global variables: There are 13 settings global variables. Each one is a cluster of related variables. These variables are created from the MIT_experiment_setting.ini by the read configuration file SubVi when the main program opens. When each sub-program is run the required variables are read from the settings globals. Any variable that is changed during sub-program operation is automatically saved into updated settings globals when the program closes. The current settings are saved by the write configuration file SubVi when the main program ends.

B.6 Type definitions

Every program in the software package is written as an event-driven state machine. The type definitions (.clt files) are used to store manipulate the current state of the machine during operation.

Appendix C

Optimisation of D_2 line EMI-AM II system

Supporting material for the results of Section 5.3.8.

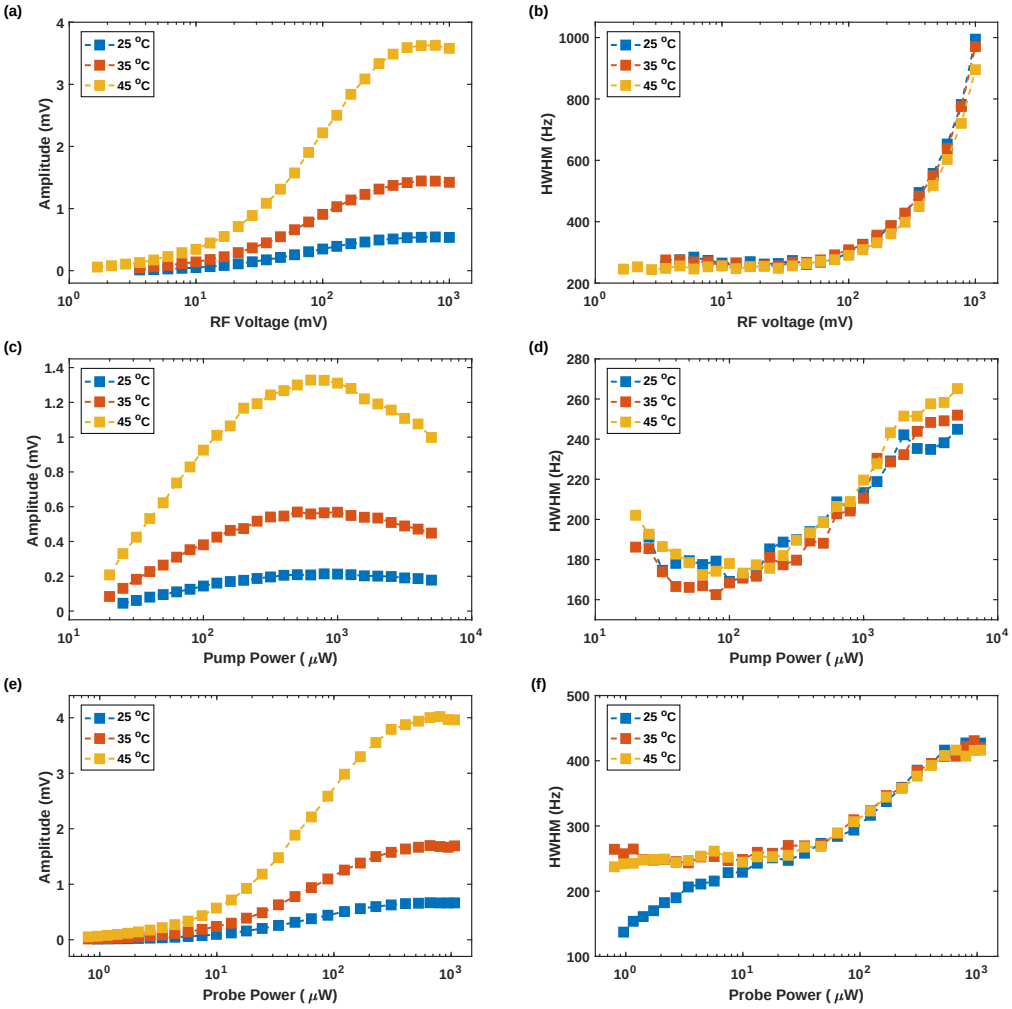

Figure C.1: D_2 line EMI-AM II optimisation: Magnetometer amplitude and HWHM as a function of: Applied RF voltage – **(a)** and **(b)**, pump beam power – **(c)** and **(d)**, and probe beam power – **(e)** and **(f)**. 100 mV was chosen as the optimum RF voltage – an applied oscillating magnetic field of 10.3 nT. The optimum pump power is 700 µW.

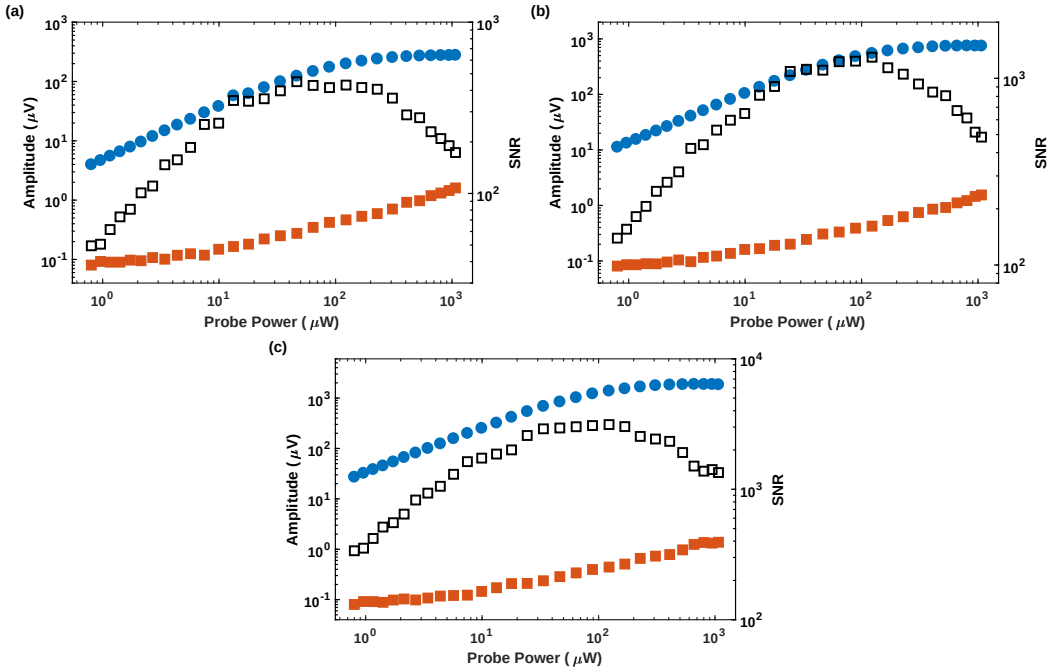

Figure C.2: Magnetometer signal, noise, and SNR as a function of probe beam power: (a) 25 °C, **(b)** 35 °C, and **(c)** 45 °C. Signal (blue, filled circles), Noise – measured with the RF field off (red, filled squares), and corresponding SNR (black, open squares). Fixed values; pump power 700 µW, RF field amplitude 10.3 nT.

Appendix D

Optimisation of the EMI-AM III system

Supporting material for Section 5.4.

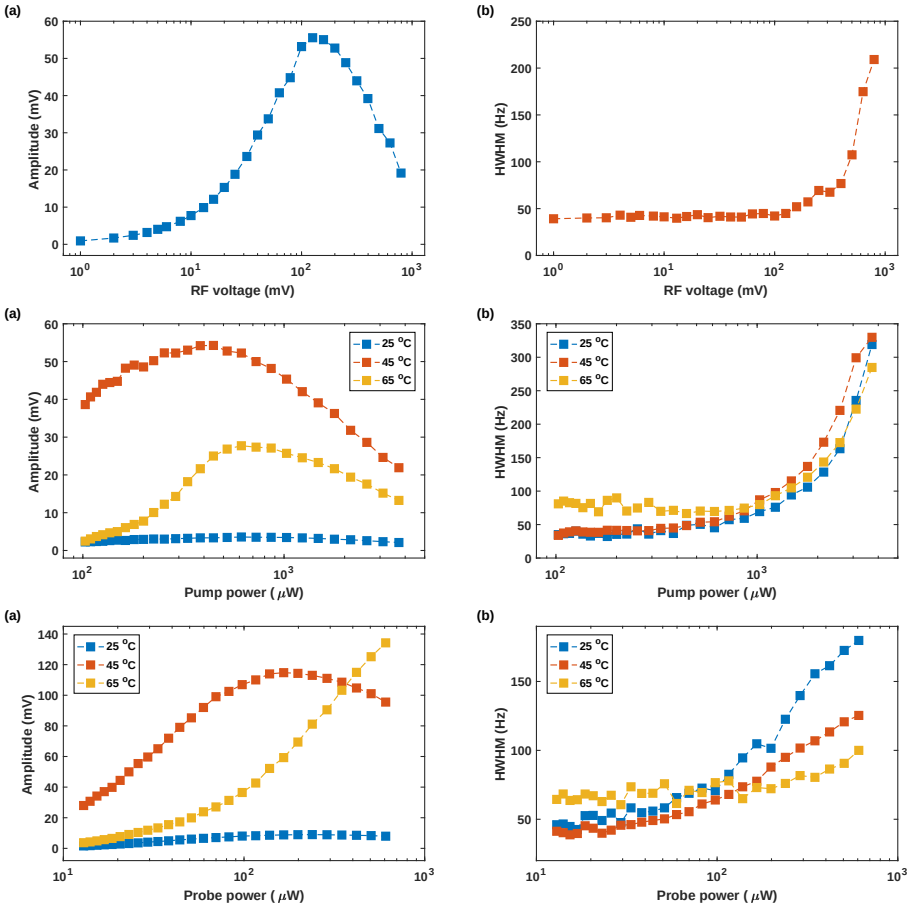

Figure D.1: EMI-AM III optimisation: Magnetometer amplitude and HWHM as a function of: Applied RF voltage – **(a)** and **(b)**, pump beam power – **(c)** and **(d)**, and probe beam power – **(e)** and **(f)**. 110 mV was chosen as the optimum RF voltage – an applied oscillating magnetic field of 4.74 nT. The optimum pump power is: 615 µW at 25 °C, 330 µW at 45 °C, at 615 µW for 65 °C.

Figure D.1 provides details of the optimisation procedure for the EMI-AM III system.

To allow comparisons with the previous experiments, the operation frequency was again chosen to be 100 kHz. In this experiment, the vapour cell is isotopically enriched ^{87}Rb, along with 20 Torr of N_2 buffer gas.

The response of the RF-AM's amplitude and HWHM to the RF voltage is shown in Figures D.1(a) and D.1(b). The pump and probe beam powers are set to small values to limit their effect – 300 µW and 25 µW, respectively. The chosen operation point was 110 mV. It implies an applied oscillating field of 4.74 nT. This value remains fixed throughout rest of the measurements. This was only done at one temperature as the atomic density does not affect the RF power broadening (see also Figure C.1(b)).

Figures D.1(c) and D.1(d) explore the effect of the pump beam power. The probe power remains fixed at 25 µW. The chosen operation points are: 615 µW for 25 °C, 330 µW for 45 °C, and 615 µW for 65 °C. These values are fixed throughout the following measurements.

Finally, the effect of the probe beam power is shown in Figures D.1(e) and D.1(f). For these results, note that the saturation power increases with temperature as the optical depth of the cell decreases.

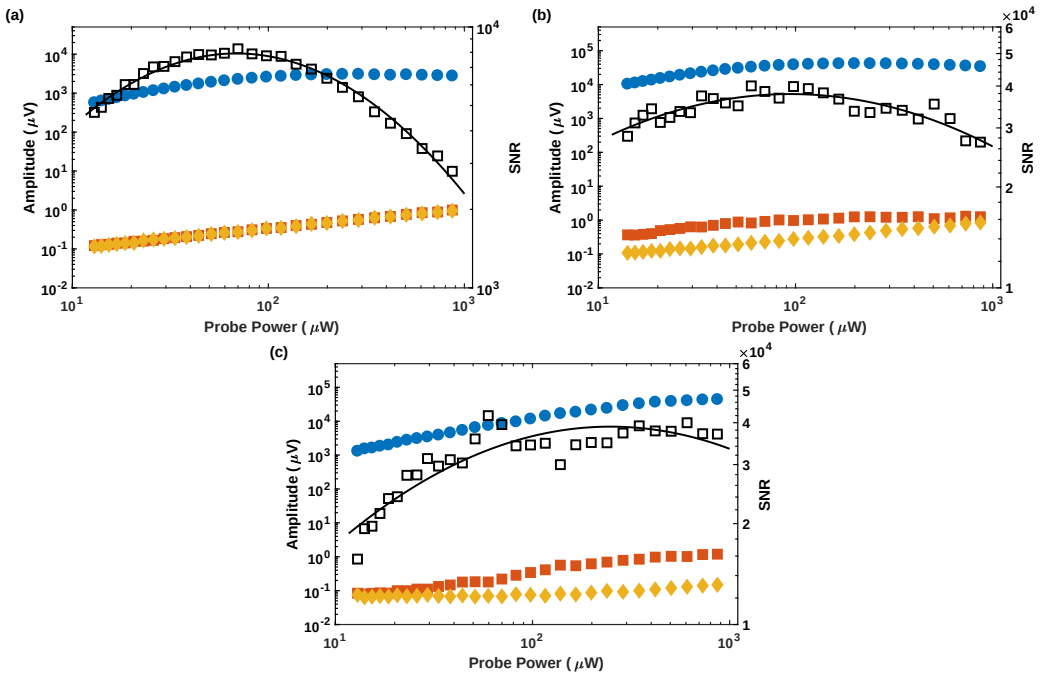

Figure D.2: Magnetometer signal, noise, photon-shot noise, and SNR as a function of probe beam power: (a) 25 °C, **(b)** 45 °C, and **(c)** 65 °C. Signal (blue filled circles), Noise – measured with the RF field off (red filled squares), Photon-shot noise – measured with the bias field detuned (yellow filled diamonds), SNR (black open squares).

Figure D.2 presents the RF-AM signal, total noise, photon-shot noise, and SNR as a function of the probe beam power. Together these results are used to derive the sensitivity values reported in Section 5.4.

Appendix E

Semiconductor imaging: supporting material

Supporting material for Section 6.4.3. Multi-frequency X and Y images of the 5000 $\mathrm{S\,m^{-1}}$ sample are shown in Figure E.1 and Figure E.2, respectively. ΔX and ΔY for each frequency are taken as the maximum variation across the corresponding image. Results are normalised with the total signal $|S|$. This is taken as the maximum of the corresponding R image. Which is simultaneously acquired. Effectively, $|S| = \max\left(\sqrt{X^2+Y^2}\right)$. The same approach is applied to the 1×10^4 $\mathrm{S\,m^{-1}}$, 1000 $\mathrm{S\,m^{-1}}$, and 500 $\mathrm{S\,m^{-1}}$ samples. For each sample, the data is excluded when the frequency is not sufficient to generate a clear response (for example 100 kHz below).

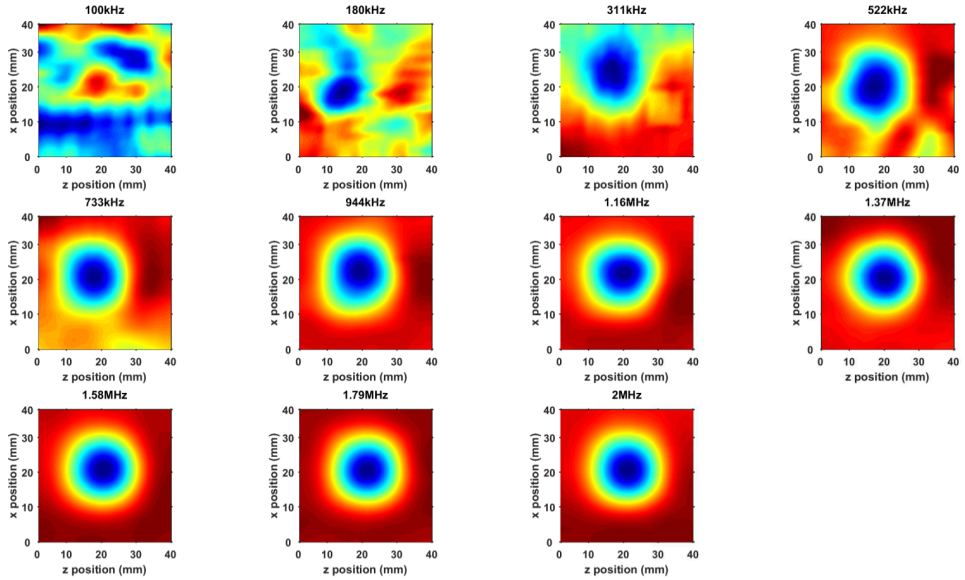

Figure E.1: Multi-frequency EMI imaging (i): X images of the 5000 $\mathrm{S\,m^{-1}}$ sample at multiple frequencies. ΔX at each frequency is taken as the maximum variation across the image.

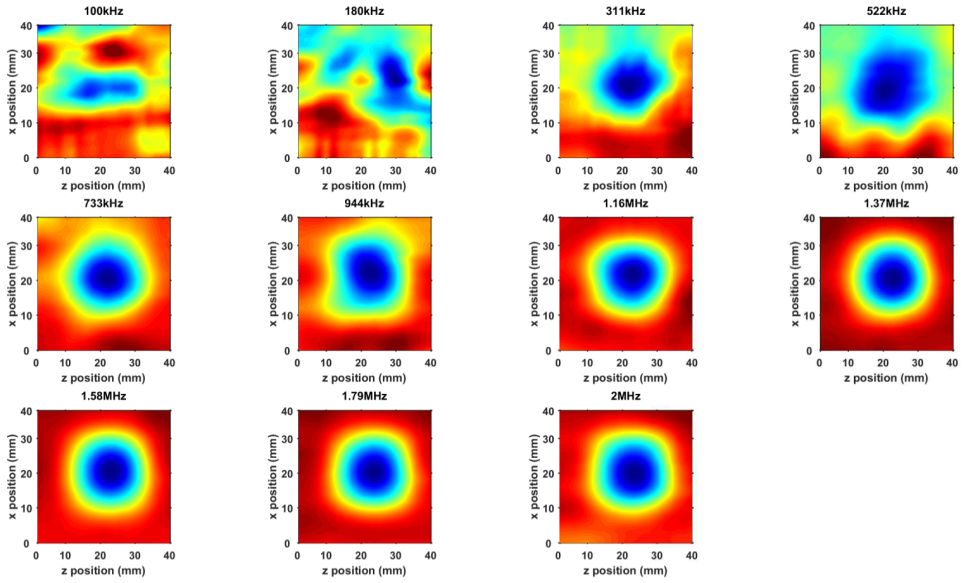

Figure E.2: Multi-frequency EMI imaging (ii): Y images of the $5000\,\mathrm{S\,m^{-1}}$ sample at multiple frequencies. ΔY at each frequency is taken as the maximum variation across the image.

Bibliography

[1] C. Deans, L. Marmugi, S. Hussain, and F. Renzoni. Electromagnetic induction imaging with a radio-frequency atomic magnetometer. *Applied Physics Letters*, 108(10): 103503, 2016. doi:10.1063/1.4943659.

[2] L. Marmugi, L. Gori, S. Hussain, C. Deans, and F. Renzoni. Remote detection of rotating machinery with a portable atomic magnetometer. *Applied Optics*, 56(3): 743–749, 2017. doi:10.1364/AO.56.000743.

[3] C. Deans, L. Marmugi, and F. Renzoni. Through-barrier electromagnetic imaging with an atomic magnetometer. *Optics Express*, 25(15):17911–17917, 2017. doi:10.1364/OE.25.017911.

[4] C. Deans, L. Marmugi, and F. Renzoni. Active underwater detection with an array of atomic magnetometers. *Applied Optics*, 57(10):2346–2351, 2018. doi:10.1364/AO.57.002346.

[5] C. Deans, L. D. Griffin, L. Marmugi, and F. Renzoni. Machine learning based localization and classification with atomic magnetometers. *Physical Review Letters*, 120 (3):033204, 2018. doi:10.1103/PhysRevLett.120.033204.

[6] C. Deans, L. Marmugi, and F. Renzoni. Sub-picotesla widely tunable atomic magnetometer operating at room-temperature in unshielded environments. *Review of Scientific Instruments*, 89(8):083111, 2018. doi:10.1063/1.5026769.

[7] P. Bevington, R. Gartman, W. Chalupczak, C. Deans, et al. Non-destructive structural imaging of steelwork with atomic magnetometers. *Applied Physics Letters*, 113(6): 063503, 2018. doi:10.1063/1.5042033.

[8] L. Marmugi, C. Deans, and F. Renzoni. Atomic magnetometry-based electromag-

netic imaging of low-conductivity semiconductors. *[Submitted: May 2018]*, 2018. URL `https://arxiv.org/abs/1805.05743`.

[9] L. Marmugi, S. Hussain, C. Deans, and F. Renzoni. Magnetic induction imaging with optical atomic magnetometers: towards applications to screening and surveillance. In *Optics and Photonics for Counterterrorism, Crime Fighting, and Defence XI; and Optical Materials and Biomaterials in Security and Defence Systems Technology XII*, volume 9652, page 965209. International Society for Optics and Photonics, 2015. doi:10.1117/12.2195482.

[10] C. Deans, L. Marmugi, S. Hussain, and F. Renzoni. Optical atomic magnetometry for magnetic induction tomography of the heart. In *Quantum Optics*, volume 9900, page 99000F. International Society for Optics and Photonics, 2016. doi:10.1117/12.2227538.

[11] S. Hussain, L. Marmugi, C. Deans, and F. Renzoni. Electromagnetic imaging with atomic magnetometers: a novel approach to security and surveillance. In *Detection and Sensing of Mines, Explosive Objects, and Obscured Targets XXI*, volume 9823, page 98230Q. International Society for Optics and Photonics, 2016. doi:10.1117/12.2222547.

[12] C. Deans, L. Marmugi, and F. Renzoni. Electromagnetic induction imaging with atomic magnetometers. In *Imaging and Applied Optics 2017 (3D, AIO, COSI, IS, MATH, pcAOP) (2017), paper ITu3E.5*, page ITu3E.5. Optical Society of America, 2017. doi:10.1364/ISA.2017.ITu3E.5.

[13] E. Mariotti, G. Bevilacqua, V. Biancalana, R. Cecchi, et al. Forty years after the first dark resonance experiment: an overview of the COSMA project results. In *19th International Conference and School on Quantum Electronics: Laser Physics and Applications*, volume 10226, page 102260K. International Society for Optics and Photonics, 2017. doi:10.1117/12.2264896.

[14] Z. Z. Yu, A. T. Peyton, M. S. Beck, W. F. Conway, and L. A. Xu. Imaging system based on electromagnetic tomography (EMT). *Electronics Letters*, 29(7):625, 1993. doi:10.1049/el:19930418.

[15] H. Griffiths. Magnetic induction tomography. *Measurement Science and Technology*, 12(8):1126, 2001. doi:10.1088/0957-0233/12/8/319.

[16] H. Griffiths, W. R. Stewart, and W. Gough. Magnetic induction tomography: A measuring system for biological tissues. *Annals of the New York Academy of Sciences*, 873(1):335–345, 1999. doi:10.1111/j.1749-6632.1999.tb09481.x.

[17] H. Scharfetter, H. K. Lackner, and J. Rosell. Magnetic induction tomography: Hardware for multi-frequency measurements in biological tissues. *Physiological Measurement*, 22(1):131, 2001. doi:10.1088/0967-3334/22/1/317.

[18] L. Marmugi and F. Renzoni. Optical magnetic induction tomography of the heart. *Scientific Reports*, 6:23962, 2016. doi:10.1038/srep23962.

[19] D. L. Longo, A. S. Fauci, D. L. Kasper, S. L. Hauser, et al. *Harrisons principles of internal medicine: 18th Edition*. McGraw Hill Professional, 2012.

[20] P. Sanders, O. Berenfeld, M. Hocini, P. Jas, et al. Spectral analysis identifies sites high-frequency activity maintaining atrial fibrillation in humans. *Circulation*, 112 (6):789–797, 2005. doi:10.1161/circulationaha.104.517011.

[21] S. M. Narayan, D. E. Krummen, and W. Rappel. Clinical mapping approach to diagnose electrical rotors and focal impulse sources for human atrial fibrillation. *Journal of Cardiovascular Electrophysiology*, 23(5):447–454, 2012. doi:10.1111/j.1540-8167.2012.02332.x.

[22] M. Haissaguerre, M. Hocini, A. J. Shah, N. Derval, et al. Noninvasive panoramic mapping of human atrial fibrillation mechanisms: A feasibility report. *Journal of Cardiovascular Electrophysiology*, 24(6):711–717, 2013. doi:10.1111/jce.12075.

[23] T. Christ, N. Rozmaritsa, A. Engel, E. Berk, et al. Arrhythmias, elicited by catecholamines and serotonin, vanish in human chronic atrial fibrillation. *Proceedings of the National Academy of Sciences*, 111(30):11193–11198, 2014. doi:10.1073/pnas.1324132111.

[24] A. N. Ganesan, N. J. Shipp, A. G. Brooks, P. Kuklik, et al. Long-term outcomes of catheter ablation of atrial fibrillation: A systematic review and meta-

analysis. *Journal of the American Heart Association*, 2(2):e004549, 2013. doi:10.1161/jaha.112.004549.

[25] R. Merwa, K. Hollaus, O. Bir, and H. Scharfetter. Detection of brain oedema using magnetic induction tomography: A feasibility study of the likely sensitivity and detectability. *Physiological Measurement*, 25(1):347, 2004. doi:10.1088/0967-3334/25/1/038.

[26] W. Pan, Q. Yan, M. Qin, G. Jin, et al. Detection of cerebral hemorrhage in rabbits by time-difference magnetic inductive phase shift spectroscopy. *PLOS ONE*, 10(5): e0128127, 2015. doi:10.1371/journal.pone.0128127.

[27] M. Zolgharni, P. D. Ledger, D. W. Armitage, D. S. Holder, and H. Griffiths. Imaging cerebral haemorrhage with magnetic induction tomography: Numerical modelling. *Physiological Measurement*, 30(6):S187, 2009. doi:10.1088/0967-3334/30/6/S13.

[28] A. J. Surowiec, S. S. Stuchly, J. R. Barr, and A. Swarup. Dielectric properties of breast carcinoma and the surrounding tissues. *IEEE Transactions on Biomedical Engineering*, 35(4):257–263, 1988. doi:10.1109/10.1374.

[29] W. T. Joines, Y. Zhang, C. Li, and R. L. Jirtle. The measured electrical properties of normal and malignant human tissues from 50 to 900 MHz. *Medical Physics*, 21(4): 547–550, 1998. doi:10.1118/1.597312.

[30] W. Daily and A. Ramirez. Environmental process tomography in the United States. *The Chemical Engineering Journal and the Biochemical Engineering Journal*, 56(3): 159–165, 1995. doi:10.1016/0923-0467(94)02911-3.

[31] A. J. Peyton, M. S. Beck, A. R. Borges, J. E. De Oliveira, et al. Development of electromagnetic tomography (EMT) for industrial applications. Part 1: Sensor design and instrumentation. In *1st World Congress on Industrial Process Tomography*, pages 306–312, 1999. URL `http://super-sensing.org/pdfs/wcipt1/h1_1.pdf`.

[32] B. J. Darrer, J. C. Watson, P. Bartlett, and F. Renzoni. Magnetic imaging: A new tool for UK national nuclear security. *Scientific Reports*, 5:7944, 2015. doi:10.1038/srep07944.

[33] B. J. Darrer, J. C. Watson, P. Bartlett, and F. Renzoni. Electromagnetic imaging through thick metallic enclosures. *AIP Advances*, 5(8):087143, 2015. doi:10.1063/1.4928864.

[34] L. Perez, J. Le Hir, C. Dolabdjian, and L. Butin. Investigation in detection of fatigue cracks under rivet head airframe using improved GMR magnetometer in an eddy current system. *Journal of Electrical Engineering*, 55(10s):73–76, 2004. URL `http://iris.elf.stuba.sk/jeeec/data/pdf/10s_104-20.pdf`.

[35] L. Ma and M. Soleimani. Electromagnetic imaging for internal and external inspection of metallic pipes. *Insight-Non-Destructive Testing and Condition Monitoring*, 54(9):493–495, 2012. doi:10.1784/insi.2012.54.9.493.

[36] M. Cheney, D. Isaacson, and J. C. Newell. Electrical impedance tomography. *SIAM review*, 41(1):85–101, 1999. doi:10.1137/S0036144598333613.

[37] G. J. Saulnier, R. S. Blue, J. C. Newell, D. Isaacson, and P. M. Edic. Electrical impedance tomography. *IEEE Signal Processing Magazine*, 18(6):31–43, 2001. doi:10.1109/79.962276.

[38] A. M. Sinton, R. W. M. Smith, F. J. McArdle, and B. H. Brown. Fast display for real-time electrical impedance tomography. In *Engineering in Medicine and Biology Society, 1992 14th Annual International Conference of the IEEE*, volume 5, pages 1708–1709. IEEE, 1992. doi:10.1109/IEMBS.1992.5762002.

[39] Q. S. Zhu, C. N. McLeod, C. W. Denyer, F. J. Lidgey, and W. R. B. Lionheart. Development of a real-time adaptive current tomograph. *Physiological Measurement*, 15(2A):A37, 1994. doi:10.1088/0967-3334/15/2A/005.

[40] M. Cheney and D. Isaacson. Distinguishability in impedance imaging. *IEEE Transactions on Biomedical Engineering*, 39(8):852–860, 1992. doi:10.1109/10.148393.

[41] D. Holder. *Clinical and Physiological Applications of Electrical Impedance Tomography*. CRC Press, 1993.

[42] J. C. Newell, P. M. Edic, X. Ren, J. L. Larson-Wiseman, and M. D. Danyleiko. Assessment of acute pulmonary edema in dogs by electrical impedance imag-

ing. *IEEE Transactions on Biomedical Engineering*, 43(2):133–138, 1996. doi:10.1109/10.481982.

[43] A. Ramirez, W. Daily, D. LaBrecque, E. Owen, and D. Chesnut. Monitoring an underground steam injection process using electrical resistance tomography. *Water Resources Research*, 29(1):73–87, 2010. doi:10.1029/92WR01608.

[44] A. Ramirez, W. Daily, A. Binley, D. LaBrecque, and D. Roelant. Detection of leaks in underground storage tanks using electrical resistance methods. *Journal of Environmental and Engineering Geophysics*, 1(3):189–203, 1996. doi:10.4133/jeeg1.3.189.

[45] Q. Marashdeh, F. L. Teixeira, and L. Fan. Electrical capacitance tomography. In *Industrial Tomography*, pages 3–21. Elsevier, 2015. doi:10.1016/B978-1-78242-118-4.00001-0.

[46] R. Guilizzoni. *A resonant system for electromagnetic induction imaging of concealed conductive targets*. PhD thesis, UCL (University College London), 2018. URL `http://discovery.ucl.ac.uk/10045578/`.

[47] R. Guilizzoni, J. C. Watson, P. Bartlett, and F. Renzoni. Imaging by electromagnetic induction with resonant circuits. In *Image Sensing Technologies: Materials, Devices, Systems, and Applications II*, volume 9481, page 94810Q. International Society for Optics and Photonics, 2015. doi:10.1117/12.2183180.

[48] R. Guilizzoni, J. C. Watson, P. Bartlett, and F. Renzoni. Penetrating power of resonant electromagnetic induction imaging. *AIP Advances*, 6(9):095017, 2016. doi:10.1063/1.4963299.

[49] D. Budker and M. Romalis. Optical magnetometry. *Nature Physics*, 3(4):227, 2007. doi:10.1038/nphys566.

[50] D. Budker and D. F. Kimball. *Optical magnetometry*. Cambridge University Press, 2013.

[51] H. G. Dehmelt. Modulation of a light beam by precessing absorbing atoms. *Physical Review*, 105(6):1924, 1957. doi:10.1103/PhysRev.105.1924.

[52] W. E. Bell and A. L. Bloom. Optical detection of magnetic resonance in alkali metal vapor. *Physical Review*, 107(6):1559, 1957. doi:10.1103/PhysRev.107.1559.

[53] I. K. Kominis, T. W. Kornack, J. C. Allred, and M. V. Romalis. A subfemtotesla multichannel atomic magnetometer. *Nature*, 422(6932):596, 2003. doi:10.1038/nature01484.

[54] S. Lee, K. L. Sauer, S. J. Seltzer, O. Alem, and M. V. Romalis. Subfemtotesla radiofrequency atomic magnetometer for detection of nuclear quadrupole resonance. *Applied Physics Letters*, 89(21):214106, 2006. doi:10.1063/1.2390643.

[55] D. Sheng, S. Li, N. Dural, and M. V. Romalis. Subfemtotesla scalar atomic magnetometry using multipass cells. *Physical Review Letters*, 110(16):160802, 2013. doi:10.1103/PhysRevLett.110.160802.

[56] H. B. Dang, A. C. Maloof, and M. V. Romalis. Ultrahigh sensitivity magnetic field and magnetization measurements with an atomic magnetometer. *Applied Physics Letters*, 97(15):151110, 2010. doi:10.1063/1.3491215.

[57] J. C. Allred, R. N. Lyman, T. W. Kornack, and M. V. Romalis. High-sensitivity atomic magnetometer unaffected by spin-exchange relaxation. *Physical Review Letters*, 89(13):130801, 2002. doi:10.1103/PhysRevLett.89.130801.

[58] M. P. Ledbetter, I. M. Savukov, V. M. Acosta, D. Budker, and M. V. Romalis. Spin-exchange-relaxation-free magnetometry with Cs vapor. *Physical Review A*, 77(3): 033408, 2008. doi:10.1103/PhysRevA.77.033408.

[59] V. Shah and M. V. Romalis. Spin-exchange relaxation-free magnetometry using elliptically polarized light. *Physical Review A*, 80(1):013416, 2009. doi:10.1103/PhysRevA.80.013416.

[60] M. P. Ledbetter, I. M. Savukov, D. Budker, V. Shah, et al. Zero-field remote detection of NMR with a microfabricated atomic magnetometer. *Proceedings of the National Academy of Sciences*, 105(7):2286–2290, 2008. doi:10.1073/pnas.0711505105.

[61] I. M. Savukov, S. J. Seltzer, M. V. Romalis, and K. L. Sauer. Tunable atomic magnetometer for detection of radio-frequency magnetic fields. *Physical Review Letters*, 95(6):063004, 2005. doi:10.1103/PhysRevLett.95.063004.

[62] W. Chalupczak, R. M. Godun, S. Pustelny, and W. Gawlik. Room temperature

femtotesla radio-frequency atomic magnetometer. *Applied Physics Letters*, 100(24): 242401, 2012. doi:10.1063/1.4729016.

[63] R. J. Cooper, D. W. Prescott, P. Matz, K. L. Sauer, et al. Atomic magnetometer multisensor array for RF interference mitigation and unshielded detection of nuclear quadrupole resonance. *Physical Review Applied*, 6(6):064014, 2016. doi:10.1103/PhysRevApplied.6.064014.

[64] D. A. Keder, D. W. Prescott, A. W. Conovaloff, and K. L. Sauer. An unshielded radio-frequency atomic magnetometer with sub-femtoTesla sensitivity. *AIP Advances*, 4 (12):127159, 2014. doi:10.1063/1.4905449.

[65] A. Horsley and P. Treutlein. Frequency-tunable microwave field detection in an atomic vapor cell. *Applied Physics Letters*, 108(21):211102, 2016. doi:10.1063/1.4950805.

[66] D. Budker, D. F. Kimball, V. V. Yashchuk, and M. Zolotorev. Nonlinear magneto-optical rotation with frequency-modulated light. *Physical Review A*, 65(5):055403, 2002. doi:10.1103/PhysRevA.65.055403.

[67] D. Budker, D. F. Kimball, S. M. Rochester, V. V. Yashchuk, and M. Zolotorev. Sensitive magnetometry based on nonlinear magneto-optical rotation. *Physical Review A*, 62(4):043403, 2000. doi:10.1103/PhysRevA.62.043403.

[68] S. Pustelny, A. Wojciechowski, M. Gring, M. Kotyrba, et al. Magnetometry based on nonlinear magneto-optical rotation with amplitude-modulated light. *Journal of Applied Physics*, 103(6):063108, 2008. doi:10.1063/1.2844494.

[69] M. P. Ledbetter, V. M. Acosta, S. M. Rochester, D. Budker, et al. Detection of radio-frequency magnetic fields using nonlinear magneto-optical rotation. *Physical Review A*, 75(2):023405, 2007. doi:10.1103/PhysRevA.75.023405.

[70] C. Affolderbach, M. Sthler, S. Knappe, and R. Wynands. An all-optical, high-sensitivity magnetic gradiometer. *Applied Physics B*, 75(6-7):605–612, 2002. doi:10.1007/s00340-002-0959-8.

[71] G. Liu and S. Gu. Experimental study of the CPT magnetometer worked on atomic

energy level modulation. *Journal of Physics B: Atomic, Molecular and Optical Physics*, 43(3):035004, 2010. doi:10.1088/0953-4075/43/3/035004.

[72] E. Breschi, Z. D. Gruji, P. Knowles, and A. Weis. A high-sensitivity push-pull magnetometer. *Applied Physics Letters*, 104(2):023501, 2014. doi:10.1063/1.4861458.

[73] H. Xia, A. B. Baranga, D. Hoffman, and M. V. Romalis. Magnetoencephalography with an atomic magnetometer. *Applied Physics Letters*, 89(21):211104, 2006. doi:10.1063/1.2392722.

[74] C. N. Johnson, P. D. D. Schwindt, and M. Weisend. Multi-sensor magnetoencephalography with atomic magnetometers. *Physics in Medicine & Biology*, 58(17): 6065, 2013. doi:10.1088/0031-9155/58/17/6065.

[75] E. Boto, N. Holmes, J. Leggett, G. Roberts, et al. Moving magnetoencephalography towards real-world applications with a wearable system. *Nature*, 555(7698):657, 2018. doi:10.1038/nature26147.

[76] R. Wyllie, M. Kauer, G. S. Smetana, R. T. Wakai, and T. G. Walker. Magnetocardiography with a modular spin-exchange relaxation-free atomic magnetometer array. *Physics in Medicine & Biology*, 57(9):2619, 2012. doi:10.1088/0031-9155/57/9/2619.

[77] R. Wyllie, M. Kauer, R. T. Wakai, and T. G. Walker. Optical magnetometer array for fetal magnetocardiography. *Optics Letters*, 37(12):2247–2249, 2012. doi:10.1364/OL.37.002247.

[78] O. Alem, T. H. Sander, R. Mhaskar, J. LeBlanc, et al. Fetal magnetocardiography measurements with an array of microfabricated optically pumped magnetometers. *Physics in Medicine & Biology*, 60(12):4797, 2015. doi:10.1088/0031-9155/60/12/4797.

[79] K. Jensen, R. Budvytyte, R. A. Thomas, T. Wang, et al. Non-invasive detection of animal nerve impulses with an atomic magnetometer operating near quantum limited sensitivity. *Scientific Reports*, 6:29638, 2016. doi:10.1038/srep29638.

[80] S. Xu, V. V. Yashchuk, M. H. Donaldson, S. M. Rochester, et al. Magnetic resonance

imaging with an optical atomic magnetometer. *Proceedings of the National Academy of Sciences*, 103(34):12668–12671, 2006. doi:10.1073/pnas.0605396103.

[81] I. M. Savukov and T. Karaulanov. Multi-flux-transformer MRI detection with an atomic magnetometer. *Journal of Magnetic Resonance*, 249:49–52, 2014. doi:10.1016/j.jmr.2014.10.009.

[82] I. M. Savukov and M. V. Romalis. NMR Detection with an Atomic Magnetometer. *Physical Review Letters*, 94(12):123001, 2005. doi:10.1103/PhysRevLett.94.123001.

[83] I. M. Savukov, S. J. Seltzer, and M. V. Romalis. Detection of NMR signals with a radio-frequency atomic magnetometer. *Journal of Magnetic Resonance*, 185(2): 214–220, 2007. doi:10.1016/j.jmr.2006.12.012.

[84] G. Bevilacqua, V. Biancalana, Y. Dancheva, and L. Moi. All-optical magnetometry for NMR detection in a micro-Tesla field and unshielded environment. *Journal of Magnetic Resonance*, 201(2):222–229, 2009. doi:10.1016/j.jmr.2009.09.013.

[85] G. Bevilacqua, V. Biancalana, Y. Dancheva, A. Vigilante, et al. Simultaneous detection of H and D NMR signals in a micro-Tesla field. *Journal of Physical Chemistry Letters*, 2017. doi:10.1021/acs.jpclett.7b02854.

[86] L. Bougas, L. D. Langenegger, C. A. Mora, M. Zeltner, et al. Nondestructive inline sub-picomolar detection of magnetic nanoparticles in flowing complex fluids. *Scientific Reports*, 8(1):3491, 2018. doi:10.1038/s41598-018-21802-2.

[87] A. David, M. Cole, T. Horsley, N. Linford, et al. A rival to Stonehenge? Geophysical survey at Stanton Drew, England, 2004.

[88] V. Mathé, F. Lévêque, P. Mathé, C. Chevallier, and Y. Pons. Soil anomaly mapping using a caesium magnetometer: Limits in the low magnetic amplitude case. *Journal of Applied Geophysics*, 58(3):202–217, 2006. doi:10.1016/j.jappgeo.2005.06.004.

[89] T. W. Kornack, G. Vasilakis, and M. V. Romalis. Preliminary results from a test of CPT and lorentz symmetry using a K-^{3}He co-magnetometer. *World Scientific Publishing Company*, 1:206–213, 2008. doi:10.1142/9789812779519_0030.

[90] S. Pustelny, D. F. Kimball, C. Pankow, M. P. Ledbetter, et al. The global network of optical magnetometers for exotic physics (GNOME): A novel scheme to search for physics beyond the standard model. *Annalen der Physik*, 525(8-9):659–670, 2013. doi:10.1002/andp.201300061.

[91] M. V. Balabas, D. Budker, J. Kitching, P. D. D. Schwindt, and J. E. Stalnaker. Magnetometry with millimeter-scale antirelaxation-coated alkali-metal vapor cells. *JOSA B*, 23(6):1001–1006, 2006. doi:10.1364/josab.23.001001.

[92] V. Shah, S. Knappe, P. D. D. Schwindt, and J. Kitching. Subpicotesla atomic magnetometry with a microfabricated vapour cell. *Nature Photonics*, 1(11):649, 2007. doi:10.1038/nphoton.2007.201.

[93] W. C. Griffith, S. Knappe, and J. Kitching. Femtotesla atomic magnetometry in a microfabricated vapor cell. *Optics Express*, 18(26):27167–27172, 2010. doi:10.1364/OE.18.027167.

[94] QuSpin. Quspin zero-field magnetometer (QZFM). *[Retrieved; 30 May 2018]*, 2018. URL `https://quspin.com/products-qzfm/`.

[95] R. L. Fagaly. Superconducting quantum interference device instruments and applications. *Review of Scientific Instruments*, 77(10):101101, 2006. doi:10.1063/1.2354545.

[96] R. Hari and R. Salmelin. Magnetoencephalography: From SQUIDs to neuroscience: Neuroimage 20th anniversary special edition. *NeuroImage*, 61(2):386–396, 2012. doi:10.1016/j.neuroimage.2011.11.074.

[97] F. Primdahl. The fluxgate magnetometer. *Journal of Physics E: Scientific Instruments*, 12(4):241, 1979. doi:10.1088/0022-3735/12/4/001.

[98] G. Musmann. *Fluxgate magnetometers for space research*. BoD–Books on Demand, 2010.

[99] R. H. Koch, J. G. Deak, and G. Grinstein. Fundamental limits to magnetic-field sensitivity of flux-gate magnetic-field sensors. *Applied Physics Letters*, 75(24):3862, 1999. doi:10.1063/1.125481.

[100] S. Tumanski. Induction coil sensors: A review. *Measurement Science and Technology*, 18(3):R31, 2007. doi:10.1088/0957-0233/18/3/R01.

[101] L. Rondin, J. Tetienne, T. Hingant, J. Roch, et al. Magnetometry with nitrogen-vacancy defects in diamond. *Reports on Progress in Physics*, 77(5):056503, 2014. doi:10.1088/0034-4885/77/5/056503.

[102] J. M. Taylor, P. Cappellaro, L. Childress, L. Jiang, et al. High-sensitivity diamond magnetometer with nanoscale resolution. *Nature Physics*, 4(10):810, 2008. doi:10.1038/nphys1075.

[103] J. R. Maze, P. L. Stanwix, J. S. Hodges, S. Hong, et al. Nanoscale magnetic sensing with an individual electronic spin in diamond. *Nature*, 455(7213):644, 2008. doi:10.1038/nature07279.

[104] S. Hong, M. S. Grinolds, L. M. Pham, D. Le Sage, et al. Nanoscale magnetometry with NV centers in diamond. *MRS bulletin*, 38(2):155–161, 2013. doi:10.1557/mrs.2013.23.

[105] M. S. Grinolds, S. Hong, P. Maletinsky, L. Luan, et al. Nanoscale magnetic imaging of a single electron spin under ambient conditions. *Nature Physics*, 9(4):215, 2013. doi:10.1038/nphys2543.

[106] A. Waxman, Y. Schlussel, D. Groswasser, V. M. Acosta, et al. Diamond magnetometry of superconducting thin films. *Physical Review B*, 89(5):054509, 2014. doi:10.1103/PhysRevB.89.054509.

[107] P. Appel, M. Ganzhorn, E. Neu, and P. Maletinsky. Nanoscale microwave imaging with a single electron spin in diamond. *New Journal of Physics*, 17(11):112001, 2015. doi:10.1088/1367-2630/17/11/112001.

[108] H. Griffiths, W. Gough, S. Watson, and R. J. Williams. Residual capacitive coupling and the measurement of permittivity in magnetic induction tomography. *Physiological Measurement*, 28(7):S301, 2007. doi:10.1088/0967-3334/28/7/S23.

[109] A. Wickenbrock, F. Tricot, and F. Renzoni. Magnetic induction measurements using an all-optical 87rb atomic magnetometer. *Applied Physics Letters*, 103(24):243503, 2013. doi:10.1063/1.4848196.

[110] A. Wickenbrock, S. Jurgilas, A. Dow, L. Marmugi, and F. Renzoni. Magnetic induction tomography using an all-optical ^{87}Rb atomic magnetometer. *Optics Letters*, 39 (22):6367–6370, 2014. doi:10.1364/OL.39.006367.

[111] A. Wickenbrock, N. Leefer, J. W. Blanchard, and D. Budker. Eddy current imaging with an atomic radio-frequency magnetometer. *Applied Physics Letters*, 108(18): 183507, 2016. doi:10.1063/1.4948534.

[112] H. Griffiths, W. R. Stewart, and W. Gough. Magnetic Induction Tomography: A Measuring System for Biological Tissues. *Annals of the New York Academy of Sciences*, 873(1):335–345, 1999. doi:10.1111/j.1749-6632.1999.tb09481.x.

[113] A. Korjenevsky, V. Cherepenin, and S. Sapetsky. Magnetic induction tomography: Experimental realization. *Physiological Measurement*, 21(1):89, 2000. doi:10.1088/0967-3334/21/1/311.

[114] H. L. Libby. *Introduction to electromagnetic nondestructive test methods*. Krieger, 1971.

[115] A. Vander Vorst, A. Rosen, and Y. Kotsuka. RF/microwave interaction mechanisms in biological materials. In *RF/Microwave Interaction with Biological Tissues*, pages 63–92. Wiley-Blackwell, 2006. doi:10.1002/0471752053.ch2.

[116] E. C. Jordan and K. G. Balmain. Electromagnetic waves and radiating systems, prentice hall. *Englewood Cliffs, New Jersey*, 1968.

[117] R. Casañas, H. Scharfetter, A. Altes, and J. Rosell. Magnetic induction system for non-invasive measurement of susceptibility and conductivity of biological tissues. In *Proceedings*. XI ICEBI, 2001.

[118] W. J. Duffin. *Electricity and magnetism*. McGraw-Hill, 1980.

[119] E. R. Dobbs. *Basic electromagnetism*. Springer Science & Business Media, 2013.

[120] B. I. Bleaney and B. Bleaney. *Electricity and Magnetism, Volume 2*. Oxford University Press, 2013.

[121] R. M. Fish and L. A. Geddes. Conduction of electrical current to and through the human body: A review. *Eplasty*, 9, 2009. URL `https://www.ncbi.nlm.nih.gov/pubmed/19907637`.

[122] T. J. C. Faes, H. A. van der Meij, J. C. de Munck, and R. M. Heethaar. The electric resistivity of human tissues (100 Hz – 10 MHz): A meta-analysis of review studies. *Physiological Measurement*, 20(4):R1, 1999. doi:10.1088/0967-3334/20/4/201.

[123] R. Merwa, K. Hollaus, P. Brunner, and H. Scharfetter. Solution of the inverse problem of magnetic induction tomography (MIT). *Physiological Measurement*, 26(2):S241, 2005. doi:10.1088/0967-3334/26/2/023.

[124] K. Hollaus, C. Magele, R. Merwa, and H. Scharfetter. Numerical simulation of the eddy current problem in magnetic induction tomography for biomedical applications by edge elements. *IEEE Transactions on Magnetics*, 40(2):623–626, 2004. doi:10.1109/tmag.2004.825424.

[125] R. Merwa, K. Hollaus, B. Brandsttter, and H. Scharfetter. Numerical solution of the general 3D eddy current problem for magnetic induction tomography (spectroscopy). *Physiological Measurement*, 24(2):545, 2003. doi:10.1088/0967-3334/24/2/364.

[126] A. R. Borges, J. E. De Oliveira, J. Velez, C. Tavares, et al. Development of electromagnetic tomography (EMT) for industrial applications. Part 2: Image reconstruction and software framework. In *Proc. 1st World Congr. Industrial Process Tomography*, pages 219–225, 1999. URL `http://citeseerx.ist.psu.edu/viewdoc/summary?doi=10.1.1.548.2972`.

[127] A. Tarantola. *Inverse problem theory and methods for model parameter estimation, Volume 89*. SIAM, 2005.

[128] D. A. Steck. Rubidium 85 D line data (2008). *[Revised; 20 September 2013]*, 2001. URL `http://www.steck.us/alkalidata/rubidium85numbers.pdf`.

[129] D. A. Steck. Rubidium 87 D line data (2001). *[Revised; 13 January 2015]*, 2008. URL `http://www.steck.us/alkalidata/rubidium87numbers.pdf`.

[130] G. Breit and I. I. Rabi. Measurement of nuclear spin. *Physical Review*, 38(11):2082, 1931. doi:10.1103/PhysRev.38.2082.2.

[131] W. Happer. Optical Pumping. *Reviews of Modern Physics*, 44(2):169, 1972. doi:10.1103/RevModPhys.44.169.

[132] S. J. Seltzer. *Developments in alkali-metal atomic magnetometry*. PhD thesis, Princeton University, 2008. URL `http://adsabs.harvard.edu/abs/2008PhDT.....309S`.

[133] U. Volz and H. Schmoranzer. Precision lifetime measurements on alkali atoms and on helium by beamgaslaser spectroscopy. *Physica Scripta*, 1996(T65):48, 1996. doi:10.1088/0031-8949/1996/T65/007.

[134] F. Bloch. Nuclear induction. *Physical Review*, 70(7-8):460, 1946. doi:10.1103/PhysRev.70.460.

[135] A. Abragam. *The principles of nuclear magnetism*. Oxford University Press, 1961.

[136] S. Appelt, A. B. Baranga, C. J. Erickson, M. V. Romalis, et al. Theory of spin-exchange optical pumping of ^{3}He and ^{129}Xe. *Physical Review A*, 58(2):1412, 1998. doi:10.1103/PhysRevA.58.1412.

[137] C. J. Erickson. *Measurements of the magnetic field dependence of the spin relaxation rate in alkali metal vapors*. PhD thesis, Princeton University, 2000. URL `http://adsabs.harvard.edu/abs/2000PhDT.....21E`.

[138] W. Happer and B. S. Mathur. Effective operator formalism in optical pumping. *Physical Review*, 163(1):12, 1967. doi:10.1103/PhysRev.163.12.

[139] V. G. Lucivero, P. Anielski, W. Gawlik, and M. W. Mitchell. Shot-noise-limited magnetometer with sub-picotesla sensitivity at room temperature. *Review of Scientific Instruments*, 85(11):113108, 2014. doi:10.1063/1.4901588.

[140] M. A. Rosenberry, J. P. Reyes, D. Tupa, and T. J. Gay. Radiation trapping in rubidium optical pumping at low buffer-gas pressures. *Physical Review A*, 75(2):023401, 2007. doi:10.1103/PhysRevA.75.023401.

[141] F. A. Franz. Enhancement of alkali optical pumping by quenching. *Physics Letters A*, 27(7):457–458, 1968. doi:10.1016/0375-9601(68)90858-X.

[142] D. K. Walter, W. M. Griffith, and W. Happer. Magnetic slowing down of spin relaxation due to binary collisions of alkali-metal atoms with buffer-gas atoms. *Physical Review Letters*, 88(9):093004, 2002. doi:10.1103/PhysRevLett.88.093004.

[143] A. B. Baranga, S. Appelt, M. V. Romalis, C. J. Erickson, et al. Polarization of ^{3}He by spin exchange with optically pumped Rb and K vapors. *Physical Review Letters*, 80(13):2801, 1998. doi:10.1103/PhysRevLett.80.2801.

[144] M. E. Wagshul and T. E. Chupp. Laser optical pumping of high-density Rb in polarized ^{3}He targets. *Physical Review A*, 49(5):3854, 1994. doi:10.1103/PhysRevA.49.3854.

[145] T. Jeong, J. Y. Won, and H. Noh. Line shapes in polarization spectroscopy for the rubidium D1 line in an external magnetic field. *Optics Communications*, 292:106–110, 2013. doi:10.1016/j.optcom.2012.11.069.

[146] J. Belfi, G. Bevilacqua, V. Biancalana, S. Cartaleva, et al. Cesium coherent population trapping magnetometer for cardiosignal detection in an unshielded environment. *JOSA B*, 24(9):2357–2362, 2007. doi:10.1364/JOSAB.24.002357.

[147] S. J. Smullin, I. M. Savukov, G. Vasilakis, R. K. Ghosh, and M. V. Romalis. Low-noise high-density alkali-metal scalar magnetometer. *Physical Review A*, 80(3): 033420, 2009. doi:10.1103/PhysRevA.80.033420.

[148] W. M. Haynes. *CRC handbook of chemistry and physics*. CRC press, 2014.

[149] Goodfellow. Titanium/Aluminium/Vanadium foil TI010500 - Goodfellow catalogue. *[Retrieved; 10 October 2016]*, 2016. URL `goodfellow.com`.

[150] Goodfellow. Carbon foil C 007912 - Goodfellow catalogue. *[Retrieved; 10 October 2016]*, 2016. URL `goodfellow.com`.

[151] P. Echlin. *Handbook of Sample Preparation for Scanning Electron Microscopy and X-Ray Microanalysis*. Springer Science & Business Media, 2011.

[152] T. Kunz, M. T. Hessmann, S. Seren, B. Meidel, et al. Dopant mapping in highly p-doped silicon by micro-Raman spectroscopy at various injection levels. *Journal of Applied Physics*, 113(2):023514, 2013. doi:10.1063/1.4773110.

[153] J. Millan, P. Godignon, X. Perpina, A. Perez-Tomas, and J. Rebollo. A survey of wide bandgap power semiconductor devices. *IEEE Transactions on Power Electronics*, 29 (5):2155–2163, 2014. doi:10.1109/TPEL.2013.2268900.

[154] K. Yoshikawa, H. Kawasaki, W. Yoshida, T. Irie, et al. Silicon heterojunction solar cell with interdigitated back contacts for a photoconversion efficiency over 26%. *Nature Energy*, 2(5):17032, 2017. doi:10.1038/nenergy.2017.32.

[155] D. G. Gilles and R. C. Loehr. Waste generation and minimization in semiconductor industry. *Journal of Environmental Engineering*, 120(1):72–86, 1994. doi:10.1061/(ASCE)0733-9372(1994)120:1(72).

[156] V. A. Fedorov, S. A. Kozlov, N. A. Potolokov, and S. V. Nikolashin. Preparation of high-purity gallium from semiconductor fabrication waste. *Inorganic Materials*, 42 (1):S70–S89, 2006. doi:10.1134/S0020168506130048.

[157] M. Lu, W. Zhu, L. Yin, A. J. Peyton, et al. Reducing the lift-off effect on permeability measurement for magnetic plates from multifrequency induction data. *IEEE Transactions on Instrumentation and Measurement*, 67(1):167–174, 2018. doi:10.1109/TIM.2017.2728338.

[158] M. D. O'Toole, N. Karimian, and A. J. Peyton. Fast classification of non-magnetic metal targets using eddy-current based impedance spectroscopy. In *SENSORS*, pages 1–3. IEEE, 2017. doi:10.1109/ICSENS.2017.8234219.

[159] N. Jaccard, T. W. Rogers, and L. D. Griffin. Automated detection of cars in transmission X-ray images of freight containers. In *Advanced Video and Signal Based Surveillance (AVSS)*, pages 387–392. IEEE, 2014. doi:10.1109/AVSS.2014.6918699.

[160] V. V. Verbinski and V. J. Orphan. Vehicle and cargo inspection system. In *International Conference Neutrons in Research and Industry*, volume 2867, pages 235–239. International Society for Optics and Photonics, 1997. doi:10.1117/12.267908.

[161] V. J. Orphan, E Muenchau, J. Gormley, and R. Richardson. Advanced ray technology for scanning cargo containers. *Applied Radiation and Isotopes*, 63(5-6):723–732, 2005. doi:10.1016/j.apradiso.2005.05.033.

[162] D. R. Brown and T. Gozani. Cargo inspection system based on pulsed fast neutron analysis. *Nuclear Instruments and Methods in Physics Research Section B: Beam Interactions with Materials and Atoms*, 99(1-4):753–756, 1995. doi:10.1016/0168-583X(94)00749-7.

[163] G. Vourvopoulos and P. C. Womble. Pulsed fast/thermal neutron analysis: a technique for explosives detection. *Talanta*, 54(3):459–468, 2001. doi:10.1016/S0039-9140(00)00544-0.

[164] V. Torre and T. A. Poggio. On edge detection. *IEEE Transactions on Pattern Analysis and Machine Intelligence*, PAMI-8(2):147–163, 1986. doi:10.1109/TPAMI.1986.4767769.

[165] J. Canny. A computational approach to edge detection. *IEEE Transactions on Pattern Analysis and Machine Intelligence*, PAMI-8(6):679–698, 1986. doi:10.1109/TPAMI.1986.4767851.

[166] C. Deans, L. D. Griffin, L. Marmugi, and F. Renzoni. Datasets for machine learning based localization and classification with atomic magnetometers. *figshare [online; 19 January 2018]*, 2018. doi:10.6084/m9.figshare.c.3980910.

[167] C. Schaffer. Selecting a classification method by cross-validation. *Machine Learning*, 13(1):135–143, 1993. doi:10.1007/BF00993106.

[168] C. Cortes and V. Vapnik. Support-vector networks. *Machine Learning*, 20(3):273–297, 1995. doi:10.1007/BF00994018.

[169] S. Gabriel, R. W. Lau, and C. Gabriel. The dielectric properties of biological tissues: II. Measurements in the frequency range 10 Hz to 20 GHz. *Physics in Medicine & Biology*, 41(11):2251, 1996. doi:10.1088/0031-9155/41/11/002.

[170] V. Gerginov, F. C. S. da Silva, and D. Howe. Prospects for magnetic field communications and location using quantum sensors. *Review of Scientific Instruments*, 88 (12):125005, 2017. doi:10.1063/1.5003821.

[171] D. A. Abraham and P. K. Willett. Active sonar detection in shallow water using the Page test. *IEEE Journal of Oceanic Engineering*, 27(1):35–46, 2002. doi:10.1109/48.989883.

[172] C. Deans, L. Marmugi, and F. Renzoni. Video demonstration of active detection with an array of atomic magnetometers. *[Online; 12 November 2017]*, 2017. doi:10.6084/m9.figshare.5674795.

[173] W. Ellison, A. Balana, G. Delbos, K. Lamkaouchi, et al. New permittivity measurements of seawater. *Radio Science*, 33(3):639–648, 1998. doi:10.1029/97RS02223.

[174] G. Benelli and A. Pozzebo. RFID under water: Technical issues and applications. In *Radio Frequency Identification from System to Applications*. InTech, 2013. doi:10.5772/53934.

[175] M. El Hachemi Benbouzid. A review of induction motors signature analysis as a medium for faults detection. *IEEE Transactions on Industrial Electronics*, 47(5): 984–993, 2000. doi:10.1109/41.873206.

[176] J. De Fauw, J. R. Ledsam, B. Romera-Paredes, B. Nikolov, et al. Clinically applicable deep learning for diagnosis and referral in retinal disease. *Nature Medicine*, page 1, 2018. doi:10.1038/s41591-018-0107-6.